Imperial College
London

Study of RF Breakdown in Muon Cooling Cavities

A thesis submitted for the Degree of Doctor of Philosophy of the
Imperial College London
and
Diploma of Imperial College

By
Arash Zarrebini-Esfahani

October 2015

Department of Mechanical Engineering

Imperial College London

SW7 2AZ

To My Parents …

Acknowledgements

The work carried out during this study was only made possible with the support of some special people, few of whom I would like to thank here.

First and foremost I should express my highest degree of appreciation to my project supervisors Dr Mike Ristic and Professor Ken Long. Their insight, enthusiasm, advice, patience and constant unconditional support over the past few years was essential to the success of my work.

I am extremely thankful to Dr Morteza Aslaninejad and Dr Rebecca Seviour who gave me many invaluable suggestions and made productive comments on my work. I am indebted to them and my work would not be where it is without their inputs and collaboration.

Special thanks goes to Dr. Jurgen Pozimski, all members of HEP group, Dr Matt Stables, Alan Bross, and other MICE members for their constructive discussions and helpful meetings.

I would like to thank John Everard for manufacturing my test samples and providing the material. I like to extend my acknowledgements to Dr. Andrew Bowfield for taking the XPS measurements.

I would also like to thank my friends, colleagues and members of staff at Imperial College London for their support.

Last but by no means last, I am sincerely grateful to my parents, brother and sister, without whom my accomplishments in life would have no meaning.

Declaration

I declare that this thesis is a record of the original work carried out by myself under the supervisions of Dr. M Ristic and Prof. K Long in the Department of Mechanical Engineering at Imperial College London during the period of September 2006 to October 2015. The thesis has not been presented elsewhere in consideration for a higher degree. Due acknowledgement must always be made of the use of any material contained in, or derived from this thesis.

Arash Zarrebini-Esfahani

Abstract

Particle accelerators are devices that are capable of forcing charged particles to very high energy levels. Modern particle accelerators are required to produce conditions of extremely high electromagnetic fields in the Radio Frequency (RF) range and produce extremely high accelerating gradients. This has led to various practical issues, one of the most significant being the phenomenon of RF breakdown in the accelerating cavities.

When exposed to an intense electromagnetic field, a conducting surface can emit electrons. In the case of an accelerating cavity, these electrons are further accelerated by the RF field. Such emissions are capable of inflicting irreversible damage on the cavity surface and need to be avoided. Among the factors responsible for initiating such emission, the quality of the cavity surface in combination with the operating conditions has been identified as the main one. The mechanisms involved in the initiation of RF breakdown need to be better understood and related to the cavity design criteria, such that they can lead to correctly specified and reproducible designs.

The cavity surface quality may be characterised in terms of surface finish and its chemical composition, both of which are strongly affected by the manufacturing processes. Unlike previous studies, this research has focused on the analysis of the effects of fabrication procedures on surface quality. The work involved manufacture and surface characterisation of button shaped samples, which were produced using relevant metal forming and polishing techniques, in preparation for future experimentation in a test system at Fermilab, USA.

Although RF breakdown may be initiated locally at the metallic surface, its effects propagate globally across the entire cavity. Surface defects and impurities act as emission sites by inducing local field enhancements. Simulation methods were developed in order to simultaneously study electron emission due to local field enhancement and electron propagation across the cavity, with the benefit of being able to perform tracking in 3D and to verify enhancement factors obtained by theoretical measurements using the surface properties observed on the buttons.

This research was conducted in close collaboration with Daresbury Laboratory and Lancaster University in UK as well as the MTA group Fermilab USA.

List of Figures

List of Tables

Nomenclature

Symbol	Definition
A	Local Emitter Area
Å	Angstroms
a	Acceleration of a Particle
ALD	Atomic Deposition
B	Magnetic field
B_{Comsol}	Static field component 2
Be	Beryllium
b	Asperity Base
b_f	Bravery Factor
$\vec{B}$	Magnetic Field Component
C	Heat Capacity
c	Speed of light
CKOV	Cherenkov Detector
CLA	Centre Line Average
Cu	Copper
D	Cavity gap
DFT	Density Functional Theory
E	Electric field
E_b	Binding Energy of Electron
E_{Comsol}	Static field component 1
E_f	Energy of Fermi Level

E_k	Kilpatrick Limit
E_{ke}	Kinetic Energy of Electron
E_{local}	Local Electric Field
E_m	Effective Energy for SEY Creation
E_p	Energy of the incoming particle
E_{Surf}	Surface Electric Field
E_{Tip}	Electric Magnetic Field
$\vec{E}$	Electric Field Component
EP	Electro Polishing
EPL	Electro Plating
f	Cavity Frequency
FEM	Finite Element Method
Fermilab	Fermi Nation Lab
h	Planck's constant
h_v	Photon Energy
Ha	Hartree Energy
HDPE	High Density Polyethylene
I	Maximum Measured Current per Meter
I_{FN}	Fowler and Nordheim Current
i	Current Density
IDS	International Design Study
JLab	Thomas Jefferson Lab
L	Sample Length
LBNL	Lawrence and Berkley National Lab
λ	Wavelength

M	Field at the tip of the defect
M_{TC}^2	Energy of the target particle
m	Mass of particle
MICE	Muon Ionisation Cooling Experiment
Mo	Molybdenum
MP	Multipacting
MTA	MuCool Testing Area
n	Total Number of Particles
OFHC	Oxygen Free High Conductivity Copper
Q	Cavity Quality Factor
q	Electron Charge
R	Radius of Cavity
R_a	Arithmetic Average Roughness
R_q	Root Mean Square Roughness
r	Radius of Curvature
R_a-R_q	Surface Uniformity
RAL	Rutherford Appleton Laboratory
RK	Runge-Kutta
RF	Radio Frequency
SE	Secondary Electron
SEY	Secondary Electron Yield
T	Tesla
Ti	Titanium
UHV	Ultra High Vacuum
V_0	Angular Frequency

ν	Velocity of Particle
TiN	Titanium Nitride
y	Surface Profile
W	Spectrometer Work Function
XPS	X-ray Photoelectron Spectroscopy
Z	Number of Electrons
ß	Enhancement Factor
γ	Relativistic factor
δ_m	Angle of primary electron
λ_s	Effective Secondary Emission Escape Depth
ρ	Particle momentum
ρ_t	Density of Target Material
Φ	Material Work Function
ω	Operating frequency of cavity in Comsol

Table of Contents

Chapter 1.

Introduction

1.1 Background

Accelerators are devices that are capable of forcing matter to higher energy levels. The term particle accelerator is used to define a device capable of accelerating subatomic charged particles to high speeds and reaching higher energies compared to their rest-mass energy. Particle accelerators give scientists a unique tool for probing the ultra-small scale around us, from the origins of the universe to the structure of the human genome. Nevertheless, accelerators are not just the domain of a research scientist. Over the years, particle accelerators have found their way into various practical applications and have become necessary industrial as well as research tools. The first accelerators were simple machines involving only an electrical potential applied across a gap, but they have evolved over time to become the highly engineered, large machines seen today.

Although particle accelerators have evolved immensely, there are many areas where further improvements are still needed. The new challenges faced by the next generation of accelerators require substantial R&D, primarily because of the need for major improvement in beam intensity, stability, delivery and reachable energy levels. They must significantly out-perform present facilities without a major increase in the size of the structures. One of such systems is the Neutrino factory which is looked into in more detail in 2.3.

A crucial parameter affecting the design, construction and cost of a particle accelerator is the accelerating gradient. Any reduction in the size of an accelerating structure requires that the accelerating gradient is maximised, especially the gradient of the Radio Frequency (RF) cavity. Modern day structures are required to operate in extreme conditions due to the presence of high magnetic field and accelerating gradients. The effect of such conditions can manifest themselves through a phenomenon known as RF breakdown, where a dramatic change in the transmission and reflection of the RF power is observed. Loss of stored energy and reduction in efficiency is a direct result of RF breakdown.

Breakdown regimes have been a serious concern in the accelerator community for many years. One may look at this problem as a direct result of an efficient coupling between the stored energy in the cavity's electromagnetic field (EM) and a small section of the surface material. Although extensive research has been conducted, no conclusive answers have been established for the precise mechanism of RF breakdown. Several causes have been identified, but the complex nature of the problem makes them difficult to predict as introduced in Chapter 3.

1.2 Aims and Objectives

Manufacture of high gradient RF cavities for the Neutrino factory has proved difficult. Achievable accelerating fields have been low as shown in various studies while manufacturing processes to fabricate a series of cavities have been poor. A number of possible explanations for poor reproducibility and lower than predicted performance of high gradient cavities have been proposed. The original aim of this research was to investigate current manufacturing techniques for RF cavities and to propose improvements to the manufacturing process. However, a closer look at the

processes has revealed shortcomings in the fundamental understanding regarding some of the key manufacturing processes. This lack of understanding can jeopardise the reliability of future accelerating structures. For instance RF cavity breakdown is a phenomenon which severely limits the performance of the accelerator. The quality of the RF surface has been identified as a major factor contributing to RF breakdown, but the required surface characteristics from an engineering point of view have been hard to define.

In order to develop better means of production, it is vital to improve our understanding of how the fabrication procedure influences the chemical and physical characteristics of the cavity surface. Hence, this research aims to provide an improved understanding of the surface science and engineering methods needed to develop techniques that ensure reproducibility with the highest achievable gradient. This work introduces the systematic approach used to characterise various stages of cavity production.

Charge carrier dynamic is also important for the operation of high gradient cavities. The accelerating electric field (E) in each cavity is coupled to the magnetic field (B), inducing currents in the cavity surface. Any factors that limit the current flow on the surface will limit the achievable accelerating gradient. Therefore, this research also aims to investigate the effects of cavity surface characteristics on the charge carrier dynamics. The behaviour of free electrons emitted from the cavity surface is of particular interest.

Cavities represent a significant part of the overall accelerating structure and improvements in the efficiency in the manufacturing procedure are needed. As well as being an interesting surface science in its own right, the research carried out can

also provide useful knowledge in parallel with other findings in the research area. The overall objectives of this research are:

- Characterisation of the cavity surface quality at various stages of manufacture
- Performance evaluation of the manufactured cavity surface under design conditions
- Development of suitable methods to analyse the changes made to RF field and electron behaviour inside an RF cavity due to surface defects
- Identify and propose improvements to the current production procedure

1.3 Structure of the Thesis

This work investigates the production techniques for RF cavities and the effects of surface features on the behaviour of electrons during RF cavity operation. The outline of the thesis is summarised below.

Chapter 2 highlights the need for particle accelerators and provides a brief look at their history and evolution. The Neutrino Factory complex is presented together with the MICE experiment and the MTA testing area.

RF breakdown is introduced in Chapter 3, where it is identified as a major challenge to the RF cavity operation. Several previously identified breakdown regimes are discussed followed by a series of obtained MTA results.

Chapter 4 provides a detailed description of the experimental setup designed to manufacture and characterise a series of test samples. This includes the overall production steps taken and the surface characterisation techniques employed.

The experimental results and their analysis are presented in Chapter 5. This highlights the effects of various production techniques on the overall quality of the produced RF surface.

Chapter 6 presents the theoretical work used to investigate charge carrier dynamics. Various FEM simulation models are introduced and a detailed description of the particle tracking algorithm, developed in this work is presented.

The simulation studies and their results are presented in Chapter 7. The details of model setup, meshing procedure and defect modelling are presented. The tracking algorithms were evaluated through conducting various particle tracking algorithms. The results from a scaling study are presented.

The conclusions of this research are presented in Chapter 8. Future improvements and suggestions for further research are also proposed.

Chapter 2.

Particle Accelerators

2.1 The Need for Particle Accelerators

The structure of an atomic nucleus can be revealed by bombarding it with suitable particles and analysing the elastic scattering energy of the released particles. It is vital to use a particle beam with a resolution small enough to effectively penetrate the nucleus. De Broglie's expression states that particle can exhibit properties of waves where their wavelength (λ) is inversely proportional to the particles momentum [1, 2].

$$\lambda = \frac{h}{p} \tag{2-1}$$

where h is the Planck's constant (J.s) and p is the linear momentum of the particle.

For smaller particles to be identified, the momentum of the incident beam particle, and the energy level required needs to be increased. For instance, 1 GeV of energy is required for a proton beam with a particle diameter of about 10^{-15} m to be visible. To obtain more detailed information, the energy level and luminosity of the incident beams has to be considerably higher [1-4]. Typically the rest mass of a particle is expressed in terms of energy through Einstein's equivalence of mass and energy equation given below, where m and c are the mass of particle speed of light.

$$E_p = mc^2 \tag{2-2}$$

It is possible to create particle-antiparticle pairs through inelastic collision of an energetic particle and a target nucleus. For instance, a proton-antiproton pair would require just 2 GeV to be created. In practice however, only part of the energy carried by the incoming proton is available for an inelastic reaction during such collisions. The available energy for creation of particle can be defined as [1, 3, 4]:

$$Enery\ available\ in\ centre\ of\ mass = \sqrt{2E_p M_T C^2} \tag{2-3}$$

where E_p is the energy of the incoming particle and M_TC^2 is the rest energy of the target particle. Because of this, 6.5 GeV is needed to create a proton-antiproton pair, highlighting the need for higher energy levels to produce heavier particles. This has been a motivation for the development of accelerating structures with progressively increasing energy levels.

The true extent of such developments was shown by Livingston in the mid 1950's [1, 2, 4-8]. Every given family of accelerators reaches a saturation point after some time just to be overtaken by a new and more advanced machinery [4, 5, 7, 8]. The Livingston chart demonstrates nearly six decades of continued growth in the energy reach of accelerators. This was driven by continues innovation in acceleration techniques, developed to keep pushing the energy frontier [9]. However, the rate of progress has slowed as shown in an updated Livingston chart shown below in Figure 2-1. It is possible to see that the rate of development no longer proceeds at the rate seen over the previous sixty years, due to difficulties in the developing new technologies. The current energy levels are either twenty years behind or 100 TeV short of the projected Livingston line.

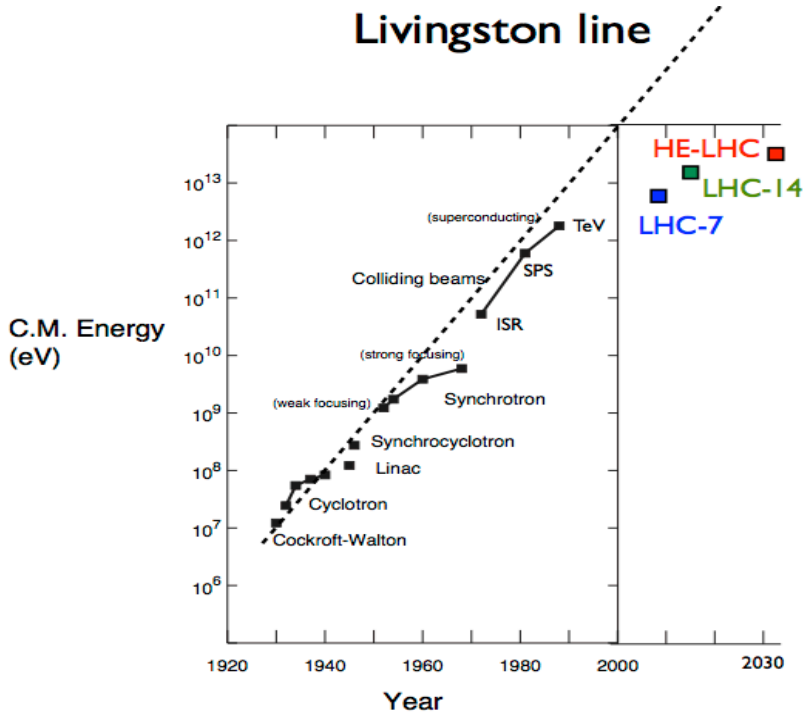

Figure 2-1: Livingston chart [5, 10] demonstrating the progress in the construction of particle accelerators, which shows years on the horizontal axis and collision energy on the vertical axis. The chart is updated to include future developments such as later stages of the LHC

While particle physics research continues to be the dominant driving force behind new accelerator developments, there is also an increasing number of practical applications that have benefited from the use of particle accelerators. Table 2-1 gives a rough estimate on the number of accelerators currently in operation.

Table 2-1: Accelerators in the world [6, 11]

Category	***Number***
Ion implanters and surface modifications	7000
Accelerators in industry	18,700
Accelerators in non-nuclear research	1000
Radiotherapy and medical isotopes	5200
Research in nuclear and particle physics	180

2.2 Classification of Particle Accelerators

Research in accelerator physics can be dated back to as early as 1905 [3], where it was noticed that electrical sparks can travel longer distances in rarefied air tubes. Accelerators are classified into two main types known as the electrostatic and oscillating field accelerators. The basic operating characteristics of each type are introduced below.

2.2.1 Electrostatic Accelerators

Electrostatic accelerators use static electric field to accelerate particles. The first example of such systems goes back to 1838 when Michael Faraday generated light by using a rarefied, air-filled glass tube. This was reproduced by Plucker and Hittorf in 1858 and 1860 respectively through a device known as Geisler tube. These are early examples of cathode ray tubes that are used in television sets and X-ray machines [1, 2, 4-8]. The two most common electrostatic accelerators are the Cockcroft-Walton voltage multiplier and the Van De Graff accelerator as shown in Figure 2-2. Cockcroft and Walton performed the first artificial nuclear disintegration using a high DC voltage generated from a low voltage AC of a pulsating DC input.

A new accelerator design was introduced by Van de Graff in 1931. In this design, the high voltage terminal and acceleration tube is placed in a common tank, allowing spark formation by charging each sphere with an opposite electric charge. Although electrostatic accelerators greatly out-number any other type, they are more suited to lower energy studies due to electrical breakdown [7, 8, 12].

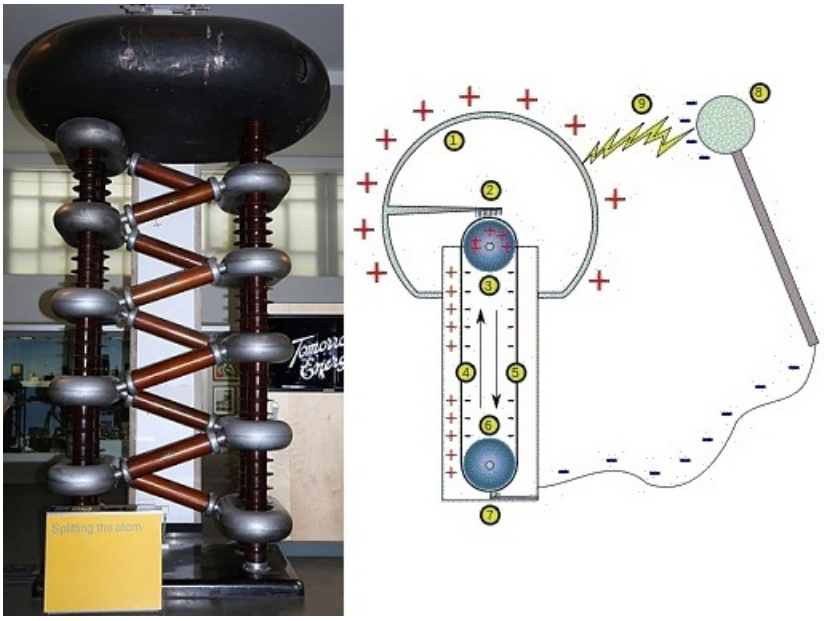

Figure 2-2: Cockcroft-Walton voltage multiplier (left), where a rectifier multiplier produces the applied high voltage. The voltage is practically limited to somewhat above 1 MV due to breakdown of insulation. Van de Graff accelerator (right) using the concept of charge transport. In practice, it is possible to reach voltages of up to 25 MV [3]

2.2.2 Oscillating Field

To avoid the sparking problems observed in electrostatic accelerators, oscillating field accelerators use RF electromagnetic fields to reach higher energies. This idea was initially suggested by Ising in 1924 [8]. Depending on the design, particles can be accelerated either in a straight line or in a circular path.

2.2.2.1 Linear Accelerator

Particles in a linear accelerator travel in a straight line towards a fixed target. As shown in Figure 2-3, a series of tubes, called drift tubes, are used for acceleration when connected to an alternating high electric field. Particles are attracted towards the next tube since it has an opposite polarity. To maintain acceleration, the polarity is switched so that the plate repels the particle once it has travelled through. Linear accelerators are often used to provide an initial low-energy kick to particles before they are injected into circular accelerators [1, 7, 8].

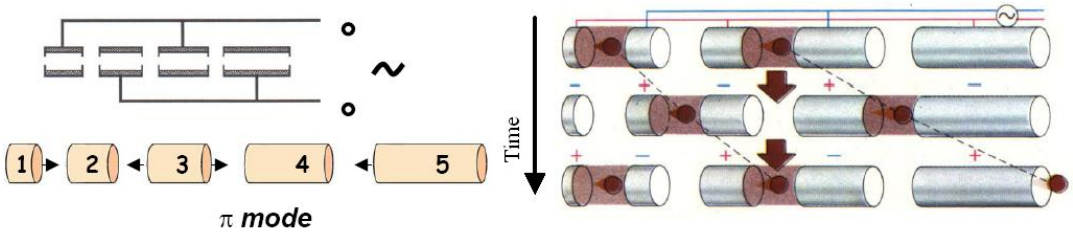

Figure 2-3: Basic operation of the Wideroe linac operating in the μ mode [13]. An element of accelerating column is driven by an alternating voltage, in such way that consecutive electrodes are connected to opposite polarity of the RF generator. The particle is accelerated by reaching the spacing between the electrodes at the right phase of the field. While the polarity change occurs, the particle is in the field free space of the drift tubes

2.2.2.2 Circular Accelerator

In circular accelerators, particles gain higher speeds by moving along a circular path. This invention allows more efficient and powerful accelerators to be developed in a much smaller area. Introduced by Lawrence in 1932, the Cyclotron was the earliest operational circular accelerator. A static and uniform B field is applied perpendicularly to a set of D shaped plates known as Dees, which are connected to an RF electric voltage generator. The particle starts to accelerate as soon as it is injected into the centre of the magnet. As shown in Figure 2-4, the applied (B) field would force the particle to continuously spiral outwards only to be collected at the outer edge when it has reached its maximum energy. The speed of the particle is measured in terms of its energy [4, 5, 8, 14].

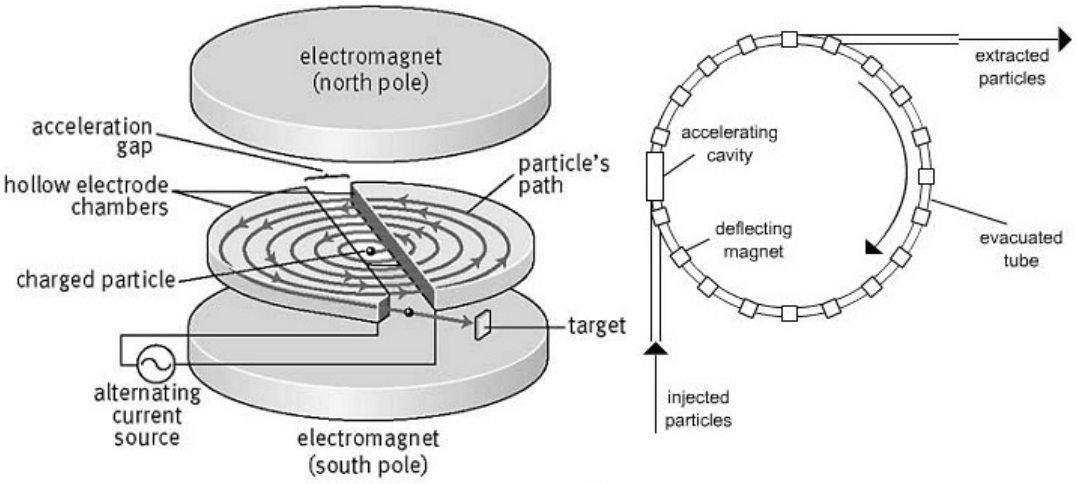

Figure 2-4: Cyclotron layout (left) where charged particles were generated at a central source and accelerated spirally outward through a fixed magnetic and alternating field. Synchrotron layout (right), descended from a cyclotron. The guiding magnetic field is time dependent, being synchronised to a particle beam of increasing kinetic energy [15, 16]

However, reachable energy levels in cyclotron are limited due to orbit instability and relativistic mass effects. Mark Oliphant eliminated this problem in a machine that is known as a synchrotron, where particles are accelerated in a ring of constant radius. This is achieved through local variation of the guiding B field, where it is adapted to the increasing relativistic mass of the particle. This is shown above in Figure 2-4 [4, 7, 12]. Other circular technologies such as betatrons and colliders, which are not covered here, are also available.

2.3 Neutrinos and the Neutrino Factory

For many years, the unsteady continuous energy spectrum of emitted electrons appeared to contradict the conservation of energy law. This contradiction continued until Wolfgang Pauli explained the apparent violation in nuclear beta decay by introducing a new, extremely light and neutral particle called neutrino. While being the most numerous matter particles in the Universe, they are also extremely elusive and were only detected in 1965 by Clyde Cowan and Fredrich

Reines. Recent experiments have shown the non-zero mass of the neutrino disproving the common old belief that the neutrino has zero mass [17-19].

In order to probe physics beyond the current Standard Model, theoretical uncertainties around the state of the Neutrino need to be resolved. This requires next generation neutrino experiments, one being the Neutrino Factory complex. Due to their nature, neutrinos must be produced through a decay process and cannot be accelerated [20, 21]. The role of a Neutrino Factory would be to add energy to the pre-decay, Muons, in order to increase the number of Neutrinos generated through the decay process.

Figure 2-5 shows the overall design of the Neutrino Factory proposed by the International Design Study [22-24]. In order to generate the required Neutrino beam, a high power proton source is needed. Pions are created by bombarding a target and are captured by a magnetic field at low energy where they are allowed to decay to muons. The phase space of the muons is controlled and shrunk through bunching and cooling, before being accelerated and injected into storage rings with long straight sections, where muons decay to produce neutrinos that are directed towards the detectors [22, 25, 26].

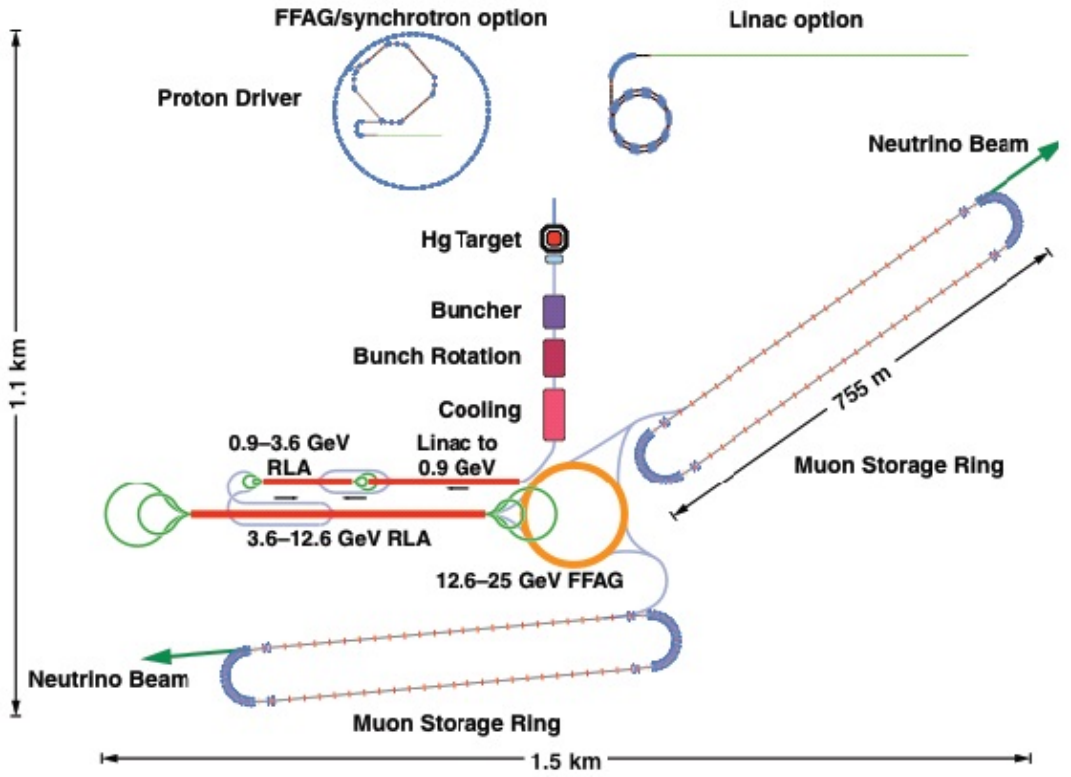

Figure 2-5: Conceptual design of the Neutrino Factory [25]. Mass production of pions that decay into muons is the start of the process. The muons are then accelerated and injected in a decay ring where they decay into neutrinos. This produces a well-defined neutrino beam

There are many technological challenges in each of the systems that need to be evaluated and overcome before a Neutrino Factory facility can be realised. A major concern in such a facility is the quality and shape of the muon beam. As well as the longitudinal phase space which is controlled by bunching, the muon beam also has a transverse phase space issue. The transverse emittance needs to be reduced in order to match the acceptance of the downstream accelerating stages [26, 27]. This is achieved through a technique known as ionisation cooling.

2.4 Ionisation Cooling and the MICE Experiment

Cooling a charged particle beam means reducing its normalised emittance. This phenomenon has been used for over thirty years in accelerator physics to make

beams brighter and to achieve better physics results. Cooling has been a successful ingredient in colliders, where it has led to an increase in beam luminosity [28]. In the case of a muon beam in the Neutrino factory, it is essential to reduce the transverse emittance of the beam by cooling. However, current techniques such as stochastic, electron and laser cooling are not feasible due to the muon's short lifetime of 2.2 μs observed in the Neutrino factory design [21, 26, 29-31]. Ionisation cooling is proposed as a possible solution, where muon beam is cooled through energy loss by passing through absorbing material such as liquid hydrogen. The basic setup consists of a block of absorbing material in which the particles lose energy. This is followed by an accelerating gap such as an RF cavity where the lost energy is restored. The overall process is shown in Figure 2-6.

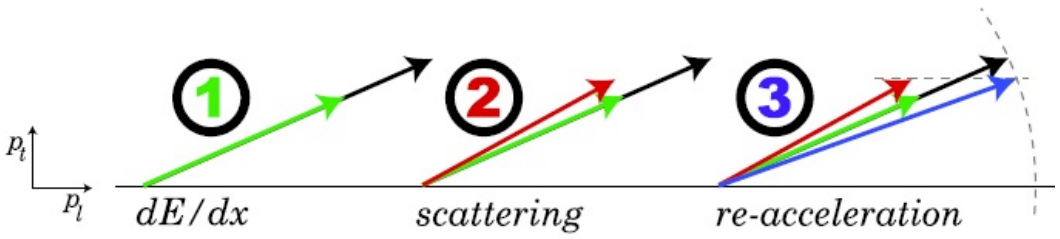

Figure 2-6: The principle of transverse ionisation cooling [26]. A particle passes through an absorber and loses momentum uniformity. This is followed by the longitudinal momentum being restored at the last phase pf the process

Losses in the absorber reduce both the longitudinal and transverse momentum of the particle. When a charged particle passes through matter, it is scattered elastically off the nuclei of the absorber, usually by a small angle. The angular scattering introduces heating of the longitudinal and transverse emittance. The net effect of transverse cooling can be achieved if the longitudinal momentum is restored [26, 28]. This is achieved by RF cavities where only the longitudinal component of the momentum is restored.

The principle of ionisation cooling is well understood theoretically, but it has not been realised in practice. This calls for an extensive R&D program to justify the use of the proposed techniques. The MICE experiment is essentially a proof-of-principle experiment based at the Rutherford Appleton Laboratory (RAL). The objectives of MICE as set in the MICE proposal are [21, 32, 33]:

- To engineer and build a section of the cooling channel capable of giving the desired performance for a Neutrino Factory
- To investigate the limits and practicality of cooling by placing it in a muon beam and measure its performance in various modes of operation

As shown in Figure 2-7, the MICE experiment consists of a cooling section positioned between a pair of particle spectrometers. The 200 MeV muon beam is generated from the ISIS 800 MeV proton beam. Time of flight counters and a Cherenkov detector are used to ensure excellent muon purity by eliminating any proton and pion contamination. The MICE cooling channel consists of tracker and focusing coils, accelerating coupling coils and RF cavities [21, 32, 34].

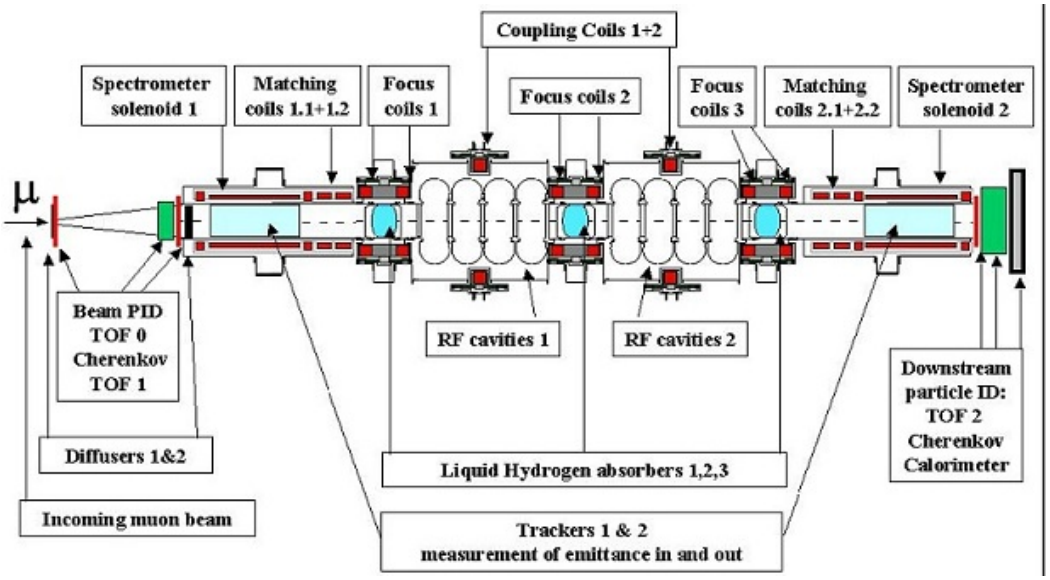

Figure 2-7: Schematic view of the MICE experiment with two accelerating sections [21]

2.4.1 MICE RF Channel

Ionisation energy loss reduces the transverse and longitudinal momentum of a muon beam. However to achieve transverse cooling, the energy lost in the longitudinal direction must be restored. As shown above in Figure 2-7, the MICE cooling channel employs two assemblies of RF cavities each consisting of four 201 MHz cavities. These cavities would be responsible for the restoration of the lost energy of the muon beam and are situated in a focusing solenoid.

As shown in Figure 2-8, the cavity design consists of a round closed pillbox with a 420 mm diameter beam iris. This is to accommodate the large transverse emittance of the muon beam. In order to keep the shunt impedance of the cavity at the desirable level, beryllium windows are used to terminate the RF field at the beam iris. The re-entrant rounded profiles of the cavity ensure lower peak surface fields and higher shunt impedance for a given RF power [21, 34-36].

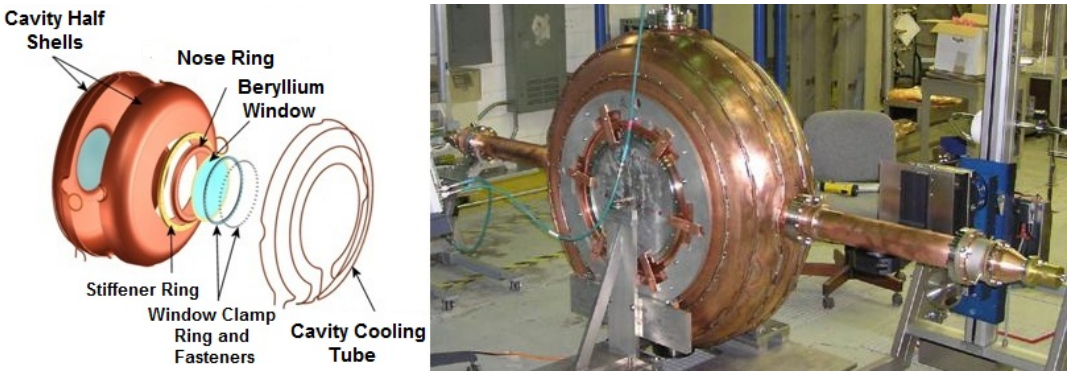

Figure 2-8: MICE cavity layout (left) [37] MICE cavity with RF couplers attached (right) [38]. The cavity uses a series of clamps that are responsible for regulating the operating frequency of the cavity by applying pressure o the stiffener rings. The cavity is kept cool by allowing water to pass through the cooling tubes on the cavity shell

Copper stiffener rings are used to increase the overall rigidity of the cavity structure. RF couplers, vacuum pumps and diagnostics are attached to the cavity through four ports on the edge of the structure. To keep the temperature stable,

chilled water is circulated around the cavity though a series of copper tubes brazed onto the outer surface. The main cavity parameters are given in Table 2-2.

Table 2-2: MICE 201 MHZ cavity parameters [21, 36]

Parameter	Value	Unit
Cavity diameter	121.7	cm
Cavity gap	42	cm
Beam iris diameter	42	cm
Be window thickness	0.38	mm
Cavity quality factor Q	53000	

2.5 MUCOOL Testing Area (MTA)

As noted earlier, RF cavities will be used to restore the lost longitudinal energy in the MICE muon beam. However, such cavities are required to operate in harsh conditions with high accelerating gradient, surface fields and externally applied magnetic fields. In the case of the Neutrino Factory, these conditions will be even more extreme. An extensive R&D program is required to investigate and solve a number of problems regarding high gradient RF fields in low frequency structures.

The MuCool Test Area (MTA) is a dedicated facility built at Fermilab in Chicago, to support technology development for muon ionization cooling channels. The main purpose of the MTA is to assess the characteristics of an RF cavity under the same conditions experienced in a ionisation cooling channel [39, 40]. The main instruments at the MTA are the 201 MHz MICE test cavity and a higher frequency 805 MHz button test cavity. The button experiment conducted in this study is based on the 805 MHz test cavity due to available suitable magnet in the MTA testing area. This is due to available equipment such as a suitable magnet to create

the desired magnetic field needed for such experiment. Figure 2-9 shows the 805 MHz test cavity positioned inside a 4 Tesla (T) superconducting solenoid.

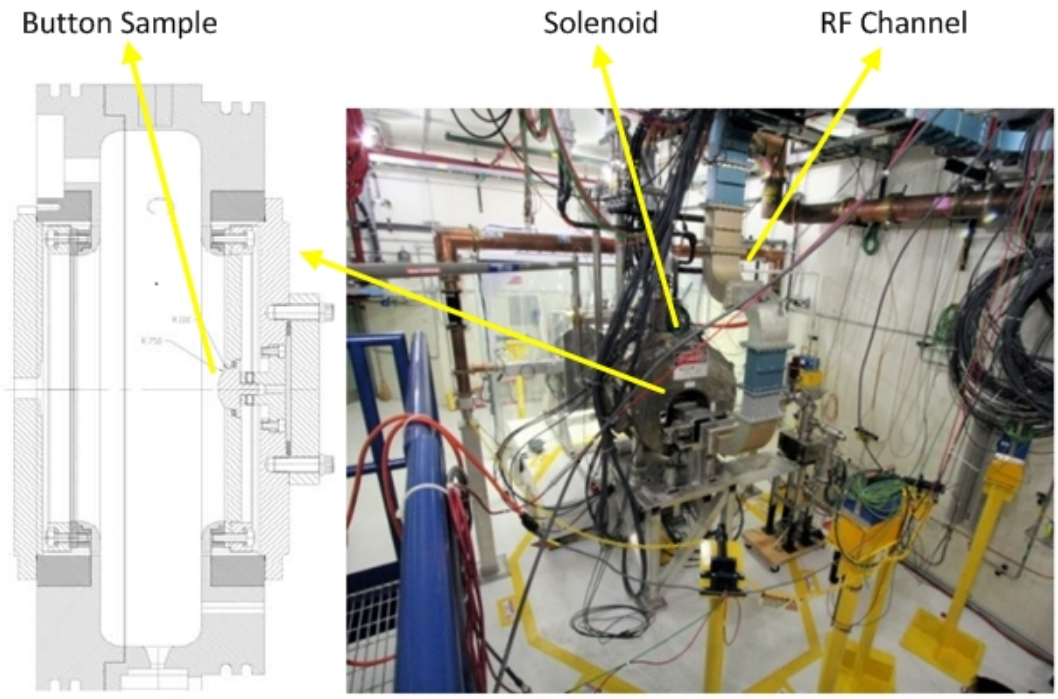

Figure 2-9: 805 MHz with button sample attached (left) [40], 805 MHz cavity inside the 4 T MTA solenoid [41]. The cavity is placed inside a 4T solenoid in order to create operating environment as close as possible to the conditions set by the MICE and Neutrino factory designs. This is to allow for further investigations into effects of magnetic field on RF breakdown to be made

The 805 MHz test cavity closely resembles a cylindrical pillbox cavity with Be windows covering the irises. RF power is fed through a coupler, attached to a kidney shaped coupling slot. The experiment has been designed to allow for demountable windows to be installed. Therefore, various physics can be investigated through tests using different button samples. RF probes, view ports and thermo-couple ports are available for measuring peak RF power inside the cavity [39-42]. The main parameters of the cavity are given below in Table 2-3.

Table 2-3: MTA 805 MHz cavity parameters [43]

Parameter	Value	Unit
Cavity radius	15.62	cm
Gap length	8.1	cm
Be windows thickness	0.127	mm
Cavity shunt Impedance	32	MΩ/m
Cavity quality factor Q	18800	

A major goal of the MTA program is to test and investigate the performance of different materials and surface treatments in the presence of high E and B fields. The 805 MHz cavity as shown in Figure 2-9 incorporates a button shaped sample where it is manufactured using various materials [44]. This would allow for a quick and easy access to a wide variety of materials for testing. The button shape can enhance the field locally, in order to ensuing that any possible breakdown occurs on the button surface. The performance of the sample is analysed by increasing the field in steps until the RF breakdown occurs [42, 45]. This facility forms the focus of the experimental program carried out by this research, where button samples are produced using various manufacturing techniques. This is outlined in Chapter 4.

Chapter 3.

RF Cavity Breakdown

3.1 Introduction

The primary purpose of an accelerator is to accelerate charged particles using a metallic chamber filled with electromagnetic (EM) fields. Power in an RF cavity is provided by a RF power source operating at a specific frequency that is coupled to the accelerating structure. The RF cavity designed to have a specific size and shape so that EM waves become resonant and build up inside the structure. Charged particles passing through the cavity are accelerated by the force being applied through the EM field, pushing them forward in the direction of the electric field.

Cavities are classified according to their operational frequencies. For cavities operating at a few hundred MHz, pillbox cavities with nose cone or disk loaded geometry can be used. At lower frequencies, coaxial geometry is commonly employed. When operated at extreme conditions, all variations of RF cavities exhibit loss of performance due to a phenomenon known as RF breakdown. This chapter sheds light of various breakdown regimes and factors influencing them.

3.2 RF Breakdown

Accelerator research is rapidly progressing on two main frontiers by pushing the beam energy and intensity to higher levels. As shown previously in Figure 2-1,

next generation accelerators have to be an order of magnitude higher in energy levels in order to probe new physics. The design and construction of a particle accelerator is influenced by the required operating accelerating gradient. The extreme operating conditions lead to a phenomenon known as RF breakdown, where a dramatic change in the transmission of the RF power is observed.

During a breakdown event, much of the stored energy in the cavity is directed towards the wall, causing localised melting and contamination of the surrounding surface. Various mechanisms seem to be responsible for initiating RF breakdown with no agreement on the cause of such behaviour. This is due to the rapid and unpredictable nature of the observed process [46-48]. An RF breakdown event is typically characterised by a burst of x-rays and bright flash of visible light. This limits the achievable accelerating gradient it can produce irreversible surface damage to high power RF components and RF sources [49].

The Complexity of RF breakdown phenomena and the absence of a proven theoretical explanation make it difficult to apply experimental results on breakdown limits from one RF structure to another. An overview of the relevant publication introducing the F phenomena can be studied in more details in various publications which are out of the scope of this study [46, 50-52]. The most commonly observed RF breakdown events are introduced in this chapter followed by method of mitigating such events.

3.2.1 Field Emission

Field emission is the most frequently encountered problem in vacuum systems, where the electric field causes electrons to be emitted from the cavity surface. This can either act as a direct cause of breakdown or as precursor for other secondary

effects. The basic principle of field emission can be explained as a quantum mechanical tunnelling process [46, 53]. Figure 3-1 illustrates the original field emission theory developed by Fowler and Nordheim in 1928 [54].

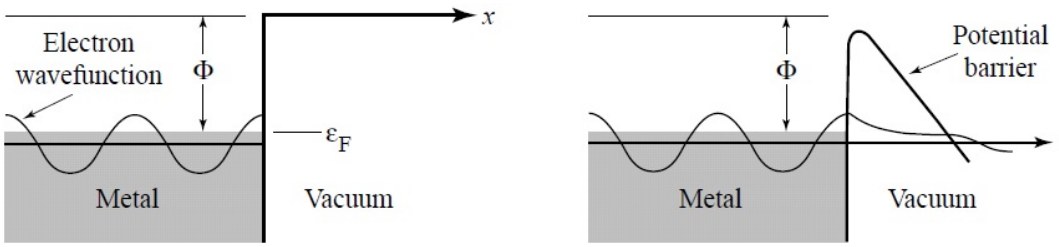

Figure 3-1: Electrostatic potential of the metal-vacuum interface, without electric field (left) with an externally applied electric field (right) [46]. The work function ϕ is the minimum energy needed to remove an electron from a solid to a point in the vacuum immediately outside the solid surface. The application of an electric filed alters the behaviour of the potential barrier, reducing the required energy level needed for electrons to be released

Electrons are initially confined within the cavity walls due to their insufficient energy to escape. The energy required should be greater than the work function of the material (ϕ), usually represented in electron volts (eV). With the application of an E field, the infinitely thick barrier is transformed into a finite thickness triangular shape. The gradient of the barrier is directly related to the amount of E field at the surface [46]. The new configuration initiates field emission by allowing electrons with a lower energy level to escape the material. Fowler and Nordheim predicted the current density level of a planar surface to be [52, 55]:

$$I_{FN} = \frac{1.54 \times 10^{-6} \times 10^{4.52\phi^{-0.5}} E^2}{\phi} exp\left(-\frac{6.53 \times 10^9 \phi^{1.5}}{E}\right) \quad (3\text{-}1)$$

where I_{FN} is the current density in A/m^2, E is the surface electric field in V/m and ϕ is the material work function in eV.

In reality, the surface of an accelerating cavity is far from being planar and free from impurities. This is due to the presence of dust inclusions, debris from

previous breakdown events, voids, grain edges and other distortions present on the surface. These irregularities can play a major role in breakdown events by acting as field emission sites [56, 57]. RF breakdown normally occurs when the field emitted current densities of 10^{12} -10^{13} A/m^2 are reached. The local field is enhanced to 7 – 10 GV/m, much higher than the surface fields observed in most accelerators. The field enhancement factor ß can be expressed as [46, 48, 52, 55, 58, 59]:

$$\beta = \frac{E_{Local}}{E_{Surface}} \tag{3-2}$$

where E_{local} is the E field at the defect and $E_{surface}$ is the E field observed across the surface of the cavity. The enhancement factor is linked to the radius of curvature (r) and it is dependent on the shape of the emitter [50, 55, 60]. Figure 3-2 shows the theoretical definition of a series of observed emitter shapes.

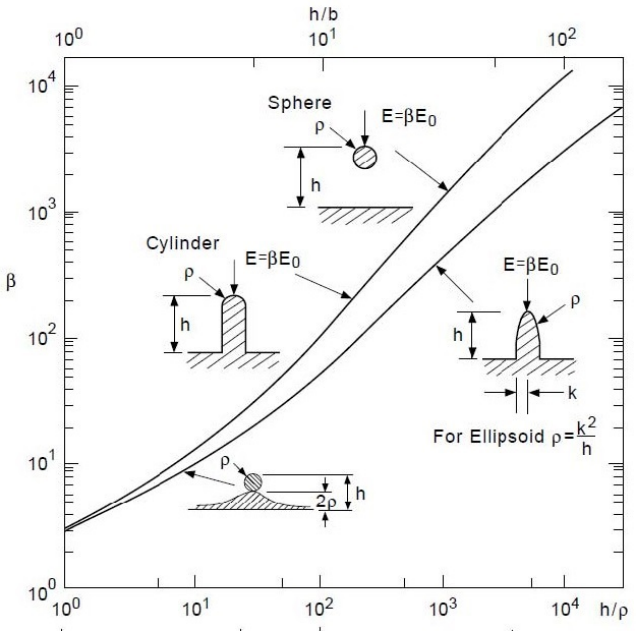

Figure 3-2: A theoretical representation of the field enhancement factor ß caused by a series of idealised surface features commonly found on the surface of RF cavities [55]

When the surface electric field exceeds the threshold level, electrons trapped in the metal by the work function begin to tunnel out into the vacuum. Subsequently,

a stream of emitted electrons is accelerated towards the opposing cavity wall. Such a discharge leads to the collapse of the field by absorbing the RF energy [56, 61]. The field enhancement characteristics of a surface defect are strongly influenced by the shape of the geometry in question. A typical shape of a surface defect used in various MTA research is shown below in Figure 3-3, where the defect is modelled as a semi spheroid [58, 61, 62]. The enhancement factors observed can be explained using equation (3-3) [62, 63].

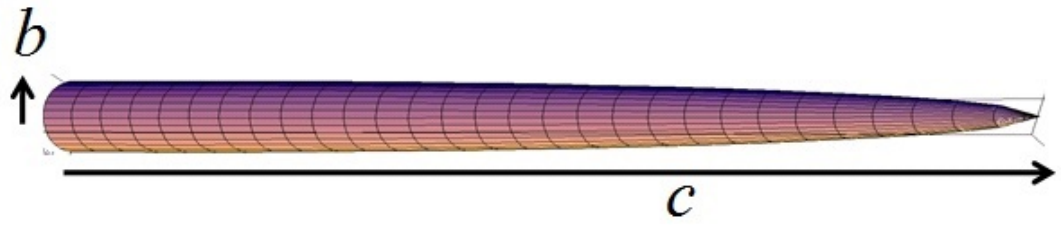

Figure 3-3: Representation of a surface defect used in the MTA studies [62] showing the base length and the height used to define the generated ß factor by the surface defect

$$E_{Tip} = \frac{E_{Surf}(c^2/b^2)}{(\ln\left(2\frac{c}{b}\right) - 1)} = \beta E_{surf} \tag{3-3}$$

where c, b, E_{Surf}, E_{Tip} and ß represent asperity height, asperity base, surface field around the defect, field at the tip of the defect and enhancement factor respectively. In order to produce the 10 GV/m field strength observed at the tip of a defect during field emission, a field enhancement factor of 184 is needed. This requires the base of the defect to be around 0.7 µm wide with a height of 16µm [61].

3.2.1.1 Kilpatrick Limit

Sparking takes place in a field emission between two metal electrodes, where an abrupt dissipation of the stored electrical energy occurs across the gap. This limits the maximum achievable E field due to RF breakdown. These limits were tested for vacuum systems at various frequencies in the 1950s by W. D. Kilpatrick. The

conditions that would result in breakdown-free operation were defined [52, 55, 64], while the results were formulated by T. J. Boyd [65]. This is given below as:

$$f\ (MHz) = 1.64E_k^2 e^{-8.5/E_k} \tag{3-4}$$

where f is the frequency and E_k is the Kilpatrick limit in megavolts per meter. The obtained results can be plotted as shown below in Figure 3-4.

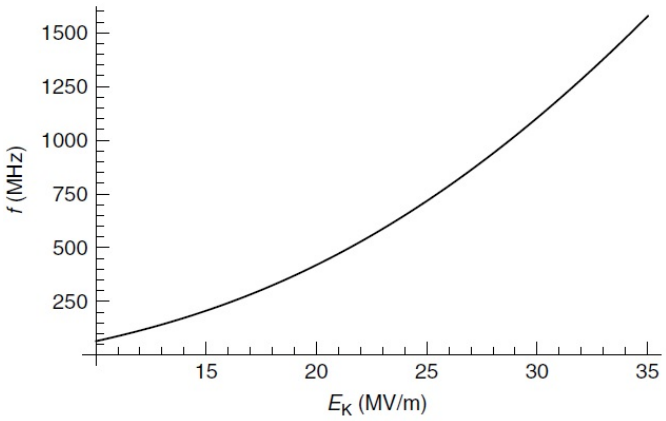

Figure 3-4: A plot showing the Kilpatrick Limit observed in RF cavities [65]. The maximum achievable electric field is limited by a process known as RF breakdown. The reliable limits for various RF frequencies were tested experimentally by W. D. Kilpatrick and are used in the design of RF cavities

The criterion used to define the Kilpatrick limit was based on using metal electrodes that had no special preparation and no external magnetic fields were present. The accelerator structures were operating with vacuum levels of 10^{-5} torr where there was little dependence of RF breakdown on vacuum level below this level [64, 65]. Under such circumstances, vacuum sparking occurred at lower voltages than would be explained by field emission.

Kilpatrick criterion is considered relatively conservative by today's standard of accelerating structures. This is shown below in Figure 3-5, where modern day cavities exceed Kilpatrick limit by a factor of two [66].

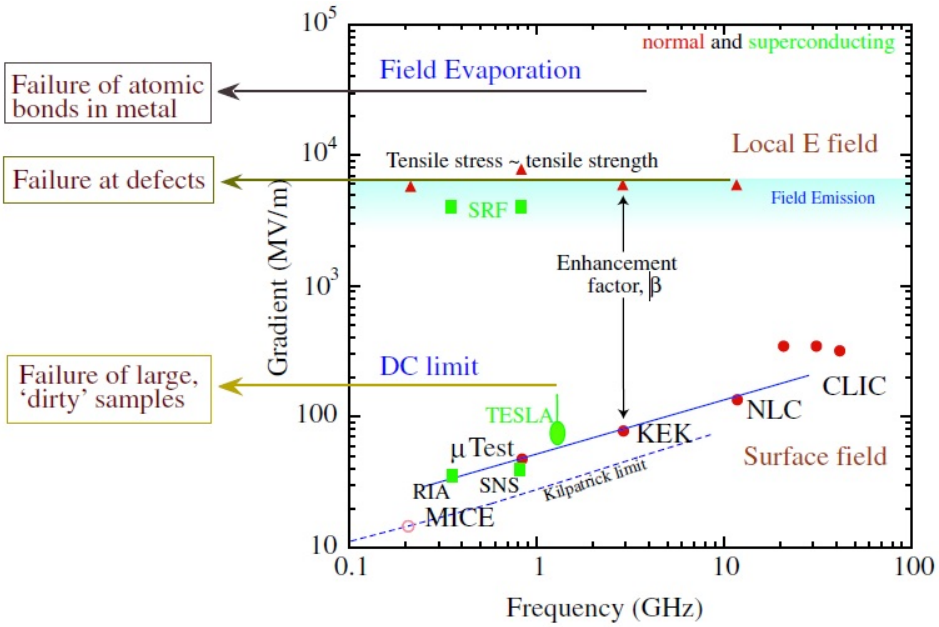

Figure 3-5: Local and average surface electric fields as a function of frequency for superconducting and normal RF accelerating cavities [66]. Improvements in technologies in manufacturing RF cavities mean modern structures are capable of operating at energy levels greater than Kilpatrick limit. The normal conducting technology used in MICE cavities dictate the achievable accelerating gradient based on the Kilpatrick limit defined for a 201 MHz structure

In modern practice, it has been found that this limit can be exceeded by various factors. This is due to improvements in technologies used to manufacture RF cavities and the clean vacuum levels achieved. Nevertheless, the same expression is commonly used for choosing the design field level for accelerating cavities. The actual peak surface field Es is expressed as [65, 67]:

$$E_s = b_f E_k \tag{3-5}$$

where b_f is known as the bravery factor with typical chosen values between 1 to 2.

3.2.2 Multipacting

Multipactor is a microwave breakdown discharge occurring in vacuum conditions caused by the formation of an electron avalanche. The energy deposited during a primary impact with the cavity surface can initiate an avalanche by

releasing secondary electrons. This leads to the creation of a plasma, reducing the power output and increasing heating in the cavity wall [50, 65].

The most common Multipacting (MP) event seen in the 1970s was the one point MP, which was a major limiting factor in the operation of superconducting cavities [68, 69]. This normally occurs in regions where the B field is uniform and the E field has a non-zero normal component. In a single point MP the electrons are emitted from, and return to the same surface near the emission site [46, 65]. The return time of travel for the electron is an integral number of the RF period. As shown below in Figure 3-6, single point MP can be mitigated by using an elliptical cavity [46, 65, 68, 69]. Unlike the pillbox cavity, an elliptical cavity forces the emitted electron to drift towards the cavity equator, where the electric field is not strong enough for secondary emissions to occur [65].

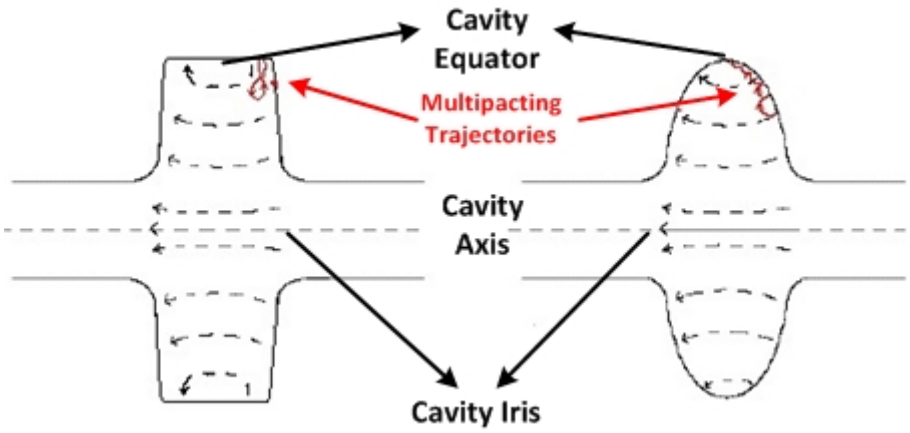

Figure 3-6: Comparison of Multipacting trajectories in rectangular (left) and elliptically shaped (right) RF cavities [70]. The shape of an elliptical cavity would force an emitted electron to slowly move towards the cavity equator through secondary emission. It is at this point where the E field is at minimum, lowering the probability of RF breakdown events

Another emission problem commonly observed in RF cavities is the two point MP. As shown below in Figure 3-7, an emitted electron is accelerated between two opposing points. Secondary electrons are released upon impact, repeating the process on the initial surface. The flight time between impacts is a half integer

multiple of the RF period [46, 68, 69]. The round wall geometry of an elliptical cavity tends to suppress the MP process by pushing the succeeding generations of electrons towards the equator of the cavity, where the E field is at minimum. An example of an 1.3 GHz cavity is given below in Figure 3-7 [46, 69].

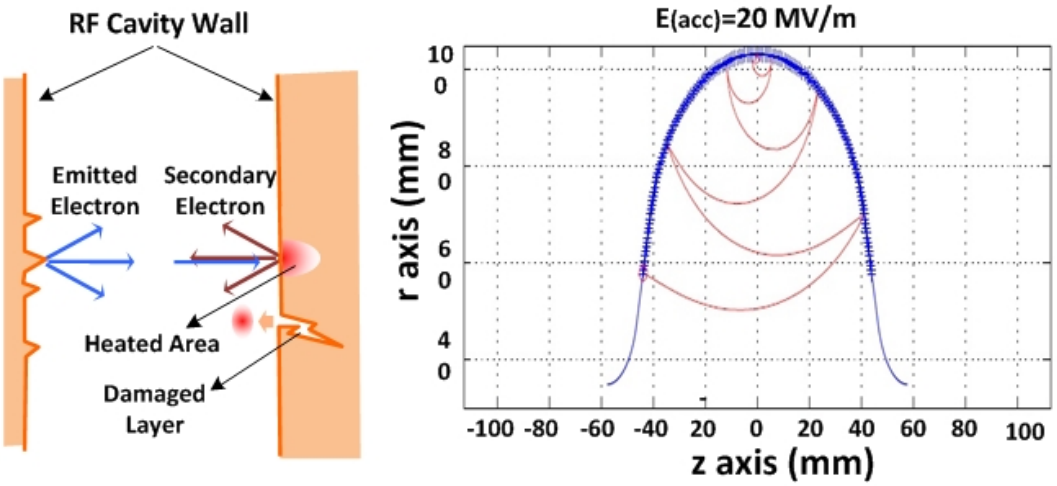

Figure 3-7: Standard model of Multipacting (left) Two point Multipacting in a single cell 1.3 GHz TESLA cavity (right) [68]. The released energy at the point of impact would cause secondary electrons to be released. The process is repeated until the stored energy of the cavity is depleted

During an MP event, the accelerating gradient remains constant even if the power input is increased. Shown below in Figure 3-8, the Q value of the cavity is abruptly reduced at the Multipactor barrier. Also the stored energy inside the cavity is subject to change once MP is encountered [46].

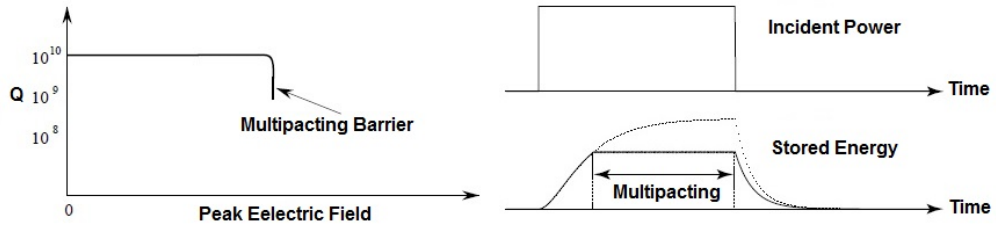

Figure 3-8: Plot showing the Q vs. $E_{(peak)}$ curve for a superconducting cavity when Multipacting is encountered (left) and the Stored energy of a cavity that is subject to Multipacting (right) [46]. A Multipacting event would dramatically reduce the level of stored energy inside and RF cavity, limiting the achievable accelerating gradient

A sustained MP over a long period of time can increase the internal pressure of the cavity through outgassing, allowing for a corona discharge to develop. Such

discharge alongside a rise in temperature can lead to thermal breakdown and destruction of superconducting cavities.

3.2.2.1 Secondary Electron Yield

Secondary emission is a physical phenomenon where a primary incident particle of sufficient energy releases secondary particles when it hits or passes through material. In the case of MP, this particle is an electron being emitted from surface defects. The terminology used for electron emission is secondary electron (SE) emission. The number of secondary electrons emitted per incident particle is also referred to as secondary electron yield (SEY) (δ) [71]. As shown below in Figure 3-9, the SEY is a function of impact energy and angle of the primary electron. This is dependent on E_m and δ_m as the two material dependent parameters, where they in turn determine two energies at which the yield is equal to unity. These are referred to as the first and second cross over points E_1 and E_2 respectively [72]. For most metals, E_1 and E_2 are typically in the range of 80 eV to 1 keV [73].

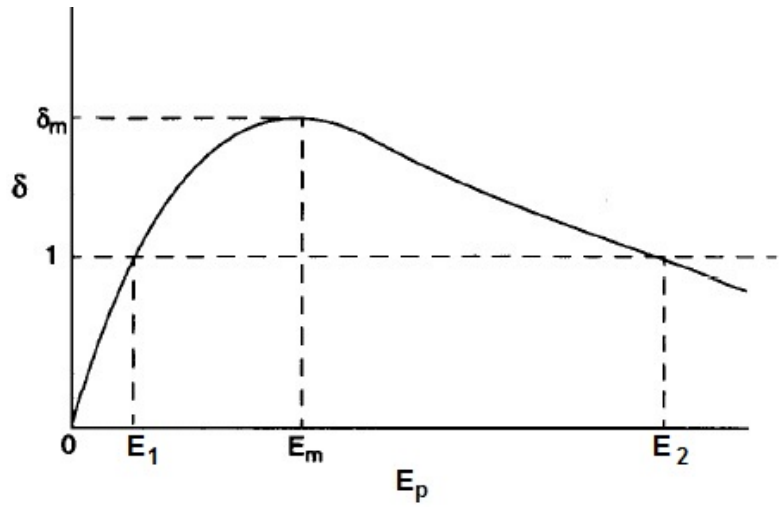

Figure 3-9: Plot showing the profile of secondary emission yield δ as a function of primary impact energy E_p based on Vaughan's empirical formula [72]. Multipactor grows only for impact energies in between E_1 and E_2 where δ>1

Resonant build up can only be achieved when the impact energy of the particle E_p is between E_1 and E_2, where δ is greater than unity. Equation (3-6) can be used to analytically describe the SEY as a function of the primary particle [71].

$$\delta = 0.5\frac{(E_p)^{1-n}}{\varepsilon}.\frac{\lambda_s}{B}\left(1 - e^{-R/\lambda_s}\right) \tag{3-6}$$

where E_p, λ_s, Ɛ and ρ_t represent the energy of the primary particle, effective SE emission escape depth, effective energy required to produce an SE and density of the target material in grams per cubic centimetre. For an impact energy of 1 keV, n and B are set to 1.67 and 76 nm respectively [71] .

Influenced by material properties, various metals exhibit different emission characteristics [71, 73, 74]. This is shown in Figure 3-10 for a series of metal alloys [74]. It is evident that aluminium alloys has the largest SEY in comparison to copper used in the production of RF cavities.

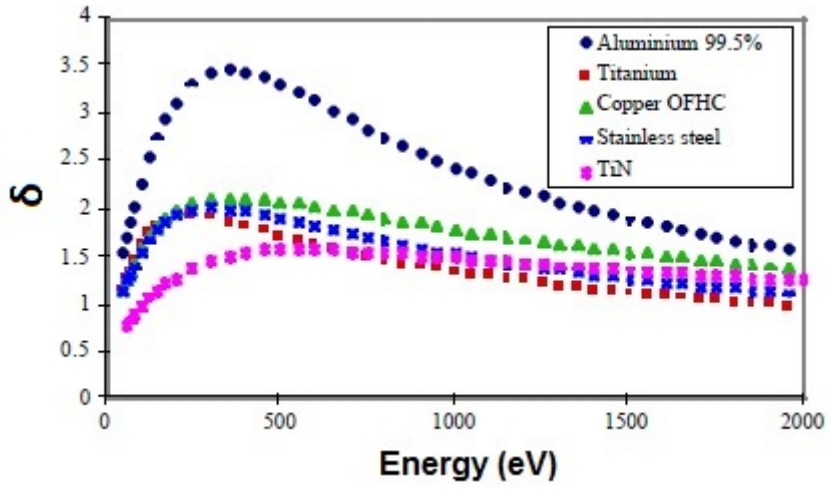

Figure 3-10: Plot showing the secondary electron yield for a series of materials [74]. It is possible to see some materials such as aluminium are capable of emitting more electrons for the same impact energy in comparison to OFHC surfaces

The different secondary electron yield observed in various materials opens the possibility of reducing MP by simply choosing materials with smaller SEY rather

than having to alter the geometry of the RF cavity. Alloys with lower SEY can be used as coating material to improve the characteristics of the more commonly used material in the production of RF cavities. Ti and TiN are used to coat the internal surfaces of couplers and cavities due to the low SEY of the material [74-76].

The majority of the data available are only applicable to pure metals. However, these cannot be used for technical materials such as aluminium alloys and stainless steel [74, 76]. The differences between pure metals and technical surfaces are shown in Figure 3-11 for a copper sample undergoing surface treatment.

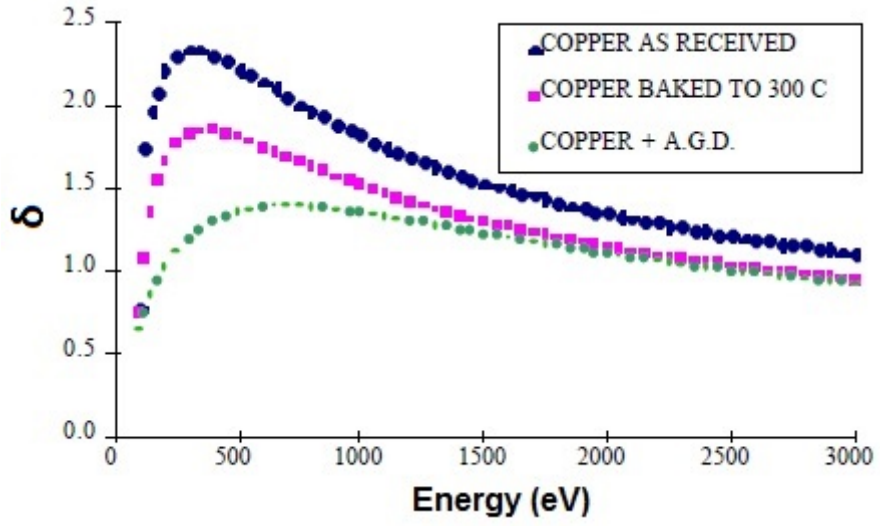

Figure 3-11: Plot showing the SEY of a copper surface having undergone different surface treatment techniques [74]. Copper A.G.D has been exposed to argon for 24 hours. The SEY of a surface can be lowered if the surface is treated to remove sources of field emission. Hence, creating surfaces that are better suited for the operation of RF cavities

The highest yield is obtained for the copper samples with no treatments while the SEY is improved through baking. The difference between pure materials and technical materials is due to the presence of contaminations such as oxide, which can be removed through treatment [74]. Further information regarding pure metals and technical surfaces can be found in the literature [71, 73-77].

An alternative method for determining the SEY characteristics of a material is to evaluate the energy band structure of the solid in question. The band structure describes the energy ranges of electrons within the solid known as energy band [3]. Energy bands consist of a large number of closely spaced energy levels in a material. They can be thought of as the collection of the individual energy levels of electrons surrounding each atom. The band gap is the minimum amount of energy required for an electron to break free of its bound state.

Density Functional Theory (DFT) is a quantum mechanical modelling which can be used to define the energy band structure of a material by investigating the electronic structure of atoms. One of the more commonly used simulation programs using DFT is Dmol, which is used to predict properties of material both in solid and gas phase. Further information regarding DMOL can be found in the literature [78]. DFT simulation carried out in 2004 by Dr Seviour [79], reveal the band structure of pure copper sample in Figure 3-12.

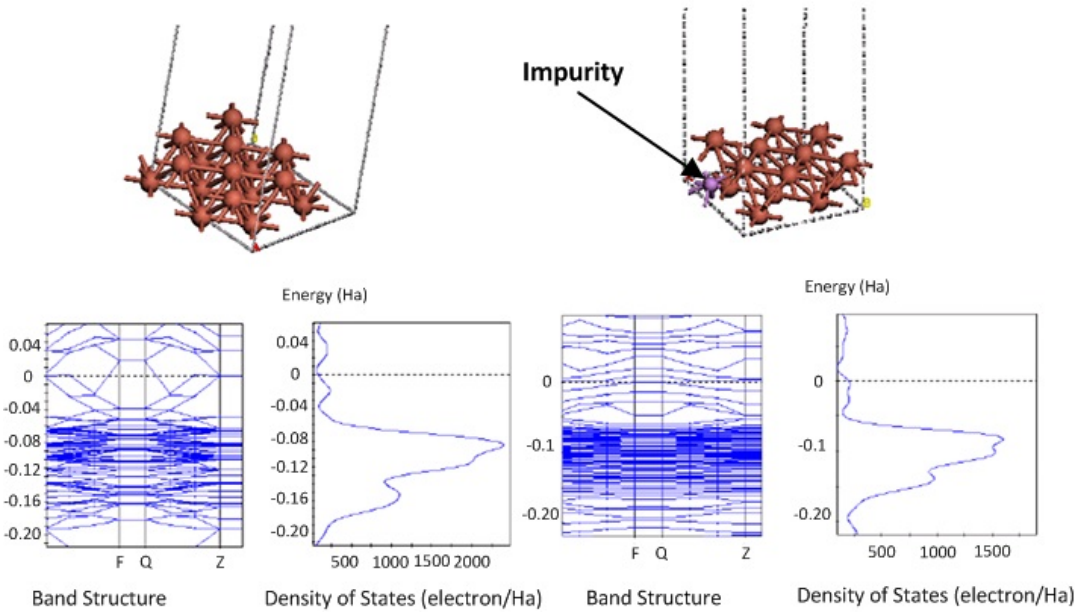

Figure 3-12: Band structure obtained from Dmol3 for pure Copper (left) and Copper with added phosphorus impurity (right) [79]. H_a represents the Hartree energy which defines the amount of energy required to release an electron from the specific band structure. The introduction of a phosphorus atom changes the band structure and lowers the energy required to release electrons from copper surfaces

The DFT simulations reveal changes in the energy band structure of copper when a phosphorus atom is introduced in the molecular mix. This is achieved by analysing the Hartree energy (Ha) of the structure [3, 79]. This is a physical constant equal to the twice the binding energy of the electron in the ground state of the hydrogen atom. When a hydrogen atom is in this state, an amount of energy equal to 0.5 Hartree is necessary to free an electron. The value of the Hartree energy is approximately 4.36x10-18 Joule (J) or 27.2 electron-volts (eV) [3].

Shown below in Figure 3-13, the shape of energy bands can influence the SEY of various materials. It is evident that Be with a dispersed band structure has a much lower SEY in comparison to AL_2O_3 with a dense band structure. This is due to the relatively low number of states seen in the Be.

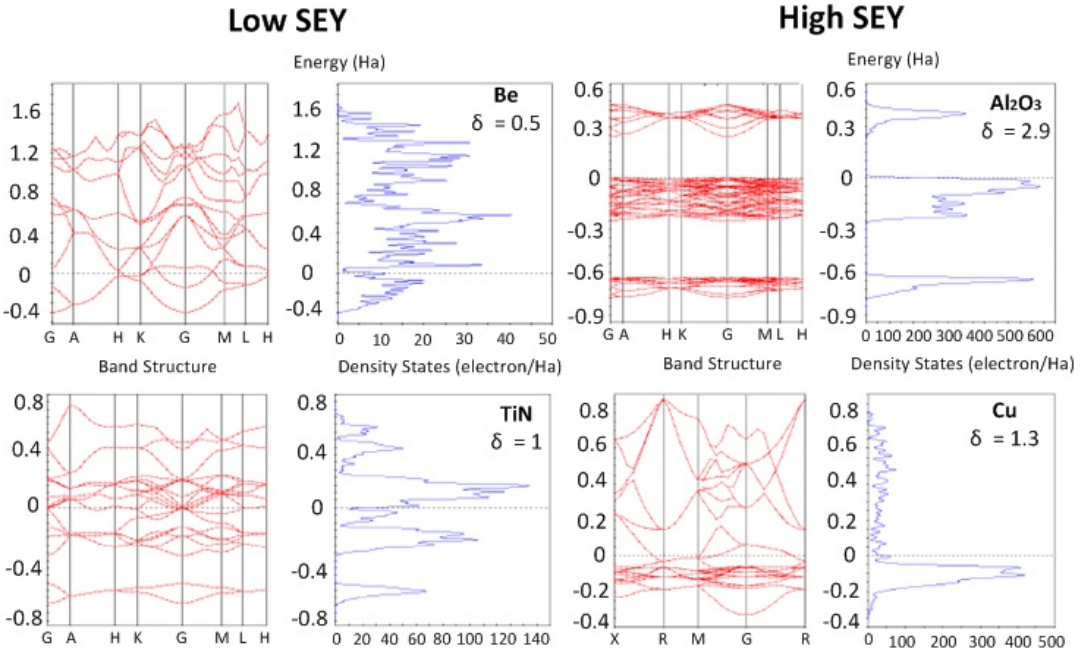

Figure 3-13: Plot showing the secondary electron yield of various material [79]. The SEY is dependable on the shape of the band structure where more defined energy levels with defined band gaps would result in a higher emission rates per electron impact

The state of energy bands is of much importance when analysing the surface quality of cavities and investigating RF breakdown probability. The above findings

show that an introduction of foreign material in the structure of a metallic surface can lead to changes in band structure and hence altering the SEY of the material. This highlights the potential limitation a bad surface quality can bring to the operation of and RF cavity by limiting the achievable accelerating gradient.

3.3 RF Breakdown Mechanism

Many field emission cases follow the Fowler Nordheim relation, where the level of field enhancement is related to the geometry of microscopic asperities being present on the cavity surface. These could include perturbances, cracks, grain boundaries or other causes of local field enhancement. Most breakdown models use two mechanisms to explain the process leading to initiation of RF breakdown. These are the mechanical fracture and localised ohmic heating of the metal surfaces [80]. In both cases emitters are activated abruptly with high E field [46].

3.3.1 Mechanical Fracture Model

The mechanical fracture model, or field evaporation as it is known, indicates that the breakdown mechanism is related to the electrostatic outward mechanical tension exerted on the metal surface [47, 58, 80]. Due to the instantaneous nature of a breakdown event, it is impossible to directly measure the parameters of the breakdown site, just before the event itself. Indirect measurements on the other hand can be taken using field emitted electrons. Current MTA measurements from the 805 MHz cavity have shown high levels of electric stress. This is due to the local geometry of the surface features observed on the cavity wall [47, 66].

The properties of the emitter site can be obtained by analysing field emission which follows the basic Fowler Nordheim current and field relation. Figure 3-14

shows how emitter sharpness and area can be extracted from data by fitting the dark current versus accelerating field behaviour of the cavity [57]. This is the flow of current in the absence of light and the main sources of dark current are ohmic leakage due to imperfect insulation and thermionic emission. The local field required for field emission is in the region of 5 – 10 GV/m obtained from the Fowler Nordheim parameterisation. It is at this point where the associated tensile stresses applied on surfaces approaches 275 to 344 MPa [47, 57]. As shown in Figure 3-14, this is comparable to the tensile strength of copper.

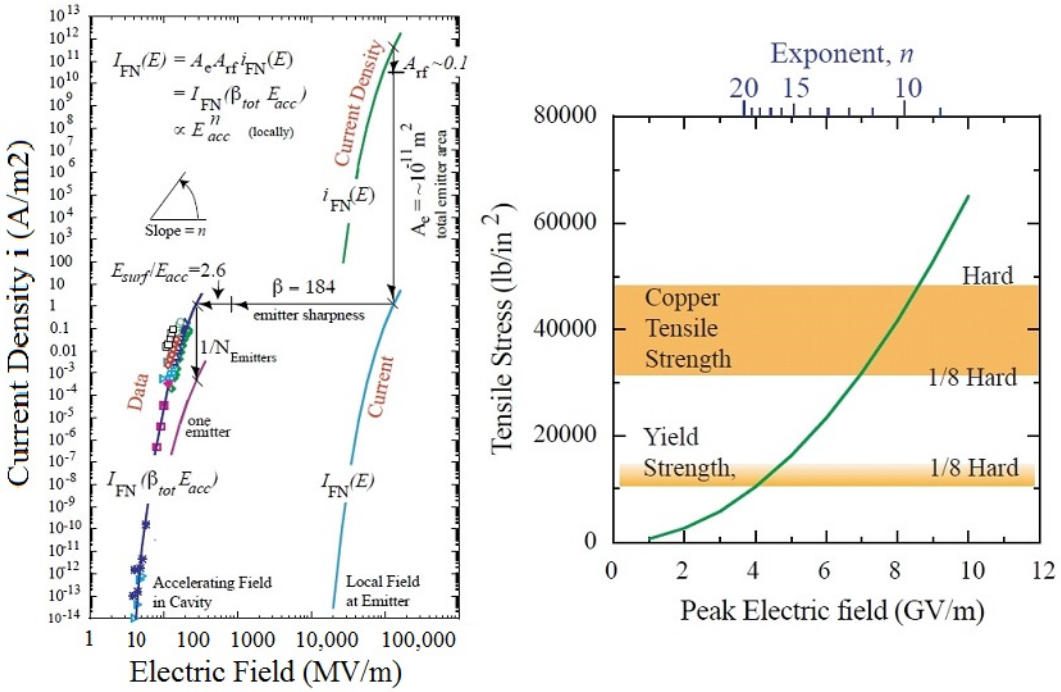

Figure 3-14: Dark Current and Fowler Nordheim model (left) copper stress (right)

The applied high stresses would eventually lead to fragmentation of the surface, mainly at the edge of a crater or at weaker locations on the cavity wall. Such fragmentations tend to leave sharper corners that could then produce further fragmentations of its own. The broken piece is then carried away by the outward electrostatic tension, and is bombarded by field emitted electrons from the

remaining asperity and becomes vaporised and ionised. This results in the creation of local plasma, which can short out the cavity [58].

3.3.2 Ohmic Heating

The second major breakdown regime is Ohmic heating, where a sufficient current density can initiate breakdown by melting the tip of an asperity or damaged area [58]. This differs from the previous breakdown model, as Fowler Nordheim plots show field enhancement factors of no more than 50, even if there are many crater formations [81]. The increasing local current density I_{FN} would lead to heat dissipation in the form of ohmic loss $i^2\rho$, where ρ is the resistivity of the medium. Due to rapid nature of this event, the heat does not have time to be conducted away, raising the temperature of the local material by ΔT (˚C). The time taken for such an event can be expressed as [81]:

$$\Delta t = \frac{4.18 \times 10^6 MC\Delta T}{i^2\rho} \tag{3-7}$$

where M is density in gram/cm^3, C is heat capacity per gram and ρ is measured in ohms-cm.

Breakdown is initiated by a small piece of the material being broken off the asperity surface and melted due to ohmic heating. This is then lifted away from the remains of the asperity and exposed to field emission where it is further heated and vaporised. This is then ionised which in turn creates a plasma [57]. As shown below in Figure 3-15, the process can continue with new emission sites being created, where ohmic heating can take place once more [82].

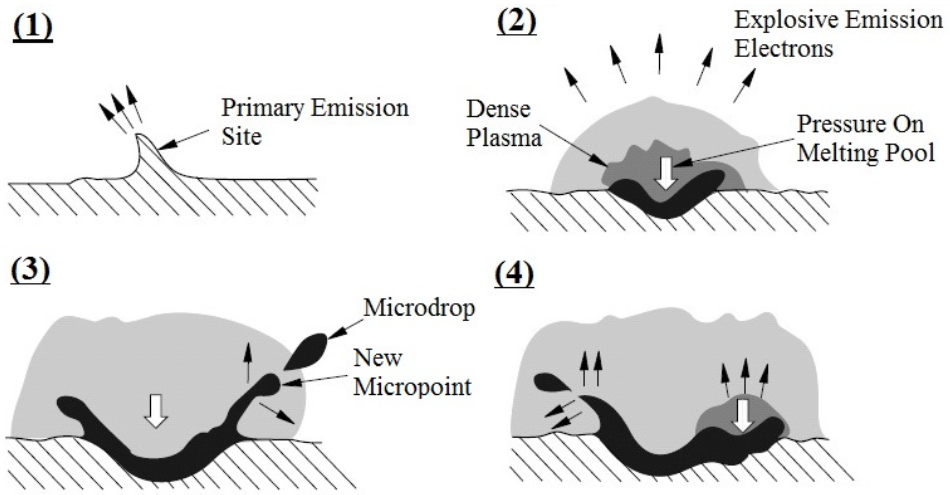

Figure 3-15: Development of surface damage in the case of breakdown initiated by ohmic heating [81]. The stored energy at the emission site would eventually lead to the destruction of the emission site, leading to the creation of further secondary emission sites

Therefore, copper grains can be heated both ohmically by dark current beams within the structure, or by dark current beams through ionisation heating during fragmentation. Heating is more severe in the latter case, as no conduction losses are present due to the loss of thermal contact between the grain and the wall [57].

3.4 Applied Magnetic Field

The breakdown models examined in this study did not take magnetic field into consideration. However, majority of accelerating structures do operate in the presence of externally applied magnetic fields. They are applied for various purposes such as bending particle beams in synchrotrons or reducing beam circumference in the case of MICE and Neutrino Factory experiments. The effects of applied magnetic field are relatively unknown and are subject of much investigation through various studies.

It is thought that magnetic field can facilitate breakdown by exerting additional forces in the form of torques on field emitters. In this model, the emitters is assumed to be conical and aligned roughly parallel to the applied magnetic field.

As shown below in Figure 3-16, the radial component of the current density is determined by the cone angle of the emitter and is perpendicular to the magnetic field. The perpendicular pressure exerted by the magnetic field is [83]:

$$P = \frac{i \times B}{A} = \frac{\sin\theta IB}{A} \tag{3-8}$$

where i is the current density at the surface of an emitter, I is the maximum measured current per emitter, A is the local emitter area, θ is the cone angle and B is the applied magnetic field.

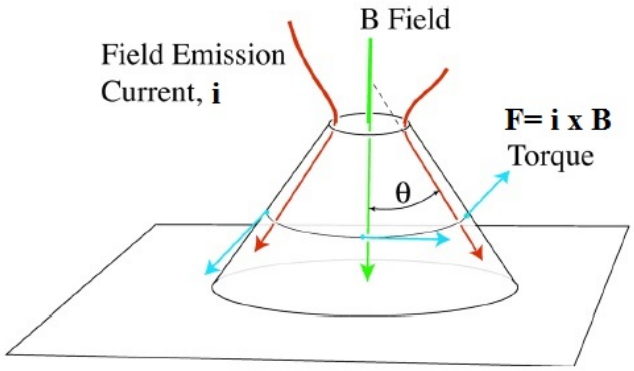

Figure 3-16: Applied torque on an asperity by an externally applied B field during field emission [83]

In order to create current densities in the region of 10^{10} A/m^2, local emitter surface area of 10^{-14} m^2 with a maximum measured current of 0.1 mA is required. If the emitter is subject to a 2 tesla (T) magnetic field, the applied pressure would be in the order of 10,000 MPa, which is more than enough to trigger fracture [83]. Such pressure is applied in a circular patter around the emitter tip, causing further damage and reducing the electric field necessary to initiate breakdown.

3.5 Cavity Conditioning

The surface of a newly fabricated RF cavity consists of a wide range of asperities with various enhancement factors. The surface is usually dominated by a

few potentially hot breakdown sites. It is necessary to burn these off if maximum accelerating gradient is to be reached. This can be achieved through a number of semi-controlled RF breakdowns, caused by increasing the RF power very slowly over a period of time. This process is referred to as RF conditioning.

Prior to operation, it is essential to condition an RF cavity when being turned on. At low operating fields, the hottest emitters are destroyed and not replaced. Each burnt emitter deposits molten material on the surrounding area, producing a spectrum of weaker secondary emitters. The enhancement factors of the active emitters are decreased continuously as the process is continued. An equilibrium state is reached when the emitters produced during breakdown events are on average as active as the ones being destroyed.

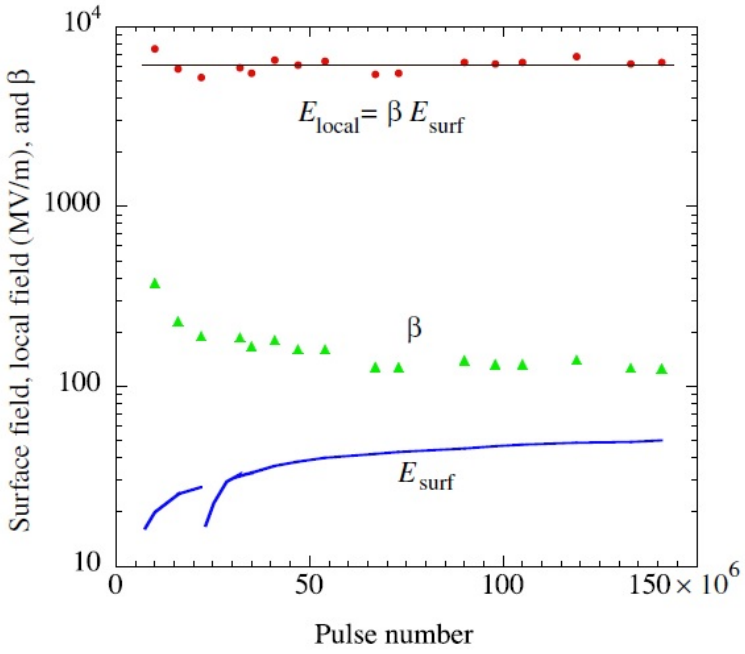

Figure 3-17: Local electric fields in KEK data during conditioning [66]. The field enhancement caused by the asperity induces localised field concentration, increasing the probability of RF breakdown

During the conditioning process, both the enhancement factor ß and the E_{surf} are subject to change. However, their product, the E_{local} remains constant. This can be

explained by the data collected at KEK in Japan, as shown in Figure 3-17. Although the accelerating field E_{surf} is increased by a factor of 2, the enhancement factor is decreased by the same factor. Hence, E_{local} is constant during conditioning.

3.6 Mitigation of RF Breakdown

Most studies over the past 100 years have been directed at finding a way of mitigating the breakdown process to allow RF structures to cope better with cumulative damage during operation [70]. The underlying cause of RF breakdown is the micro-roughness and structure of the metal surfaces. These are difficult to control or measure, but can be improved to mitigate RF breakdown.

Constrains imposed on the performance of RF cavities due to material have not been fully explored, where many electrical and mechanical parameters are involved. In order to predict and optimise the performance of a given material, a great deal of knowledge needs to be developed. Various materials exhibit their own unique properties where they can bring various benefits to the operation of RF cavities by increasing the operating gradient. This can be seen in many carefully measured data available in the literature [60, 66, 84].

The maximum achievable surface field is dependent on the mechanical properties of the material. Hence, choosing material with higher tensile strength or with better condition spectra can be used to improve the achievable accelerating gradient. Figure 3-18 highlights the performance improvements based on various materials. It is possible to see softer material such as gold and silver breakdown easily in comparison to harder materials like stainless steel.

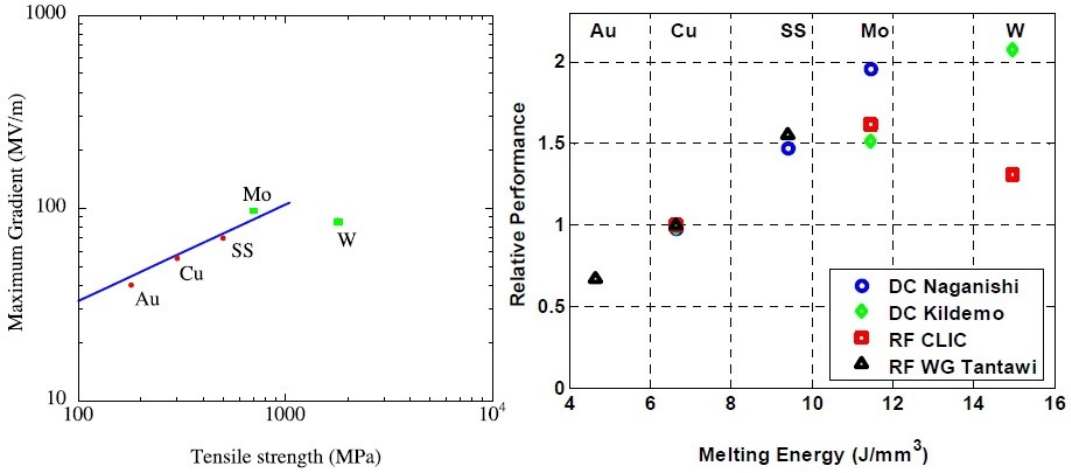

Figure 3-18: Plot showing material tensile strength vs. maximum gradient from SLAC and CERN data [66] (left) and Material dependence of the maximum achievable surface field [84] (right). It is possible to improve cavity performance by using material that can maintain higher local fields

In order to lower the risk of transporting molten material during breakdown, it is possible to use materials that produce no sharp secondary emitters when they cool down. This can highly improve the performance of the cavity by lowering the overall factors seen across the cavity surface.

As discussed earlier, field emission is related to the quality of the surface. Therefore, it is desirable to build cavities with good surfaces and fewer asperities with sufficiently lower enhancement factors. This in principle should lower the need for significant conditioning, reducing the risk of secondary emitters and damage to the surface [58, 60, 66]. As seen with super-conducting RF cavities, this can be achieved by atomic deposition (ALD) [58]. Furthermore, contaminations such as oxide layers can alter the behaviour of the surface by lowering the mechanical strength of the material [60].

Moreover, gas filled cavities have been used in some cases to lower the risk of RF breakdown in normal-conducting cavities. Although the gas pressure is a controllable variable, it has not been proven to be directly linked to the rate of RF

breakdown [66]. The addition of gas can help to slow down the field emitted currents. This would prevent plasma formation, which would otherwise move freely along the E and B fields [60]. The result would be a reduction in ohmic heating. Gas filled cavities are vulnerable to gas breakdown which is a separate phenomenon leading to cavity breakdown.

3.7 MTA Findings

As noted previously, the experimental work in McCool test area at Fermilab is well underway since 2001. There are three major experiments using one multi-cell 805 MHz cavity and two 201 and 805 MHz pillbox cavities. The open cell cavity is to be used in the ionisation cooling lattice of a Neutrino Factory and is shown below in Figure 3-19. Both the open cell and 805 MHz cavity have been tested under externally applied magnetic fields with initial results shown below.

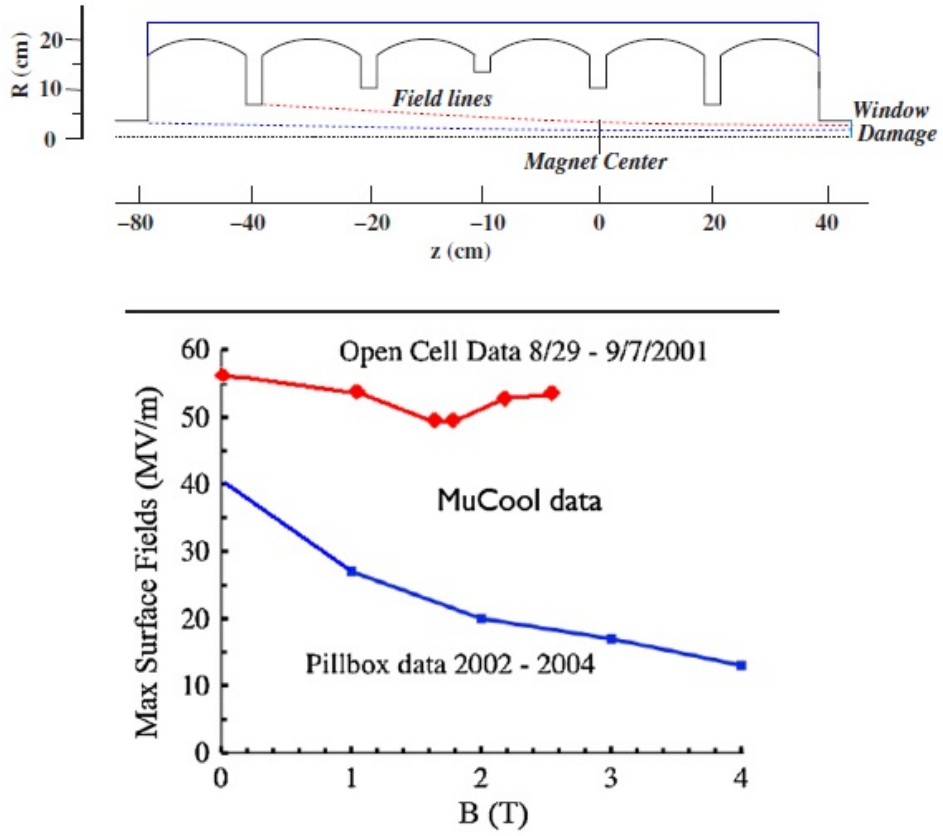

Figure 3-19: Magnetic field lines extending from two irises to the end window of the MTA 805 Multi-cell cavity (top) Maximum surface field vs. axial magnetic field in the 805 MHz pillbox cavity [58]. The application of external magnetic field severely reduces the performance of the 805 MHz MTA cavity. This was caused by increase in surface damage observed around the iris [85]

The maximum achievable surface gradient in the open cell cavity reaches high values of 55 MV/m and is comparable to those in conventional gas filled cavities. X-rays were greatly increased and loss of vacuum occurred due to extensive damage on the end vacuum window [58].

In the second test, an 805 MHz pillbox cavity was mounted in the centre of a solenoid with both irises being terminated once by a Beryllium (Be) window and then a Copper (Cu) window. As shown in Figure 3-19, the maximum achievable gradient of the pillbox cavity was lower than of the open cell design. However, this was reduced by as much as 60% under the influence of an externally applied B

field [61]. This is of major concern for the MICE and Neutrino Factory complex due to the presence of similar operating requirements.

Furthermore, the performance of the cavity deteriorated over time, raising the issue of maintaining the required gradients. After weeks of conditioning, only a gradient of 16.5 MV/m was achieved with an applied B field of 4 T [43]. This was due to extensive damage observed in the iris area, where copper particles were deposited on the surface of both windows as shown below in Figure 3-20. Similar tests of the 201 MHz cavity showed a gradient reduction from 21 MV/m to just 10 MV/m. However, the field did not go higher than 18 MV/m when the magnet was switched off due to the extensive damage to the cavity surface [86].

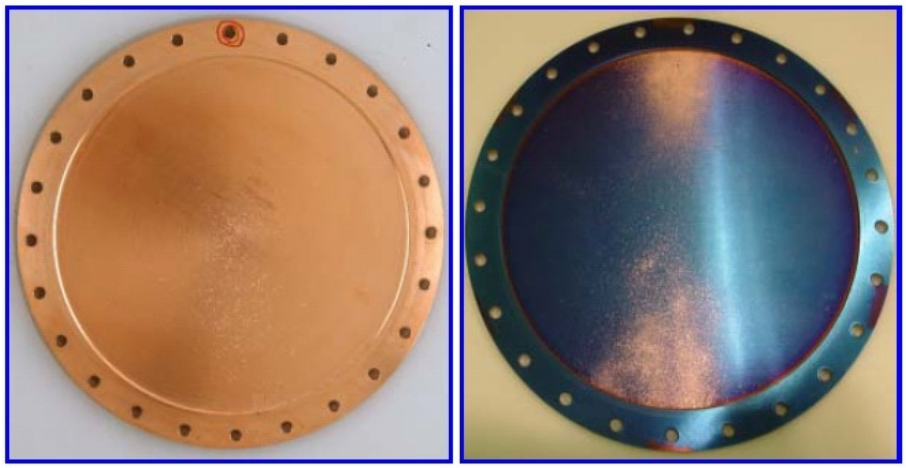

Figure 3-20: Surface damage observed after cavity conditioning both on Copper window (left) and Beryllium window (right) [43]. The copper deposited on the Beryllium window was removed from the cavity iris on the opposing side of the cavity. This extensive damage manifested itself in reduction in accelerating gradient as shown previously

Further experiments were carried out at the MTA, with the aim of analysing the performance of various materials and coatings in the presence of B field. As shown previously in section 2.5, the cavity material program used button samples to perform various tests. The small shape of the sample provides ease of replacement and handling. The buttons produced a tip enhancement greater than the rest of the

cavity, ensuring that the breakdown takes place away from the cavity iris. Figure 3-21 shows the maximum achievable surface electric gradient for various materials as a function of B field. Each test was carried out after considerable cavity conditioning and measurements were taken in stable and repeatable conditions [42]. The buttons tested were made out of Molybdenum (Mo), Tungsten (W) and Titanium Nitrite (TiN) coated copper. It is important to note that two different sets of TiN coated buttons were manufactured at Fermilab and Lawrence Berkley Nation Lab (LBNL), each using a different coating method.

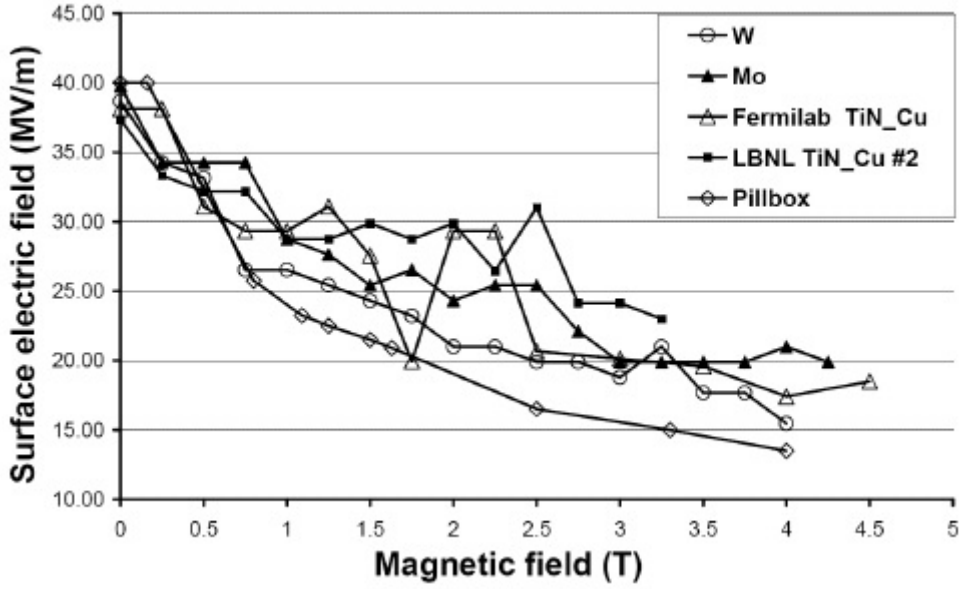

Figure 3-21: Maximum achievable surface electric field on buttons made of various materials as a function of external magnetic field [42]. In all cases, the achievable gradient is reduced with the introduction of an externally applied magnetic field

The cavity performance was improved for all materials in comparison to the original pillbox cavity. Mo outperformed other materials consistently as it was able to withstand higher electric field than W. Although the LBNL TiN coated button performed much better than all the other material, there was a big difference in performance between the two coated buttons. As shown below in Figure 3-22, this

was due to poor coating layer quality produced at Fermilab. Almost 80% of the coating material was peeled off.

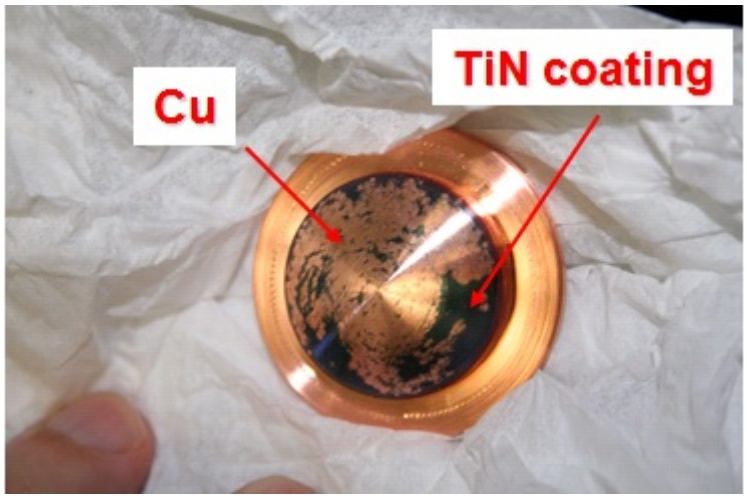

Figure 3-22: Damage observed on TiN coated copper button at Fermilab after conditioning [45]. The TiN coating was removed due to high concentration of local field at the tip of the test button

3.8 Concluding Remarks

Limitations of RF breakdown strongly influence the development of accelerators since it lowers the maximum achievable gradient. Field emission is well established as a source of dark current and RF breakdown trigger in accelerator structures. The level of field emission is influenced by the quality of the surface and the features present on the RF surface.

Although RF breakdown has been the subject of many investigations both experimentally and theoretically, there is a surprising amount of uncertainty regarding the mechanism involved. What is still missing is a deeper understanding of what exactly makes up the value of field enhancement factor and how it relates to and is predicted from an observed surface condition.

Experiments at the MTA have revealed the negative effects of externally applied magnetic fields on the performance of RF structures by lowering the maximum achievable gradients. The observed damage in MTA cavities operated in magnetic field may be caused by the impact of field emitted electrons focused by the magnetic field onto the copper surfaces. Small metal sections are electrostatically drawn from the surface due to fatigue, becoming vaporised and ionised by field emission from the remaining damage. The model examined in this study presumed that breakdown occurs in steps as below.

- Dark current electrons are emitted from asperities and accelerated by the RF fields and impact another location of the RF cavity. With sufficient magnetic field, the emitted electrons are focused and bombard small sports on the opposing surface.
- The cavity surface temperature rises from the impact.
- In the presence of magnetic fields, the surface material probably is severely damage by fatigue induced by repeated deposition of local energy.
- The relative amount of surface heating and therefore the probability of fatigue failure depends on the materials properties

The relatively low gradient breakdowns observed in both 805 and 201 MHz cavities are a source of concern for future Neutrino factory complexes. These predicted breakdown events occur at significantly lower gradients than the operating levels specified for such facilities and much more work is needed to rectify any possible sources of RF breakdown.

Chapter 4.

Manufacturing Processes and Surface Finish

4.1 Introduction

During production of an RF cavity, the metallic surface can be subjected to both mechanical and chemical alterations. Hence the quality of the RF surface is directly influenced by the manufacturing techniques employed during production. As noted earlier in Chapter 3, the quality of the RF surface can influence the probability of an RF breakdown event being initiated. If we are to obtain a better understanding of cavity performance and thereby develop better means of production, the fabrication procedure needs to be investigated further. The MTA research program outlined in Chapter 2, has been performing a series of high power tests on button shaped samples using an 805 MHz copper cavity. The aim is to investigate the RF breakdown limit of various materials by exposing each to high E and B fields [39-41]. This research on the other hand focused on the manufacturing techniques rather than material properties.

The complexity of RF breakdown phenomena and the absence of a proven theory make it difficult to apply experimental results on breakdown limit from one RF structure to another [49]. To allow comparisons to be made with current MTA

findings, similar button tests have been carried out. Buttons were manufactured in batches using a single material and different manufacturing procedure. By investigating the breakdown limit of each button in the MTA 805 MHz cavity, it is possible to analyse the effect of the manufacturing process on the breakdown limit of each button. Both the manufacture and surface treatment stages of the production can alter the surface characteristics and need to be analysed. A systematic approach to carry out such investigations was developed in this work and the major steps carried out are shown below in Figure 4-1.

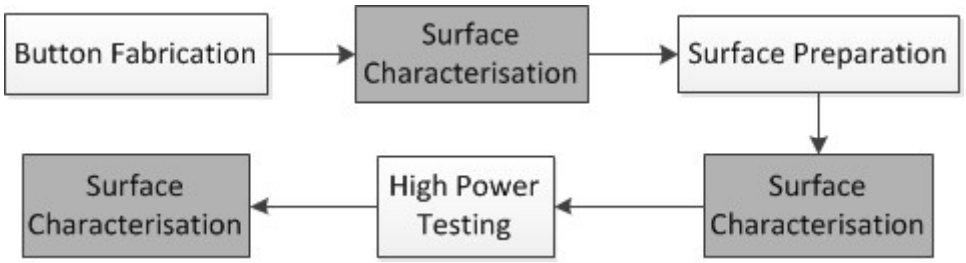

Figure 4-1: Flow chart showing the steps taken to prepare button pieces for High power testing. Each button was fabricated in house and a series of surface treatment processes was carried out to achieve the desired surface quality. Furthermore, surface measurements were taken at several intervals in order to analyse the changing characteristics of the surface defects

The mechanical and chemical structure of the surface for each button is characterised after each stage of production. The findings alongside current MTA results provide the back bone for improvements in cavity design and manufacture of the proposed Neutrino Factory RF cavities. This chapter introduces the design and manufacturing steps taken to fabricate the new test buttons alongside the surface treatment procedure employed by this research.

4.2 MICE Cavity and Button Fabrication

The various shapes and sizes of RF cavities dictate the fabrication technique that need to be used in their production. As shown below in Figure 4-2, the MICE

cavity 201 MHz was spun using two flat metal sheets until the desired shape was achieved. By welding both half shells together, the cavity structure was manufactured. Prior to welding, a step was machined out of the edges of each shell to allow a stable platform to attach both shells together. In order to manufacture a complete cavity, a combination of techniques such as spinning, metal pulling and machining had to be utilised. Details of the manufacturing procedure used to fabricate the MICE cavity can be found in the literature [87]. The 805 MHz cavity on the other hand was machined from a copper block due to its smaller size.

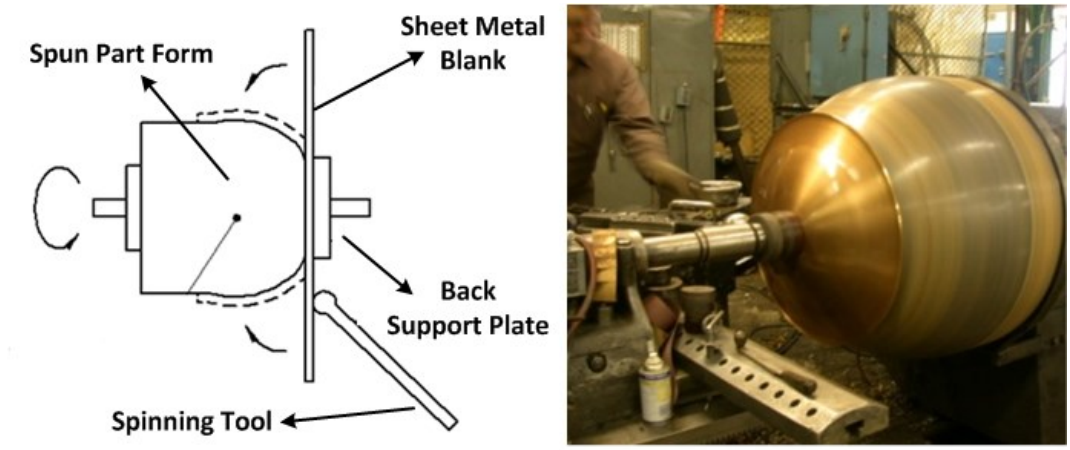

Figure 4-2: Schematic view of spinning fabrication process used widely in various industries (left) MICE 201 MHz cavity half shell being spun prior to cavity fabrication (right) [87]

In order to analyse and improve current production techniques used in MICE and the MTA, it is vital to fabricate each button test piece using similar processes. However, current MTA buttons are machined from a large metal slab in one piece. This limitation has been imposed by the current deign of the MTA button, where most fabrication techniques are not applicable. This research has addressed this limitation by developing a new button design.

4.2.1 New Button Design

In order to fit into the current MTA program and the 805 MHz cavity, the overall shape and size of the button had to be kept the same. During operation inside of the MTA cavity, only the top curved surface of the button is subject to RF fields. This factor was taken into account when redesigning the button test piece as shown below in Figure 4-3. The new button design consists of two separate parts referred to as the removable Cap and Holder. The cap is subject to RF fields inside the cavity and is held in the correct position by the holder. A major benefit of such a design is the ability to use a wider range of fabrication techniques due to simpler design. Both the design and manufacture of the new button was carried out in house using the available infrastructure.

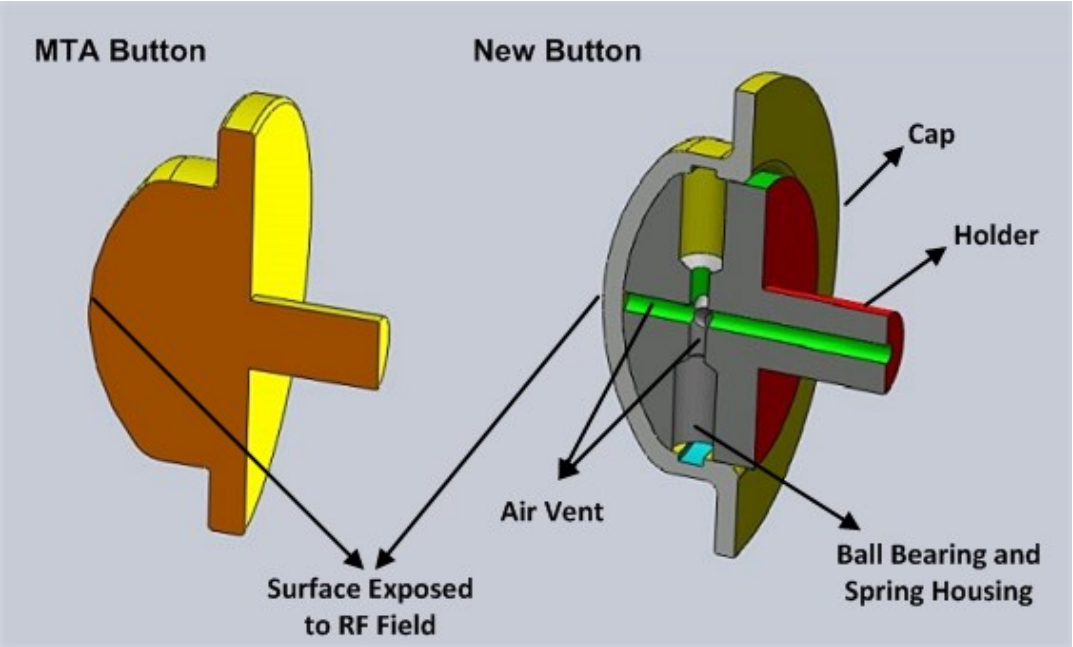

Figure 4-3: Cross sectional view of an MTA button (left) and the new button piece being designed and manufactured in this work (right). The MTA button can only be manufactured by machining while a series of fabrication methods can be used to manufacture the new button. This is due to the nature of the removable cap and the ability to use a thin sheet of copper to create the piece. The two parts are secured in place by 6 sets of securing connectors where a spring pushes a ball bearing into the internal surface of the cap. This would generate enough friction between the two parts to keep them connected

The new button will be operated similarly to previous tests and is capable of generating similar enhancement factors seen before. During testing, the cap and holder need to stay as one unit. This was achieved by drilling six equally spaced holes in the holder, where each houses a ball bearing and spring mechanism. When in position, the springs generate the necessary friction between the two parts by pushing the ball bearings towards the internal walls of the cap. Furthermore, a series of air vents are incorporated in the holder to ensure no air pockets are trapped when operating in vacuum during testing.

The design of the Cap would allow for the selection of other fabrication techniques and machining unlike the MTA button. To replicate the processes used for the production of the MICE 201 MHz cavity, the chosen fabrication method for this study is sheet metal drawing. The cap is made out of a 1 mm thick metal sheet.

Figure 4-4: Photograph showing the stages of Cap piece fabrication. A flat sheet of copper is formed into the desired shape is three steps using various pressing tools.

A series of tools were manufactured to perform the forming process in stages. As shown above in Figure 4-4, the cap was pressed in four different stages. Each was responsible for a specific feature of the cap, resulting in a steady and stable

manufacturing over extended number of samples. The staged forming process resulted in a gradual deformation of the material and it has been designed to avoid possible rupture when stretching the copper sheet.

4.2.1.1 Button Material Selection

The material of choice for normal conducting cavities is Oxygen-free high conductivity (OFHC) copper. This is generally referred to a group of wrought high conductivity coppers that has been refined to reduce oxygen levels. The cap was manufactured using OFHC to match the characteristics of MICE and MTA cavities. The copper purity level of the OFHC (C103-CW008) used in this research was 99.99% [88].

The holder on the other hand, is not subject to RF fields but needs to be operated in the presence of high magnetic fields. To fulfil such requirement, the holder was made out of 2011 (FMA) aluminium alloy. The key characteristics of this alloy are high mechanical strength and easy machining. Furthermore, attention was paid to choose austenite stainless steel for each ball bearing and spring mechanism to remove possible interactions with the applied magnetic field.

4.2.2 Button Transportation

Figure 4-1 shows the overall processing of the button, from fabrication to testing at high power. However, the process was carried out in various locations due to the availability of the required equipment in different institutions. As shown in Figure 4-5 below, the button assembly had to be transported a number of times between several institutions to be manufactured and tested.

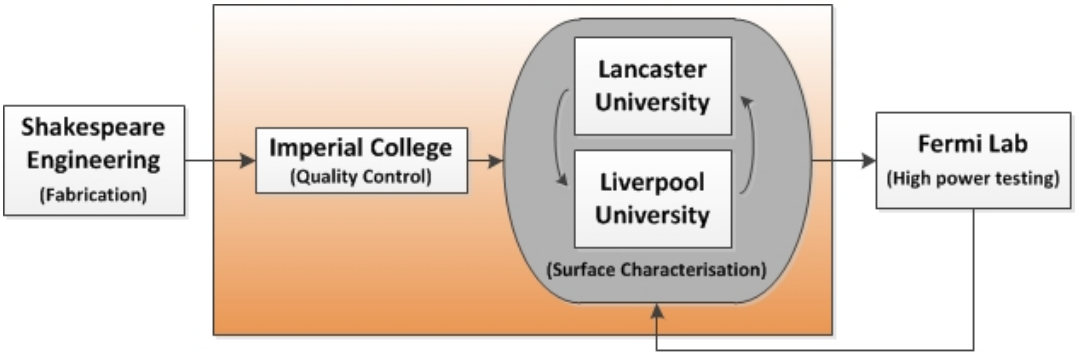

Figure 4-5: Flowchart showing the various steps in the transport of the button assembly from the point of fabrication to the point where the button arrives or high power testing. After being fabricated, the buttons are sent back for surface characterisation. The section The buttons are then sent to Fermilab for high power testing where they will be sent back to Lancaster university. The section highlighted in orange was carried out in house by the candidate. High power testing at Fermilab has not been performed due to refurbishment process underway at the facility

It was therefore vital to protect the surface integrity of the assembly while in transport. To meet this requirement, the transport jig shown below in Figure 4-6 was produced. The jig was made out of 1050 (s1c) aluminium alloy, which is a low strength and easily worked material.

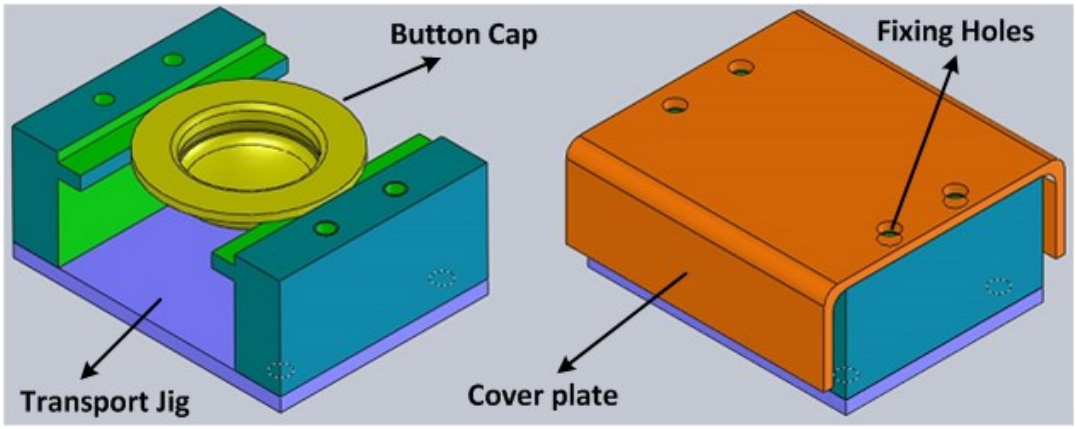

Figure 4-6: Demonstration of a Transport jig with button Cap in place (left) and with protected cover plate in position (right). The transport jug was designed and manufactured in house, and is used to transport the button cap safely between various institutions mentioned earlier in Figure 4-5. The main aim is to protect the surface from any possible physical damage

Once in place, a second plate is attached to the jig by a series of screws. This holds the cap in place and removes any possible threat of scratching. Furthermore, it was equally important to minimise oxidation of the RF surface by

removing direct contact with the atmosphere. This was achieved by placing the transport assembly inside a Nitrogen filled protective bag as shown in Figure 4-7.

Figure 4-7: Photograph showing Nitrogen filled protective bad being sealed off. Each Transport jig is placed inside a protective bad filled with nitrogen in order or protect the surface of the button from chemical reactions with the atmosphere and eliminate oxidisation. This process is carried out before the button assembly is to be transported between the various facilities

4.3 Surface Preparation

Surface preparation is generally considered to be the most vital aspect in the production of high gradient RF cavities. The importance of purity in terms of both grain structure and chemical composition of the RF surface has been discussed in previous studies [43]. The grain characteristics of a typical copper plate are shown below in Figure 4-8. The existence of the various layers is highly dependent on the environment in which the metallic surface was stored and manufactured.

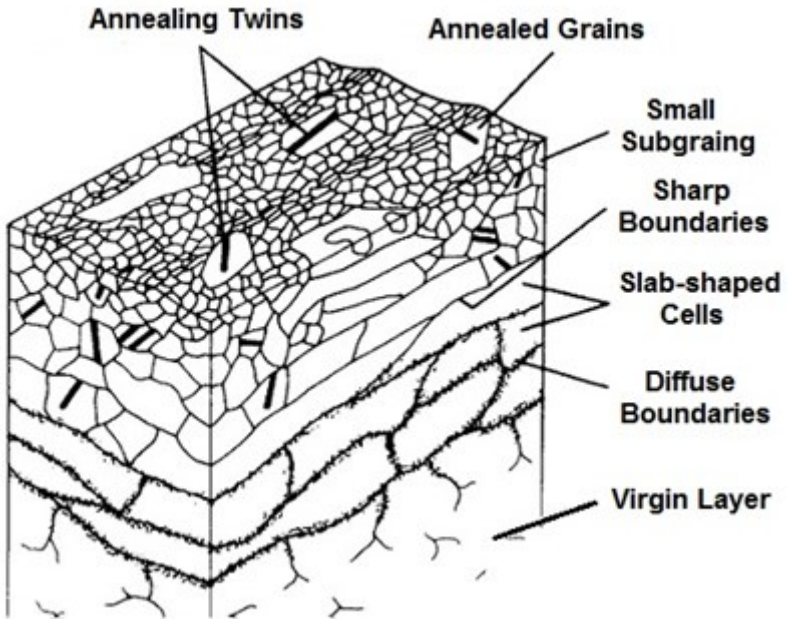

Figure 4-8: Representation of the different layers being present on the surface of a typical copper plate. The outer layer is known as the damaged layer where most of the physical and chemical misconfigurations are resent. The virgin copper sits at the heart of the metal and is the desired surface for the operation of an RF cavity [89]

The outermost layer consists of small sub-grains with an approximate depth of 1500 Angstroms (Å). With increasing depth, such grains are replaced by larger cells known as slabs with sharp boundaries. This trend is generally continued until all boundaries are fully diffused and the virgin copper layer is reached. The plastically deformed layer sitting on top of the virgin copper is a direct result of the production processes, exposed to foreign contamination and oxidisation. This layer is smoothly attached to the virgin layer and has variable thickness [90]. The aim of any surface preparation exercise has to be to reduce the damaged and contaminated layer to expose as much of the virgin layer as possible.

In this section, the processes used to treat the surface of the cap piece are introduced and comparisons are made to the procedure currently used to manufacture MICE cavities and MTA button pieces.

4.3.1 Electro Polishing (EP)

Electro polishing (EP) is an electrochemical process that removes material from the metallic surfaces. The primary objective of this process is to minimise micro-roughness or brightening and passivating metallic surfaces [91]. Materials that work well for electro-polishing include soft stainless steels, aluminium alloys and copper alloys. Hence, this is the most common surface preparation technique used to manufacture both normal and superconducting RF cavities. A typical result achieved through EP is shown below in Figure 4-9.

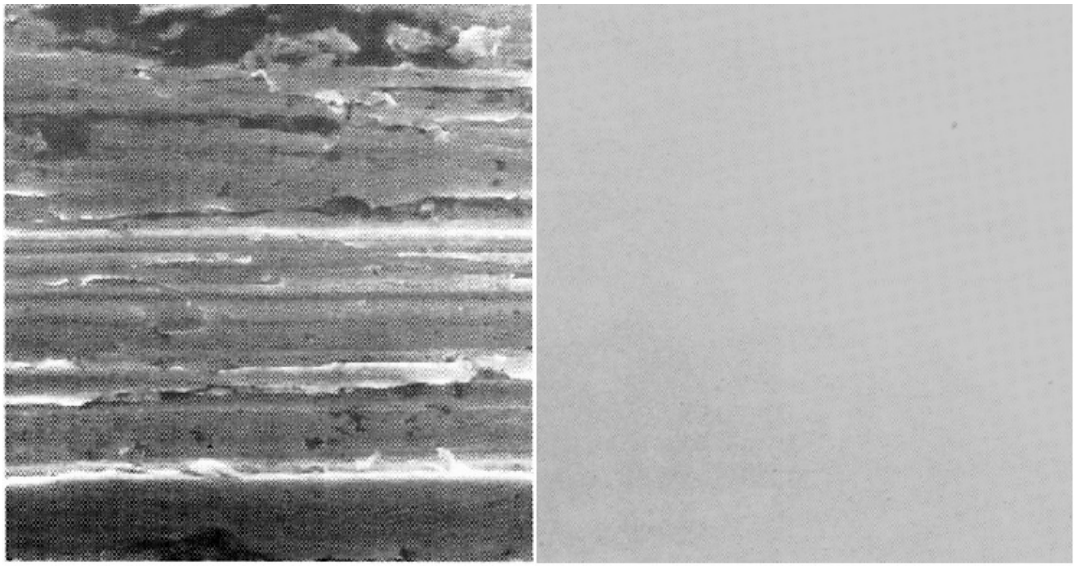

Figure 4-9: Photograph showing the surface of a stainless steel part being mechanically polished (left) after electro polishing was performed (right). The deep grooves, cavities, torn metal and microscopic imperfections are removed after performing EP. This would create a non-contaminating, non-participating and non-gassing surface as observed under high magnification [91]

The history of EP dates back to as early as 1912, but it was not until 1935 that copper was successfully electro polished by Jacquet [89, 90, 92]. Jacquet credited EP to the formation of a viscous layer around the polishing sample. He noted the fluctuating thickness of this layer across the material, leading to different Ohmic resistance from the cathode to the anode. The removal of sharp edges occurs due to such alteration, as the thickness of the viscous layer fluctuates based on the surface

profile. Higher field enhancements are observed on the edges in comparison to the depressed parts, resulting in the creation of a more uniform surface profile [92-94]. Further information regarding EP is available in the literature [89, 90, 92-94]. A typical EP setup is shown below in Figure 4-10.

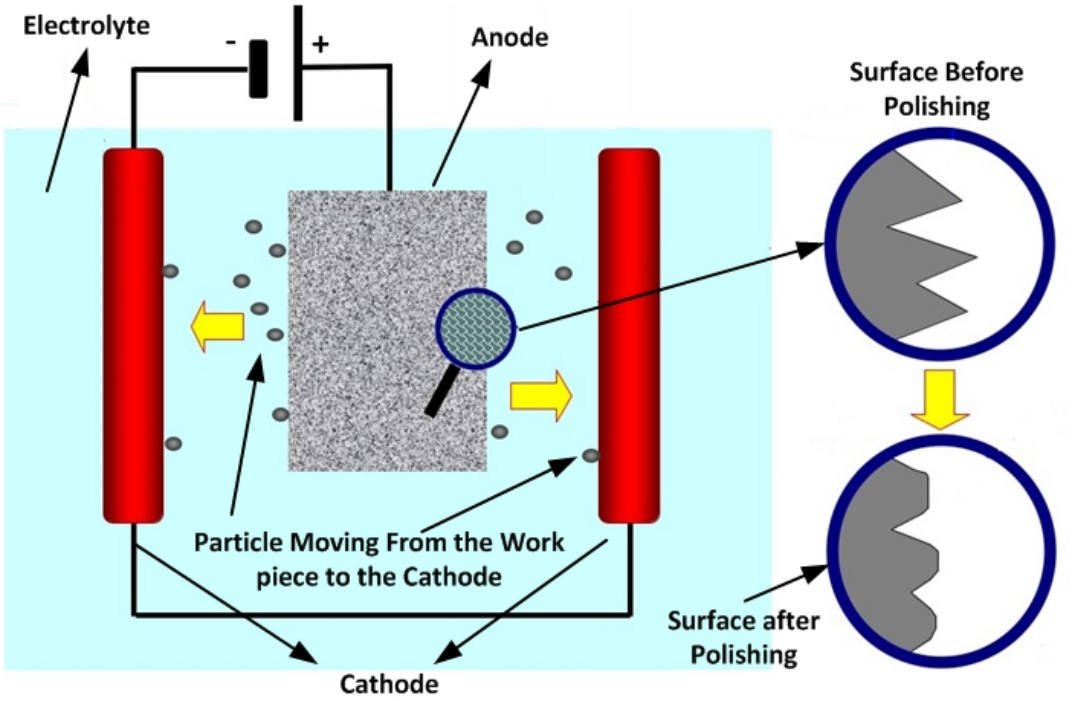

Figure 4-10: Schematic view of an electro polishing bath. The work piece is connected to the positive terminal and serves as anode. This is immersed in a bath of electrolyte alongside the cathode which is connected to the negative terminal. A current passes from the anode, where metal on the surface is oxidised and dissolved in the electrolyte, to the cathode. A Typical electrolyte consists of high viscosity phosphoric acid [3].

EP is still regarded as a black art despite wide spread industrial and research applications. Many in the accelerator community still use Jacquet's model to explain the EP process, which follows a typical I-V plot to explain the polishing characteristics as shown in Figure 4-11. The three major regions of a polishing process are identified as pitting, polishing and gas evolution [89, 92, 94].

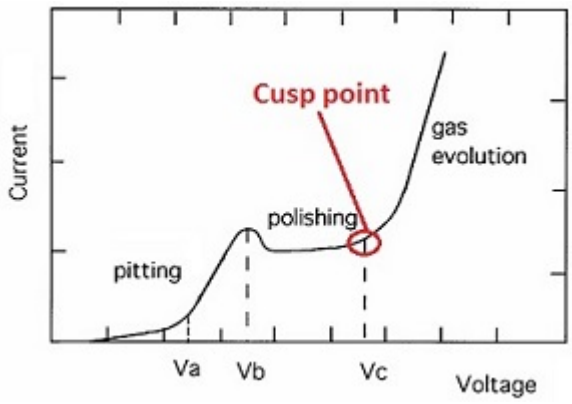

Figure 4-11: Jacquet's current vs. voltage plot for copper within an phosphoric acid electrolyte [89]. The voltage-current density plot represents the mechanism by which pitting and polishing occurs. Below V_a the primary mechanism is the direct dissolution of the metal, where etching occurs. Between V_b and V_c the passivation layer occurred before this becomes stable and dissolution of the metal occurs primarily by diffusion through this layer. By increasing the voltage, the passivation layer breaks down as the oxygen evolution occurs at the surface.

The characteristics of the I-V curve is dependent on the initial surface quality and the surface area ratio of cathode and anode [94]. The polishing process is initiated by the creation of an oxide layer between regions V_a and V_b. Due to the establishment of a diffusion layer, the current density up to point V_c is independent of the applied voltage. This flat region is referred to as the polishing plateau. Further increases in the applied voltage would result in formation of oxygen bubbles near the anode, which is the surface to be polished [89, 90, 92, 94]. Optimum polishing results are achieved in the region known as the cusp point. This location marks an area where maximum voltage can be applied while keeping the current levels fairly constant. Oxidation can follow beyond this point [92, 95, 96].

Applying the incorrect voltage can result in the creation of damaged surfaces through EP. Typically, pitting is observed at voltages below V_b and oxygen bubble damage is experienced at voltages higher than the cusp point. This is simply due to the differing dissolution rates observed at both regions [90, 92, 96, 97]. An example of a pitted surface is shown below in Figure 4-12.

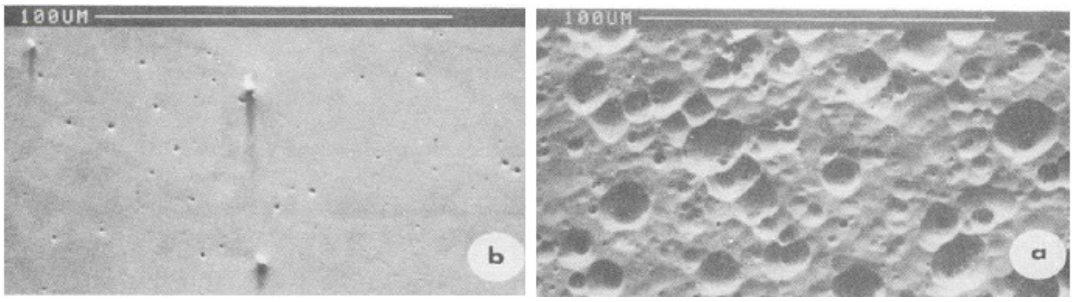

Figure 4-12: Photograph showing the surface of a stainless steel after EP (left) and the same surface being pitted (right) [90]. This highlights the importance of choosing the correct voltage level as close as possible to the cusp point in order to achieve the best polishing results

Surface features on a shorter wavelength are removed by the EP process, while features with a longer wavelength are left behind [94]. Hence, it is important to ensure the sample has the best possible surface prior to EP. This can be achieved by generating a scratch depth shallow enough to provide shorter wavelength surface profiles for EP to be effective.

4.3.1.1 MICE Cavity and MTA Button EP Procedure

Both the MICE cavity and the MTA buttons were polished using the facilities at Thomas Jefferson Lab (JLAB). The electrolyte used consisted of 85% Phosphoric acid and 15% Butanol. The former is responsible for levelling the surface profile while the latter is used to provide greater conductivity through the electrolyte [98]. The size and shape of the MICE 201 MHz cavity presented many challenges during polishing and special techniques were developed at JLAB in order to EP the cavity. As shown below in Figure 4-13, the cavity surface was buffed mechanically to remove deeper scratches left behind from the spinning tool. The cavity shell acts as both the anode and the container for storing the electrolyte mixture.

Figure 4-13: Photograph showing a half shell of an MICE 201 MHz cavity after being mechanically buffed [87]. This step is important to remove any visible damaged layer prior to EP

As shown in Figure 4-14, the cavity was held in position by a series of supports and could rotate around its axis. The bottom of the cavity shell stored the acid, where a U shaped cathode was inserted to optimise the polishing performance. Once polished, the cavity was rinsed using high pressure water.

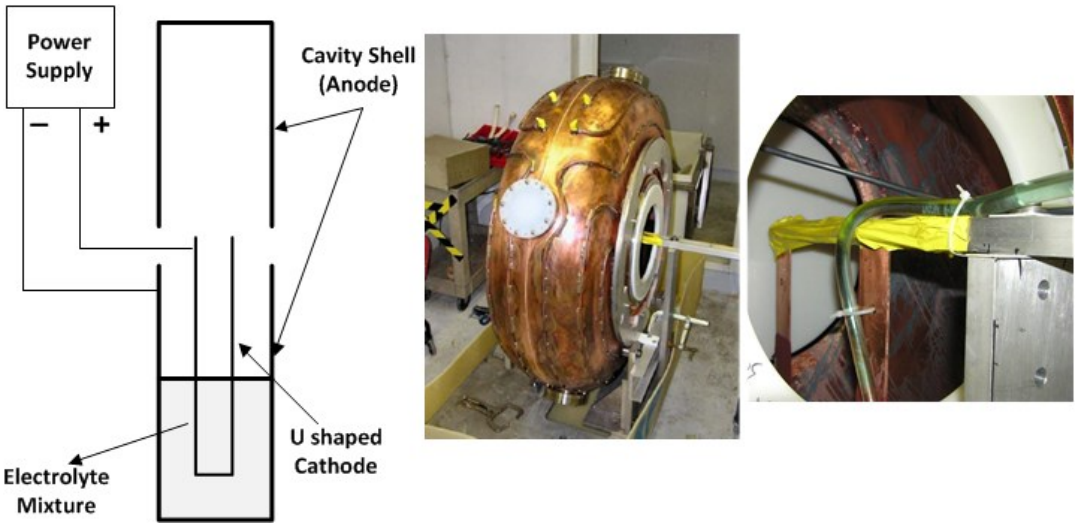

Figure 4-14: Schematic view of the EP setup used for polishing MICE 201 MHz cavities (left) A MICE 201 MHz cavity during polishing (middle) [87] a view of the shaped cathode used for EP (right) [87]. The cavity sits on a specially designed stand and rotates around its axis. Only half of the internal surface is in contact with the phosphoric acid at any point, increasing the chance of an uneven polishing result

A major flaw of this technique was the lack of protection against oxidation. As the cavity shell rotated, the polished surface was exposed to the atmosphere during

EP. Furthermore, no real control on the applied voltage and subsequent current flow was observed. This led to inconsistent polishing results being achieved.

The same facilities at JLAB were used to polish the MTA buttons. As shown below in Figure 4-15 a special High Density Polyethylene (HDPE) holder was produced. The holder held four samples with a cylindrical cathode in the middle and was immersed inside an acid container. The level of applied voltage was based on the polishing surface area and was dependent on the number of samples [98].

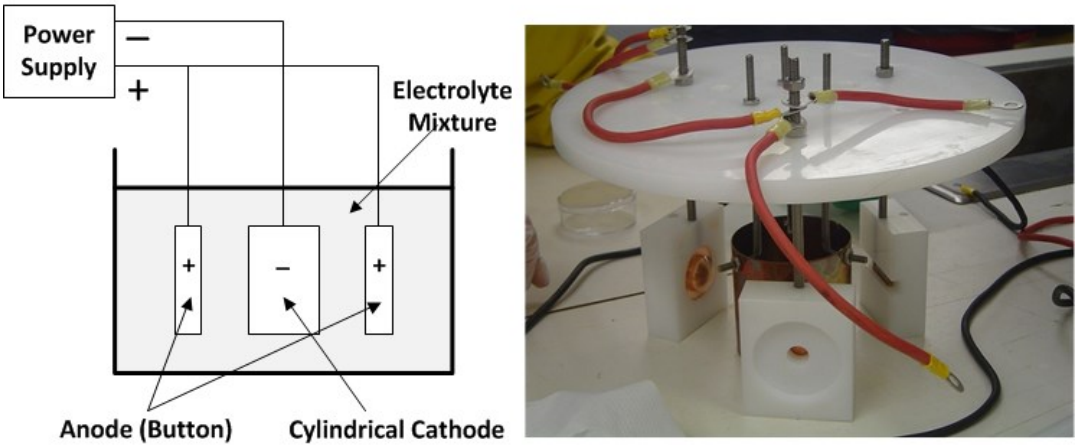

Figure 4-15: Schematic view of the EP setup used to polish MTA buttons at JLAB (left) A view of the JLAB button holder with a copper tube used as the cathode (right). The button is fully immersed into the electrolyte during the process, marking an improvement compare to the setup used for the cavity

The process lacked the ability to evaluate and apply the correct I-V curve to the sample during EP. Once more, this led to inconsistent polishing results. Furthermore, each button underwent EP straight from the manufacturing.

4.3.1.2 Improved EP Procedure

In order to achieve more consistent polishing results, the overall process was reassessed and improved in this research. As shown below in Figure 4-16, in the new procedure the cap underwent several preparation stages prior to EP. Each individual task was responsible for preparing the cap surface in a specific way to

ensure best polishing results were achieved. The effectiveness of each stage has been verified and tested using several test samples.

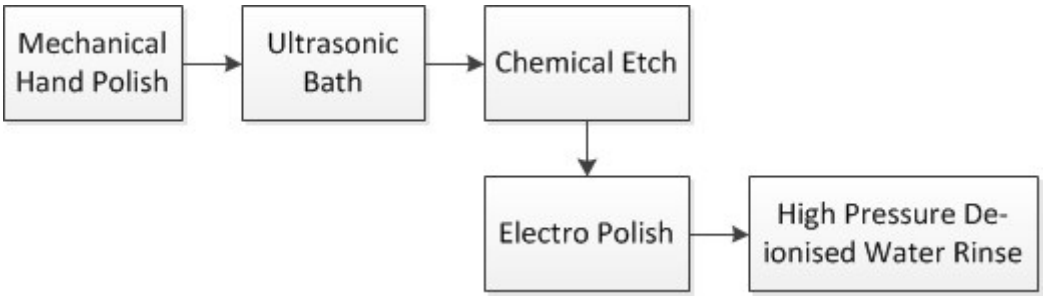

Figure 4-16: Flow chart showing the various steps used during the EP process carried out in this this study. The addition of Ultrasonic bath and chemical etching prior to EP would ensure maximum removal of oily residue and damaged oxide layers. The process designed in this work is simple and robust, enabling repeated samples to be polished with little alterations in the setup

Once received from the manufacturer, each cap was hand polished. This was performed using 400 to 1200 grade silicon carbide sand paper. Each paper grade ensured the removal of a specific type of surface damage. The hand polished cap and the holder were then washed in an ultrasonic bath to remove possible oily deposits on the surface. The cap was then chemical etched by immersing the piece into phosphoric acid. The button was then finally electro polished once the pre-treatments were completed. At the end, each sample was washed using a high pressure rinse. The first two stages can be seen below in Figure 4-17.

Figure 4-17: Photograph showing the ultrasonic wash bath being used to clean the bolder piece (left) Chemical Etching of a button cap after being hand polished (right). Both processes would ensure the removal of any oily contamination alongside oxide damaged layers. The chemical etching removes the edges of large scratches and generates an uneven surface through an uncontrolled process

The I-V characteristics of an EP system depends on factors such as orientation of the anode and cathode, cathode material, anode to cathode surface area ratio, electrolytic bath age and temperature [92, 96, 97]. In order to build on previous achievements at JLab and to address the above issues, the EP setup used to polish the new buttons was modified.

As shown below in Figure 4-18, an electrolytic cell was formed by immersing two copper electrodes in an electrolyte and applying a voltage applied between them. The positive and negative electrodes consisted of the samples to be polished and the cathode respectively. In order to achieve a dedicated I-V curve for each sample, only one cap piece was polished at any given time. By slowly increasing the applied voltage, the cusp point was reached and maintained. To ensure the polishing quality was maintained, the electrolyte mixture was only used for two buttons before being replaced with a fresh mix.

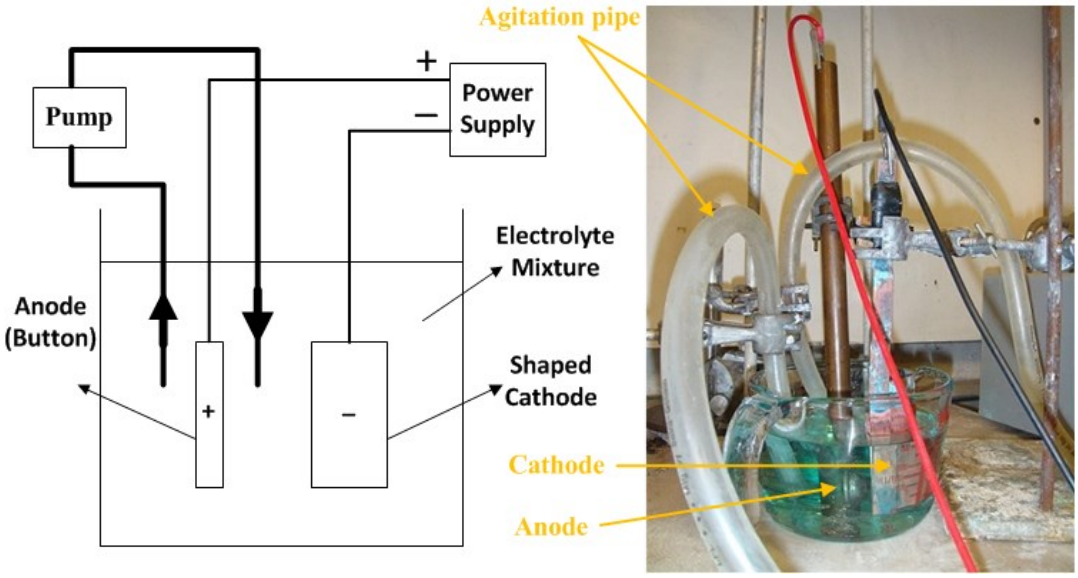

Figure 4-18: Schematic view of the EP setup designed and manufactured in this study to carry out EP of the new button pieces (left) a button cap being polished using the new setup (right). The process has been improved by adding an agitation pump in order to circulate fresh electrolyte around the cathode. Simplicity was in mind when designing the setup, ensuring very little change from test to test.

The dimensions of the cap posed many problems in all aspects of the surface preparation. In order to maintain an even electric field within the electrolyte bath, the cathode was shaped to conform as closely to the profile of the cap as possible. This is a major improvement in comparison to the setup used at JLab.

There are several problems associated with the JLab mixture. One is the formation of oxygen bubbles around the anode once the input voltage reaches V_b. This reduces the effectiveness of the polishing process significantly through insulating the anode [90, 96-98]. This issue was addressed by agitating the mixture in order to disperse such bubbles during formation. Shown below in Figure 4-19, a set of pipes were used to generate the desired agitation levels.

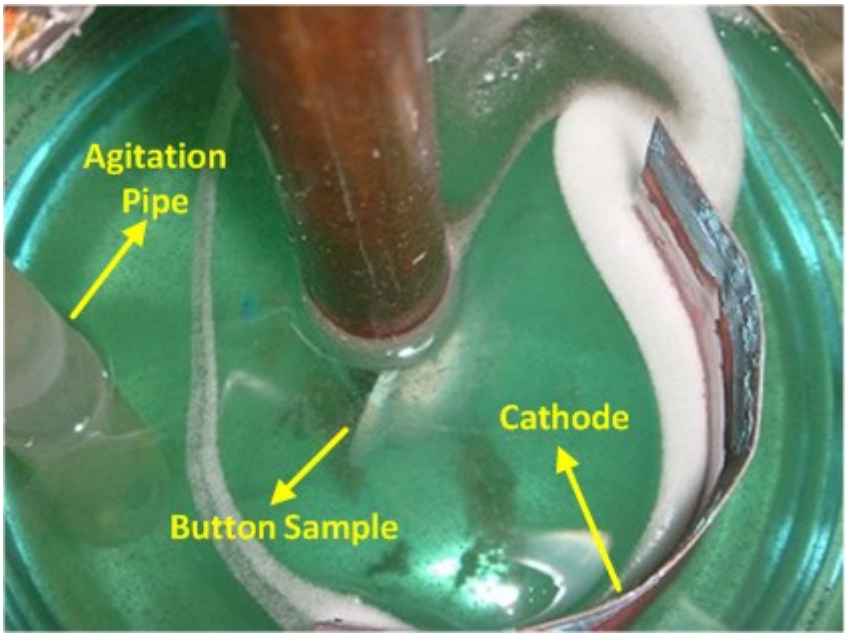

Figure 4-19: Photograph showing bubble formation due to oxygen release near the anode.

A peristaltic pump was used to generate the suction needed for the acid to be extracted and replaced by fresh mix around the cathode. This technique contributed in maintaining the polishing cusp point and replicating Jacquet's I-V characteristics

profile more accurately. The bubbles caused by oxygen formation disappear when the system is stabilised near the cusp point.

4.3.2 Electroplating (EPL)

The second surface preparation method used in this study is electroplating. This is the application of electrolytic cells in which a thin layer of metal is deposited onto an electrically conductive surface. Illustrated in Figure 4-20, the process is referred to as electro-deposition. Electrical current is used to reduce cations of a metal from a solution and coat a conductive object with a thin layer of the metal. Electroplating has come a long way since the simple but pioneering gold plating attempt of Luigi Brugnatelli back in 1800. Due to its cost efficiency and high end product quality, many industries employ this method of production.

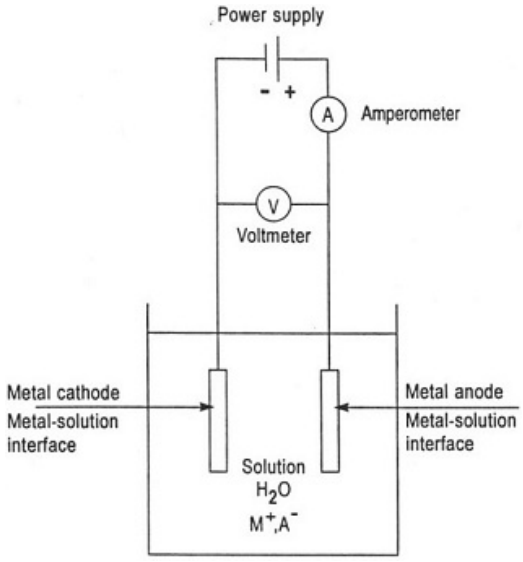

Figure 4-20: Schematics of an electrolytic cell for plating metal M from a solution of metal salt MA [99]

The main components of an electroplating setup consist of:

- External circuit consisting of the direct current (DC) source
- Negative electrode or cathode, which is the component to be plated

- Plating solution known as the bath
- Positive electrode or anode, which is made of the metal to be deposited

Both cathode and the anode are connected to an external power supply. The bath electrolyte consists of a solution containing one or more dissolved metal salts as well as other ions that ensure good conductivity. The anode is oxidised through direct current supplied by the power supply, allowing positively charged cations to be dissolved in the solution. The dissolved metal ions are then reduced at the cathode, plating it with thin layers of metal. The rate at which the anode is dissolved normally equals the rate at which cathode is plated. This ensures that ions in the electrolyte bath are continuously being replenished by the anode. The general form of the reactions occurring at cathode and anode are [3, 99, 100]:

At cathode $$M_{(aq)}^{Z+} + Ze^{-} \longrightarrow M_{(s)} \quad (4\text{-}1)$$

At Anode $$M_{(s)} \longrightarrow M_{(aq)}^{Z+} + Ze^{-} \quad (4\text{-}2)$$

where Z represents the number of electrons. The electrolytic process can be explained by the two Faraday's laws [100]:

- The amount of chemical change produced by an electrical current is proportional to the total integrated current.
- The amount of different substances liberated by a given quantity of current is inversely proportional to their chemical equivalent weights.

The weight (w) in the first law is in grams or ounces and the quantity of electricity is in coulombs. This relationship can be defined as [100]:

$$w = I_{(amps)} \times t_{(s)} \quad (4\text{-}3)$$

This demonstrates the importance of the time that the current is passed through. These laws can predict the amount of chemical changes produced through measuring the integrated current.

In order to ensure a good adhesion of the coated layer on to the surface, the pre-treatment of the surface is extremely important [101]. A successful electroplating process heavily depends on eliminating any contamination and damaged films from the substrate. Organic and non-metallic films can lead to poor adhesion and in some cases may prevent adhesion. Surface contaminations can be either extrinsic, such as organic debris and mineral dust or intrinsic like native oxide layers [96, 101]. Substrates can be cleaned through physical or chemical cleaning. The first method introduces mechanical energy to release both extrinsic and intrinsic contaminations while the latter employs active materials being dissolved or emulsified in the cleaning solution.

This study employs the electroplating technique as a second alternative method to treat button samples. Each button is electroplated in a copper bath, in order to be compared to the EP process. Although electroplating has become a highly sophisticated technique based on various sciences, it is still regarded as an art in many cases. This highlights the role of user's past experience in producing the desired surface. Figure 4-21 demonstrates the setup used to prepare and electroplate each button sample.

Figure 4-21: Photograph showing different stages of the platting process which consists of the pre-cleaning (left), De-ionised water wash (right) and Electroplating bath (bottom). The button is required to be degreased in a cleaning solution first then followed by a rinsing in de-ionised water. The button is then immersed inside a liquid copper mixed and placed between four electrodes where current is passed through the mixture. The copper is then slowly deposited onto the surface slowly

Each sample first undergoes an EP process to ensure the removal of the intrinsic contamination, explained above. Organic debris is removed by placing the sample inside a mixture of warm de-ionised water and electrolytic cleaning salt. As shown in Figure 4-21, a current of 0.1 amps is passed through the mixture [96], followed by de-ionised water wash.

The longer the sample remains in the bath, the thicker the resulting electroplated layer will be. The geometric shape and contour of the object being plated affects the thickness of the deposited layer. In general, objects with sharp corners and features will tend to have thicker deposits on the outside corners and thinner layers in the recessed areas. This is due to more DC current flow around sharp edges than the less accessible recessed areas. Initial experiments on flat samples demonstrated the deposit rate of 1μ per minute. This is dependent on the surface area to be plated

and the required current and can obtained by equation (4-4), where A is the surface area in $cm^{2,}$ I is current in amps and 0.03 is a coefficient of normalisation [96]. This is impartially estimated and can be material dependent.

$$I = 0.03 \times A \tag{4-4}$$

4.4 Surface Characterisation

After each stage of production, the surface of the cap is to be characterised. This consists of analysing the surface quality and chemical composition of the RF surface. By highlighting the changes made during production, it is possible to understand the effects of each production technique further.

4.4.1 Mechanical Surface Evaluation

Surface roughness is a measure of surface texture and is quantified by the vertical deviations of the real surface from its ideal form. Evaluation of surface roughness is highly important for many applications and therefore the measurement of surface roughness has been a key element in many experimental and theoretical investigations. Although surface roughness can be quantified using various parameters [102], only two parameters were used to take the required measurements in this study. The two most common techniques for taking measurements are the stylus method [103] and optical profiling [104]. For the purposes of this study, optical profiling was chosen as a more suitable method.

Roughness parameters can be measured in either 2D or 3D, where measurements are taken along a single line or an area respectively. 3D measurements are better representation of the surface as more information is

collected over the sampling area. The two roughness parameters generally used are the arithmetic average roughness (Ra) and root mean square roughness (Rq).

4.4.1.1 Arithmetic Average Roughness (R_a)

The arithmetic average height, also known as centre line average (CLA), is the most commonly used surface roughness parameter. It is defined as the area between the roughness profile and the mean line. This is calculated based on the average absolute deviation of the roughness irregularities from the mean line, over the sampling length [102]. This is shown in Figure 4-22. Ease of measurements and general description of height variation are the advantages of the R_a. However, it does not provide any information about the wavelength and it is not sensitive to small variations. The arithmetic average roughness can be expressed as [102]:

$$R_a = \frac{1}{L}\int_0^L |y(x)|dx = \frac{1}{n}\sum_{i=1}^{n}|y_i| \qquad (4\text{-}5)$$

where L is sampling length, n the total number of samples and y is the surface profile being investigated.

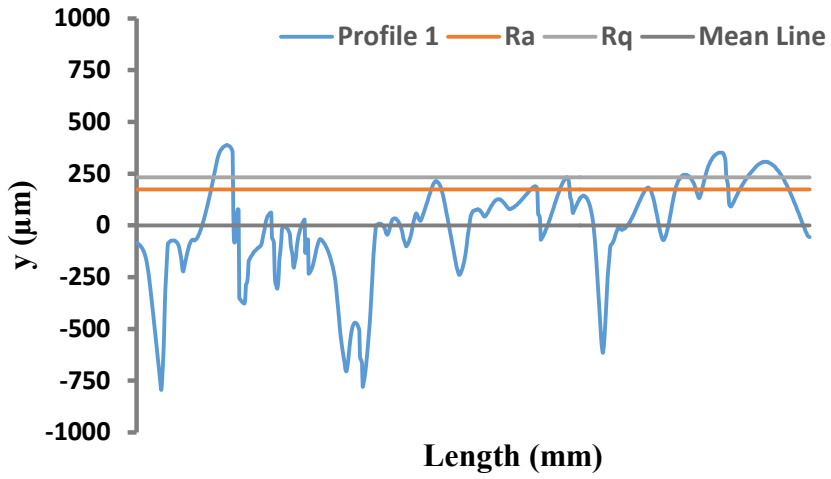

Figure 4-22: Sampling profile showing the R_a and R_q values for a imaginary surface. This highlights the difference between the two parameters where R_q has a bigger value in comparison to R_a

4.4.1.2 Root Mean Square Roughness (R_q)

Root mean square roughness, also known as RMS roughness, represents standard deviation of the surface heights distribution which is shown in Figure 4-22. The advantage of this parameter compared to arithmetic average roughness is the sensitivity of this parameter to small deviation from the mean line. The root mean square roughness can be expressed mathematically as [102]:

$$R_q = \sqrt{\frac{1}{n}\sum_{i=n}^{n} {y_i}^2} \tag{4-6}$$

4.4.1.3 Surface Uniformity (R_q-R_a)

In this study a new parameter (R_q-R_a), referred to as surface uniformity was introduced. This was be used to compare the height distribution of the peaks and valleys over the sampling area. The significance of this parameter is explained through an example shown below in Figure 4-23, where two profiles with different peak and valley heights are being compared.

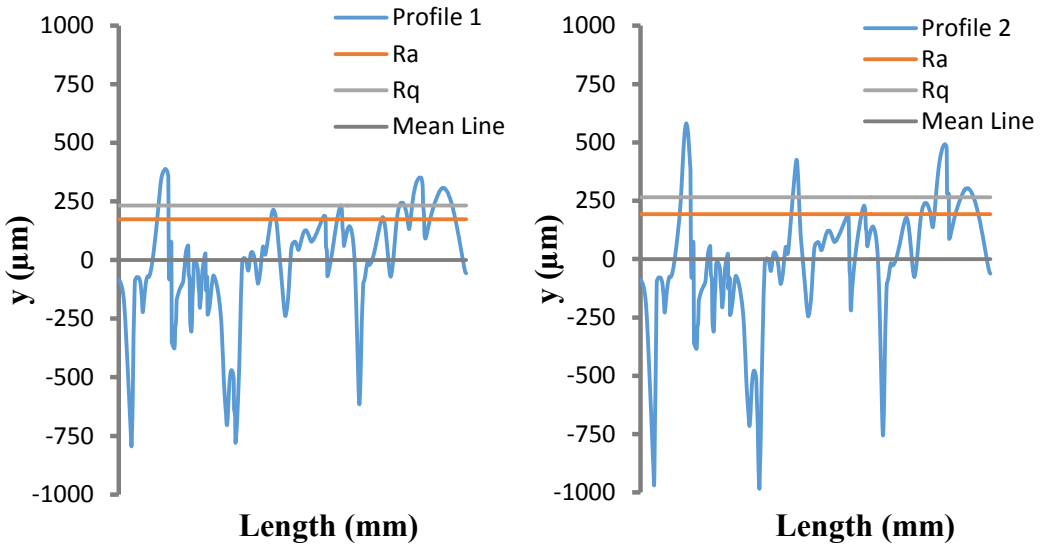

Figure 4-23: Plot showing two different surface profiles of an imaginary object with similar R_a values by different (R_q-R_a) values. This highlights the fact that although the roughness values are regarded to be similar, the quality of the surface can be different. This variation in surface quality can be expressed by the use of the surface uniformity parameter (R_q-R_a)

The increase in peak height in profile 2 was cancelled out by a similar increase in valley depth. This resulted in little variation seen in the value of R_a between both profiles. However, the value of the RMS roughness exhibits greater sensitivity due to its mathematical representation. The difference between the behaviour of each parameter shown in the above example highlights the fact that R_a alone is not enough to provide an accurate representation of the surface profile.

However, it is possible to use surface uniformity parameter (R_q-R_a) as the means to emphasise the differences between the overall peaks and troughs of two profiles shown above. The surface is more uniform as this parameter is lowered. A low surface uniformity represents a narrower height distribution of peaks and troughs in the profile, whereas a higher surface uniformity represents a larger height distribution of peaks and troughs. This parameter can be used to make comparisons between two surfaces with similar R_a values and analyse the overall quality of each surface. Table 4-1 shows the quantitative comparison of the R_a, R_q and surface uniformity of the profiles presented in Figure 4-23 the above example.

Table 4-1: Table showing the values for the roughness parameters R_a and R_q alongside surface uniformity for the surface profile examples used in Figure 4-23. Although both surfaces have almost similar R_a values, profile 1 exhibits a much improved surface uniformity

Name	R_a (µm)	R_q (µm)	R_q-R_a (µm)
Profile 1	173.88	232.45	58.57
Profile 2	180.70	253.12	72.42

It is possible to see that although the two surface profiles have changed, the value of the R_a was kept relatively constant and R_q was increased. However, the alterations made in the height of the peaks and troughs were easily detected by the surface uniformity parameter of (R_q-R_a).

4.4.2 Roughness Measurement Methodology

As shown below in Figure 4-25, WYKO NT1100 [105] optical profiling measurement system was used to take the necessary measurements. This is a white light interferometer capable of taking 3D measurements by vertically scanning the sample. The vertical scanning surface area was only 736 by 480 microns (μ). In order to provide a more general and accurate representation of the surface profile, measurements were taken at various locations on the sample. As shown in Figure 4-24, a total of 4 data rings and sixteen data points were defined by this study. The overall surface roughness parameters were derived by averaging the data points.

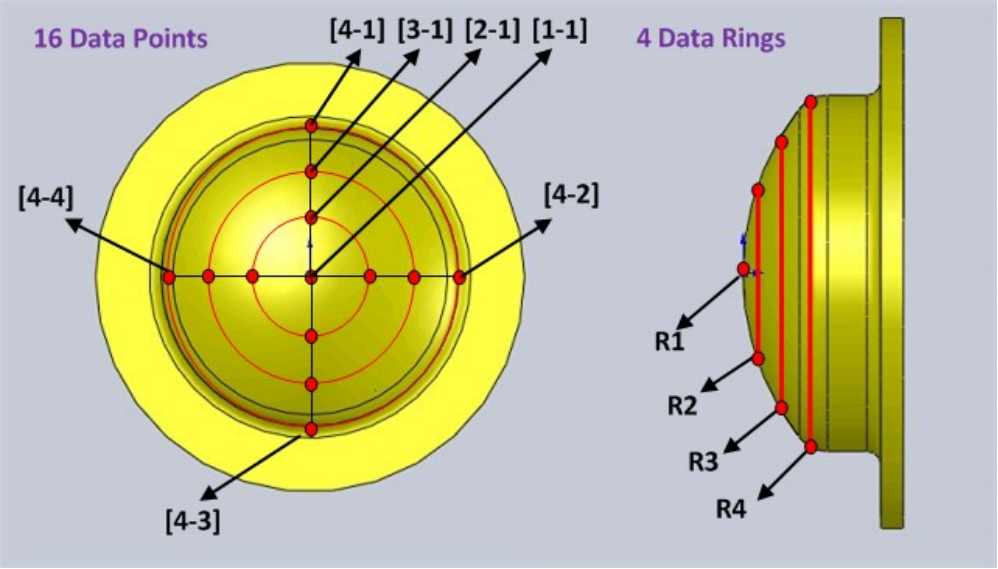

Figure 4-24: Representation of the various data points and rings chosen for taking surface measurements across the surface of the cap. There are a total of 16 data points and 4 data rings, each being given a number for better visualisation

To preserve the accuracy of measurements, it was vital to ensure the incident light was orthogonal to the Cap surface. Any interruptions in the return of the incident light would result in the loss of data and accuracy of the surface plots being generated. To achieve this, a special scanning holder had to be designed and manufactured. Shown in Figure 4-25, the scanning holder consists of 4 bases with

various base heights. Depending on which data ring was being analysed, the scanning holder with the most suitable angle was used.

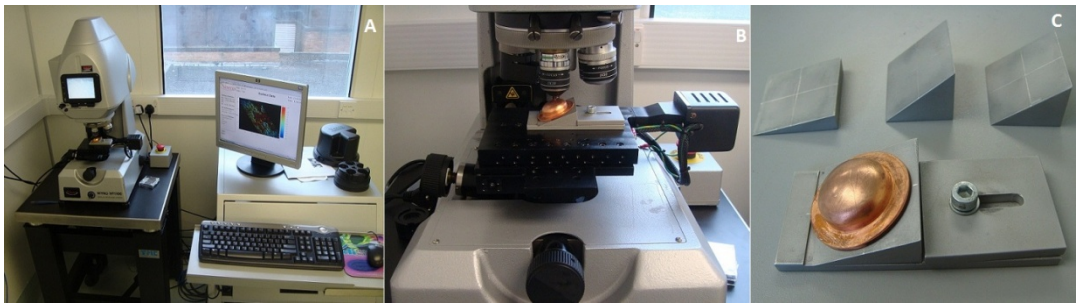

Figure 4-25: Photograph showing the interferometer setup (A) button cap under the 20X lens (B) and purpose built scanning holder for buttons (C). The button scanning holder was designed and manufactured in this work. It is responsible for ensuring the button is placed at the right angle under the interferometers to allow best possible data to be extracted from the relevant data ring

4.4.3 Chemical Composition Measurements

X-ray Photoelectron Spectroscopy (XPS) is the most widely used technique to define chemical composition of metallic surfaces. This is due to its relative simplicity in data interpretation, and is the chosen method to analyse the chemical mix of the Cap surface. Being based on Einstein's idea of the photoelectric effect, it was developed by Siegbahn in mid-sixties and used mostly for chemical analysis of gas molecules. Their application was expanded with the development of Ultra-High Vacuum (UHV) technology [3].

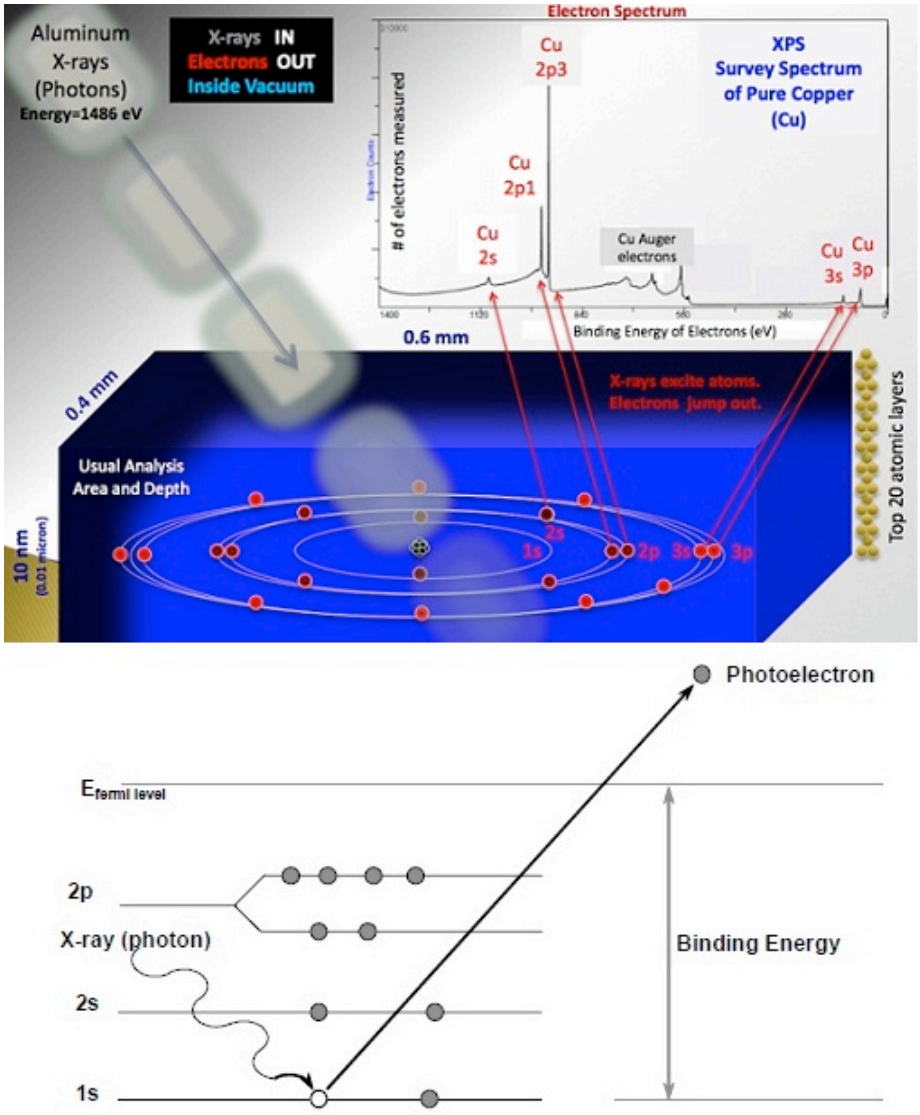

Figure 4-26: Schematic of XPS physics (top) [3], schematic representation of XPS process (bottom) [106]

An X-ray source is used to ionise the surface electrons of a solid sample, liberating them from the specimen. The binding energy of each electron is measured by an energy analyser, revealing the initial state and chemical composition of the irradiated solid. Figure 4-26 demonstrates the process by which an electron is emitted from the 1s shell of an atom.

An electron is excited by photon with an energy level of h_v. If the excitation energy is sufficient, the electron is ejected from the atom with a kinetic energy

of E_k. The atom is left in an excited ionised state due to an energy hole being left in the electron shell. The binding energy E_b of the electron can be measured with respect to the vacuum level by the expression [107, 108]:

$$E_b = h_v - E_k - W \tag{4-7}$$

where W is the spectrometer work function defined as the difference between the energy of the Fermi Level E_f and level E_v. This is the minimum amount of energy needed for an electron to escape and is expressed mathematical as [107, 108]:

$$W = E_f - E_v \tag{4-8}$$

Each element produces a unique set of electrons with a specific energy level. By measuring the number of these electrons as a function of kinetic energy, an XPS spectrum is obtained. The chemical state of the sample is defined from the position and intensity of the peaks in the energy spectrum. XPS can detect all elements with an atomic number greater than three. Hence, Hydrogen and Helium are the only un-detectable elements. This technique can analyse the average surface chemistry of a sample up to a depth of approximately 5 nm. The XPS technique is used in various sectors such as:

- Measuring surface contaminants
- Ultra-thin film and oxide layer thickness measurements
- Measuring effect of surface preparation treatments
- Composition of powders and fibres
- Composition depth profiling for multilayer and interface analysis

Figure 4-27 shows the XPS machine based at Liverpool University, used to take measurements for this study. Once more, the dimensions of the cap piece posed a

series of problems as the equipment are tailored to take measurements of flat shaped samples. Special tooling had to be designed in order to allow for each cap to be inserted into the chamber of the XPS equipment.

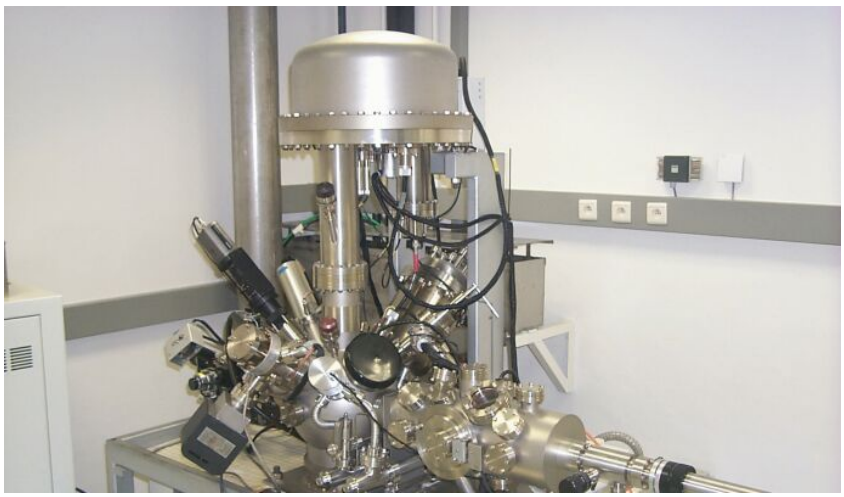

Figure 4-27: Photograph showing the XPS setup based at Liverpool University. The XPS measurements were taken by a third party

Chapter 5.

Surface Quality Analysis

5.1 Introduction

The quality of the RF surface is of much importance for the overall performance of any accelerating structure. The changing characteristics of the RF surface throughout the production process were analysed by testing the manufactured button samples. As described earlier, sheet metal pressing has been used to fabricate all samples. However, the RF surface was prepared using two different surface treatment methods. Roughness parameters and the chemical mix of the RF surface were measured using a white light interferometer and an XPS technique. By taking measurements after each major stage of productions, it was possible to identify the changing surface characteristics of each sample.

5.2 Surface Preparation - Method 1

The first surface treatment method to be tested in this study was the EP. This enabled the user to predict the achievable surface quality of MICE cavities and the MTA buttons prepared by this technique. The major steps taken in Method 1 are shown below in Figure 5-1. Each button was initially hand polished and chemical etched prior to EP. This was to remove the most contaminated and damaged layer in order to improve the final outcome of the surface quality. A total of six buttons were prepared using surface preparation Method 1.

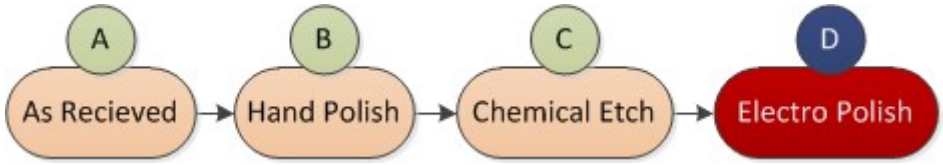

Figure 5-1: Major steps taken during the surface treatment process used in method 1. The process was repeated for button 1 to 6 keeping the conditions as steady as possible

Metal pressing is known to result in a relatively poor surface finish. This is simply due to the nature of the process, where the metallic surface is in extreme contact with the pressing die and results in high levels of surface stress. Furthermore, the surface is contaminated by foreign particles such as manufacturing grease and oxide layer due to atmospheric conditions. Figure 5-2 shows typical results of surface quality analysis following pressing.

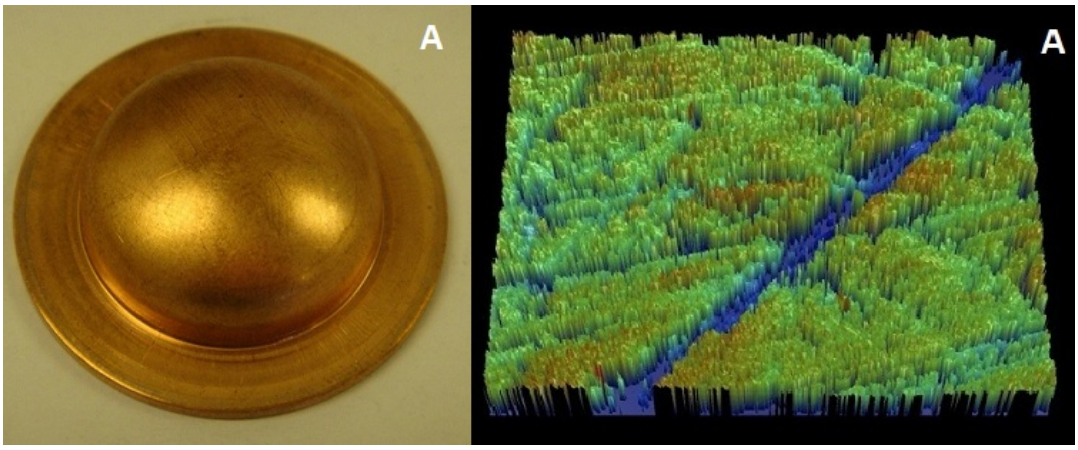

Figure 5-2: Photograph showing the surface of button 1 after leaving the manufacturing line (left) 3D Interferometer scan of the surface taken at data location (2-1) (right)

Hand polishing was subsequently performed in several steps using progressively finer grades of sand paper. Each step was responsible for removing a specific type of damage in order to achieve the desired surface finish. As shown in Figure 5-3, deeper cuts were replaced with random arrays of smaller scratches. Generally, such scratches tend to follow the movement of the abrasive paper during hand polishing. A major achievement of process B was the removal of the damaged layer seen

previously due to fabrication procedure. Metallic dust and paper contaminations were removed by washing the button in an ultra-sonic bath.

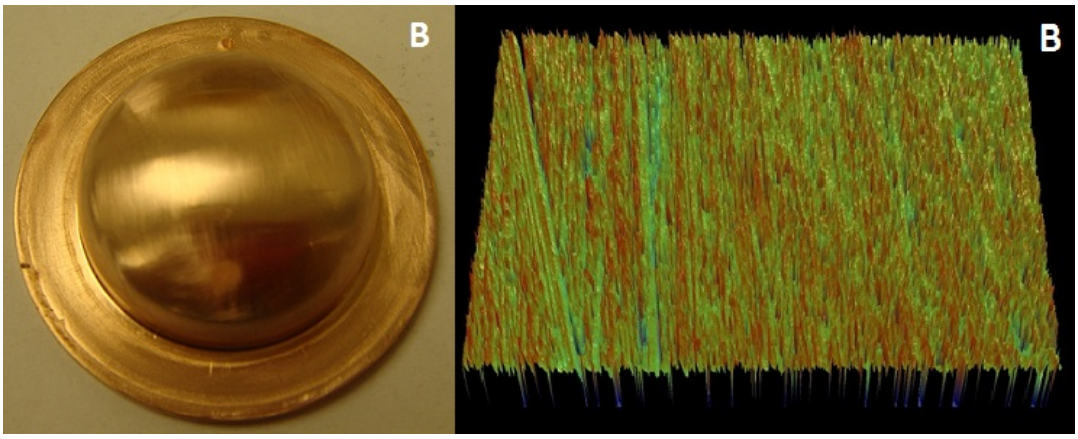

Figure 5-3: Photograph showing the surface of button 1 after being hand polished (left) 3D Interferometer scan of the surface taken at data location (2-1) (right)

The next step in the surface preparation was chemical etching. The button was submerged into phosphoric acid, where the acid attacks the sharp edges of the scratches left behind after hand polishing. Figure 5-4 shows button one after being chemical etched for two hours. The surface no longer contained recognisable scratches, and the surface profile appears random. The surface profile generated in process C enabled better results to be obtained during the subsequent EP stage.

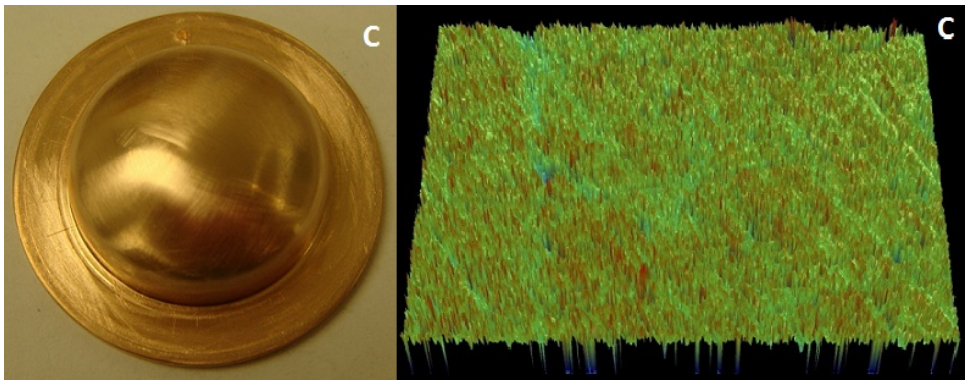

Figure 5-4: Photograph showing the surface of button 1 after being chemical etched (left) 3D Interferometer scan of the surface taken at data location (2-1) (right)

At the final stage of surface preparation Method 1 the sample was electro polished in order to expose the virgin copper by removing adequate layers of

material. As shown below in Figure 5-5, all surface damages visible to the naked eye are removed. The quality of the surface generated is evident as there are no visible scratches on the button surface, resulting in a surface resembling a mirror.

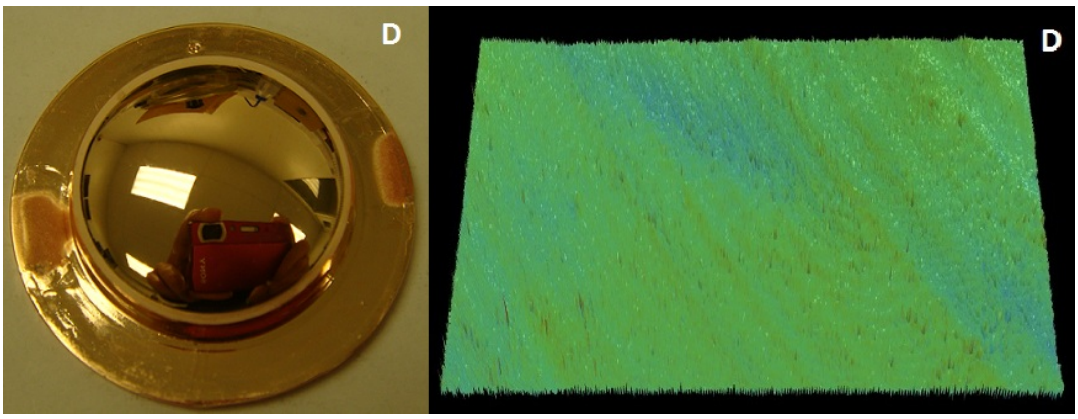

Figure 5-5: Photograph showing the surface of button 1 after being electro polished (left) 3D Interferometer scan of the surface taken at data location (2-1) (right)

5.2.1 Optimisation of the Electro Polishing Process

Similar to the MTA studies, the electrolyte mix was clear and colourless and consists of 85% phosphoric acid and 15% butanol. The shape of the cap and the nature of the polishing setup require a great deal of attention to detail in order to maintain the quality of the polished surface. As noted in Chapter 4, it is vital to achieve and maintain a reasonable polishing plateau. The I-V ratio plays a significant role in defining the quality of the surface and it is related to the polishing area, spacing between cathode and the anode and the electrolyte mixture.

Once the electric current is passed through the mixture, the condition of the electrolyte is subject to continuous change. Shown in Figure 5-6, the colourless electrolyte is transformed into a blue mixture. Furthermore, the mixture was turned opaque due to excessive creation of oxygen bubbles. The conductivity of the mixture eventually fades away due to changing characteristics of the electrolyte.

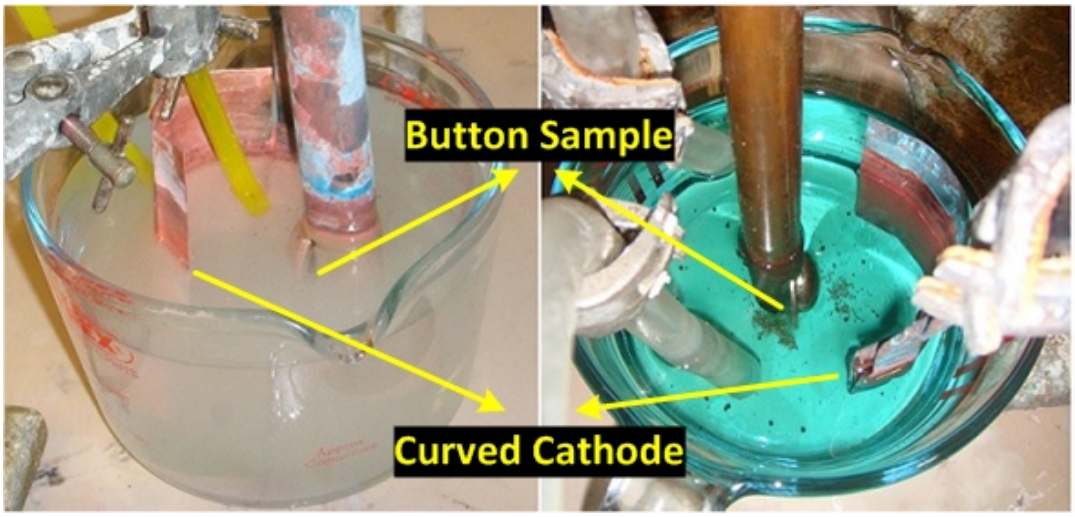

Figure 5-6: Photograph showing a comparison between a fresh and used electrolyte mixture. Once electric current is passed through the mixture, the colour and appearance of the electrolyte is changed from colourless and clear (left) to blue and opaque respectively (right)

As noted earlier, the cathode was curved in order to better match the shape of the button and allow a more even distribution of the current across the surface of the cap. Fresh acid was circulated around the anode by continuously agitating the mixture. In order to determine the optimal polishing parameters, a series of tests were conducted on test samples T_1 to T_9. Three configurations were tested as shown in Figure 5-7.

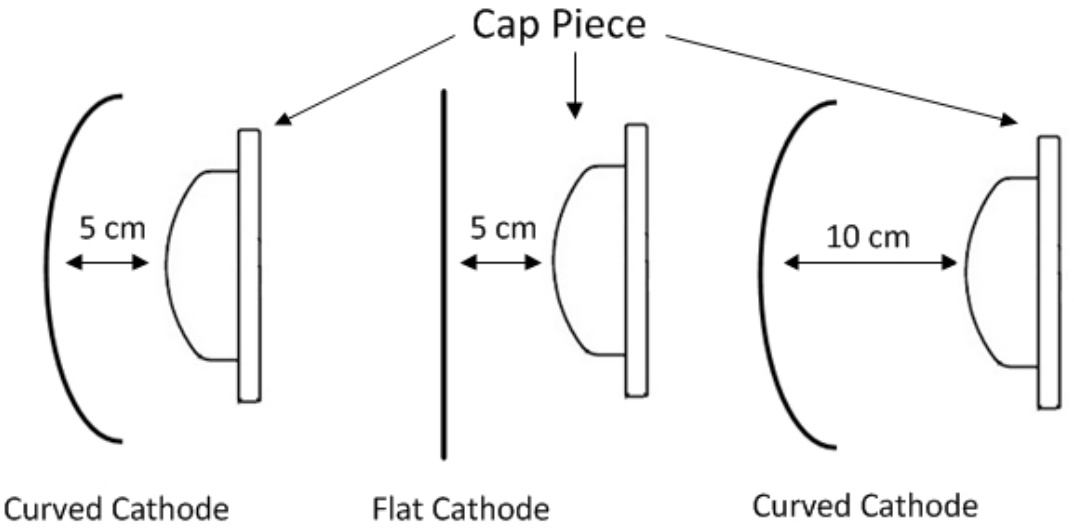

Figure 5-7: The shape and position of the Cathode in relation to the anode or the button sample is of great importance can alter the polishing outcome. Various configurations were tested and are shown I the figure for test samples T_1-T_6, T_9 (left) T_7 (middle) T_8 (right)

The setup conditions used for samples T_1 to T_6 were kept constant and were similar to the parameters chosen for polishing the button cap. The voltage was slowly increased in small steps of 0.025 (V) each time, allowing for the polishing plateau to be detected. As shown below in Figure 5-8, the polishing plateau achieved for samples T_1 to T_6 were fairly similar, highlighting the importance of using a standard setup to achieve similar polishing results.

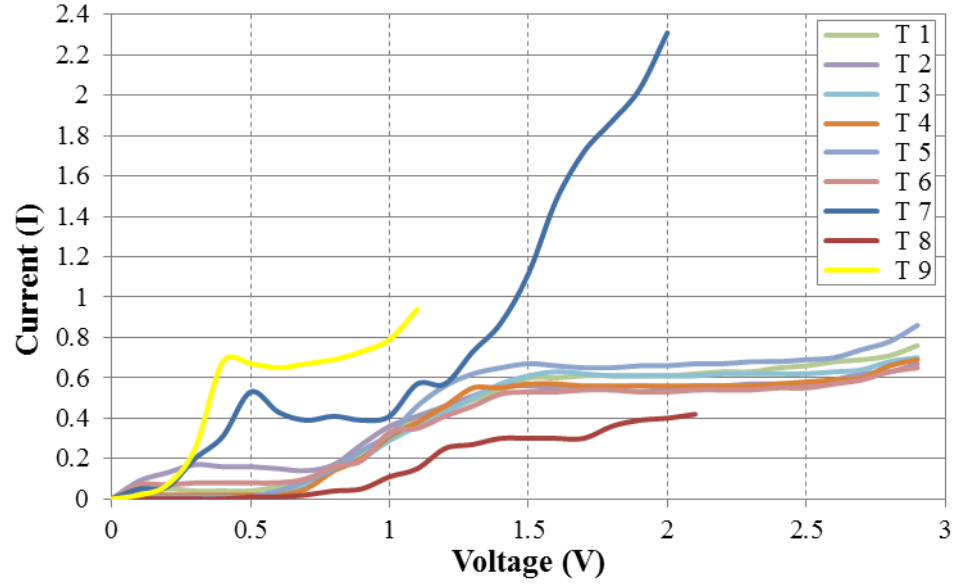

Figure 5-8: Plot showing the changing current vs. applied voltage for test samples T_1 to T_9. A steady current plateau for samples T_1 to T_6 is generated due to the conditions of the test being carried out. Test piece T_7 was polished using a flat cathode while the distance between the anode and cathode was increased in test T_8. Test T_9 was carried out without agitating the electrolyte mixture

Test T_7 was carried out with a flat copper sheet as the cathode while other conditions were kept the same. The differences in the shape caused an uneven gap between the surfaces of the anode and the cathode, resulting in the uneven application of current across the surface of the cap. As a result, the I-V plateau was not stable and it was hard to detect.

Test sample T_8 was polished using the curved cathode, but it was positioned further away from the anode. It was evident that the larger the gap between the two

electrodes, the lower the applied current at a particular voltage. Although weaker in comparison to the first six samples, the polishing plateau could still be observed.

Test sample T_9 was polished using the same curved cathode used for samples T_1 to T_6 with similar distance between the cathode and the anode. However, the agitation pump was removed from the polishing setup. The effects were clear as higher current levels were reached in a much shorter time. However, over time the current dropped down as the polishing process continues. A major reason for such behaviour is the saturation of the mixture near both electrodes and the increase in the viscous layer between the two. This led to an insulation barrier being created, causing an artificial spike in the I-V plateau. The quality of the surfaces generated was notably lower as shown in Figure 5-9.

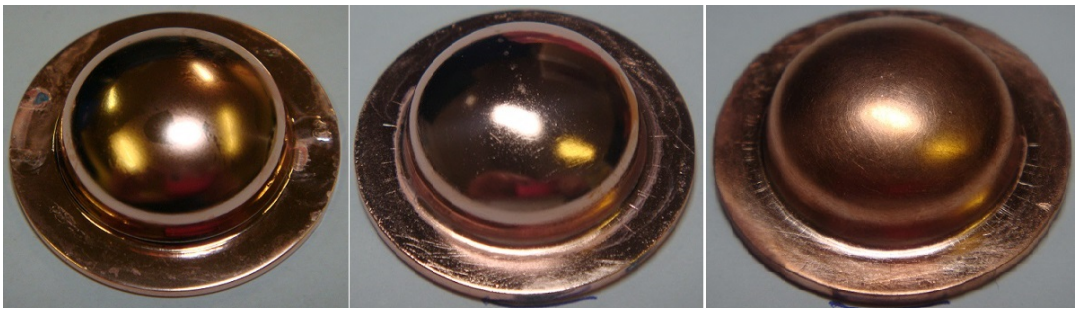

Figure 5-9: Photograph showing the final polished surface for test sample T_7 (left) T_8 (middle) T_9 (right). The poor surfaces created are a direct result of changing conditions during the polishing process

It is evident that changing the polishing setup can alter the outcome of the polishing process dramatically. A series of parameters were defined to keep the operating conditions constant. The pump speed was set to 50 (rpm), ensuring adequate agitation of the electrolyte. The time required to reach the cusp point varied based on the mixture behaviour. The button was polished for two hours once the cusp point was reached. The necessary parameters to polish each button used in

Method 1 are given below in Table 5-1. To preserve the electrolyte characteristics, each mixture was only used twice before being disposed.

Table 5-1: The values of parameters used to setup the electro polishing process performed on button samples 1 to 6. The prep time is the time taken to reach the cusp point of the current plateau. The electrolyte mixture was only used twice in order to ensure maximum polishing rates

Button (B)	Acid	Prep Time (min)	Voltage (v)	Current (amp)
1	New	30	1.525	0.73
2	Used	20	1.65	0.75
3	New	25	1.6	0.83
4	Used	30	1.55	0.7
5	New	20	1.525	0.77
6	Used	35	1.55	0.71

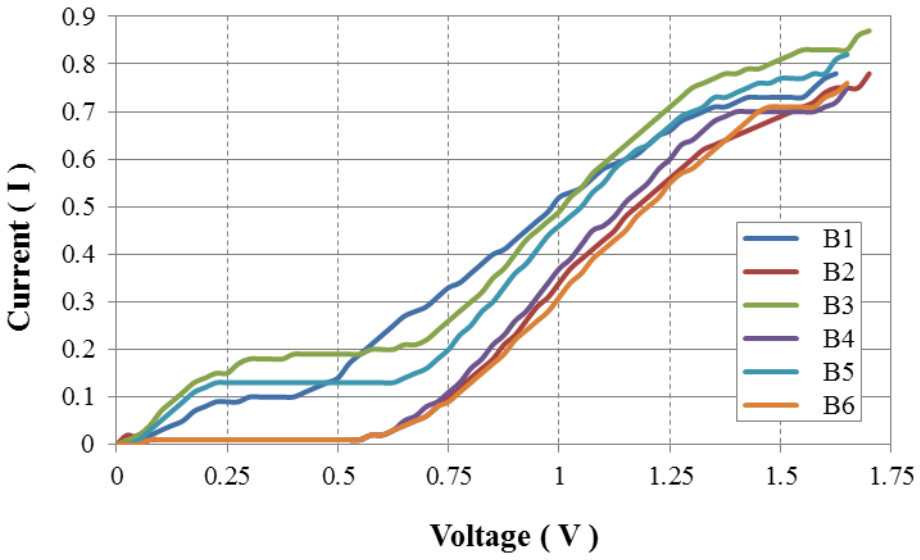

Figure 5-10: Plot showing the current vs. applied voltage for buttons 1 to 6. The steady nature of the current plateau demonstrates the robust nature of the process designed in this study. This is evident by the little variation seen in the applied current for a given voltage

Figure 5-10 shows consistency of the polishing plateaus reached for buttons 1 to 6, highlighting the robust nature of the setup used to polish the cap pieces.

5.2.2 Surface Roughness

Surface roughness measurements presented in Chapter 4 was performed on all button samples. For ease of comparison, an average of the roughness parameters obtained from across the surface of button 1 is presented in Table 5-2. Furthermore, the range of measurements is also presented in various figures.

Table 5-2: Table showing the measured average roughness (R_a) and root mean square (R_q) observed across the surface of button 1. The final value was obtained by averaging the measurements taken from all the sixteen data points

Process	**A**	**B**	**C**	**D**
R_a (nm)	491	279	298	154
R_q (nm)	631	364	415	194

Based on images shown in Figure 5-2, it was suggested that the surface quality was at its lowest, once the button left the production line. This was validated based on surface measurements taken throughout surface preparation method one. Average roughness was gradually reduced throughout the process apart from a slight rise seen during process C. This was simply due to the nature of the chemical etching and should not be regarded as deterioration in the quality of the surface. Chemical etching was performed to blunt the sharp edges of any small scratches present, preparing the surface for EP. As a result of the uncontrolled nature of the process, the acid also ate into the surface. This led to an increase in average roughness, while generating a more suitable surface profile for the EP.

In addition to average roughness R_a, this study also employed surface uniformity (R_q-R_a) as the two suitable parameters to investigate the changing surface quality. Figure 5-11 shows the roughness parameters for button 1, obtained

by averaging the measurements from all the collected data points. It was possible to observe the improvement in the quality of the surface through the reduction of surface roughness and better uniformity. Each error bar represents the variations seen across the collected data points for the specific process in question. For instance, the scale of variation between obtained parameters of process A show the uncontrollable nature of the production techniques used to fabricate the button.

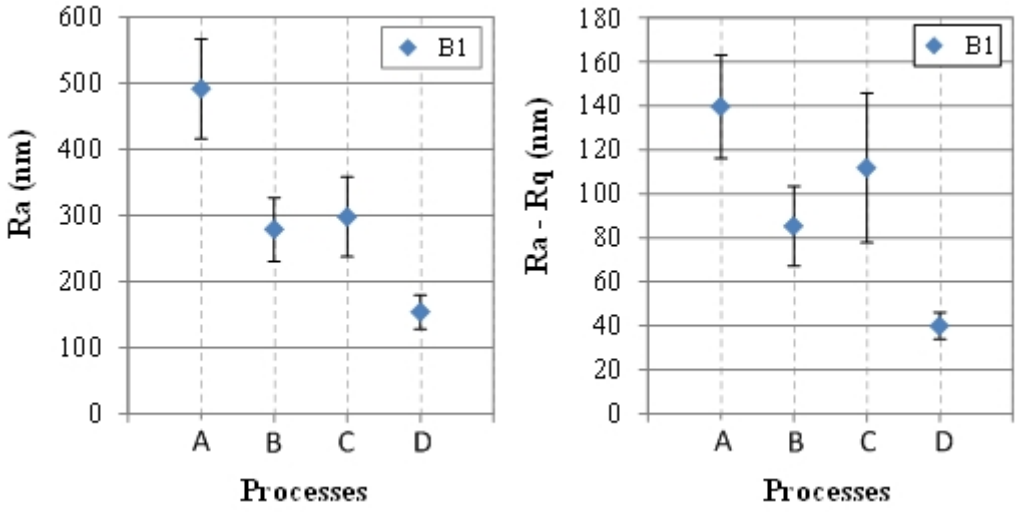

Figure 5-11: Plot showing the changes in surface quality based on surface roughness measurements taken for Button 1. Average roughness R_a (left) and surface uniformity R_q-R_a (right). An average of all the sixteen data points across the surface of the button has been used. The overall surface quality is improved after each stages of the surface treatment process utilised in this study. The error bars show the upper and lower limits of the collected data

By enabling the user to have better control over the outcome of processes B and C, lower variations in surface roughness parameters were observed across the button surface. The average roughness was dramatically reduced once EP was performed, while the overall uniformity was improved. The small variations seen between the parameters measured across the button surface during process D highlights the robust nature of the EP setup. To provide a more detailed look at the changing surface quality, roughness parameters of data rings should be

investigated alongside individual data points. Figure 5-12 shows the measured parameters of such rings for button 1 throughout all the processes.

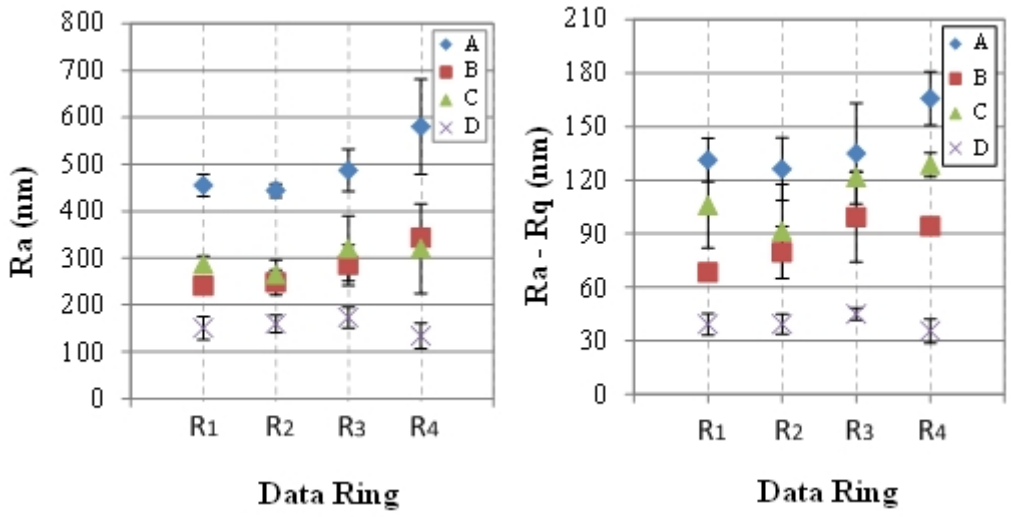

Figure 5-12: Plot showing the changes in surface quality based on roughness measurements taken for Button 1, R_a (left) and R_q-R_a (right). The results are taken by averaging the values for each data ring in order to make comparisons between each stages of the treatment procedure. The overall surface quality is improved after each stage while data ring 4 exhibits the lowest surface quality. The poor polishing results are due to the shape of the button around data ring 4. The error bars show the upper and lower limits of the collected data

During fabrication, the outer edges of the button tend to receive a harsher treatment due to the shape of the sample. This is clearly evident in Figure 5-12, where R4 showed higher surface roughness and a lower surface uniformity. It was also possible to see a great variation across the data points in comparison to inner rings such as R2. This trend was also observed in process B, where the shape of the button did not allow a consistent hand polishing to be performed. The outcome of process C was directly related to the surface profile generated previously, exhibiting similar behaviour. All data rings demonstrated an improving trend throughout the treatment procedure, with process D generating the best surface profile. However, R3 indicated a slight increase in the average roughness during EP. The shape of the cathode can be at blame, where both electrodes were

positioned the furthest at this location. For all the process, the variation across the measured parameters increased towards the outer edges of the button.

Further investigations could be made through analysing each rings and investigating how the surface roughness changes after each process. The results are shown below in Figure 5-13.

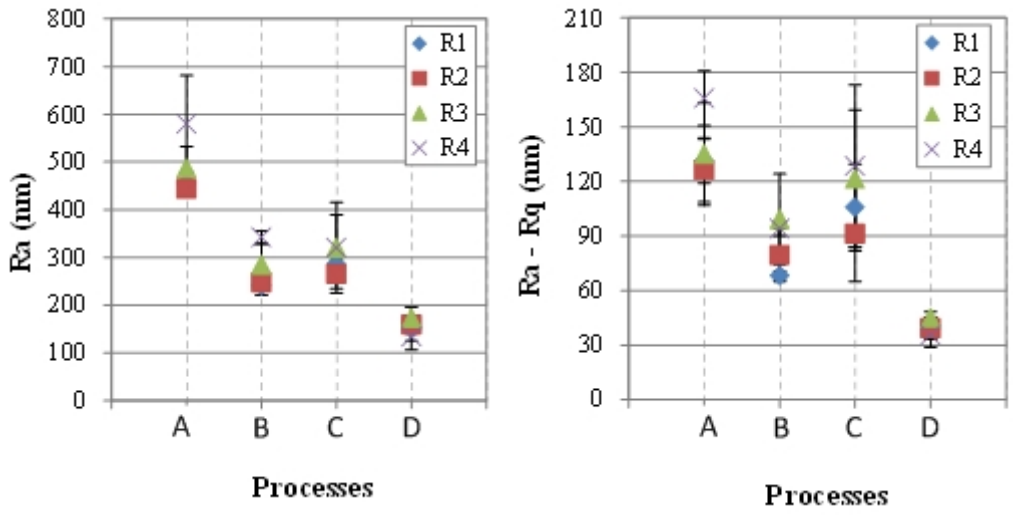

Figure 5-13: Plot showing the changes in surface quality based on roughness measurements taken for Button 1, R_a (left) and R_q-R_a (right). The results are taken by averaging the values for each data ring in order to make comparisons between each stages of the treatment procedure. The overall surface quality is improved after each stage while data ring 4 exhibits the lowest surface quality. Although process c blunders the edges of deep scratches on the surface, it generates a less uniform outcome. This is due to the uncontrolled nature of process C. The error bars show the upper and lower limits of the data

Average roughness was reduced systematically for all data rings throughout the treatment procedure, while surface uniformity was improved dramatically. Process D exhibited far less variations, showing the level of control over the process in comparison to earlier stages. The overall surface profile tends to be fairy similar across the button surface once EP is performed.

5.2.3 Method 1 Validation

To ensure the reliability of any findings, it was critical to investigate the reproducibility of the techniques employed when developing a procedure. In this

study, the procedure was repeated for six buttons and the findings are shown below in Figure 5-14. Average roughness and surface uniformity values were calculated using the average of all data points. All buttons followed the improved trend in surface profile observed previously for button 1.

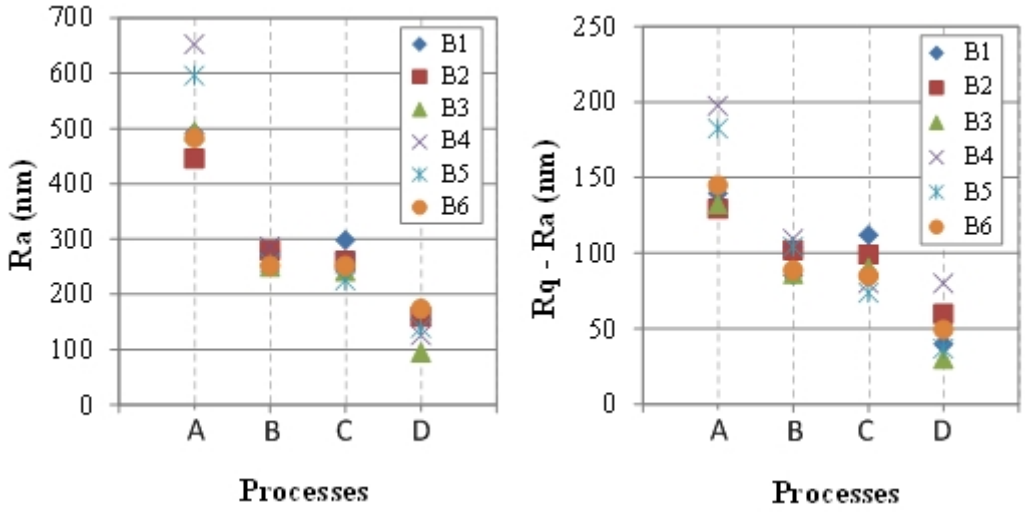

Figure 5-14: Plot showing the changes in surface quality based on roughness measurements taken for Buttons 1 to 6, R_a (left) and R_q-R_a (right). The results are taken by averaging the sixteen data points for all six buttons after each stage of the treatment process. The overall surface quality is improved in all buttons after each stage of the treatment process. Little variation in surface quality is observed across all buttons, indicating the robust nature of the treatment process developed in this study

In comparison to the process with a degree of control, process A showed a larger degree of variations across the six buttons. This validates the assumption made earlier, demonstrating the nature of the processes being tested. Individual rings have also been investigated after each process, using the average of the data rings for all buttons. As shown in Figure 5-15, surface quality was improved after each process with shrinking variations seen across all buttons.

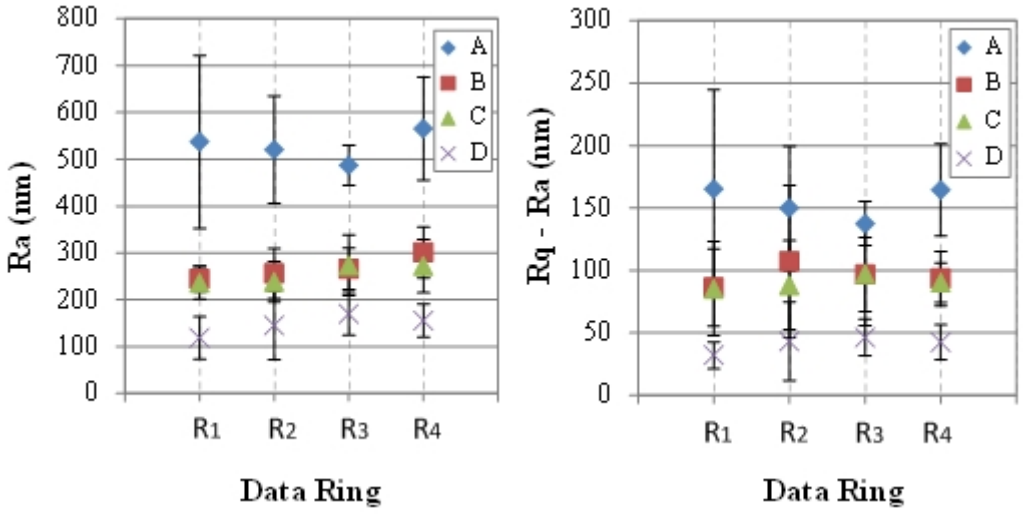

Figure 5-15: Plot showing the changes in surface quality based on roughness measurements taken for Buttons 1 to 6, R_a (left) and R_q-R_a (right). The results are taken by averaging the values for the relevant data rings of all buttons. The overall surface quality is improved after each stages of the treatment procedure. In the same way as button 1, data ring 4 exhibits the least quality due to lack of polishing based on the shape of the button. The error bars represent the upper and lower limits of recorded data

5.3 Surface Preparation - Method 2

In the previous section, the electro polishing was the chosen process for surface treatment. Method two on the other hand, employed EP as a pre-treatment procedure and focused on electroplating as chosen surface treatment technique. The aim was to make comparisons between the two generated surface profiles, highlighting any potential improvement. Similar to previous method, six buttons were prepared using the procedure. Figure 5-16 shows the major steps taken to prepare each button sample with process *E* being the main focus.

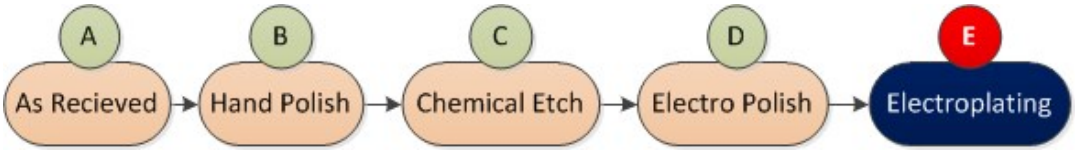

Figure 5-16: Major steps taken during the surface treatment process used in method 2. The process was repeated for button 7 to 12 keeping the conditions as steady as possible

Similar to the previous method, the button went through processes A to D before being electroplated. As shown below in Figure 5-17, the surface was prepared in order to allow the application of the best possible coating layer.

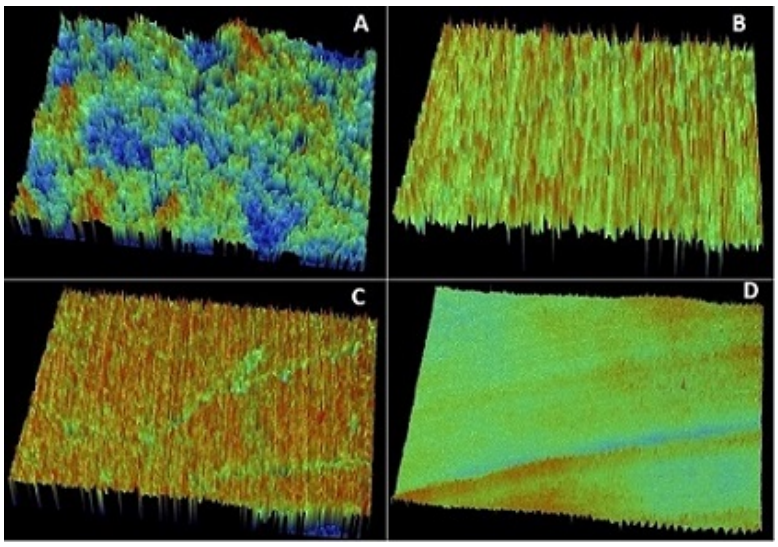

Figure 5-17: 3D Interferometer scan taken from the surface of Button 7 at data location (2-3). The plot shows the changing nature of the surface quality during stages A to D, demonstrating similarities to the results obtained from the surface of Button 1

Once EP was performed, each copper button was coated with OFHC copper. This was to achieve a different surface profile in comparison to the electro polished copper, while keeping the same characteristics of copper. The outcome of the electroplated button is shown below in Figure 5-18.

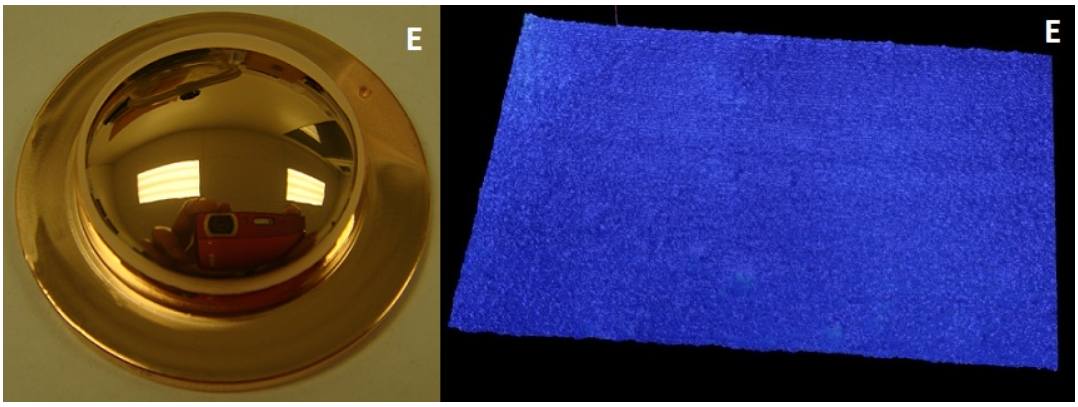

Figure 5-18: Photograph showing the surface of Button 7 after being copper plated (left) 3D Interferometer scan of the surface taken at data location (2-3) (right)

It is possible to see the mirror like characteristics seen previously for an electro polished button. This can be an indication of the quality of the deposited layer and the cohesion made with the underlying electro polished surface.

5.3.1 Copper Plating Process Optimisation

The same level of care was required to electro polish each button in the process two, prior to performing copper plating. The EP parameters used for all six buttons are given below in Table 5-3. The polishing plateau for the new set of buttons resembles the current behaviour observed when polishing buttons 1 to 6. However, a slight increase in the applied voltage can be seen. Slight changes in the polishing setup can be the source of such alteration such as the quality of the electrolyte mixtures. Figure 5-19 also shows the polishing plateaus achieved for buttons 7 to 12. All buttons tend to follow similar pattern, demonstrating the stability of the system in Method 2.

Table 5-3: The values of parameters used to setup the electro polishing process performed on button samples 7 to 12. The prep time is the time taken to reach the cusp point of the current plateau. The electrolyte mixture was only used twice in order to ensure maximum polishing rates

Button	Acid	Prep Time (min)	Optimal Voltage (v)	Optimal Current (amp)
7	Used	35	1.65	0.66
8	New	20	1.5	0.62
9	Used	30	1.5	0.61
10	New	30	1.8	0.64
11	Used	25	1.65	0.65
12	New	30	1.65	0.67

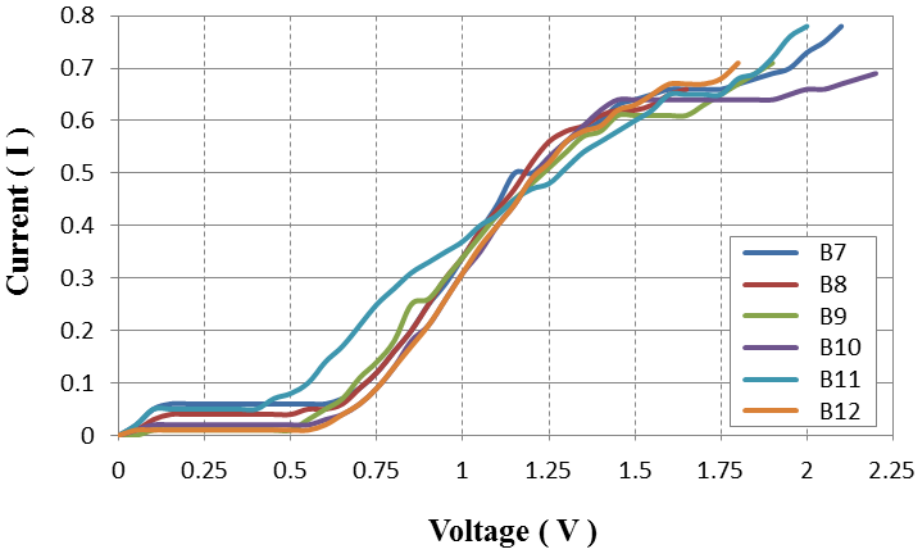

Figure 5-19: Plot showing the current vs. applied voltage for buttons 7 to 12. The steady nature of the current plateau is demonstrated by the little change in the applied current for a given voltage. This shows the robust nature of the process designed in this study. In comparison to the polishing plateau obtained for buttons 1 to 6, the results shows very little variation

According to equation (4-4), the rate of deposition is based on the input current, which is directly related to the surface area being plated. Based on the 16.59 cm^2 surface area of the button, an input current of 0.6 amps is required to deposit 1 μ of coating per minute. This current was applied to plating test sample 1, where the button was plated for thirty minutes. The outcome can be seen below in Figure 5-20, where the poor quality of the coated layer is clearly visible.

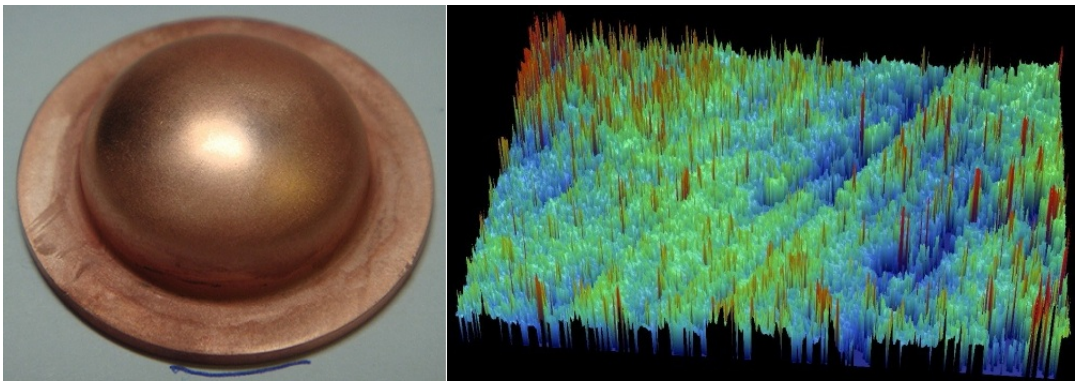

Figure 5-20: Photograph showing the surface of test sample 1 after being copper plated (left) 3D Interferometer scan of the surface taken at data location (2-2) (right). The poor quality of the surface finish is a direct result of incorrect configuration of the setup being used

A naked eye investigation can reveal the stark difference in surface quality between plating test sample 1 and button 7. This can be blamed on deficiencies in the amount of applied electric current during the process. A possible explanation is the current being applied to a greater surface area than initially anticipated. Shown below in Figure 5-21, the button was secured in place using a makeshift holder made out of copper. Once inserted into the tank, this increased the surface area exposed to the applied electric current. Due to the crude nature of the designed holder, a series of tests were carried out to discover the adequate parameters needed to achieve acceptable coating levels of button 7. Figure 5-22 on the other hand shows plating test sample 2, where the applied current was increased to 2 amps and the process was executed for two hours.

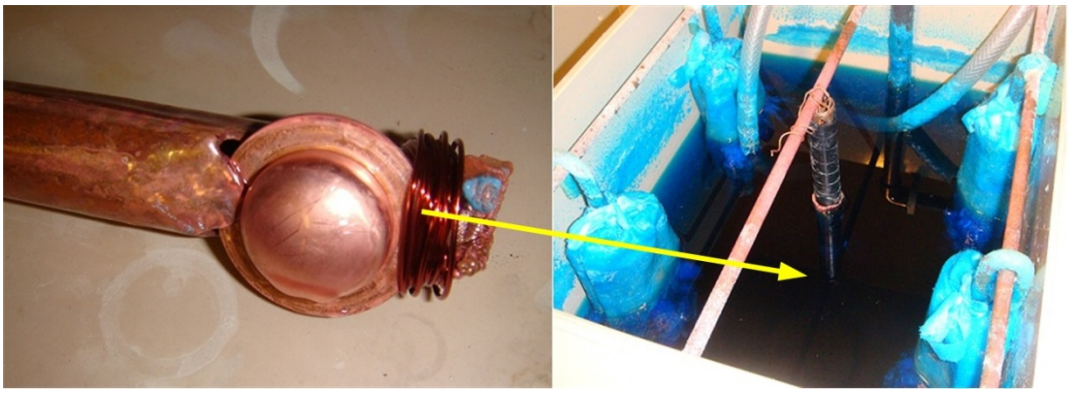

Figure 5-21: Copper plating holder assembly with a button piece being held with wire wrapping (left) button samples held in position with the plating assembly in between 4 electrodes (right)

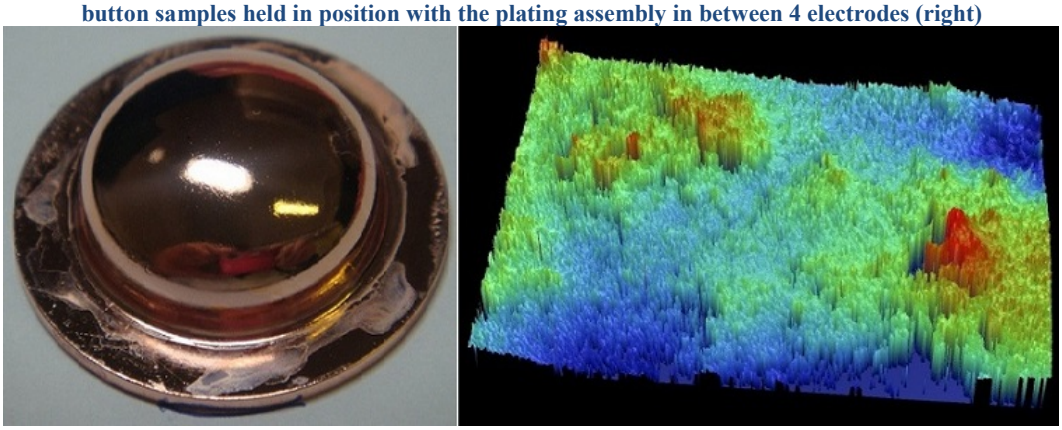

Figure 5-22: Photograph showing the surface of plating test sample 2 after being copper plated (left) 3D Interferometer scan of the surface taken at data location (2-2) (right). The quality of the surface is slightly improved as the applied voltage is increased

Although the surface quality was improved, the overall average roughness was lowered slightly from the high of 1195 nm to 605 nm. While not visible to the naked eye, the surface quality was much lower than when the sample left the production line in process A. To improve the quality, the applied current was increased to 5 amps and plating test button 3 was plated for two hours. As shown in Figure 5-23, the coated layer exhibited much improved visual conditions and the average roughness was lowered to just 73 nm. Higher applied current coupled with longer coating process dramatically improved the quality of the coated layer. Hence, the parameters used for plating test sample 3 were chosen as the standard coating parameters for buttons 7 to 12.

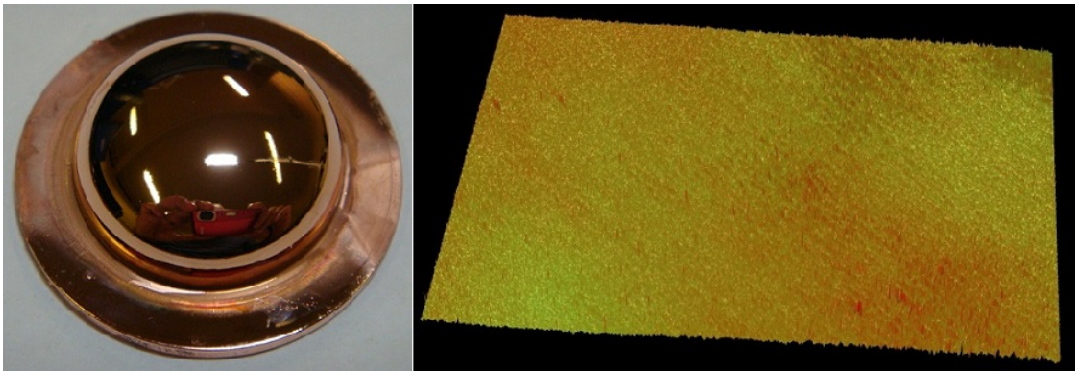

Figure 5-23: Photograph showing the surface of plating test sample 3 after being copper plated (left) 3D Interferometer scan of the surface taken at data location (2-2) (right). The quality of the surface is improved greatly and a mirror like surface is created. This was due to the improvements made to the copper plating setup used in this study

5.3.2 Surface Roughness

As before, surface measurements were performed in order to quantify the results. The Roughness parameters obtained for button 7 are given below in Table 5-4. As expected, the surface profile of button 7 followed a similar trend seen previously in method 1 for processes A to D. Hence, the main focus in this stage was the alterations made due to process E.

Table 5-4: Table showing the measured average roughness (R_a) and root mean square (R_q) observed across the surface of button 7. The final value was obtained by averaging the measurements taken from all the sixteen data points

Process	A	B	C	D	E
R_a *(nm)*	434	240	228	95	62
R_q *(nm)*	564	284	315	126	79

Similar to the previous method, a series of plots were used to visualise the changes in surface profile. The error bars represent the variations seen across the collected data points and show the lower and upper limits. At first, the roughness parameters of button 7 were investigated as shown in Figure 5-24.

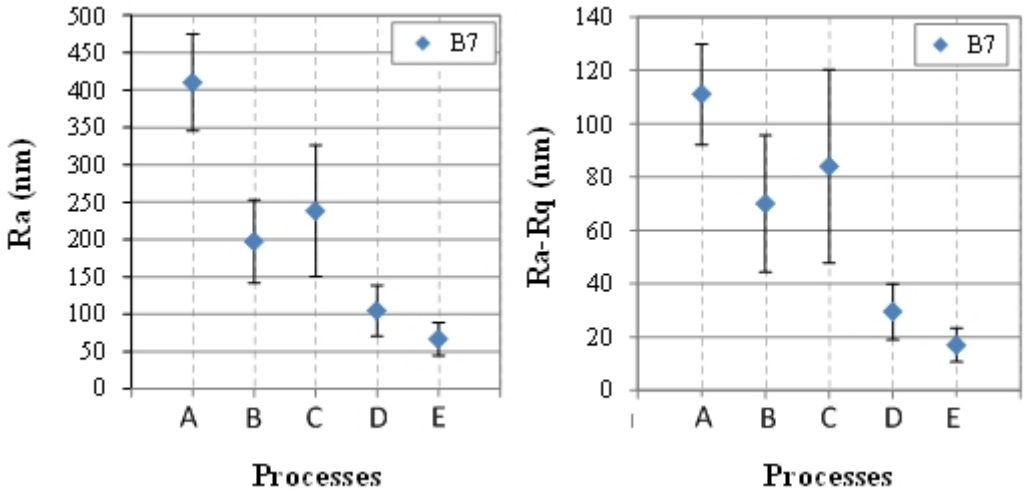

Figure 5-24: Plot showing the changes in surface quality based on surface roughness measurements taken for Button 7. Average roughness R_a (left) and surface uniformity R_q-R_a (right). An average of all the sixteen data points across the surface of the button has been used. The surface quality has improved even further by performing copper plating as the final stage of treatment process. Furthermore, the variation across the surface of the button is reduced as shown by the error bars

It can be seen that copper plating resulted in the average roughness reaching the lowest values achieved so far. By observing the improvement in surface uniformity, it was possible to assume process E is capable of producing a higher quality RF surface. The reduction in variations seen across the data points is a clear indication of the quality of the setup used to coat button 7. However, the sub

surface produced throughout processes A to D plays an integral role in achieving such standards. This sub surface, alongside improved process parameters, allowed for a stable and high quality coating layer to be applied.

Figure 5-25, shows the improvements seen across individual data rings as the button 7 underwent various stages of the second surface treatment procedure.

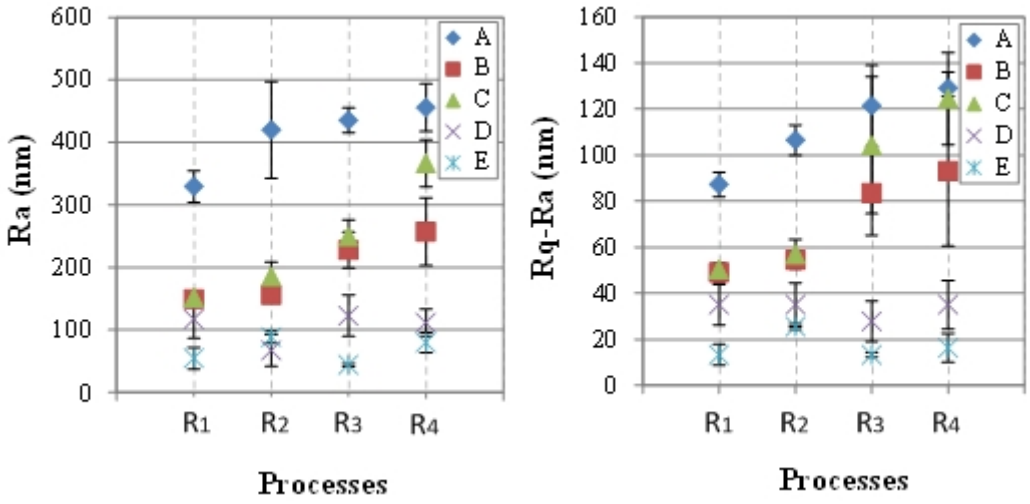

Figure 5-25: Plot showing the changes in surface quality based on roughness measurements taken for Button 7, R_a (left) and R_q-R_a (right). The results are taken by averaging the values for each data ring in order to make comparisons between each stages of the treatment procedure. The overall surface quality is improved after each stage while data ring 4 exhibits the lowest surface quality. The poor polishing results are due to the shape of the button around data ring 4. The error bars show the upper and lower limits of the collected data

While the overall surface quality was improved throughout Method 2, the inner data ring R1 tends to show better surface parameters in comparison to R4. This however was not the case for processes D and E, where surface quality was fairly unchanged across the button surface. This was a direct result of the high quality polishing result of the EP process followed by a uniform application of the coated layer on the button surface. A major improvement in surface uniformity was observed once coating was performed. The small variation in the roughness measurements across the surface of the button is an indication of the robust nature

of the surface treatment procedure developed in this study. Figure 5-26 provides a different view on how button 7 is behaving while being treated.

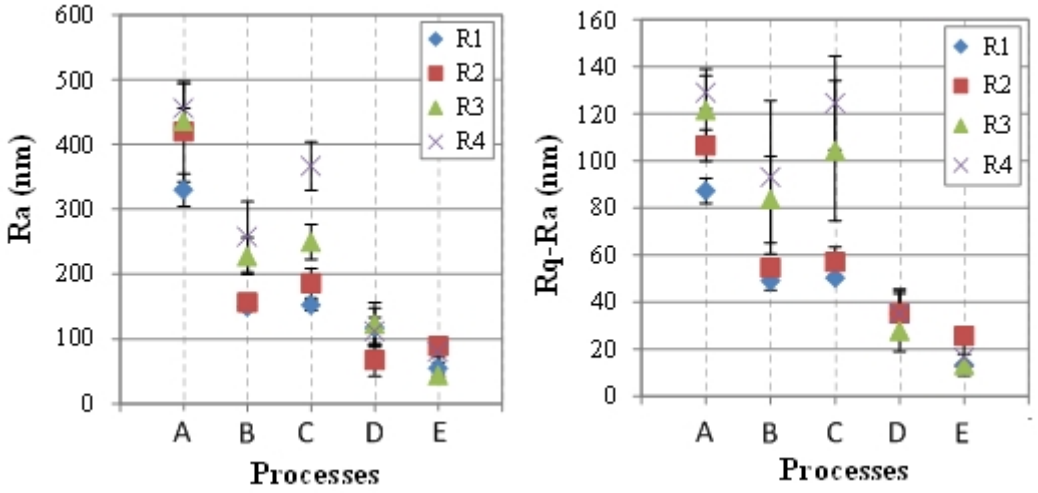

Figure 5-26: Plot showing the changes in surface quality based on roughness measurements taken for Button 7, R_a (left) and R_q-R_a (right). The results are taken by averaging the values for each data ring in order to make comparisons between each stages of the treatment procedure. The overall surface quality is improved after each stage while data ring 4 exhibits the lowest surface quality. Process E produces a superior surface quality in comparison to EP across the surface of the button. The error bars show the upper and lower limits of the data

It is possible to see that process E was able to build on the improvements achieved previously by the EP process. The final outcome was a button surface where all four data rings exhibit similar roughness parameters and surface uniformity with negligible variation across the collected data points.

5.3.3 Method 2 Validation

The procedure of Method 2 was repeated for six buttons in order to demonstrate the consistency of the findings. Figure 5-27 shows the roughness parameters of buttons 7 to 12, obtained throughout processes A to E. The findings are a strong indication of the reliability offered by the designed procedure to reproduce the above results. In all cases, the quality of the surface was improved even further once copper plating was performed. The final surface of each button enjoyed

improved roughness and better surface uniformity. Very low levels of variation were observed between the final surface qualities of the six samples, highlighting the stable nature of the coating procedure.

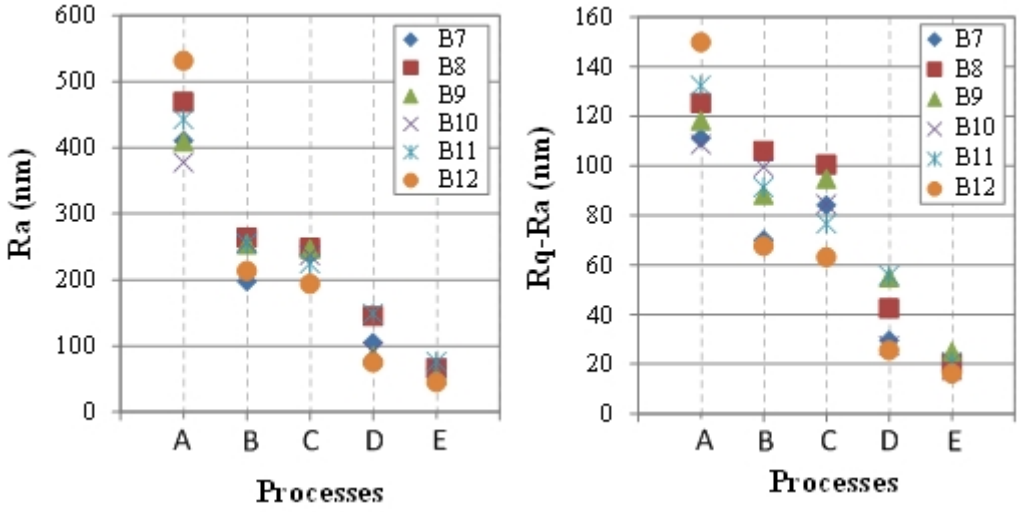

Figure 5-27: Plot showing the changes in surface quality based on roughness measurements taken for Buttons 7 to 12, R_a (left) and R_q-R_a (right). The results are taken by averaging the sixteen data points for all six buttons after each stage of the treatment process. All buttons exhibit an improving surface quality after each stage of the treatment procedure. Little variation in surface quality is observed across all buttons, indicating the robust nature of the treatment process developed in this study

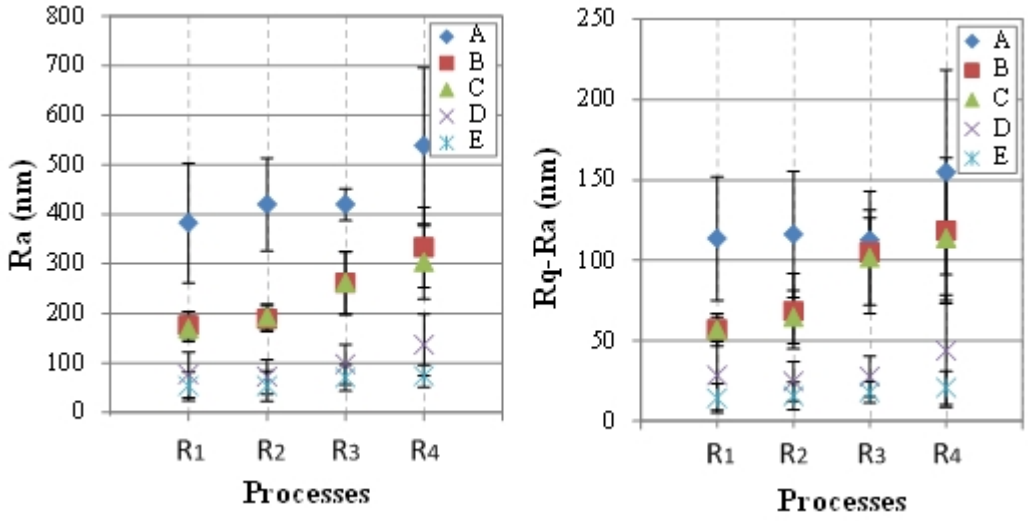

Figure 5-28: Plot showing the changes in surface quality based on roughness measurements taken for Buttons 7 to 12, R_a (left) and R_q-R_a (right). The results are taken by averaging the values for the relevant data rings of all buttons. The overall surface quality is improved after each stages of the treatment procedure. In the same way as button 7, data ring 4 exhibits the least quality due to lack of polishing based on the shape of the button. The error bars represent the upper and lower limits of recorded data

The surface quality observed in each individual data ring is shown below in Figure 5-28. An average of all the respective data points from buttons 7 to 12 has been used and the error bars represent the variations. In all cases, the higher quality of the inner ring of R1 in comparison to the outer ring of R4 is observed. However, surface quality tends to be more uniform across the button after process E.

5.4 Chemical Composition

In addition to the surface topology, the chemical composition of the RF surface was analysed by taking XPS measurements using a standard source. Three buttons were prepared, where Method 1 was used for surface treatment. Figure 5-29 shows the changing chemical mix of the RF surface during processes A and B, using the average of three buttons to construct the figures.

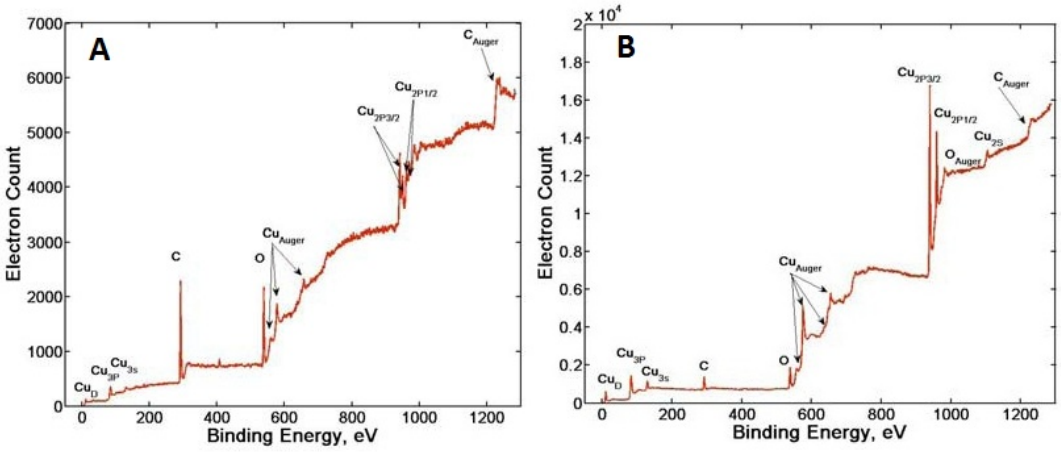

Figure 5-29: Binding energies of released electrons based on 3 buttons, following process A (left) and B (right) [109, 110]

The heavily oxidised button in process A, revealed the existence of the $Cu_{p1/2}$ and $Cu_{p3/2}$ doublets at the binding energies of 940 - 970 eV. The two distinct sets of Cu_{2p} peaks, suggests that copper was bound to two separate sites. While one set originated from the Cu_0 over layer, the other set was positioned below the layer.

The doublet however, was removed once the button was hand polished. A 58% reduction in the oxide layer and the carbon contents of the cap surface was noticed after hand polishing [96]. This highlights the importance of process B in removing the damaged layer left behind after fabrication.

The procedure was conducted for processes C and D and the results are shown in Figure 5-30. During chemical etching, both the oxide layer and carbon contents of the button surface were removed by as much as 96% [96]. The results demonstrate the ability of this surface treatment to remove contaminations introduced during fabrication. This however, was no longer the case after performing EP. The oxygen and carbon contents of the surface were increased by 25% and 100%, respectively, once EP was performed [96].

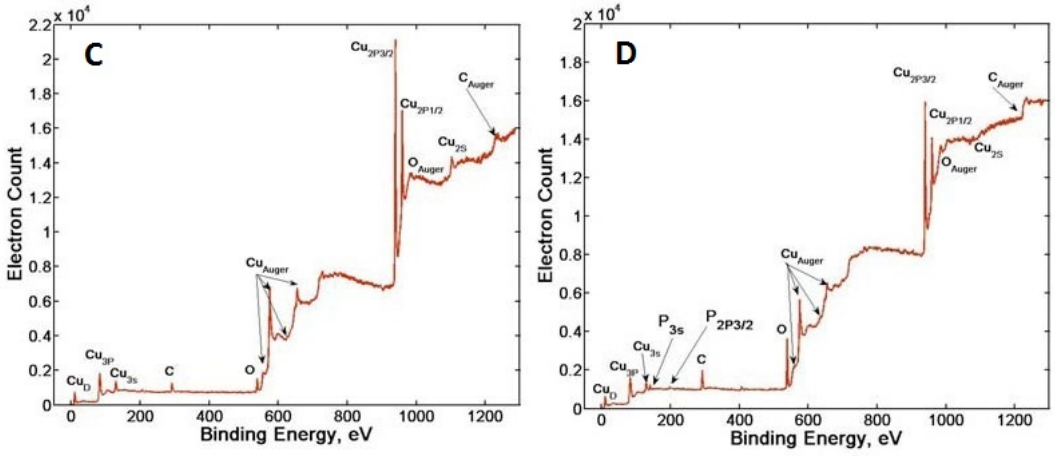

Figure 5-30: Binding energies of released electrons based on 3 buttons, process C (left) D (right) [109, 110]

Although the exposer time of the button to the atmosphere is short, this can be be the main cause of the increase seen in oxygen count. This however cannot explain the increases seen in the carbon content. A possible explanation can be the electrolyte mix of phosphoric acid and butanol used for EP. However, the same electrolyte mix was used to chemical etch the button during process C. Hence, one

may come to the conclusion that the electrolyte alone was not the cause of contamination the cause lies in the EP process.

Furthermore, one can see the introduction of phosphorous in the chemical mix of the surface after EP, most likely from the phosphoric acid used in the electrolyte. This reaffirms concern that contamination is introduced during the EP process itself. As presented previously in Chapter 3, this can play a major role in changing the secondary emission yield of the material by altering its band structure. It has become apparent that the chemical mix observed for several samples, tends to follow a similar trend seen above. Hence, it was not considered necessary to perform XPS measurements for every individual button sample analysed by this study.

5.5 Concluding Remarks

A series of buttons were manufactured using sheet metal pressing and processed using two surface treatment methods. The surface of each button was characterised and the surface roughness and chemical composition of the RF surface was evaluated using white light interferometry and XPS techniques.

In Method 1, the effects of EP on copper were assessed. Measurements showed how the surface was both chemically and physically altered at each step of surface preparation. Interferometry results showed that the condition of the surface was significantly improved using EP. The importance of removing the damaged surface layers and chemical contaminations was also demonstrated. Almost 99% of all surface contaminants were removed by mechanical and chemical polishing. And after EP, the surface consisted of virgin material free from the stresses introduced during fabrication.

The evaluation of surface roughness revealed that the addition of electro plating in Method 2 has produced a smoother and more uniform surface compared to Method 1. The pre-treatment carried out prior to EPL allows for a steadier and stable application of the copper layer. Each treatment process was optimised in order to achieve an optimum finished quality of the surface. However, the EP process could be optimised further by employing higher quality equipment such as purpose built electrolyte bath, cathode and anode pieces. Furthermore, improvements to the electrolyte recipe can be made by using other acids or additives such as peg or citric acid,

Chapter 6.

Finite Element Modelling and Particle Tracking Simulation

6.1 Introduction

Many aspects of design and operation of RF cavities have been investigated through simulation, one being particle tracking inside the structure. This can consist of either tracking beam particles entering the cavity or particles emitted from the RF surface. The investigations carried out in this work focused on the latter, analysing the emission of electrons due to surface defects. In order to allow for comparisons to be made with current MTA findings, the chosen operating frequency for the modelled cavities was 805 MHz.

A new particle tracker was developed in this work, which uses the electromagnetic field solution generated by the FE models of the cavity. The majority of previous studies concentrated on two dimensional (2D) modelling [58, 61], using codes such as Parmela and Cavel [111, 112]. This limits the ability to analyse models with surface defects where symmetry conditions cannot be satisfied. A three-dimensional (3D) particle tracker was developed to overcome such limitations and to allow for a more detailed analysis to be carried out. This chapter introduces the finite element models used to generate the EM field distribution and the algorithms developed to perform particle tracking.

6.2 Finite Element Method

Finite Element Method (FEM) is commonly used for continuum systems in which the distribution of one or more unknown variables such as displacement or field is required. The continuum region is initially discretised into subdivisions known as elements, which are interconnected at joints called nodes. The type and number of the elements must be set so that the distribution of field variables throughout the body is approximated with a sufficient accuracy [113, 114].

Comsol [115] has been chosen as the finite element solver for generating the necessary EM fields. The physical models of Comsol provide a flexible platform to carry out multi-physics simulations. Comsol provides a number of physics interfaces, each solving a set of relevant partial differential equations (PDE). Comsol is capable of simulating an EM field both in 2D and 3D by solving the Maxwell's equations that are subjected to boundary conditions. Maxwell's equations state the relationships between the fundamental EM quantities that must be satisfied by both the E and B fields. They can be expressed either in differential or integral form. For the purposes of the finite element method, the four Maxwell's equations are presented in the differential form as follows [116-119]:

$$Ampere's\ Law \qquad \nabla \times \vec{H} = \vec{J} + \frac{\delta \vec{D}}{\delta t} \tag{6-1}$$

$$Faraday's\ Law \qquad \nabla \times \vec{E} = -\frac{\delta \vec{B}}{\delta t} \tag{6-2}$$

$$Gauss\ Law\ (electricity) \qquad \nabla \cdot \vec{D} = \rho \tag{6-3}$$

$$Gauss\ Law\ (magnetism) \qquad \nabla \cdot \vec{B} = 0 \tag{6-4}$$

E, D, H, B, ρ, J and t represent the electric field intensity, electric displacement, magnetic field intensity, magnetic flux density, electric free charge density, free current density and time, respectively.

Most particle accelerators use a standing wave to generate the field in a RF cavity. The mathematical method for solving such models is the Eigenfrequency solver [97, 120]. This measures the characteristic frequency of the structure from the fundamental mode. Higher order modes can be excited based on harmonic components of the input RF power. The geometry, material properties and the desired outputs are set by the user [115, 116].

6.2.1 Three Dimensional (3D) Cavity Model

The chosen geometry for this study is the MTA 805 MHz cavity. This is to allow practical comparisons to be made between previous findings of collaborating studies and new findings obtained in this work [53]. Unlike the MICE 201 MHz cavity, the MTA cavity offers the advantages of less complicated geometry and smaller physical size. It is possible to make further modelling simplifications of the geometry by modelling a pillbox cavity shown below in Figure 6-1. The equivalent pillbox cavity has the same operating frequency as the elliptical MTA cavity. The simpler geometry of the pillbox cavity requires a lower number of mesh elements.

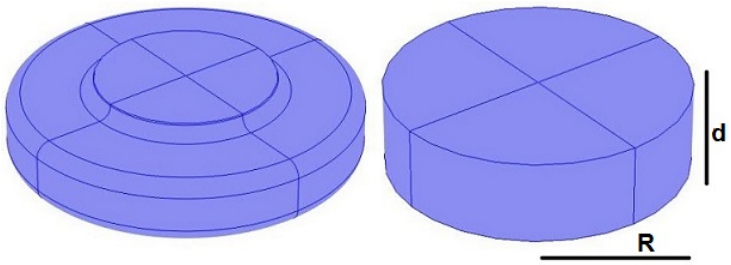

Figure 6-1: MTA 805 MHz cavity (left) simplified pillbox (right) while the pillbox cavity has a much more simplified physical shape, the operating frequency is kept the same due to similar radius R

The maximum achievable accelerating gradient in both elliptical and pillbox cavities is observed on the cavity axis. One can expect to observe the field profiles shown below in Figure 6-2, where the strength of the field can be influenced by the input energy, the shape of the cavity and the operating frequency.

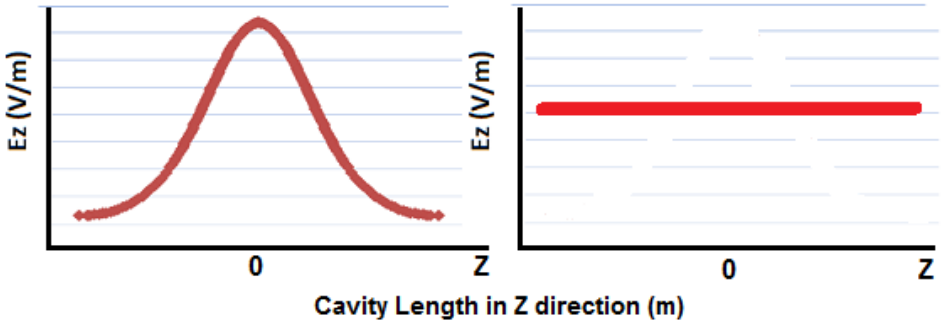

Figure 6-2: Maximum E field along cavity axis for elliptical cavity (left) is greatest at the centre of the cavity while for pillbox (right) is constant along the cavity axis

The operating frequency of a pillbox RF cavity is dictated by its radius R (Figure 6-1) can be expressed as [8, 121]:

$$\omega = \frac{2.405}{\sqrt{\mu\varepsilon}R} \quad \rightarrow \quad R = \frac{2.405}{\sqrt{\mu\varepsilon}(2\pi f)} \tag{6-5}$$

where $\mu = 4\mu\times10^{-7}$ H/m is the permeability and $\varepsilon = 8.854\times10^{-12}$ F/m is the permittivity of vacuum. The equivalent cavity radius (R) and gap (d) were chosen so that the resonant frequency (f) and volume of the structure are very similar to that of the MTA cavity. The basic dimensions of both cavities are given below in Table 6-1. The internal volume of the cavity was set to vacuum. Each model was meshed using tetrahedral elements where more information is given in Chapter 7.

Table 6-1: Basic geometrical information of both cavities modelled in this work

	Radius (R)	Height (d)	Units	Frequency
MTA Cavity	15.6	8.3	cm	805 MHz
Pillbox	14.26	7.8	cm	803 MHz

The boundary condition used to model copper cavities is the perfect electric conductor, where lossless metallic surfaces are modelled by setting the tangential component of the electric field to zero. This will eliminate possible sources of heat generation on the cavity wall.

The advantage of modelling in 3D is the ability to introduce any surface irregularities at desired locations in the model. A few examples are shown below in Figure 6-3, highlighting the need for a 3D model when investigating non symmetric models.

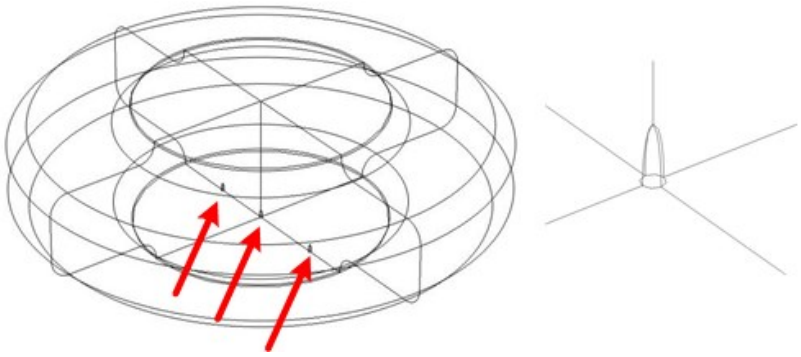

Figure 6-3: An MTA cavity with surface defects at three locations (left) a single surface defect (right) highlighting the flexibility of a 3D model to place surface defects away from the cavity axis

6.2.2 Two Dimensional (2D) Model

In the absence of local surface defects the cavity may be considered to be perfectly axisymmetric, in which case it may be adequately modelled in 2D. This requires a significantly less computation and memory storage. Shown in Figure 6-4, both the MTA and the equivalent pillbox cavities were modelled. Perfect electric conductor was the chosen boundary condition. Meshing was performed using triangular elements, and it is presented in more detail in Chapter 7.

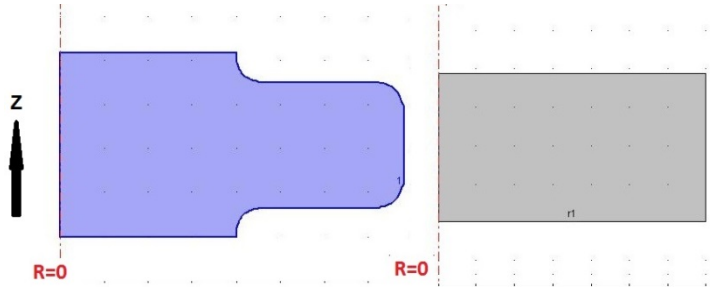

Figure 6-4: 2D models of the MTA cavity (left) and pillbox (right) corresponding to the 3D axisymmetric cavities where no surface defect are present. Both models have an operating frequency of 805 MHz due to having a similar radius

6.3 Particle Tracker

The particle tracker developed in this work was implemented in Matlab and uses the Comsol live link interface to couple the FEM simulation with the Matlab programing tool. The particle tracker had access to the E and B fields calculated by Comsol. Various algorithms were developed in order to allow both 2D and 3D simulations to be carried out. In all cases, the forces exerted by the E and B components of the EM field were used to define the motion of a travelling particle.

While in motion, a charged particle is subject to the Lorentz force [117, 122, 123]. At particle velocities comparable to the speed of light, the relativistic effects should be taken into account. For a particle with a velocity $\vec{v}$ and rest mass m, the momentum can be expressed as $\vec{P} = \gamma m\vec{v}$ and therefore force $\vec{F}$ is expressed as:

$$\vec{F} = \frac{d\vec{P}}{dt} = \frac{d(\gamma m\vec{v})}{dt} = q(\vec{E} + \vec{v} \times \vec{B}) \tag{6-6}$$

where, γm, q, $\vec{E}$ and $\vec{B}$ are relativistic mass, charge, electric and magnetic fields, respectively. The relativistic factor γ is defined by

$$\gamma = (1 - v^2/c^2)^{-1/2} \tag{6-7}$$

where (c) is the speed of light in vacuum. Equation (6-6) can be re-written as:

$$\gamma m\frac{d\vec{v}}{dt}+m\vec{v}\frac{d\gamma}{dt}=q(\vec{E}+\vec{v}\times\vec{B}) \tag{6-8}$$

From $\gamma=(1-v^2/c^2)^{-1/2}$ we can calculate $\frac{d\gamma}{dt}$ in the following.

$$\frac{d\gamma}{dt}=\frac{\gamma^3}{c^2}\vec{v}.\frac{d\vec{v}}{dt} \tag{6-9}$$

but $\vec{v}.\frac{d\vec{v}}{dt}$ is readily calculated from equation (6-8) as follows:

$$\gamma m\vec{v}.\frac{d\vec{v}}{dt}+mv^2\frac{d\gamma}{dt}=q(\vec{v}.\vec{E}) \tag{6-10}$$

If we now substitute $\vec{v}.\frac{d\vec{v}}{dt}$ from equation (6-10) into the equation (6-9), we obtain:

$$\frac{d\gamma}{dt}=\frac{\gamma^3}{c^2}\left[\frac{q}{\gamma m}(\vec{v}.\vec{E})-\frac{mv^2}{\gamma m}\frac{d\gamma}{dt}\right] \tag{6-11}$$

or

$$\frac{d\gamma}{dt}\left(1+\frac{\gamma^2v^2}{c^2}\right)=\frac{\gamma^2q}{mc^2}(\vec{v}.\vec{E}) \tag{6-12}$$

But the expression in the parentheses on the right hand side is equal to γ^2:

$$1+\frac{\gamma^2v^2}{c^2}=1+\frac{\frac{v^2}{c^2}}{\left(1-\frac{v^2}{c^2}\right)}=\frac{1}{\left(1-\frac{v^2}{c^2}\right)}=\gamma^2 \tag{6-13}$$

Therefore, equation (6-12) can be simplified as:

$$\frac{d\gamma}{dt}=\frac{q}{mc^2}(\vec{v}.\vec{E}) \tag{6-14}$$

Taking into account the relativistic mass, the rate of change of energy $\frac{dE}{dt}=\frac{d(m\gamma c^2)}{dt}$ should be equal to the dot product of the external force $\vec{F}=q\vec{E}$ and velocity $\vec{v}$. As the magnetic field cannot do work on the particle, it does not appear in equation (6-14). Therefore, equation (6-8) can be finally written as:

$$\gamma m \frac{d\vec{v}}{dt} + q\left(\frac{\vec{v}}{c^2}\right)(\vec{v}.\ \vec{E}) = q(\vec{E} + \vec{v} \times \vec{B}) \tag{6-15}$$

Equation (6-15) is the equation of motion and can be used to calculate the velocity and position of the travelling particle at any given time. The tracker code solves the equation of motion in order to calculate acceleration dv/dt. This is then integrated in order to find velocity of the particle, while a second integration yields the positions. The scalar components of equation (6-15) are given below.

$$\frac{dv_x}{dt} = \frac{q}{\gamma m}\left(E_x + v_y B_z - v_z B_y\right) - \left(\frac{q}{\gamma m c^2} v_x.\left(v_x E_x + v_y E_y + v_z E_z\right)\right) \tag{6-16}$$

$$\frac{dv_y}{dt} = \frac{q}{\gamma m}\left(E_y + v_z B_x - v_x B_z\right) - \left(\frac{q}{\gamma m c^2} v_y.\left(v_x E_x + v_y E_y + v_z E_z\right)\right) \tag{6-17}$$

$$\frac{dv_z}{dt} = \frac{q}{\gamma m}\left(E_z + v_x B_y - v_y B_x\right) - \left(\frac{q}{\gamma m c^2} v_z.\left(v_x E_x + v_y E_y + v_z E_z\right)\right) \tag{6-18}$$

The solution of the FE model generated by Comsol is the components of the EM field. They are used by the postprocessor command mphinterp to interpolate the necessary values needed by the tracker to solve the equation of motion. This then allows the movement of the traveling particle to be mapped [124]. The equation of motion was integrated using Matlab function ODE45, which is a 4th order Runge-Kutta (RK) method with variable step length [125, 126].

6.3.1 3D Tracking Algorithm

Figure 6-5 provides an over view of the developed algorithm for tracking a particle travelling within a 3D electromagnetic field. The charge and mass of the particle are pre-defined, while the program requires the user to manually input the location and velocity at which the particle is emitted in (x, y, z) coordinates.

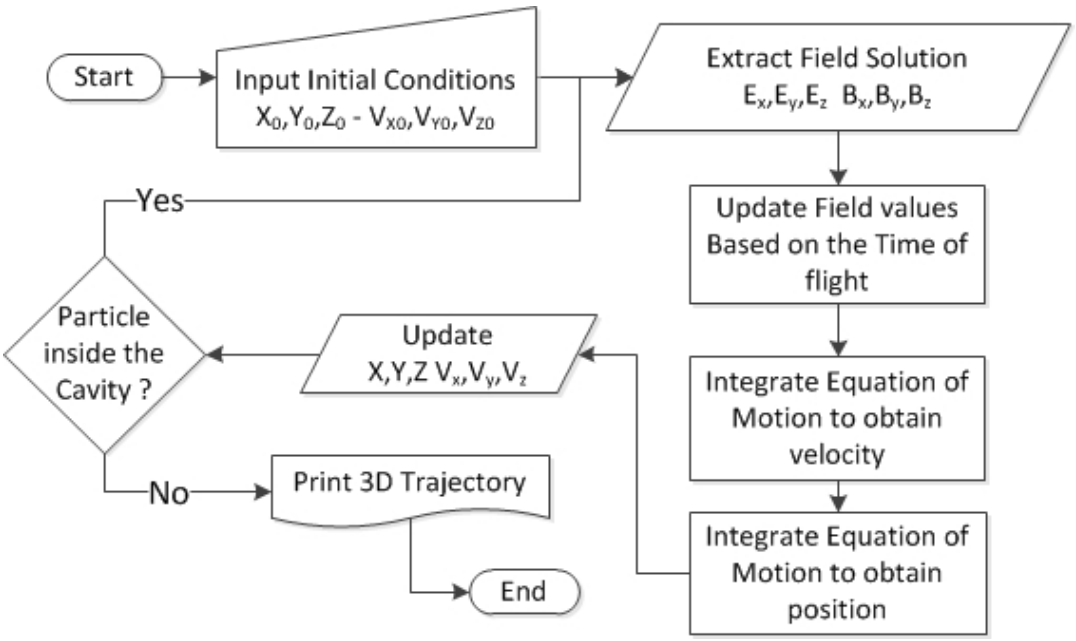

Figure 6-5: Overall steps taken by the 3D particle tracker in order to calculate the path taken inside an RF cavity. The particle is emitted from the desired location with no initial velocity while no external magnetic fields are present

The post processing command mphinterp, interpolates the necessary field values from the solution generated in Comsol. The solution generated is static and does not take into account oscillations at 805 MHz. Equations (6-19) and (6-20) were used to generate the correct time dependent field values used by the tracker. The E and B field have a 90° phase difference.

$$E = E_{Comsol} \times \sin(\omega t) \quad (6\text{-}19)$$

$$B = B_{Comsol} \times \cos(\omega t) \quad (6\text{-}20)$$

where E_{Comsol} and B_{Comsol} are static field components obtained from Comsol and ω is the operating frequency of the cavity.

The velocity and position of the travelling particle are updated at the end of each cycle and stored in a file. The path of travel is then printed once the particle exits the RF cavity.

6.3.2 2D Tracking Algorithm

When no surface irregularities were present, both the MTA and the pillbox cavities introduced earlier could be considered fully symmetrical owing to the symmetry of the geometry. Hence, it was possible to represent such geometries by a 2D model and to significantly reduce the necessary computational costs of modelling. Figure 6-6 shows the flowchart of the developed 2D tracker algorithm.

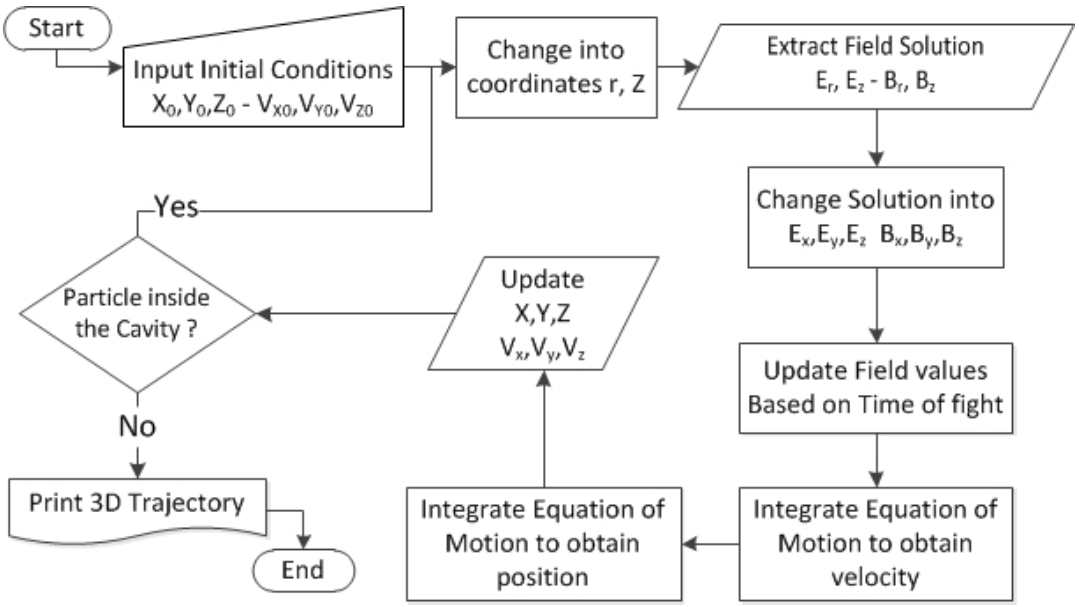

Figure 6-6: Overall steps taken by the 2D particle tracker in order to calculate the path taken inside an RF cavity. The 2D solution benefits from applied symmetry conditions and speeds up the solution generated by the tracker. The particle is emitted from the desired location with no initial velocity while no external magnetic fields are present

A major benefit of the tracker developed by this work is the ability to use a 2D FE solution in order to track a particle inside an RF cavity and produce a 3D representation of the path travelled. To achieve this, the user was required to enter the starting position and velocity of the particle using (x, y, z) components. The tracker then converted the Cartesian coordinates x and y into polar coordinate r and generate the angle φ by:

$$r = \sqrt{x^2 + y^2} \tag{6-21}$$

$$\varphi = atan2(y, x) \tag{6-22}$$

The polar coordinates r was then converted back into the Cartesian coordinates x and y using the angle φ and trigonometric functions sine and cosine as:

$$x = r\cos\varphi \tag{6-23}$$

$$y = r\sin\varphi \tag{6-24}$$

Once the necessary field values were extracted from the 2D solution by the postprocessor, (E_x, E_y) and (B_x, B_y) field components were then obtained. By including the time of travel, it was possible to generate the necessary time dependent field values used by the tracker. The equation of motion was integrated twice in order to evaluate and update the velocity and location of the particle. The process was repeated until the particle left the cavity, at which point the path taken was presented in 3D. This allowed for better representation to be made of the path taken by the particle from the emission point until the impact.

6.3.3 Particle Tracking Using Mixed 2D and 3D Geometry Models

The cavities analysed in this work are fully symmetrical and the EM field can be adequately simulated using 2D FE models. However, the nominal axis symmetry is broken by the introduction of surface defects which induce local field enhancement as discussed in Chapter 3, requiring the use of 3D models. Also, the very small size of the defects means that the 3D effects are highly localised and the axis symmetry conditions are still valid for the major part of the cavity model.

Considering the computing and memory storage costs of handling high resolution 3D models, there are considerable savings that can be made by adequately combining small scale 3D models of the geometry in the vicinity of the defect, with a large scale axis symmetric 2D model of the whole cavity. both FE models may be used in a single simulation for accurate field evaluation at various locations and employed in a 3D particle tracker. Figure 6-7 illustrates the two models used for simulation at different geometric scales.

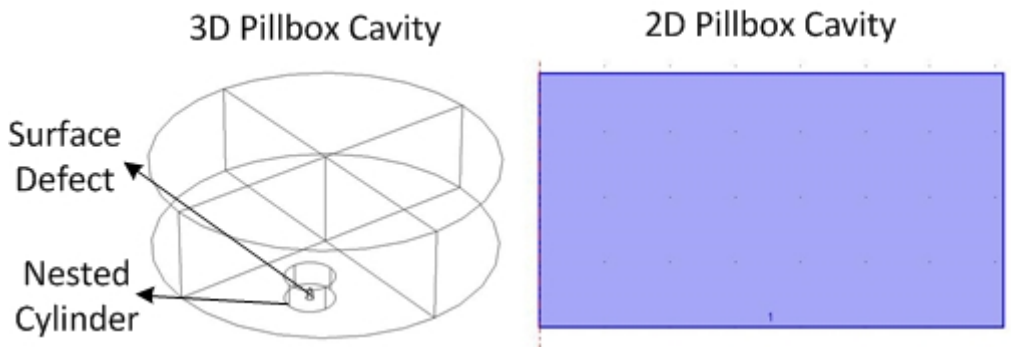

Figure 6-7: 3D 805 MHz pillbox cavity with a surface defect positioned inside a nested cylinder (left) and a 2D 805 MHz cavity with no surface defects (right). The field profile in both models is generated in Comsol and used alongside each other by the tracker.

The first model consists of a 3D region where a single surface defect was placed inside a nested cylinder away from the cavity axis and involves a FE mesh of a resolution that matches the feature size of the surface defect. the rest of the cavity involves a FE mesh that matches the feature size of the cavity itself, therefore a much larger scale than that of the nested cylinder. If the two regions are to be merged into a single mesh, then the meshes at different scales must match at the nodes. Thus the transition from small to large meshing scale can easily involve elements with unacceptably high aspect ratio. For this reason, if the two scales are vastly different, it may be necessary to explicitly define additional nested cylinder regions of increasing size around the asperity. These regions can then be used as the means by which the user exercises the control over the automatic mesh

generator in order to avoid meshing failures and to create satisfactory meshes. The size and number of nested cylinders were defined by the size of the defect and the meshing process requirements. This is explained in greater detail in Chapter 7.

The tracking algorithm has been developed in such a way to utilise the flexibility of the Comsol Live link to the best possible way. Based on the location of the travelling particle, the tracker would choose between the two FE models in order to extract the necessary field components. Based on this capability, a short part of the tracking process is carried out using the 3D model with a surface defect in comparison to the majority of the process where a simple 2D model is used. As a result, one is able to benefit from the accuracy of a 3D field solution while utilising the simple and low cost nature of a 2D solution. The steps taken to track an electron emitted from a surface defect are shown below in Figure 6-8.

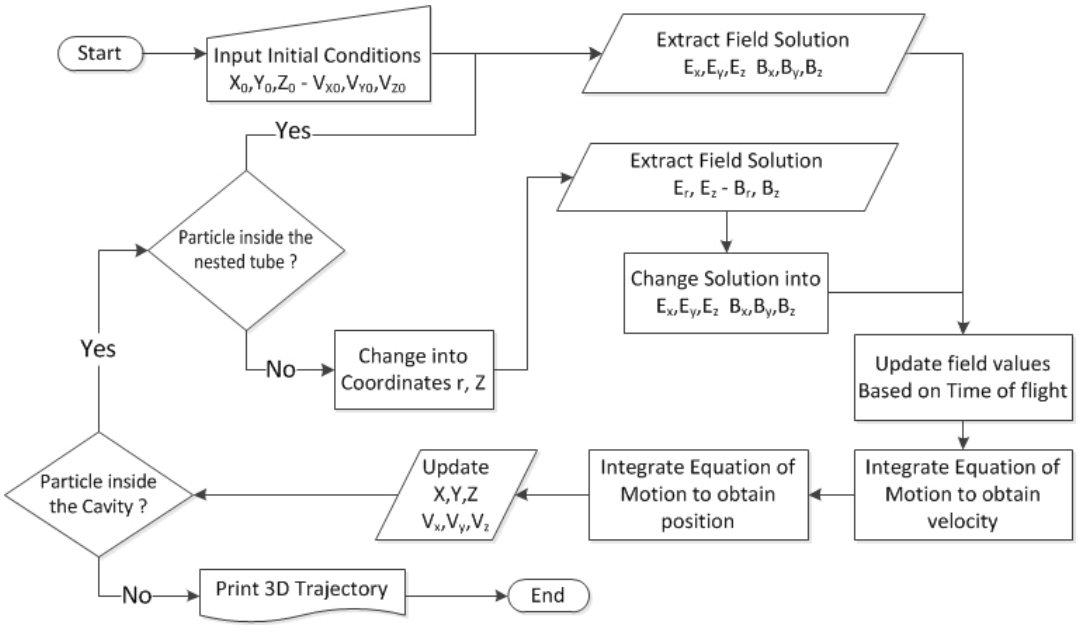

Figure 6-8: Overall steps taken by the non-symmetric particle tracker in order to calculate the path taken inside an RF cavity. Both the 2D and 3D solution can be called upon by the tracker based on the location of the travelling particle. The 3D solution is used while the particle is inside the nested tube. It is at this point where the field is no symmetrical and a 3D model has to be used to define the field profile. Symmetry conditions can once more be satisfied out of the nested tube as the localised field enhancements can no longer be felt. The tracker then utilises the 2D solution in order to reduce computational costs and reduce the time needed to track the particle

The user has to input the initial values for the position and velocity of the particle, ensuring the emission site is near the tip of the surface defect. As the particle is inside the nested tube, the tracker extracts the field vales from the 3D solution and updates the acceleration, velocity and position of the particle. The process is continued until the particle is no longer inside the nested tube. From this point onwards, the tracker starts to use the 2D FE solution in order to obtain the required E and B field values.at each step a calculated 2D field value is taken as the corresponding axis symmetric 3D value. This is continued until the travelling particle reaches the cavity wall.

6.4 Concluding Remarks

The desired frequency for the FE models was chosen to be similar to the MTA cavity in order to allow for better comparisons to be made with other MTA findings. To simplify the elliptical shape of the MTA cavity, a pillbox design with very similar operating frequency was used. A new Matlab based particle tracker was developed in this work with Live Link capability in order to extract the Comsol FE solutions of the field. The simultaneous use of 2D and 3D models corresponding to different scales was implemented as the means of realising manageable simulation models, in term of memory and computational costs. The overall particle tracking is performed in 3D.

Chapter 7.

Finite Element and Particle Trajectory Analysis

7.1 Introduction

In the previous chapter the finite element models and the particle tracking algorithms were introduced. The EM field distribution was evaluated in Comsol and used by the tracker to extract the necessary field values. This was then used to simulate the path taken by an emitted particle travelling inside an RF cavity. This chapter presents a series of analyses aimed at understanding the change in particle behaviour in relation to localised field enhancements caused by a single surface defect. The cavity modelled in this work was the MTA 805 MHz cavity introduced previously in Chapter 2. A major benefit of the adopted approach was the ability to analyse axisymmetric filed distribution in 2D and non-axisymmetric in 3D and use both sets of solutions to generate a 3D particle tracking solution.

7.2 Finite Element Model Meshing Parameters

An essential part of any simulation is the meshing process, which is crucial for obtaining the best results in the fastest possible way. To assist in choosing the correct specifications for mesh elements, Comsol Multi-physics provides nine

built-in size parameter sets. The various size parameters for free tetrahedral meshing elements used in Comsol are provided below in Table 7-1.

Table 7-1: Pre-defined parameters for tetrahedral 3D mesh elements used in Comsol [115]. The max and min element size ensures that the element size is limited while the growth rate limits the size difference between two adjacent elements. The resolution of curvature is used to create better conformity around curved edges by limiting the size of the elements used along a curved boundary

Mesh	*Max Element Size (m)*	*Min Element Size (m)*	*Element Growth Rate*	*Resolution of Curvature*
Extremely Coarse	0.156	2.19×10^{-2}	2	1
Extra Coarser	0.0937	1.69×10^{-2}	1.8	0.9
Coarser	0.0594	1.25×10^{-2}	1.7	0.8
Coarse	0.0469	8.75×10^{-3}	1.6	0.7
Normal	0.0312	5.62×10^{-3}	1.5	0.6
Fine	0.025	3.12×10^{-3}	1.45	0.5
Finer	0.0172	1.25×10^{-3}	1.4	0.4
Extra Fine	0.0109	4.69×10^{-4}	1.35	0.3
Extremely Fine	0.00625	6.25×10^{-5}	1.3	0.2

The built-in parameter sets are determined by Comsol for ease-of-use and to produce high-quality mesh elements. They can be changed when limited computer resources or the complexity of the geometry and the physics application calls for it. The predefined element sizes are simply sets of values that are available for modification. The maximum element size limits how big each mesh element can be while the minimum element size limits how small they can be. Element growth rate limits the size difference of two adjacent mesh elements where a lower value would ensure a finer mesh is achieved. Finally, the resolution of curvature limits how big a mesh element can be along a curved boundary. A finer mesh can be created by assigning a lower value.

7.2.1 3D Mesh Refinement

The geometrical parameters of the MTA and the pillbox cavity were introduced earlier in Table 6-1. The MTA cavity is an elliptical shaped cavity with several curved boundaries. An unstructured 3D mesh geometry using tetrahedral elements was used to mesh the cavity. Figure 7-1 shows the MTA cavity being meshed using the coarsest and the finest mesh elements predefined by Comsol. Although the finer mesh was much more capable of following the curved boundaries of the geometry, the number of elements was increased 230 times. The minimum element quality was also improved from 8.9×10^{-4} to 0.11. Comsol recommends a value greater than 0.1 as a general guideline to be followed [115].

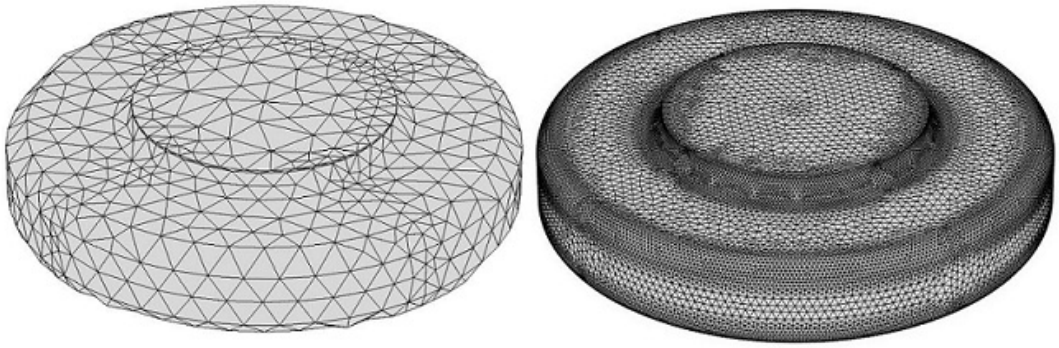

Figure 7-1: MTA cavity meshed using extremely coarse tetrahedral elements consisting of 2,685 elements (left) and extremely fine elements consisting of 600,513 (right). The mesh quality is increased as the edge length of the elements are reduced

The decision to represent the MTA cavity with a simpler pillbox cavity was taken to lower the required computational costs and was explained in Chapter 6. A simple comparison between an MTA cavity meshed using extremely fine elements and a pillbox reveals a 19 % drop in the number of elements. This is shown below in Figure 7-2, where the number of elements was reduced due to the removal of curved boundaries. The minimum element quality was improved to 0.1757.

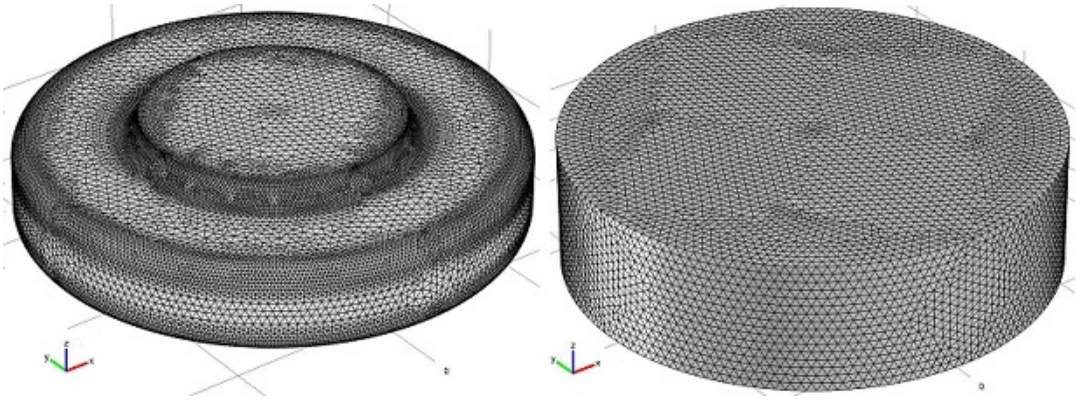

Figure 7-2: Photograph making a comparison made between the MTA cavity (left) with an 805 MHz pillbox (right) using extremely fine elements. A 19 % drop in the number of elements from 600,513 to 490,964 is observed, while the mesh quality is improved due to a simpler geometry

It is not always obvious how many elements to use in a particular problem and the choice depends on many solution parameters. In practice, one refines the mesh until the solution converges. The correct solution should not depend on the mesh and it is important to show this step in order to confirm the validity of the results. This process is known as mesh convergence analyses and it was performed in this work. Although increased mesh density can reduce error, it can increase computing time. Therefore, the smallest sufficient number of elements is desired to obtain an accurate solution.

Comsol eigenfrequency solver was used to obtain the field distribution. The solver calculates the resonant frequency of the structure and generates the field distribution values required by the tracker. A mesh convergence exercise was carried out in order to define a suitable element size for the 3D FE models used in this work. A total of nine models, each meshed using one of the pre-defined element sizes, were used. This is shown below in Table 7-2.

Table 7-2: Table presenting the variables obtained during the mesh refinement process. A total of nine models were created each being meshed with one of the pre-defined element sizes introduced previously. Although the number of elements is growing fast, the eigenfrequency is kept constant. This highlights the fact that the eigenfrequency generated by Comsol is not sensitive to mesh density and is not a suitable variable for determining the best possible element size for the meshing process. The time taken to generate each field profile also is increased as the number of elements grows

Mesh	*Element Size*	*No. of Elements*	*Eigenfrequency (Hz)*	*Time (min)*
$\mathbf{M_1}$	Extremely Coarse	5,194	8.040254×10^8	5
$\mathbf{M_2}$	Extra Coarser	7,032	8.046165×10^8	10
$\mathbf{M_3}$	Coarser	11,917	8.046536×10^8	15
$\mathbf{M_4}$	Coarse	24,113	8.046946×10^8	20
$\mathbf{M_5}$	Normal	40,133	8.047167×10^8	30
$\mathbf{M_6}$	Fine	60,160	8.047205×10^8	45
$\mathbf{M_7}$	Finer	95,446	8.047249×10^8	70
$\mathbf{M_8}$	Extra Fine	194,943	8.047285×10^8	130
$\mathbf{M_9}$	Extremely Fine	587,079	8.047301×10^8	300

It is evident that increasing mesh density has very small effect on the resulting resonant frequency, so it was concluded that resonant frequency was not a suitable parameter or mesh convergence analysis. Instead, it was decided to use for this purpose the E field distribution along the cavity axis in the Z direction. This is shown below in Figure 7-3 for models M_1 to M_9.

Large discontinuities in the E field profiles of models with coarser mesh elements were observed. The continuity and smoothness in the generated solution was improved with the growing number of elements as the mesh elements were reduced in size. The aim was to be able to generate a field distribution as close as to the profile shown previously in Figure 6-2.

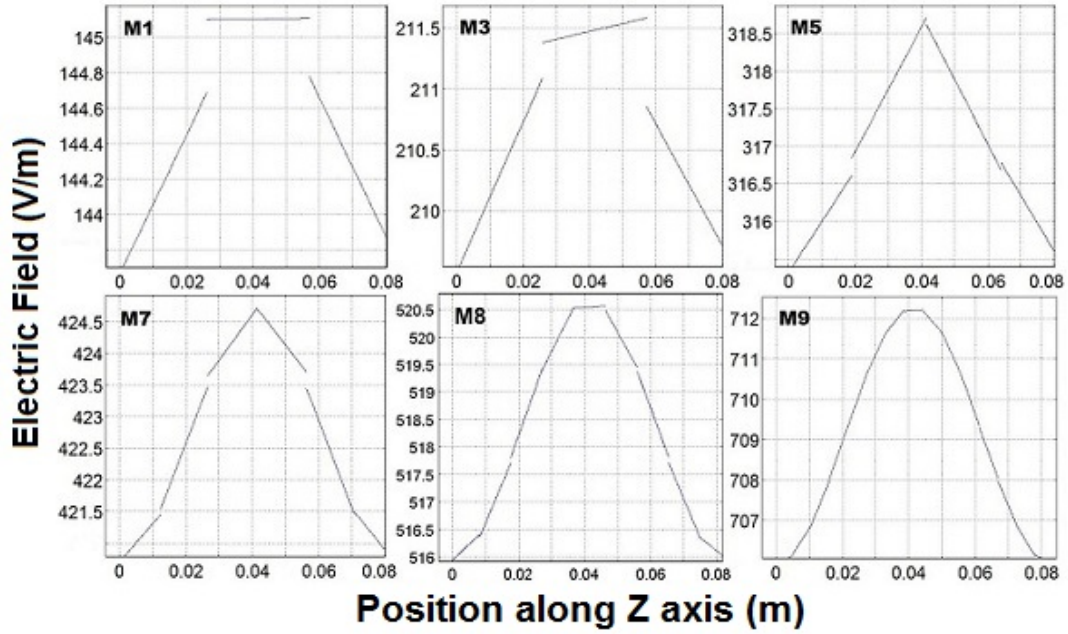

Figure 7-3: Line graph of electric field (V/m) along the MTA cavity axis in the Z direction. The E field is at maximum along the cavity axis and exhibits an elliptical profile. Large discontinuities in the field observed in models with coarser mesh elements can cause inaccuracies during particle tracking analyses. This is due to the triangulation process carried out by the postprocessor in order to obtain the necessary field values from the Comsol solution.

Although it was shown that a coarse mesh is suitable for eigenfrequency calculations, higher number of elements was required to produce the necessary field distribution for particle tracking evaluations. Model M_9 exhibits a solution with better continuity and hence extremely fine elements were chosen as the suitable elements to mesh 3D models with no surface defects.

7.2.2 2D Mesh Refinement

The extremely fine 3D mesh required for accurate field modelling was found to pose excessive demands in terms of memory storage and computing speed. As discussed in section 6.2.2 the computational costs can be significantly lowered by using a 2D model, provided symmetry conditions can be satisfied. This is applicable in the case of a plain cavity where no surface irregularities are present.

Comsol used triangular elements to mesh 2D models and the parameters of the pre-defined elements are detailed below in Table 7-3.

Table 7-3: Pre-defined parameters for triangular 2D Mesh elements used in Comsol [115]. The max and min element size ensures that the element size is limited while the growth rate limits the size difference between two adjacent elements. The resolution of curvature is used to create better conformity around curved edges by limiting the size of the elements used along a curved boundary

Mesh	*Max Element Size (m)*	*Min Element Size (m)*	*Element Growth Rate*	*Resolution of Curvature*
Extremely Coarse	0.047	0.00712	2	1
Extra Coarser	0.0285	0.00228	1.8	0.8
Coarser	0.0185	8.5×10^{-4}	1.5	0.6
Coarse	0.0143	2.85×10^{-4}	1.4	0.4
Normal	0.00955	4.27×10^{-5}	1.3	0.3
Fine	0.00755	4.27×10^{-5}	1.3	0.3
Finer	0.00527	1.78×10^{-5}	1.25	0.25
Extra Fine	0.00285	1.07×10^{-5}	1.2	0.25
Extremely Fine	0.00142	2.8×10^{-6}	1.1	0.2

The average edge length of 3D tetrahedral elements was three times larger than their 2D triangular counterparts. As shown below in Figure 7-4, the MTA cavity was meshed using the coarsest and finest mesh elements available in order to show the difference between the two element sizes. The number of elements was increased by a factor of 92 while the minimum element quality was increased from 0.57 to 0.74, thus showing a large improvement in mesh quality.

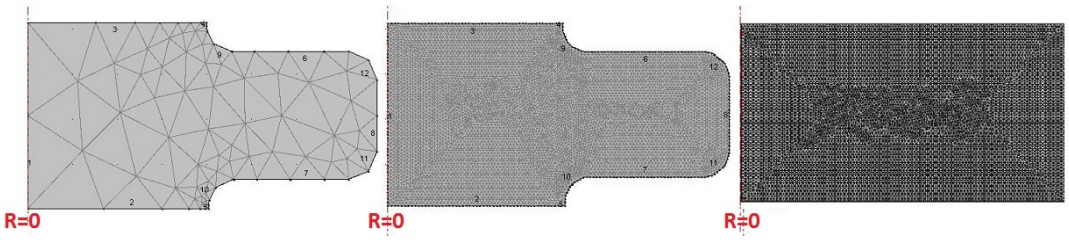

Figure 7-4: 2D MTA cavity meshed using pre-defined Extremely Coarse elements consisting of 135 elements (left) Extremely Fine consisting of 12,458 elements (middle). This is in comparison to a pillbox cavity being meshed using the extremely fine elements (right). The model consists of 14,528 elements. Mesh quality in all three models is acceptable, highlighting one of the benefits of a 2D model

A 2D 805 MHz pillbox cavity was also meshed using extremely fine elements. Resulting in the model size of 14,528 compared to 490,964 elements for the equivalent 3D model. No further improvements to the shape of the geometry can be made in order to reduce the number of elements.

Table 7-4: Variables obtained during the mesh refinement process for a 2D MTA cavity. A total of nine models were created each being meshed using a pre-defined 2D triangle elements. Similar to the 3D model, the eigenfrequency is not mesh sensitive and is not the best variable to determine the suitable element size for the meshing process. The time taken to generate a 2D field profile is far less than the 3D model, highlighting the simplicity provided by a simpler 2D geometry.

Mesh	*Element Size*	*No. of Elements*	*Eigenfrequency (Hz)*	*Time (min)*
A_1	Extremely Coarse	135	8.041793×10^8	1
A_2	Extra Coarser	155	8.040331×10^8	1
A_3	Coarser	263	8.040282×10^8	1
A_4	Coarse	373	8.040391×10^8	2
A_5	Normal	620	8.040428×10^8	2
A_6	Fine	744	8.040429×10^8	4
A_7	Finer	1229	8.040441×10^8	7
A_8	Extra Fine	2149	8.040466×10^8	11
A_9	Extremely Fine	12,458	8.040455×10^8	21

The eigenfrequency solver was used to evaluate the E and B fields of the 2D models and mesh convergence was analysed as before. The variables obtained

from models A_1-A_9 are shown above in Table 7-4. Once more, the eigenfrequency of the cavity exhibited negligible sensitivity to the increasing mesh density. The E field along the axis was analysed and the results were plotted in Figure 7-5.

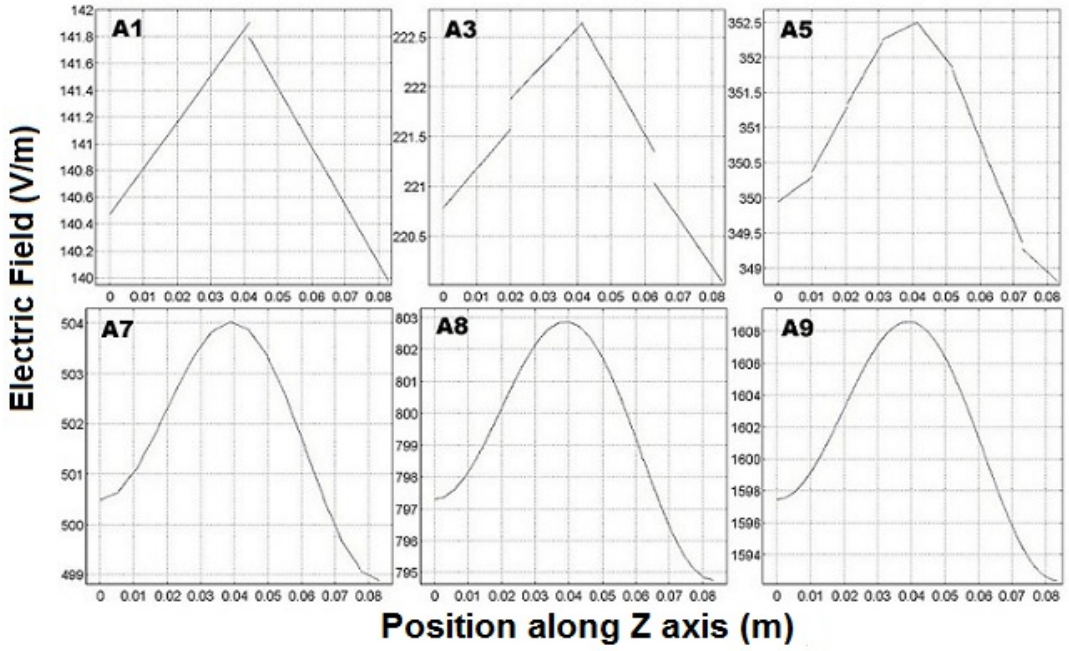

Figure 7-5: Line graph of electric field (V/m) along the cavity axis for a 2D MTA cavity. The E field is at maximum along the axis and has an elliptical profile. Large discontinuities in the field are observed in models with coarser mesh elements, which can cause inaccuracies to occur during particle tracking. This is due to the error introduced during the triangulation process carried out by the postprocessor.

Again, large discontinuities in the E field profiles of models with coarser mesh elements were observed. However, mesh refinement beyond that shown in model A_8 can be seen to bring little benefit. Hence, extra fine was chosen as the suitable element size to mesh 2D models with no surface defects. It can be seen that mesh convergence in a 2D model was achieved using at a far lower computational cost. A huge reduction in the necessary number of elements was achieved while the quality of the mesh was increased by using elements with shorted edge lengths. This allowed more detailed field profile to be generated without posing excessive demands on the computing resources.

7.2.3 Non Symmetrical Model Incorporating Surface Defect

As discussed previously, a RF cavity can be represented by a 2D model when symmetry conditions can be satisfied. However, such conditions could not be met with the introduction of features such as surface defects. For demonstration purposes, Figure 7-6 shows a single surface defect modelled on the surface of an MTA cavity. The shape of the defect was similar to the defect used in MTA studies [61, 62] and it was much larger than the usual surface defects observed on the surface of the button. Local field enhancements caused by this defect were evident.

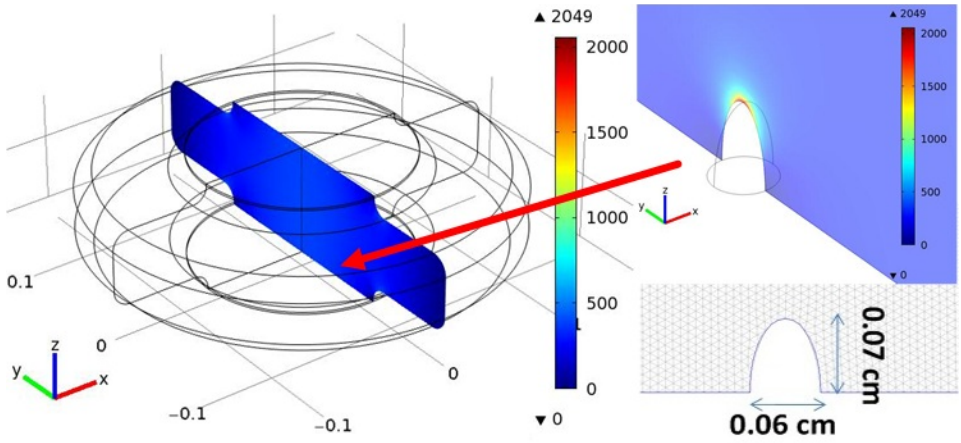

Figure 7-6: Induced localised field enhancement observed due to the introduction of a single surface defect inside an MTA elliptical cavity. The defect has a height of 700 microns and width of 600 microns. Such geometrical values are used in other MTA simulation studies and are larger than the typical surface defects observed during surface measurements taken from button samples.

Localised field enhancement due to the presence of surface defects can lead to changes in particle behaviour at the emission site. The meshing process used for plain cavities was capable of satisfying the eigenfrequency measurement and uniformity requirements. However, a more detailed mesh was needed to accurately model the field enhancement in the vicinity of smaller features. Each surface defect was modelled as a semi-ellipsoid and the edges were meshed individually. As

shown below in Figure 7-7, it was imperative to choose an element size that was small enough to accurately represent the necessary edges.

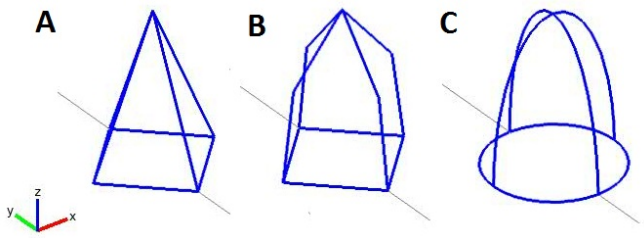

Figure 7-7: Single surface defect modelled as a semi-ellipsoid and a height of 700 µm. it was meshed using three different element sizes. The first employs normal elements with a total of 8 edge elements (left) the second used finer elements with a total of 12 edge elements (middle) and the third uses extremely fine elements with a total of 68 edge elements (right).

It was evident that the element size required to mesh a µm scale feature was several orders of magnitude smaller than that needed to mesh the rest of the cavity. Furthermore, different meshes that represent adjacent regions of different resolution had to be connected to each other without discontinuities. This was difficult to achieve using fully automatic meshing procedure and it was necessary that the user exercises a sufficient control over the meshing process. The solution to this problem was to enclose the smaller features inside a series of nested cylinders with the defect positioned in the centre. Each cylinder defined a domain that allowed the user to select and control the generation of progressively smaller element sizes. This process is shown below in Figure 7-8. The number of cylinders required to create an accurate mesh was governed by the size of the defect being modelled and the required change in mesh density between adjacent domains.

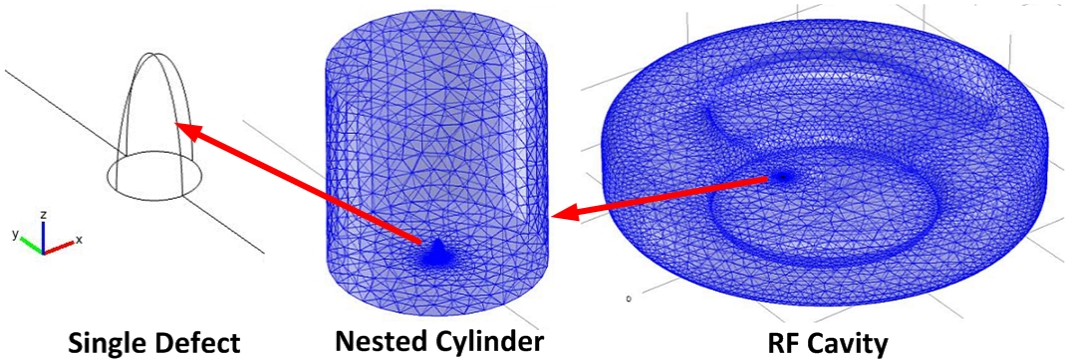

Figure 7-8: Demonstration of the multi-step meshing process used to accurately mesh models with surface defects positioned inside of the cavity. The defect is meshed using elements where the maximum element size is reduced manually in order to accurately represent the shape of the defect (left). This is then placed inside a nested cylinder where elements smaller than the pre-defined Comsol elements are used to achieve the desired mesh density (middle). In the last stage the cavity is meshed using coarser elements where a lower mesh density is required (right). An MTA cavity was used in this example

Due to the size of the surface defects modelled in this work, mesh elements smaller than Comsol pre-defined elements had to be created in order to accurately mesh the geometry. An example of such elements is shown below in Table 7-5. Each domain was meshed separately using a single nested cylinder due to the size of the surface defect being modelled.

Table 7-5: Mesh element used to mesh an MTA 805 MHz cavity with a single surface defect of height 700 µm and base of 600 µm. A total of 400 edge elements were used to mesh the defect. This was placed inside a nested tube with a height of 2000 µm and radius of 1000 µm and meshed using tetrahedral elements. The maximum element size for the defect and the tube were reduced and set to 1×10^{-4} and 1×10^{-5} respectively. The rest of the cavity was meshed using pre-defined fine elements.

	Maximum Element Size (m)	Element Grows Rate	Resolution of Curvature	No. of Elements
Defect	1×10^{-5}	1.3	0.2	400
Nested Cylinder	1×10^{-4}	1.3	0.2	57,615
Cavity	3.12×10^{-3}	1.4	0.4	36,091

In the first step of the process the defect was meshed using edge elements which are smaller than the edge length of the defect. Hence, size of the smallest pre-defined mesh element was customised and reduced to 1×10^{-5}, generating 400 elements. In order to ensure mesh continuity, the size of the elements used to mesh the nested cylinder was increased slightly to 1×10^{-5}. This generated a further 57,615 tetrahedral elements. The rest of the cavity was then meshed using pre-defined fine elements, adding an extra 37,091 elements.

Comparing the above example and model M_6 given in Table 7-2 showed a slight increase in the overall number of elements. The majority of the elements were concentrated inside the nested cylinder, as required by the feature size of the modelled defect.

7.3 Particle Tracking Simulation Results

The necessary field values were generated in Comsol and were used by the tracking algorithms to track particle both in 2D and 3D. The Lorentz force calculations were used by the tracking algorithms, taking into account the relativistic conditions of a travelling particle inside an RF cavity.

7.3.1 Tracking Algorithm Validation

The developed tracking algorithms were presented in the previous chapter. The tracker uses as the input the RF field values generated by Comsol, and user defined particle properties and emission site location. The tracker is capable of using various field profiles generated by Comsol, giving it an added advantage over existing particle tracking programs by enabling both 2D and 3D simulations.

A useful measure used in the design of RF cavities is the ratio between the shunt impedance R and quality factor Q, which is defined as [116]:

$$\frac{R}{Q} = \frac{V_0^2}{\omega U} \tag{7-1}$$

where R, Q, V_0, ω and U are shunt impedance, quality factor, voltage, angular frequency and input energy. This ratio shows the effectiveness of energy gain by a particle per stored energy for each cycle, which is only dependent on the cavity geometry [97, 115, 116, 127, 128]. In Comsol the input energy (U) is chosen automatically and varies based on the mesh density and element size. The method implemented by Comsol to evaluate the accelerating voltage is based on keeping the ratio R/Q constant at all times, hence altering the chosen input energy. Therefore, only the relative strength of the field throughout the cavity is of interest for the field evaluation, while the absolute value is subsequently scaled to meet the design specifications. The scaling factory is obtained by comparing the normalised field value on the cavity axis and the specified value required by the cavity design.

Both 2D and 3D tracking algorithms were validated using a simple test, in which a single electron was emitted from a fixed location. To satisfy symmetry conditions for the use of a 2D model, no surface defects were present. An 805 MHz pillbox cavity was meshed using the procedure introduced in Chapter 6 and the initial conditions of the travelling particle are shown below in Table 7-6.

Table 7-6: Values used to define the conditions of the emitting electron at the point of release. Both models use an 805 MHz pillbox cavity with no surface defect, while the electron is released off the cavity axis. A scaling factor is used by the tracker to normalise the E and B field values generated in Comsol. This is to allow for the accelerating field to match the UKNF design specifications.

Model	Mesh	Scaling Factor	Starting Position Coordinates (m)	Initial Energy (eV)
2D	A_8	5,300	(0, 0.05, 0)	0
3D	M_9	42,000	(0, 0.5, 0)	0

A set of 2D and 3D plain pillbox cavities were meshed using elements introduced for models A_8 and M_9. Once the field profile was generated in Comsol, the field values had to be normalised to a maximum accelerating gradient of 15 MV/m. This was to allow the correct accelerating gradient as specified in the design of the UKNF cavities to be used by the tracker [129]. Hence, all field values were multiplied by the required scaling factor, which was set at 5,300 and 42,000 for the 2D and 3D models respectively. A single electron was emitted from the cavity axis with zero initial velocity. Figure 7-9 shows the path taken by the electron using the 3D model.

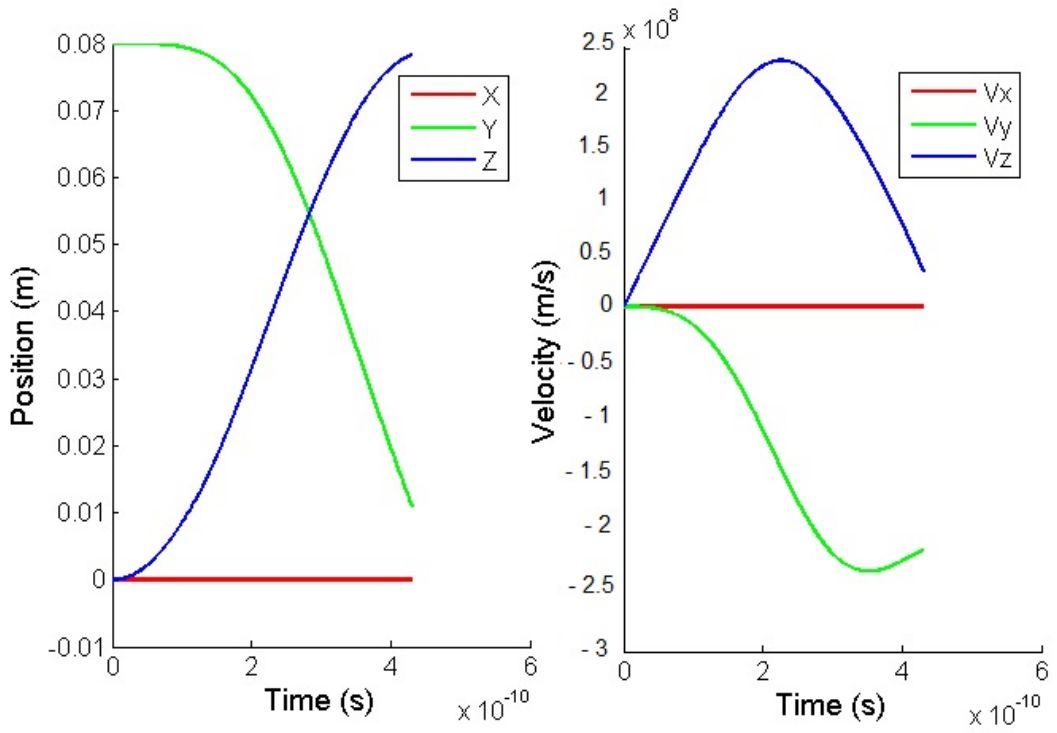

Figure 7-9: Position and Velocity components of an electron being tracked in a 3D 805 MHz pillbox cavity. The electron is accelerated from one end of the cavity towards the opposing wall due to the presence of strong E field along the Z direction. Due to the emission site being away from the cavity axis, magnetic field in Y direction is present. This leads to further acceleration in the Y direction.

The sudden impact of the transverse E field on the electron was evident, causing the electron to accelerate rapidly along the Z direction. Only the positive part of the field was present as the travel time was less than the time period of the RF field. The electron also experienced magnetic field forces due to the emission point being away from the cavity axis. This resulted in further acceleration in Y direction.

The second model used a plain 2D pillbox cavity to generate the necessary field profile. This was then used by the 2D tracking algorithm with a chosen scaling factor of 5300. The location of the emission site was similar to the 3D model while the electron had no initial velocity. The path of travel taken by the electron is shown below in Figure 7-10.

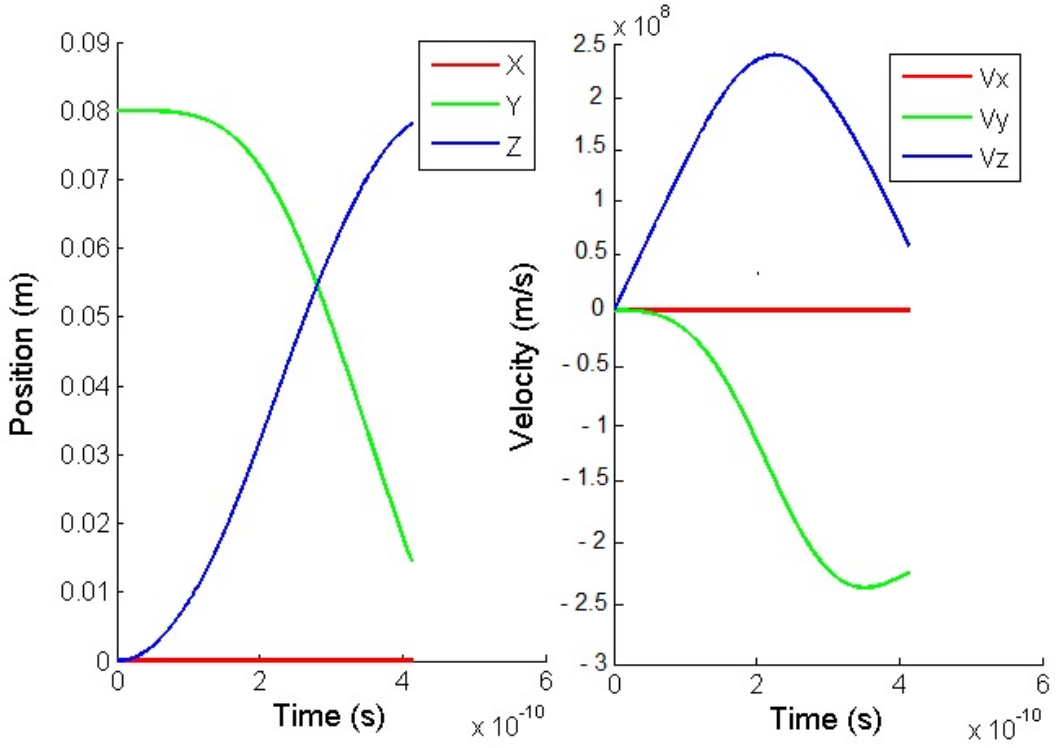

Figure 7-10: Position and Velocity components of an electron being tracked in a 2D 805 MHz pillbox cavity. 2D field values in polar coordinates of (r, θ) were used to perform the tracking while the path taken was plotted using 3D coordinates of (x, y, z). Similar to the 3D model, the electron was accelerated from one end of the cavity towards the opposing wall due to the presence of strong E field along the Z direction. Further acceleration in Y direction was achieved due to the magnetic field.

As explained previously in section 6.3.2, the tracker obtained axis symmetric field values in (r, z) coordinates using a 2D field profile generated in Comsol. This was then translated back into (x, y, z) coordinates after each step of calculation in order to provide a 3D visualisation of the path taken by the travelling electron.

In this section it was shown that both the 2D and 3D tracking algorithms were capable of calculating the position and velocity of the travelling electron using the relevant field profiles generated in Comsol. Both models yielded similar results which demonstrate the accuracy of the mathematical model used in each tracking algorithm. The technique introduced in section 6.3.3 would allow for a combination of two models to be used in order to reduce the computation costs

required to model cavities with surface defects being present. This would enable more complex models to be analysed without the need to sacrifice accuracy.

7.3.2 Effects of Surface Defects on Particle Trajectory

In this section the effects of surface defects on the behaviour of emitted electrons inside a cavity was analysed. Using the 805 MHz pillbox cavity, a series of models were created each consisting of a single surface defect. Figure 7-11 shows the schematic view of the defects modelled in this study with the variable used to model the geometry. The defect height, base length, angle with the cavity axis and effective height are represented by c, b, θ and h_e respectively.

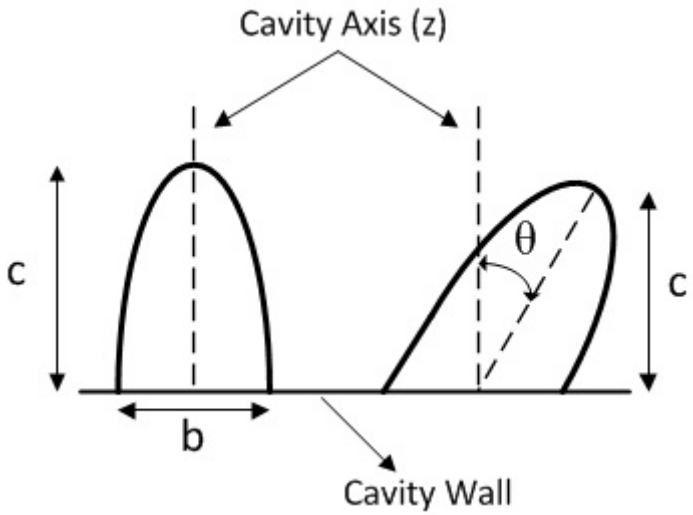

Figure 7-11: Schematic view of a surface defects, highlighting the essential parameters used to define the size and shape of the defect. This is of particular interest as the enhancement factor can be altered based on the shape of the defect. The angle between the cavity axis and the defects centreline is known as θ. Although not included in the theoretical equation defining enhancement factor ß, it is shown in this study that the bigger θ is, the lower ß gets.

Each defect was placed inside a nested tube in order to assist the meshing process and ensure uniform mesh propagation through the volume of the cavity. As shown previously in Chapter 6, the number of nested tubes used in the model was dictated by the size of the defect being modelled.

The velocity of the electron at the point of impact with the cavity wall may be influenced by the direction and strength of the force being applied to each electron at the emission site. This is directly related to the local field enhancement created due to the presence of the surface defect. The enhancement factor ß is defined by E_{tip}=ßE_{surf} and can be expressed [62] in terms of the geometry of the defect as:

$$\beta = \frac{(\frac{c}{r})}{\ln(2\frac{b}{r}) - 1} \tag{7-2}$$

where $r = {b^2}/{c}$. Therefor:

$$\beta = \frac{\frac{c^2}{b^2}}{\ln(2\frac{c}{b}) - 1} \tag{7-3}$$

The enhancement factor ß are used to define the degree at which a RF field is enhanced locally due to the presence of surface defects.

7.3.2.1 Field Enhancement and Aspect Ratio

This section presents the analysis of the effects of field enhancement on the behaviour of electrons and compares the results with equation (7-3). The impact velocity of an electron is related to the field enhancement factor generated by the surface defect at emission, the ß factor. Various models were created each containing a single surface defect of different shapes. An electron was released from the tip of the defect and the path of travel inside the cavity was plotted using the tracker program. The range of parameters used to construct the models is given in Table 7-7.

Table 7-7: Range of values used to construct the surface defect combinations used in this study. The defect height is represented by c while b and θ define the base length and angle the surface defect makes with the cavity axis respectively

c (µm)	b (µm)	θ (°)
50	50	0
100	100	15
300	200	30
500	400	45
700	600	60

Initially, the impact velocity of an electron was analysed when no defects were present. The location of the emission site at which the electron was released from was set to be the height at which the tip of a surface defect could have been based on the values given above in Table 7-7. The recorded impact velocities of each electron are shown below in Figure 7-12.

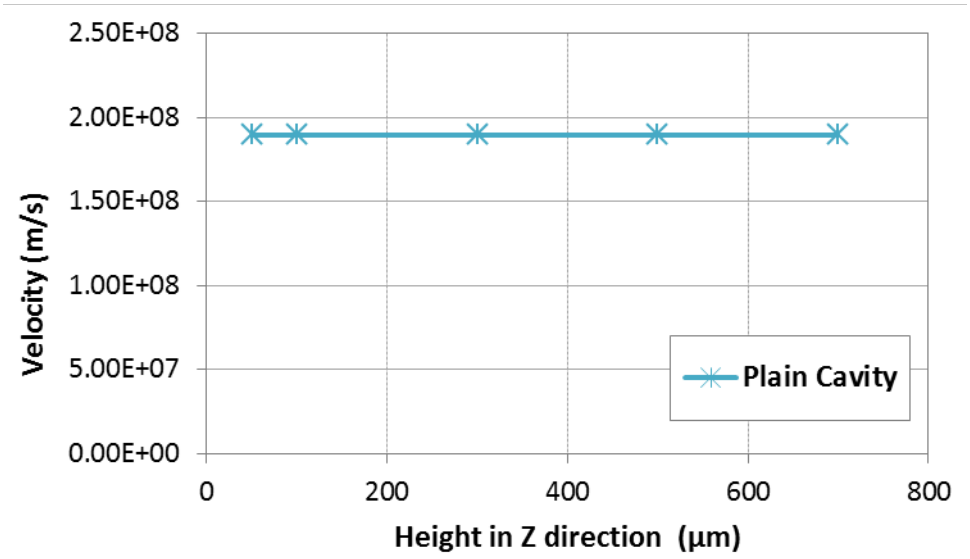

Figure 7-12: Impact velocities of electron from the surface of the cavity when there are no surface defects present. The chosen emission site corresponds to the height of surface defects used later in this study. This is used for comparison of data to evaluate the simulated field enhancement factor due to the presence of such defects. The height of the emission site is chosen from the values defined for parameter C and represents the location of a surface defect that could have been present in the model.

As expected, no major variation in the impact velocity was observed due to lack of localised field enhancements.

7.3.2.1.1 Fixed Base Length

Five model configurations were used to conduct the first stage of the analysis. The base length of the defect in all models was set to 600 µm, while the height of the defect ranged from 50 to 700 µm. This allowed for surface defects with different aspect ratios (c/b) to be created. Furthermore, the angle θ was ranged from 0 ˚ to 60˚ enabling specification of defects that are not perpendicular to the surface. The corresponding results showing impact velocity as a function of aspect ratio and angle θ are shown below in Figure 7-13.

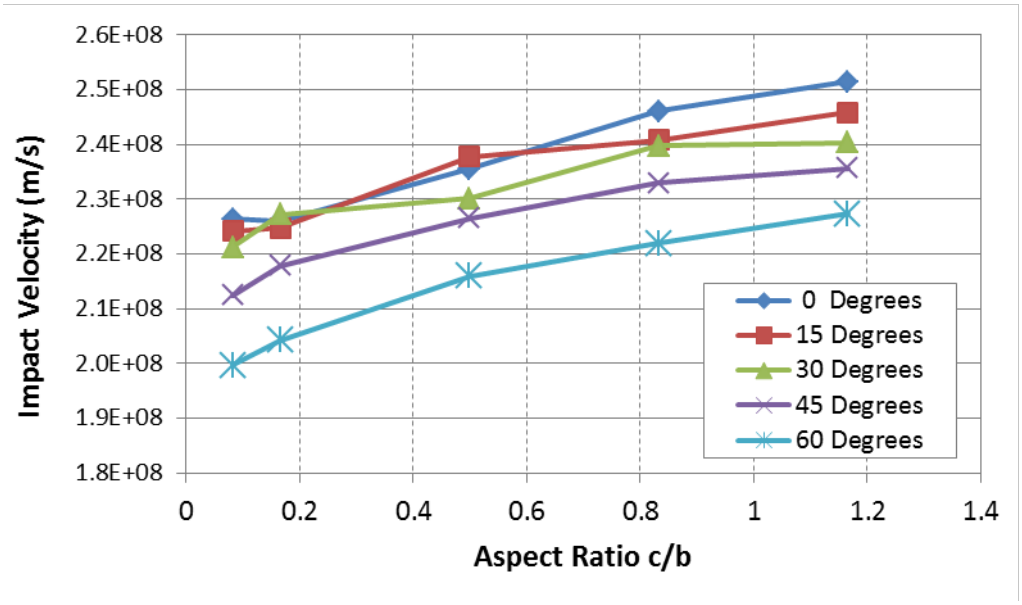

Figure 7-13: Impact velocities obtained for electrons emitted from the tip of various defects with a constant base length of 600 µm. The height of defects was chosen from the values given in Table 7-7 and five data sets were created by altering the angle θ.

A rise in impact velocity was observed as the aspect ratio (c/b) was increased. This corresponds to a higher ß value, demonstrating the influence of field enhancement on particle velocity. It is also evident that the effect of field

enhancement decreases as the value of θ is increased. This is due to the fact that the actual height of the defect is reduced, resulting in a lower localised field enhancement caused by the surface defect.

The theoretical value of the ß function for each surface defect can be calculated using equation (7-3). In order to demonstrate the direct relation between the ß value and the impact velocity of an emitted electron, one of the data sets shown in Figure 7-13 was used. All defects had a base length of 600 µm and angle θ of zero in common. By choosing the defect height values provided earlier, the desired aspect ratios were created. This is shown below in Figure 7-14 where the calculated enhancement factor is plotted alongside the recorded impact velocity of an electron emitted from the tip of the defect.

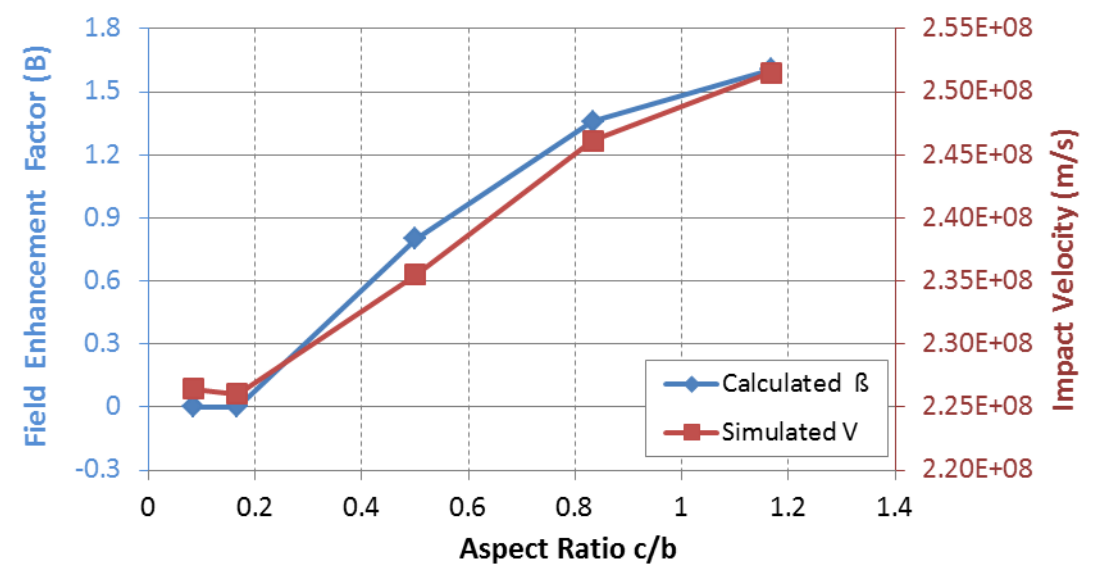

Figure 7-14: Theoretical ß values for defects with varying height and a fixed base length of 600 µm and angle θ of 0 ° (blue) recorded impact velocity for the same defects generated by the tracker program (red). It is possible to see a similar trend in both data based on the above findings. This suggests that the particle behaviour in particular the traveling velocity of an emitted electron is in direct relation to the initial energy boost received due to localised field enhancements by the surface defect.

A good agreement between the two sets of parameters is observed, indicating that the ß value directly influences the impact velocity by creating a localised field enhancement. This acts as an initial energy boost for the emitting electron.

7.3.2.1.2 Fixed Angle

A second set of models were created with changing both the height and base length of the surface defect while setting the angle θ to 0 °. The base length and height of the defects varied between 50 to 700 µm and 50 to 600 µm respectively. Figure 7-15 shows the recorded impact velocity of emitted electrons when released from the tip of each surface defect. These data sets would provide a different angle into the investigation of the link between aspect ratio and ß value.

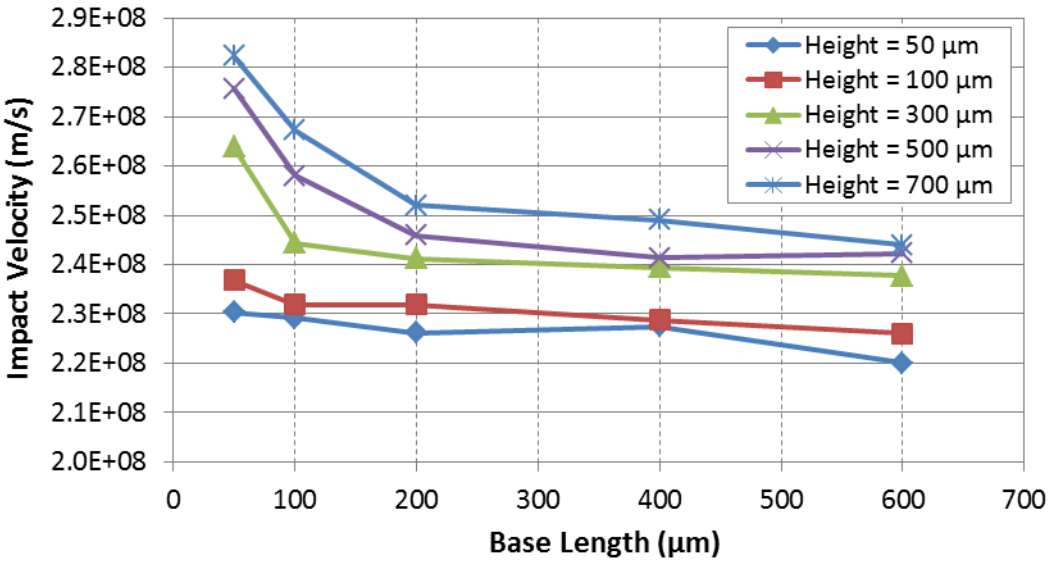

Figure 7-15: Impact velocities obtained for electrons emitted from the tip of a series of surface defects with a constant angle θ of zero degrees. The base length and the height range are from 0 to 600 µm and 50 to 700 µm respectively.

It was evident that an increase in the base length of the surface defect resulted in a reduction in the impact velocity of the travelling electron. This was due to the reduction in the aspect ratio c/b, making the localised field enhancement weaker.

However, the impact velocity of the electron became relatively constant after a certain aspect ratio was reached. This can be explained by the use of Figure 7-16.

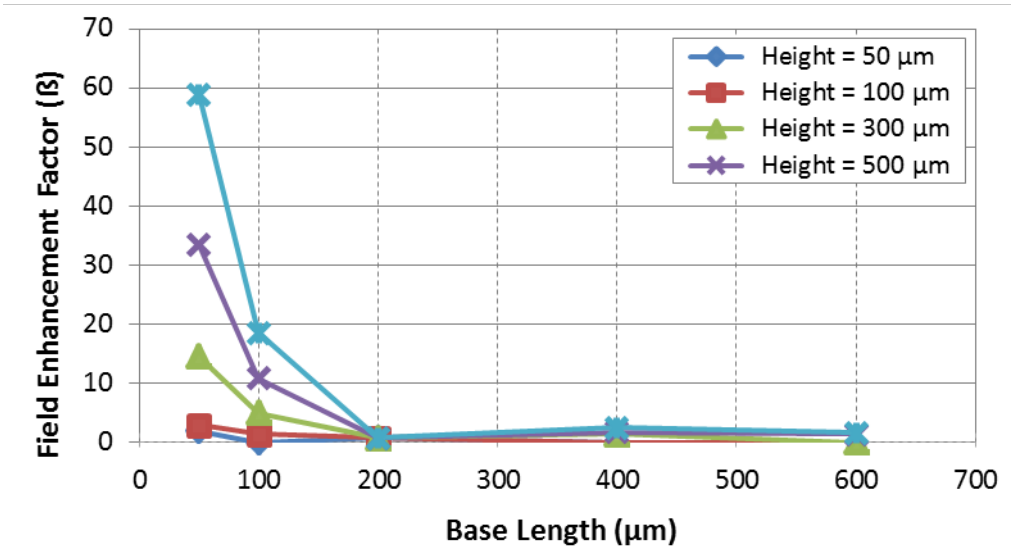

Figure 7-16: Enhancement factor ß calculated for a series of surface defects with an angle of 0 ° with the cavity axis and base length of 0 to 600 µm and height of 50 to 700 µm. The results are a further proof that localised field enhancements due to surface defects can alter the behaviour of emitted particles in particular their travelling velocity due to increased energy boost.

Figure 7-16 shows the ß values corresponding to the case presented in Figure 7-15. It is possible to see that field enhancement factor ß became negligible below certain aspect ratios. In the case of this study, such behaviour was observed for aspect ratios of below two. Similar to Figure 7-14, it was observed that the impact velocity followed a similar trend to the ß value obtained for each surface defect. This is a further indication of the relation between particle behaviour and localised field enhancements. Furthermore, this highlights the importance of surface uniformity discussed earlier in Chapter 5.

7.3.2.1.3 Fixed Height

The previous two data sets were gathered from a series of models with surface defects of fixed height of 700 µm. The base length ranged from 50 to 600 µm and

the angle θ from 0 to 60˚. Figure 7-17 shows the recorded impact velocities for an additional five data series used in this study.

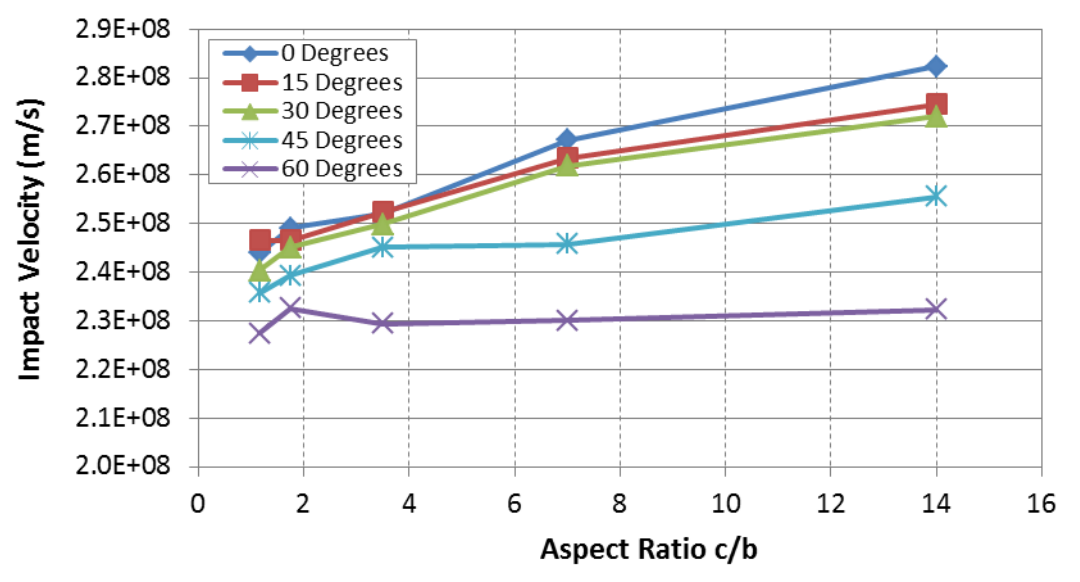

Figure 7-17: Recorded impact velocities of an emitted electron from surface defects of fixed height of 700 µm. The base length and angle θ ranged from 50 to 600 µm and 0 to 60 degrees respectively.

In all cases the impact velocity of the electron was reduced as the height of the defect was decreased. This is a further indication that a reduction in aspect ratio can influence the speed at which an electron is emitted from the surface by altering local field enhancements. A reduction in the impact velocity was also observed as the angle θ was increased. This was due to the fact that a defect with an angle tends to have a lower height which results in a lower aspect ratio.

7.3.2.2 Geometric Scale Study

As presented in Chapter 5, the quality of the surface finish achieved by some of the production techniques used in the fabrication of RF cavities was analysed through a series of measurements taken from button shaped samples. It was shown that the height of the surface defects being present across the samples ranged from several hundred nm down to a few nm.

FE modelling of the phenomena occurring simultaneously at vastly different scales is difficult for a number of practical reasons, including:

- Mesh generation methods
- Realistically manageable model size
- Numerical precision adopted by the specific FE package

As shown in Section 7.2.3, significant improvements were made in order to produce a correct FE mesh while accounting for features at geometric scale that differ by more than six orders of magnitude. However, Comsol, commonly with other FE packages, has a limit on how small the mesh elements of different features can be in a single model.

Such limits were reached when attempting to model surface defects corresponding to highly polished surfaces. Highly polished button samples have surface defects in the order of several nm. This implies feature sizes difference of more than nine orders of magnitude, which was found to be unmanageable in Comsol. Preceding studies in this chapter focused on the analysis of the effect of aspect ratio on field enhancement and impact velocity of emitting electrons. Here the aim is to examine whether these results could be extrapolated to the very small nm scale defects. As shown below in Table 7-8, three data sets were used to carry out the scaling down process. Each set contains a series of surface defects with similar aspect ratios but different sizes.

Table 7-8: Range of values chosen to construct the surface defects used in the scaling down process. The table shows that aspect ratios c/b for the defects are kept constant in all three sets while their overall size is reduced. This would enable for better comparisons between the results to be made.

Parameters	b = 300 µm				b = 30 µm				b = 3µm			
c (µm)	700	500	300	100	70	50	30	10	7	5	3	1
c/b Ratio	2.3	1.6	1	0.3	2.3	1.6	1	0.3	2.3	1.6	1	0.3

Although the size of each defect was reduced by a factor of ten in each category, their aspect ratios were kept constant. This has been colour coded for better visualisation. Figure 7-18 demonstrates the recorded impact velocities of emitted electrons from the tip of each defect given in Table 7-8.

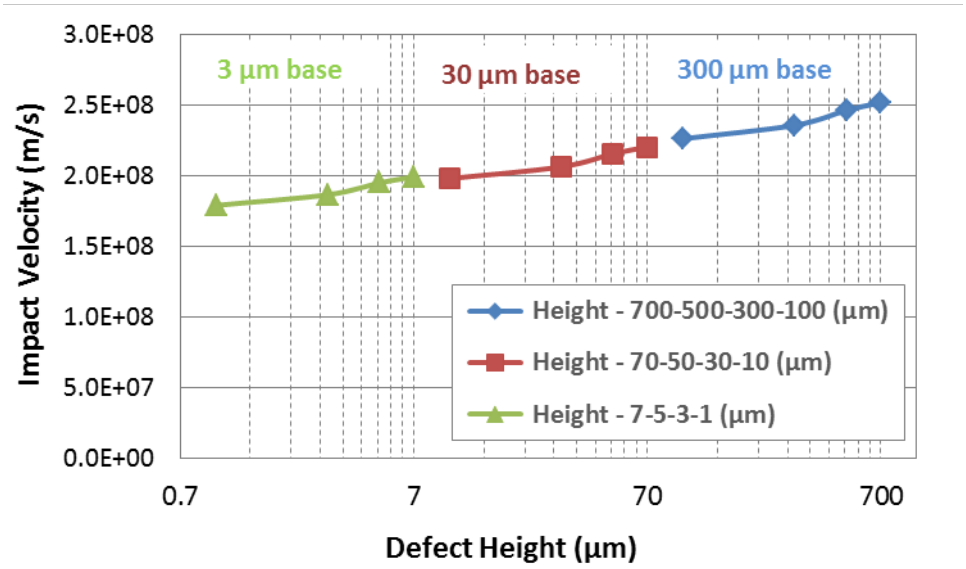

Figure 7-18: Plot showing the recorded impact velocity of emitted electrons for surface defects ranging from 700 µm in height to 1 µm with corresponding base length of 300 to 3 µm. The corresponding defect in each category is reduced is size by a factor of ten while keeping the aspect ratio constant.

In each category, the c/b ratio was lowered as the height of the defect was reduced. This resulted in smaller ß values being produced, reducing the impact velocity of the electron. However, the corresponding defects with similar c/b ratio in each category showed a reduction of the impact velocity as the size of the feature was reduced. This was due to the fact that although the ß value is the same,

the smaller defect influenced a reduced area in which the field was enhanced. The comparable aspect ratios used in each category ensured similarities in the behaviour of the emitted electrons. This is shown in Figure 7-18 where the impact velocity of the electron was reduced in a similar manner with the size of the defect.

The above findings can be used to extrapolate the impact velocity of defects down to nm scale features observed on the surface of button pieces. Four sets of graphs were created in order to investigate the impact velocity of an electron being emitted from the tip of defects in nm scale. The height and base length of the defects were reduced in size by a factor of ten and ranged from 0.7 to 0.1 μm while the base length was set to 0.3 μm. Figure 7-19 to Figure 7-22 show the relevant extrapolated values for the impact velocity based on the behaviour of emitted electrons observed around larger surface defects.

Extrapolations were made by drawing a best line of fit through the results for defects with similar aspect ratios. A power trend line was chosen as the most suitable line in comparison to other options such as a linear fit. This was due to the exponential nature of the impact velocity being investigated. A power line yields an accuracy of 99.36 % in comparison to 89.6 % reached by a linear line.

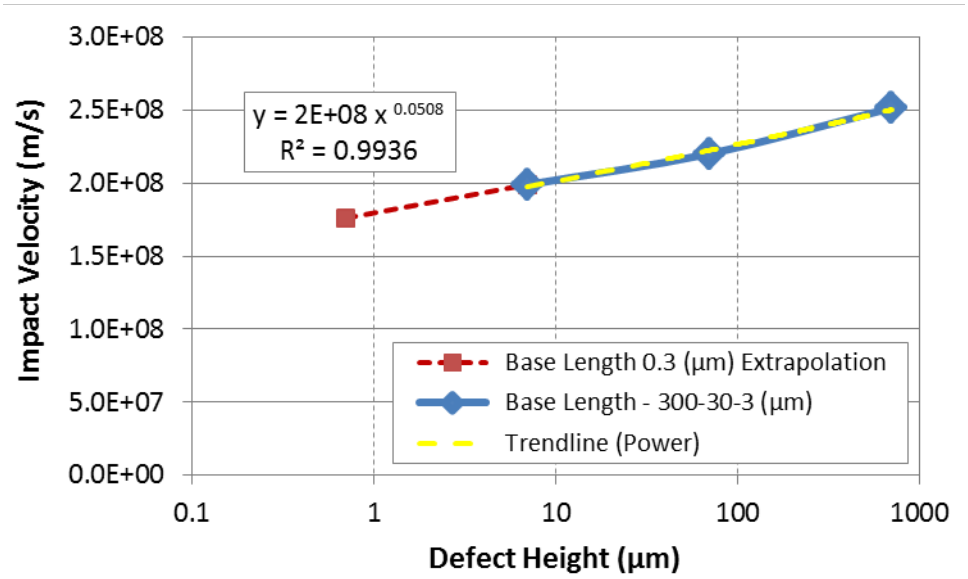

Figure 7-19: Plot showing the extrapolated impact velocity of an emitted electron from the tip of a surface defect with a height and base length of 0.7 µm and 0.3 µm respectively. Extrapolation was carried out using three additional surface defects each being larger in size by a factor of ten. The aspect ratio was kept constant at 2.3 for all defects. A power trend line was used with an accuracy of 99.36.

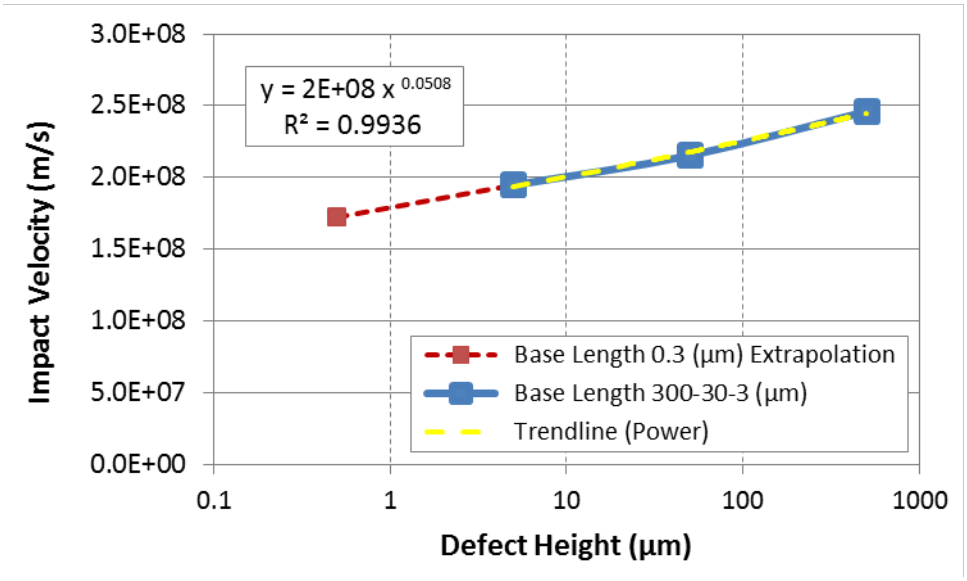

Figure 7-20: Plot showing the extrapolated impact velocity of an emitted electron from the tip of a surface defect with a height and base length of 0.5 µm and 0.3 µm respectively. Extrapolation was carried out using three additional surface defects each being larger in size by a factor of ten. The aspect ratio was kept constant at 1.6 for all defects. A power trend line was used with an accuracy of 99.36.

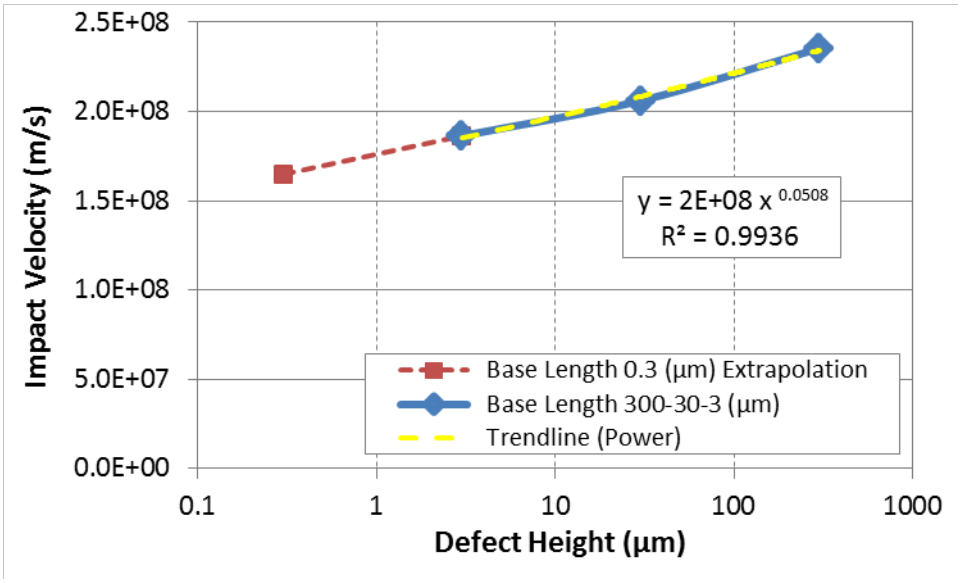

Figure 7-21: Plot showing the extrapolated impact velocity of an emitted electron from the tip of a surface defect with a height and base length of 0.3 µm and 0.3 µm respectively. Extrapolation was carried out using three additional surface defects each being larger in size by a factor of ten. The aspect ratio was kept constant at 1 for all defects. A power trend line was used with an accuracy of 99.36.

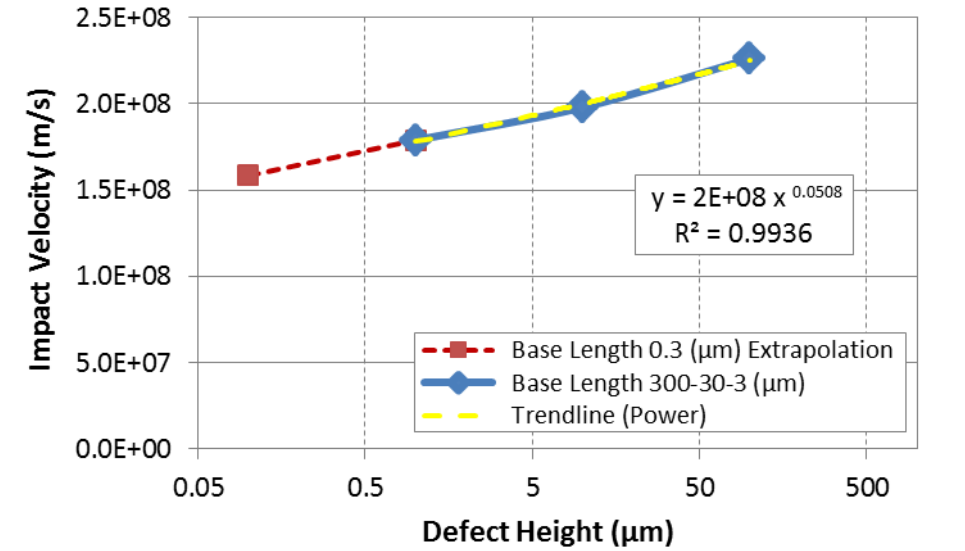

Figure 7-22: Plot showing the extrapolated impact velocity of an emitted electron from the tip of a surface defect with a height and base length of 0.1 µm and 0.3 µm respectively. Extrapolation was carried out using three additional surface defects each being larger in size by a factor of ten. The aspect ratio was kept constant at 0.3 for all defects. A power trend line was used with an accuracy of 99.36.

Although the aspect ratios of all surface defects were similar in each data set, the impact velocity of the electron was lowered as the size of the defect was reduced. This behaviour continued base on extrapolated results for surface defects in nm scale. The main reason behind such reduction in velocity is that although the

enhancement factors ß were the same, the size of the region in which the field was enhanced was smaller. This is due to a reduction in the overall size of the defect.

For better visualisation, the extrapolated impact velocity of emitted electrons from the tip of nm scale defects are plotted alongside current results in Figure 7-23. The nm scale defects modelled in this study were of similar range seen previously on the surface of the highly polished button samples. The above findings show that if aspect ratio is kept the same, a smaller surface defect results in a lower initial energy boost at the point of emission. This directly influences the impact velocity of the travelling electron, with little change in the overall behaviour of the electron.

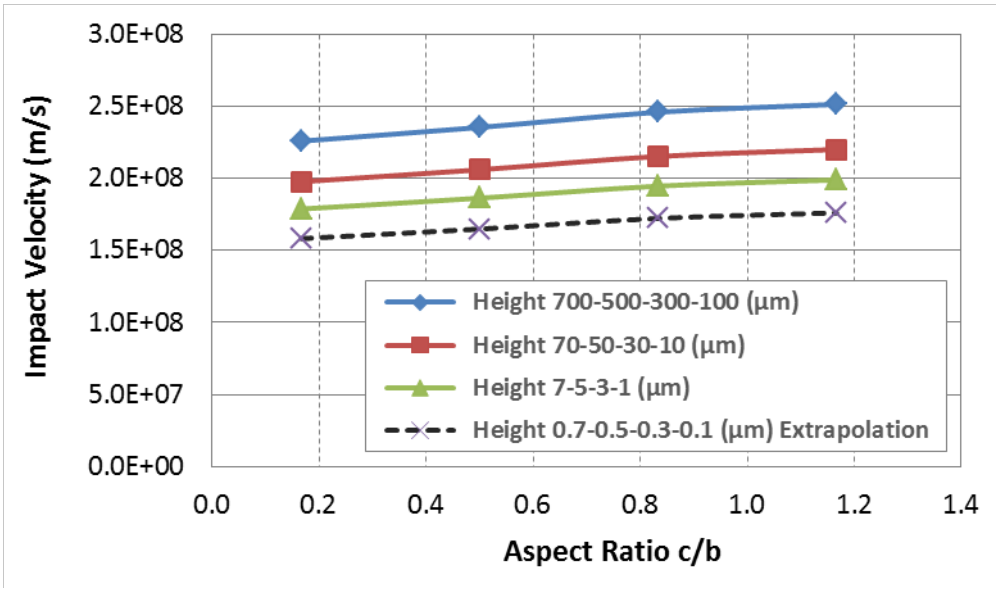

Figure 7-23: Plot showing the impact velocity of all four data sets. The extrapolated results for defects in nm scale show similar particle behaviour at the point of impact based on recorded impact velocity. This highlights the nature of field enhancement based on fixed aspect ratio. However, the strength of the initial energy boos is lowered as the size of the defect is reduced.

The main interest of this study was to investigate the effects of aspect ratio on field enhancement. It was possible to see similarities in the behaviour of the emitted electrons as the aspect ratio of the surface defects were kept constant between all data sets. The change in the overall size of the defect had only resulted in the reduction of the absolute velocity at the point of impact. Hence, the above

findings can then be used to validate the results obtained for larger surface defects shown previously in section 7.3.2.1.

7.3.2.3 Line Integral

The field enhancement factor ß determined by the aspect ratio of the surface defect, while the size of the enhanced field region is determined by the size of the defect. Such field amplifications can provide an initial energy boost at the emission sites. In order to asses this phenomenon, the change in E field for different defect sizes was analysed. As shown in Figure 7-24, measurements were taken along a line spanning between the tip of the defect and the opposite wall of the cavity.

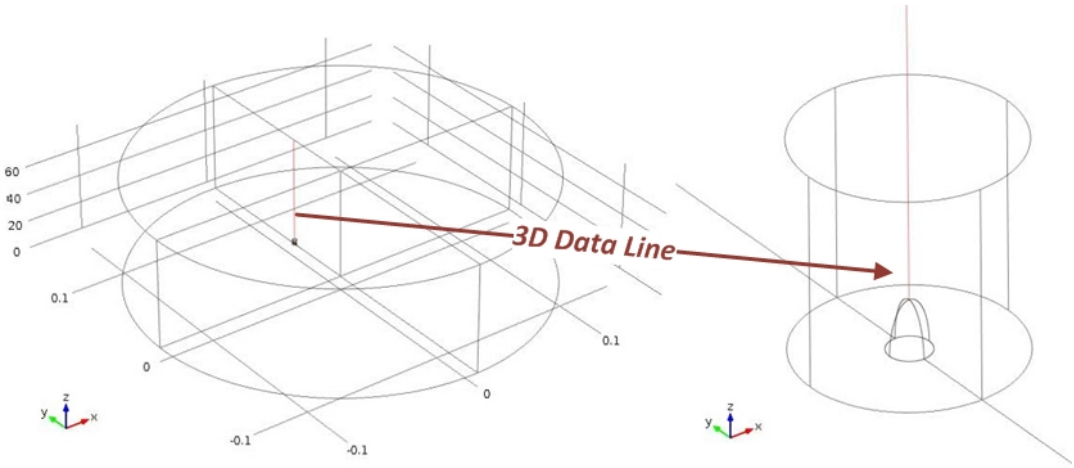

Figure 7-24: 3D data line connecting the tip of the defect and the cavity wall used by Comsol to extract the values of various field components

The electric field along this line was extracted for a series of defects as shown below in Figure 7-25 to Figure 7-28. The height of the defects ranged from 700 to 100 100 µm with a fixed base length of 600 µm. The angle θ was set to zero.

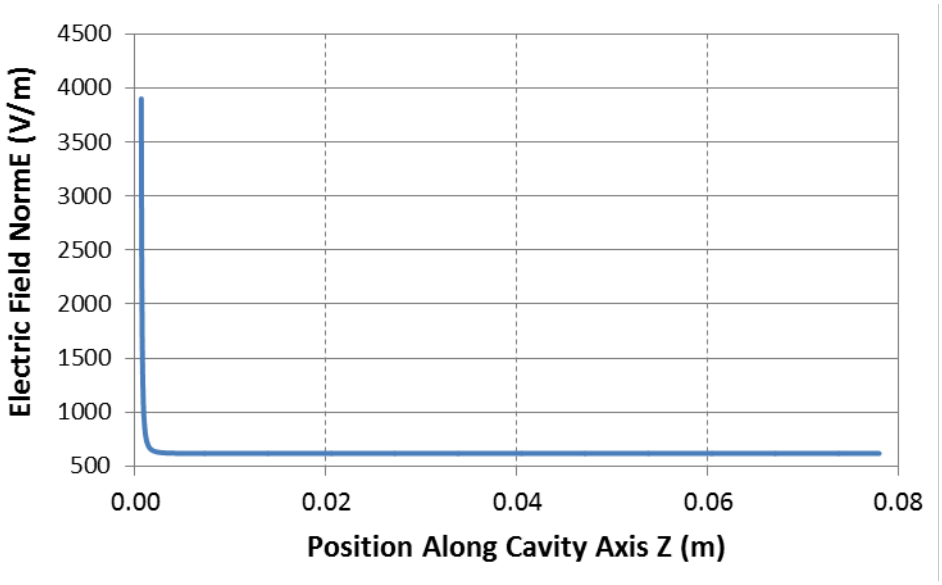

Figure 7-25: Plot showing the Electric field normE variation as a function of longitudinal axis Z along the 3D cut line for a defect with height of 700 µm and base of 600 µm

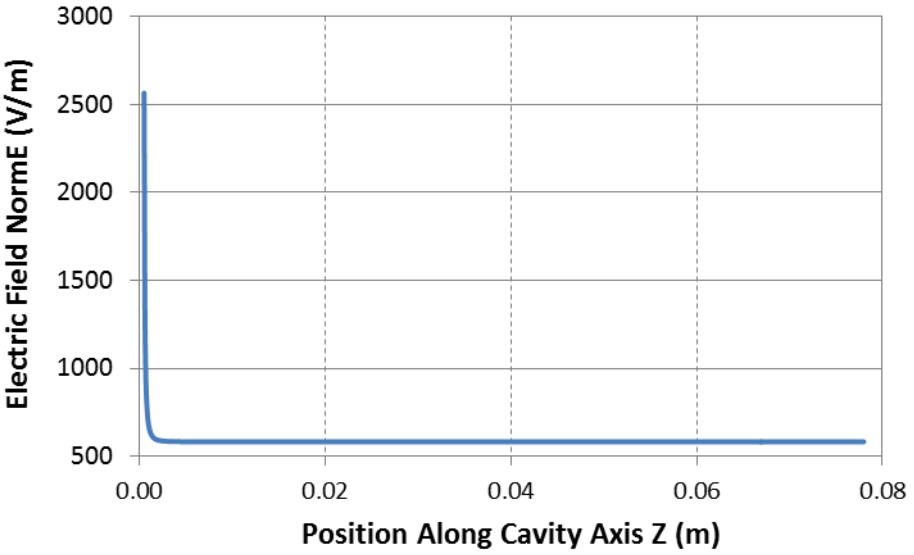

Figure 7-26: Plot showing the Electric field normE variation as a function of longitudinal axis Z along the 3D cut line for a defect with height of 500 µm and base of 600 µm

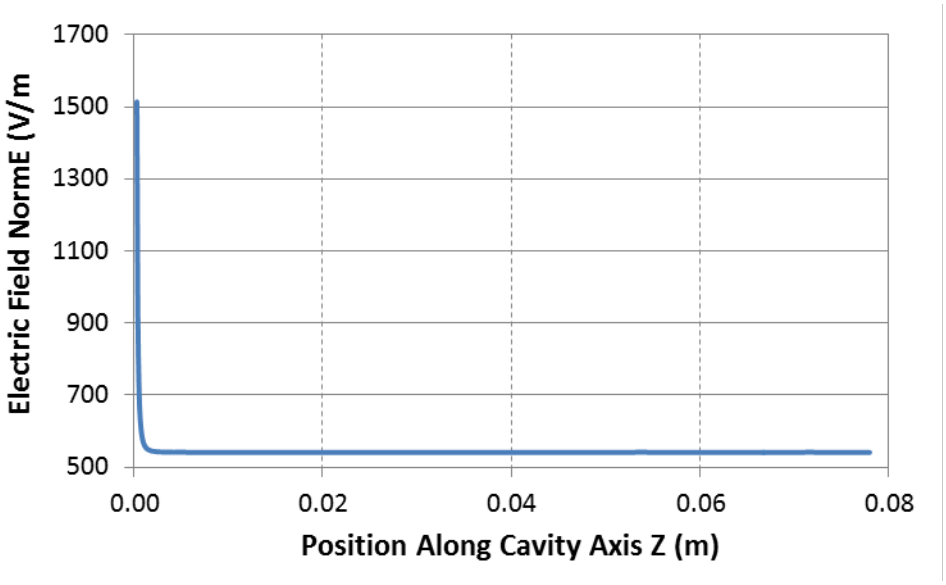

Figure 7-27: Plot showing the Electric field normE variation as a function of longitudinal axis Z along the 3D cut line for a defect with height of 300 µm and base of 600 µm

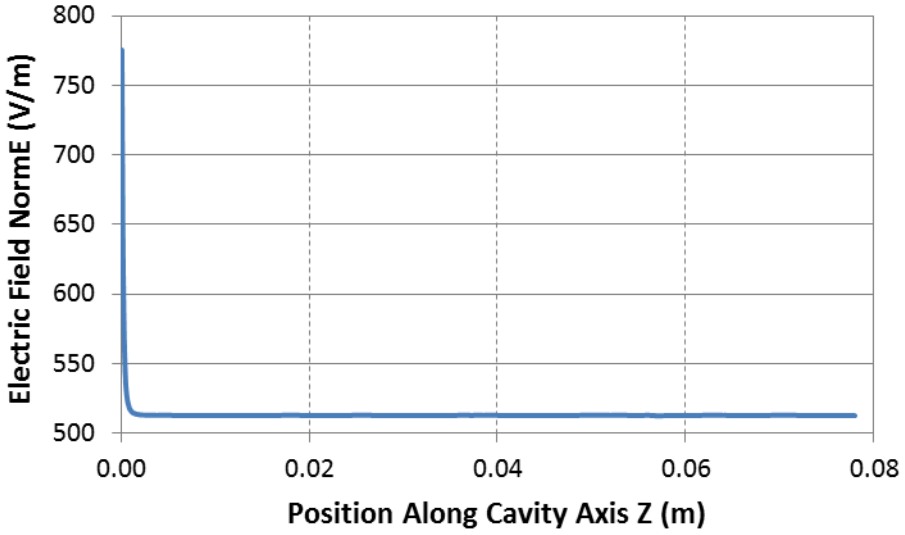

Figure 7-28: Plot showing the Electric field normE variation as a function of longitudinal axis Z along the 3D cut line for a defect with height of 100 µm and base of 600 µm

All four plots exhibited a common initial spike in the E field along the data line. This was due to the localised field enhancement and was responsible for the initial energy boost given to an emitting electron. It is possible to see that the strength of the field was directly related to the aspect ratio of the defect being present in the model. Naturally, no field alterations can be observed at distances farther away from the defect and a constant E field emerges.

The area under each plot represents the voltage generated along the data line and is a function of the size of the surface defect being modelled. The voltage is obtained through the line integration measurement and influences the behaviour of the emitted electron by providing an initial energy boost. The level of field enhancement is directly related to the size of the defect and it is greatest for a defect with a height of 700 µm and an aspect ratio of 2.3. This is shown in Figure 7-29 for defects of height of 100 to 700 µm and a base length of 600 µm.

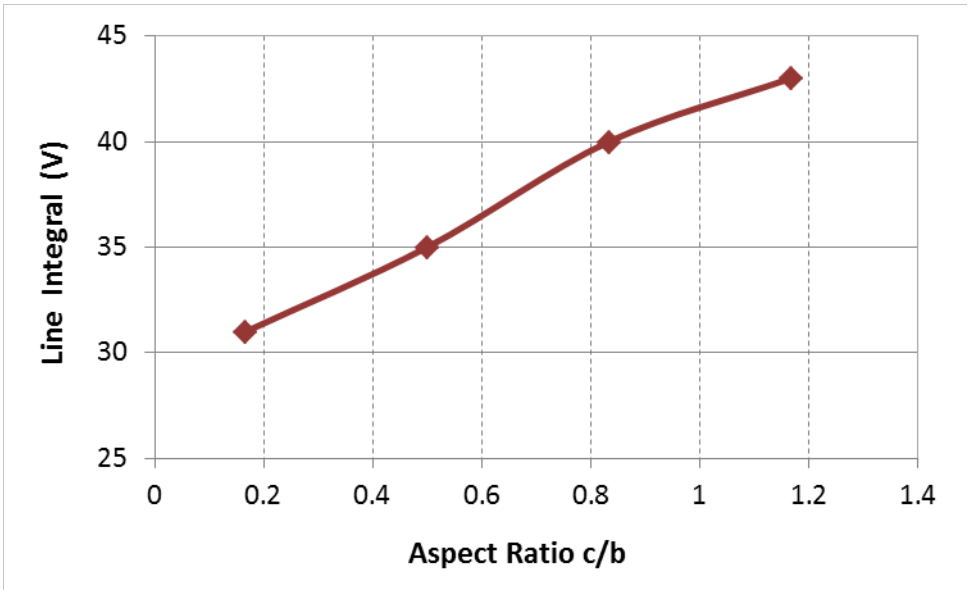

Figure 7-29: Plot showing the voltage obtained through the line integral of the electric field along the 3D cut line for defects with a height of 700, 500, 300 and 100 µm and a base of 600 µm

From the above plot it is evident that the applied voltage was directly proportionate to the size of the surface defect and the value of the c/b ratio. The measurements followed a trend in which the applied voltage was reduced as the height of the defect was lowered. This is in complete agreement with the results obtained previously in Section 7.3.2.2, where the effects of the surface defect are felt less prominently around smaller size surface defects.

7.4 Concluding Remarks

The effects of surface defects on charged carrier dynamics were investigated in this chapter. FEM modelling was used to generate the necessary field profiles inside an RF cavity and investigate changes made due to introduction of surface defects. Moreover, a particle tracker was developed in order to examine field enhancements and changes to particle behaviour in the vicinity of surface defects.

The optimum meshing process for each model was chosen by carrying out a mesh refinement study. A progressive step approach was utilised to mesh small features such as μm scale defects. 2D and 3D particle tracking algorithms were developed, allowing for a range of simulations to be carried out. The sensitivity of each algorithm to changing conditions was tested.

Correspondence between the calculated enhancement factor and simulated impact velocity of an electron was observed when emitted from the tip of the defect. It was shown that the aspect ratio c/b directly influenced the enhancement factory ß. Furthermore, the overall size of the defect defined the volume in which localised field enhancement was observed. A greater aspect ratio generated a higher field enhancement, resulting in a bigger impact velocity. However, the impact velocity of a smaller defect in comparison to a larger defect with a similar aspect ratio was lower.

The angle θ, between the defect and the cavity was found to be an important parameter, since it effectively reduced the aspect ratio of the defect and reduces the field enhancement factor.

Limitations of the available FE packages in dealing with effects at vastly different scales were identified and they severely limited the smallest size of modelled defects. In this case it would be necessary to simultaneously accommodate feature sizes ranging from few nanometres to a meter in length, but the numerical precision and the maximum manageable model complexity did not make that possible. Various detailed improvements in the model preparation and meshing led to simulations of defects as small as a few microns. Nevertheless, the simulations were able to show highly consistent trends in behaviour with decreasing defect size. This has led to a conclusion that results obtained at the scale ranging from a few microns to a few hundred microns may be safely extrapolated to the manometer scale of the defects measured in the experiments on button samples.

Chapter 8.

Conclusions and Suggestions for Future Work

8.1 Conclusions

Particle accelerators are used to force charged particles to higher energy levels. However, achievable accelerating gradients and efficiency can be limited due to the phenomenon of RF breakdown. In a short instance, much of the stored energy in the cavity is directed toward the walls. This causes irreversible damage to the quality of the cavity surface, causing loss of energy and heat dissipation.

Shortcomings in the fundamental understanding of key manufacturing processes have hindered production of RF cavities. In this research, various production techniques were investigated and their effects on the quality of the surface were quantified. The research was carried out in close collaboration with current MTA research programs and button test program. Two sets of surface treatment methods were analysed using various button test pieces. Furthermore, charge carrier dynamics were studied by developing simulation capabilities for particle tracking.

The first surface preparation method used in this research, employs electro polishing as the main technique. Prior to EP, the surface of the button undergoes two pre-treatment stages in order to remove surface damage and contaminations

introduced during fabrication. The surface is initially hand polished using sand paper followed by chemical etching using phosphoric acid. Although EP has been proven to be reliable method of surface treatment in the production of RF cavities, many factors can influence the reproducibility of the polishing results. It was shown in this research that the distance between the two electrodes, stability of the applied power, shape of the cathode, quality of the electrolyte and agitation of the mixture play an important role in the polishing process. Small alterations in each of these parameters can lead to changing the polishing qualities of the EP process. Hence, it is vital to design a robust polishing technique if reproducible surface finish characteristics are to be realised in the production of RF cavities.

The second surface preparation technique concentrates on electroplating as the main surface treatment technique. The importance of the subsurface in obtaining a desirable surface finish after EPL was highlighted. Hence, each button test piece initially underwent all stages of method one prior to EPL. This allowed for a smooth and defect free subsurface to be produced in order to increase the stability and uniformity of the copper layer being added.

In both approaches, the surface roughness of the button was quantified by using white light interferometer after each stage of the process. All test pieces showed extensive surface damage after fabrication. However, both processes were capable of achieving satisfactory quality where surface roughness is lowered and surface uniformity is improved. The investigations reveal the ability to produce a superior surface finish through EPL in comparison to EP. This opens new possibilities in the production of RF cavities by using surface treatment techniques other than the conventional EP.

Furthermore, the chemical composition of the button surface was analysed by taking XPS measurements. Due to equipment limitations, such measurements were only taken for buttons treated using method one. As expected, the surface of the untreated button was heavily contaminated and showed extensive oxide and carbon levels. Throughout the treatment procedure, both oxygen and carbon levels continued to be lowered. This indicated the gradual removal of the damaged layer and the exposing of the virgin copper. However, oxygen levels were increased once the button underwent the EP process. This was considered to be a result of the short exposure the button had with the atmosphere during removal from the EP bath. Warm de-ionised water wash may have also accelerated oxidisation.

Investigations also revealed the presence of additional phosphorus following the EP process. The source of such contamination is considered to be the phosphoric acid used in the electrolyte mixture. As shown in the previous DFT simulations, this can alter SEY of the copper by changing the energy band structure of the material. This is of particular concern as secondary emissions can be increased.

A series of FEM simulations were carried out in order to investigate charge carrier dynamics by analysing the change in electron behaviour due to presence of surface defects. A new particle tracking code was developed in Matlab, which allowed for tracking of a single electron inside a pillbox RF cavity. One of the major benefits of the proposed simulation method was the ability to perform tracking using a combination of 3D and 2D field solutions, in order to reduce the computational requirements to manageable levels. The observed surface properties of the buttons were used to allow for a realistic study to be carried out.

The limitations of existing FEM packages, including meshing methods and numerical precision, when dealing with feature sizes at vastly different scales in a single model, posed significant challenges. In this work the aim was to accommodate defect features of the order of few nanometres in a model size of the order of metres. Following detailed improvements in mesh generation that improved user control of the process, defects as small as a few microns were adequately modelled. The subsequent study of the electron emission behaviour for defects ranging from a few microns to several hundred microns revealed clear and consistent trends, which have led to a conclusion that the simulation results may be safely extrapolated to the nanometre scale.

In all models, a single ellipsoid shaped surface defect was used represent defects generating the local field enhancement. The shape and geometry of the defect was altered by changing the dimensions of the base width and height. Good agreement between enhancement factors obtained through theoretical calculations and the simulation models were observed.

The shape of the defect was also varied as a changing angle θ between the main axis of the feature and the surface normal. This has the effect of effectively reducing the aspect ratio of the feature by reducing its height, with a corresponding change in the field enhancement. This dependence was not adequately predicted by the theoretical calculations which showed disagreement with the simulation results. Therefore, a new parameter taking into account the effective height of a defect is needed to accurately predict local field enhancements.

The above findings show the importance of surface quality in altering field characteristics and charge carrier dynamics of an RF cavity. Each stage of cavity

production influences the mechanical structure and chemical mixture of the cavity surface. This influences the surface quality achieved and the operation of the RF cavity. By developing better means of production, it is possible to improve the stability and operation of RF cavities.

Additionally, surface defects alter the behaviour of field emitted electrons through local field enhancements. This increases impact energies and allows for more secondary emissions to occur. This increases the risk of structural failure due to heat generation and induced surface stress.

8.2 Recommendations for Future Work

The importance of the electrolyte and the mixture used are shown above. It is advisable to use alternative EP recipes and to make improvements on the current recipe used. Some of the suggestions can be as followed.

- Supressing excess oxygen formation by adding Polyethylene Glycol (PEG) in concentrations of 1000 ppm to lengthen the polishing plateau.
- Increasing surface uniformity by addition of citric acid to the current mixture in concentrations of 1000 ppm.

The MICE 201 MHz cavity was polished by the MTA collaboration by rotating the rotating the cavity around its axis while being half dipped inside an electrolyte bath. As a result, the cavity shell was exposed to the atmosphere while being rotated during polishing. It is highly desirable to create similar condition while performing EP on buttons in order to observe the changes made to the RF surface during production. A new polishing setup shown in Figure 8-1 can allow for two 180˚ out of phase buttons to be polished. The dual bobbing action would ensure

one button being exposed to the atmosphere while the other is immersed into the electrolyte bath. Steady voltage should be applied through two shaped cathodes.

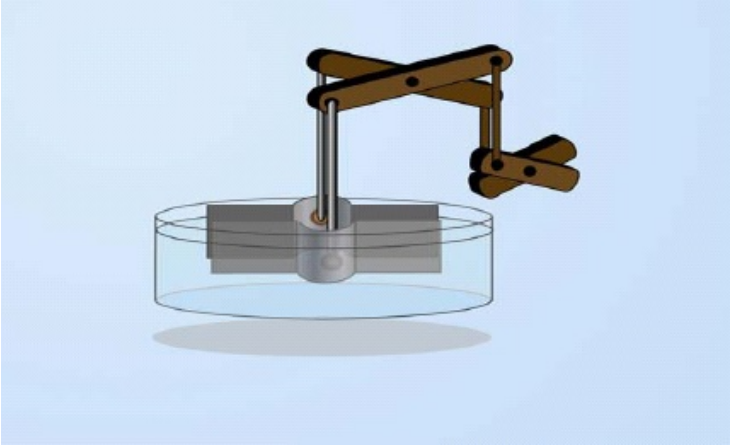

Figure 8-1: Suggestion for and improved EP setup to create similar condition used to polish the MICE 201 MHz cavity at Jlab

In this research the main goal was to investigate the fabrication and surface treatment methods that had been previously employed and are most relevant to the 201 MHz MICE copper cavity. In the future it is desirable to investigate button test pieces manufactured using other potentially relevant techniques such as:

- CNC machining (fabrication)
- Hydroforming (fabrication)
- Chemical mechanical polishing (surface treatment)
- Abrasive flow machining (surface treatment)

The tracking code developed by this research provides a great deal of flexibility, by allowing the addition of other physical properties as required. The operating environment of a RF cavity can be represented more realistically if parameters of an externally applied magnetic field are accounted for in the Lorentz force calculations.

While the work to date has focused on the effects of a single surface defect, realistic surface finish is characterised by a continuum of variation resulting in the particular surface roughness characteristic. Future work should involve modelling a surface region as a series of closely bunched surface defects of certain geometries and the resulting field enhancement characteristics. Incorporating such surface models in the overall simulation of the cavity would demand model size far in excess of those implemented in this work. The proposed approach of judiciously combining full 3D models with axisymmetric 2D models in a single simulation would be useful in keeping the overall mesh size manageably small, even if significantly more powerful computing resources are available.

The majority of breakdown studies concentrate on asperities protruding outwards from the cavity surface. However, polished surfaces may still exhibit surface damages of different nature even if the roughness parameters are low. As shown below in Figure 8-2, the surface of several button test pieces contained a series of holes after carrying out EP. It is vital to develop a theoretical representations and simulation procedure to quantify the enhancement factors posed by such deformities.

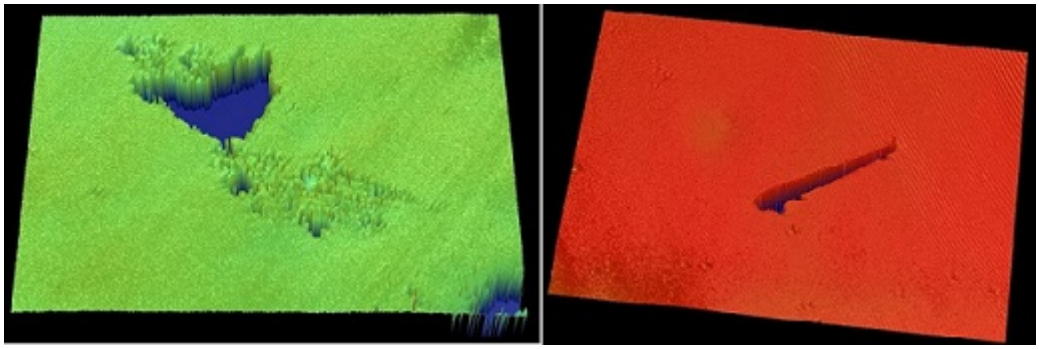

Figure 8-2: Surface defects found in electro plated samples D1, D2 at location [2-2] (left) [3-1] (right)

Due to lack of access and availability at the MTA, no button test pieces were tested inside the 805 MHz cavity. However, this is a vital stage of the experimental program if reliable suggestions are to be made for improving the production process. By characterising the surface after high power testing, it is possible to see which production technique is able to provide a more stable and resilient surface.

References

1. Crowley-Milling, M.C., *High-energy particle accelerators.* Reports on Progress in Physics 1983. **46**: p. 44.
2. Pozimski, J., *Accelerator Course IC/HEP*, 2007, Imperial College London: London. p. 165.
3. Wikipedia, in *Wikipedia* 2006-2014.
4. Wilson, E., *An Introduction to Particle Accelerators* 1st ed2001: Oxford University Press. 252.
5. Teng, L. *Particle Accelerators Outlook for the Twenty-First Century*. in *Second Asian Particle Accelerator Conference* 2001. Beijing.
6. Amaldi, U., *The Importance of Particle Accelerators* in *European Particle Accelerator Conference*2000: Vienna.
7. Bryant, P.J., *A Brief History and Review of Accelerators*, CERN: Geneva. p. 17.
8. Lee, S.Y., *Accelerator Physics*. 2nd ed2004: World Scientific Publishing Co. 575.
9. Nash, J., *Current and Future Developments in Accelerator Facilities* 2010, Imperial College London. p. 38.
10. Rohlf, J. *The Penderator: a one trick pony*. [cited 2014; Available from: http://www.quantumdiaries.org/2011/11/05/the-ponderator-a-one-trick-pony/.
11. Carter, R.G., *Acceleration technologies for charged particles: an introduction.* Contemporary Physics, 2011. **52**(1): p. 15-41.
12. Steere, A.R., *A TIMESLINE OF MAJOR PARTICLE ACCELERATORS* in *Physics and Astronomy*2005, Michigan State University: Michigan. p. 75.
13. Pagani, C. and A.C. Mueller, *High Power Accelerators*, 2002, University & Instituto Nazionale Di Fisica Nucleare Milano & Institut National De Physique Nucleaire Et De Physuque Des Particules
14. Wu Chao, A. and M. Tigner, *Handbook of Accelerator Physics and Engineering*2006: World Scientific.
15. *Your Dictionary - Cyclotron Images* 2006 [cited 2012 02-04]; Available from: http://images.yourdictionary.com/cyclotron.
16. *Particle Accelerators and Detectors*. [cited 2012 02/04]; Available from: http://universe-review.ca/R15-20-accelerators.htm.
17. *Neutrino Odyssey*. Interations.org [cited 2012 05-09]; Available from: http://www.interactions.org/pdf/neutrino_pamphlet.pdf.
18. Arns, R.G., *Detecting the Neutrino.* Physics in Perspective 2001. **3**(3): p. 21.
19. Pontekorvo, B., *NEUTRINO EXPERIMENTS AND THE QUESTION OF LEPTON CHARGE CONSERVATION.* Journal Name: Zh. Eksp. Teor. Fiz., 53: 1717-25(Nov. 1967).; Other Information: Orig. Receipt Date: 31-DEC-68, 1967: p. Medium: X.

20. Geer, S., *Neutrino beams from muon storage rings: Characteristics and physics potential.* Physical Review D, 1998. **57**(11): p. 6989-6997.
21. MICE Collaboration, *MICE Proposal* 2003, MICE Collaboration. p. 135.
22. *An international design study of a neutrino factory*. 2012 [cited 2012 Available from: https://www.ids-nf.org/wiki/FrontPage.
23. Berg, J.S., et al., *The International Design Study for the Neutrino Factory*, in *ICFA Beam Dynamics Newsletter* 2011. p. 18.
24. Berg, J.S. and I.S.S.A.W. Group, *Accelerator Design Concept for Future Neutrino Facilities*, 2009.
25. UKNF, C. *UK Neutrino Factory*. 2012 [cited 2012 Available from: http://hepunx.rl.ac.uk/uknf/.
26. Grubler, P., *Ionisation cooling for a Neutrino Factory* in *CERN PS*2001, CERN Geneva p. 102.
27. Edgecock, R., *UK Neutrino Factory Annual Report 2003*, 2004, MICE Collaboration. p. 23.
28. Mohl, D., *Beam Cooling: Past, Present and Future* in *Beam Cooling and Related Topics Workshop*, E.O.f.N. Research, Editor 2001, Cern: Geneva p. 15.
29. Drumm, P., *MICE: The International Muon Ionisation Cooling Experiment*, CCLRC Rutherford Appleton Laboratory Dicot. p. 4.
30. Kaplan, D.M., *Muon Cooling and Future Muon Facilities.* 2006: p. 4.
31. Ozaki, S., R. Palmer, and M. Zisman, *2nd Feasibility Study of a Muon Storage Ring nu Factory (Invited)*, in *19th IEEE Particle Accelerator Conference*2001: Chicago, Illinois. p. p.732-736.
32. Kaplan, D.M. and K. Long. *MICE: The International Muon Ionisation Cooling Experiment*. in *XXIII International Symposium on Lepton and Photon Interactions at High Energy*. 2007. Daegu.
33. Drumm, P., *MICE: The International Muon Ionisation Cooling Experiment*, 2005, CCLRC Rutherford Appleton Laboratory Dicot. p. 4.
34. MICE Collaboration. *MICE Technical Reference* [cited 2006-2012; Available from: http://www.mice.iit.edu/.
35. Li, D., *201 MHz NCRF: Studies and Plans*, 2005, Lawrence Berkeley National Laboratory p. 24.
36. Li, D., et al., *201 MHz Cavity R&D for MUCOOL and MICE*, 2006, Lawrence Berkeley National Laboratory California. p. 4.
37. Li, D. *RF Systems for Muon Cooling and Project X Front-End*. 2011 [cited 2012 05-09]; 23].
38. Collaboration, M. *Internation MUON Ionisation Cooling Experiment Web Page* 2012 [cited 2006-2012; Available from: http://mice.iit.edu/.
39. Johnstone, C., A. Bross, and I. Rakhno. *MUCOOL Test Area at Fermilab* in *Particle Accelerator Conference* 2005. Knoxville, Tennessee.
40. Norem, J., et al. *The RF Experimental Program in the Fermilab MUCOOL Test Area*. in *Particle Accelerator Conference* 2005. Knoxville, Tennessee.
41. Torun, Y., et al. *The MUCOOL Test Area and RF Program* in *IPAC 10*. 2010. Kyoto, Japan
42. Huang, D., et al. *RF STUDIES AT FERMILAB MUCOOL TEST AREA*. in *PAC09* 2009. Vancouver, BC, Canada: IEEE.

43. Li, D., et al. *RF TESTS OF AN 805 MHZ PILLBOX CAVITY AT LAB G OF FERMILAB*. in *Particle Accelerator Conference*. 2003. Portland, Oregon IEEE.
44. Norem, J., et al. *Recent RF results from the MuCool Test Area*. in *Particle Accelerator Conference, 2007. PAC. IEEE*. 2007.
45. Huang, D., et al., *805 MHz cavity button test - Cavity material study at MTA, FNAL*, 2008, Fermilab. p. 18.
46. Knobloch, J., *Advanced Thermometry Studies of Superconducting Radio Frequency Cavities*, 1997, Cornell University. p. 285.
47. Norem, J., Z. Insepov, and I. Konkashbaev, *Triggers for RF breakdown.* Nuclear Instruments and Methods in Physics Research Section A: Accelerators, Spectrometers, Detectors and Associated Equipment, 2005. **537**(3): p. 510-520.
48. Insepov, Z., et al., *Modeling rf breakdown arcs.* Cornell University Library 2011(4).
49. Dolgashev, V.A., et al. *RF BREAKDOWN IN NORMAL CONDUCTING SINGLE-CELL STRUCTURES*. in *Particle Accelerator Conference* 2005. Knoxville.
50. Padamsee, H.S., J. Knobloch, and T. Hays, *Rf Superconductivity for Accelerators*1998: John Wiley & Sons, Incorporated.
51. Norem, J., et al., *Dark current, breakdown, and magnetic field effects in a multicell, 805 MHz cavity.* PHYSICAL REVIEW SPECIAL TOPICS - ACCELERATORS AND BEAMS, 2003. **6**: p. 21.
52. Wang, J.W., *RF PROPERTIES OF PERIODIC ACCELERATING STRUCTURES FOR LINEAR COLLIDERS*, in *Stanford Linear Accelerator Center*1989, Stanford University. p. 155.
53. Stratakis, D. and C. Juan. *ENHANCEMENT OF RF BREAKDOWN THRESHOLD OF MICROWAVE CAVITIES BY MAGNETIC INSULATION*. in *Particle Accelerator Conference* 2011. New York.
54. Fowler, R.H. and L. Nordheim, *Electron Emission in Intense Electric Fields.* The Royal Society A, 1928: p. 173-181.
55. Kovermann, W., *COMPARATIVE STUDIES OF HIGH-GRADIENT RF AND DC BREAKDOWNS*, in *Faculty of Mathematics, computer science and science*2010, Aachen University. p. 148.
56. Leoew, G.A. and J.W. Wang, *FIELD EMISSION AND RF BREAKDOWN IN COPPER LINAC STRUCTURES.* Particle Accelerators 1990. **30**: p. 225-230.
57. Norem, J., A. Hassanein, and I. Konkashbaev. *MECHANISMS LIMITING HIGH GRADIENT RF CAVITIES*. in *Particle Accelerator Conference* 2003. Portland: IEEE.
58. Palmer, R.B., et al., *RF breakdown with external magnetic fields in 201 and 805 MHz cavities.* Physical Review Special Topics - Accelerators and Beams, 2009. **12**(3): p. 031002.
59. Norem, J., et al. *THE INTERACTIONS OF SURFACE DAMAGE AND RF CAVITY OPERATION*. in *EPAC* 2006. Edingburgh
60. Norem, J., *A tensile stress model of vacuum breakdown: linacs and light switches.* American Physical Society 2008 p. 7.

61. Stratakis, D., J.C. Gallardo, and R.B. Palmer, *Effects of external magnetic fields on the operation of high-gradient accelerating structures.* Nuclear Instruments and Methods in Physics Research Section A: Accelerators, Spectrometers, Detectors and Associated Equipment, 2010. **620**(2–3): p. 147-154.
62. Stratakis, D., J. Gallardo, and R. Palmer, *Effects of External Magnetic Fields on the operation of an RF Cavity*, 2009, Fermi National Lab RF Workshop III. p. 17.
63. Eyring, C.F., S.S. Mackeown, and R.A. Millikan, *Fields Currents from Points.* Physical Review, 1928. **31**(5): p. 900-909.
64. Kilpatrick, W.D., *Criterion for Vacuum Sparking Designed to Include Both rf and dc* American Institute of Physics 1957. **28**(10): p. 824-826.
65. Wangler, T.P., *RF Linear Accelerators*. Vol. 2nd completely revised and enlarged edition. 2008, Weinheim: Wiley-VCH.
66. Hassanein, A., et al., *Effects of surface damage on rf cavity operation.* Physical Review Special Topics - Accelerators and Beams, 2006. **9**(6): p. 062001.
67. Jameson, R.A., *RF Breakdown Limits* NATO ASI Series B, 1988. **178**: p. 497-507.
68. Geng, R.L. *Multipacting simulations for superconducting cavities and RF coupler waveguides*. in *Particle Accelerator Conference, 2003. PAC 2003. Proceedings of the*. 2003.
69. Padamsee, H., J. Knobloch, and T. Hays, *RF superconductivity for accelerators*2008: Wiley-VCH.
70. University, C. *SRF cavities A Primer Two*. 2013 [cited 2013; Available from: http://www.lepp.cornell.edu/Research/AP/SRF/SrfCavitiesAPrimerTwo.html.
71. Lin, Y. and D.C. Joy, *A new examination of secondary electron yield data.* Surface and Interface Analysis, 2005. **37**(11): p. 895-900.
72. Kishek, R.A., et al., *Multipactor discharge on metals and dielectrics: Historical review and recent theories.* Physics of Plasma, 1998. **5**(5): p. 2120-21-26.
73. Scholtz, J.J., D. Dijkkamp, and R.W.A. Schmits, *Secondary Electron Emission Properties* Philips Journal of Research 1996. **50**: p. 375-389.
74. Baglin, V., et al. *The secondary electron yield of technical materials and its variation with surface treatments*. in *EPAC* 2000. Vienna, Austria
75. Le Pimpec, F., et al., *TiN and TiZrV Thin Film as a Remedy Against Electron Cloud* 2005, SLAC. p. 24.
76. Porch, D., et al., *Measurement of Multipacting Currents of Metal Surfaces in RF Fields*, in *IEEE Particle Accelerator Conference* 1996, IEEE. p. 1776-1778.
77. Hilleret, N., C. Scheuerlein, and M. Taborelli, *The secondary-electron yield of air-exposed metal surfaces.* Applied Physics A, 2003. **76**(7): p. 1085-1091.
78. Accelrys. *DMOL3*. 2011; Available from: http://accelrys.com/products/datasheets/dmol3.pdf.

79. Seviour, B., *Density Functional Theory Simulations for SEY Analysis* 2004, Lancaster University.
80. Mahalingam, S., S.A. Veitzer, and P.H. Stoltz. *High-gradient RF box cavity breakdown simulations using 3-D particle tracking code VORPAL*. in *Power Modulator and High Voltage Conference (IPMHVC), 2010 IEEE International*. 2010.
81. Wang, J.W. and G.A. Loew. *Field emission and RF breakdown in high gradient room temperature linac structures* in *Joint CERN-US-Japan Accelerator School: Course on Frontiers of Accelerator Technology: RF Engineering for Particle Accelerators*. 1996. Tsukuba, Japan
82. Norem, J., et al. *The Interactions of Surface Damage on RF Cavity Operation*. in *EPAC*. 2006. Edinburgh, Scotland.
83. Moretti, A., et al., *Effects of high solenoidal magnetic fields on rf accelerating cavities.* Physical Review Special Topics - Accelerators and Beams, 2005. **8**(7): p. 072001.
84. Dobert, S., et al. *High Gradient Performance of NLC/GLC X-Band Accelerating Structures*. in *Particle Accelerator Conference, 2005. PAC 2005. Proceedings of the*. 2005.
85. Jana, M.R., et al., *Investigation of Breakdown Induced Surface Damage on 805 MHz Pillbox Cavity Interior Surfaces* in *North American Particle Accelerator Conference* 2013, PAC13: Pasadena, CA, USA. p. 1007-1009.
86. Stratakis, D., J. Gallardo, and R. Palmer. *RF Breakdown in Magnetic Fields: Previous Work, Recent Theory, and Future Plans*. in *AIP Conference Proceedings*. 2009. Chicago, Illinois: American Institute of Physics
87. DeMello, A., *MICE RF Cavity Mechanical Design and Analysis*, 2008, Lawrence Berkeley National Lab.
88. Smiths Metal Centres Ltd. *Material Guide* 2007 [cited 2007; Available from: http://www.smithmetal.com/.
89. Palmieri, V. *Fundamentals of Electrochemistry - The electrolytic Polishing of Metals: Application to Copper and Niobium* in *11th Workshop on RF Superconductivity*. 2003. Lübeck-Travemünder, Germany.
90. Landolt, D., *Fundamental aspects of electropolishing.* Electrochimica Acta, 1987. **32**(1): p. 1-11.
91. *Electropolishing - A User's Guid to Applications, Quality Standards and Specifications* 2003, Delstar Metal Finishing INC. . p. 30.
92. Chandra, A., *On the Mechanism of Niobium Electropolishing*, in *Materials Science and Engineering*2012, Ohio State University. p. 132.
93. Lilje, L., et al., *Improved surface treatment of the superconducting TESLA cavities.* Nuclear Instruments and Methods in Physics Research Section A: Accelerators, Spectrometers, Detectors and Associated Equipment, 2004. **516**(2–3): p. 213-227.
94. Schulz, E., et al., *ENGINEERING SOLUTIONS FOR THE ELECTRO-POLISHING OF MULTI-CELL SUPERCONDUCTING ACCELERATOR STRUCTURES*, in *10th Workshop on RF Superconductivity*2001: Tsukuba, Japan. p. 4.

95. Stables, M. *UK Neutrino Factory - RF Surface Processing*. 2008 [cited 2010; Available from: http://hepunx.rl.ac.uk/uknf/rf/Project%20Background%20and%20Aims/.
96. Stables, M. and R. Seviour, *Personal Communication* 2008: Lancaster University
97. Seviour, R., M. Aslaninejad, and J. Pozimski, *Personal Communication* 2008-2011.
98. Rimmer, R., A. Bross, and S. Virostek, *Personal Communication* 2008.
99. PAUNOVIC, M. and M. SCHLESINGER, *FUNDAMENTALS OF ELECTROCHEMICAL DEPOSITION*. 2nd ed. The Electrochemical Society Series 2006: JOHN WILEY & SONS. 374.
100. Poyner, J., *Electroplating* 1987: Argus Books
101. Schlesinger, M. and M. PAUNOVIC, *Modern Electroplating* 5th ed. The Electrochemical Society Series2010: John Wiley and Sons 730.
102. Gadelmawla, E.S., et al., *Roughness parameters.* Journal of Materials Processing Technology, 2002. **123**(1): p. 133-145.
103. Teague, E.C., et al., *Three-dimensional stylus profilometry.* Wear, 1982. **83**(1): p. 1-12.
104. Poon, C.Y. and B. Bhushan, *Comparison of surface roughness measurements by stylus profiler, AFM and non-contact optical profiler.* Wear, 1995. **190**(1): p. 76-88.
105. *NT1100 Data Sheet*. 2015; Available from: http://www.veeco.com/.
106. *DSI Materials Science Laboratory* 2012 [cited 2012; XPS Equipments]. Available from: https://fas.dsi.a-star.edu.sg/equipments/xps_10.aspx.
107. Brundle, C.R. and A.D. Baker, *Electron Spectroscopy: Theory, Techniques and Applications* Vol. 2. 1978: Academic Press. 80.
108. Watts, J.F. and J. Wolstenholme, *An Introduction to Surface Analysis by XPS and AES*2003: John Wiley & Sons. 225.
109. Stables, M. and R. Seviour, *Results of Surface characterisation and Preparation* 2008, Lancaster University. p. 5.
110. Bowfield, A., P. Unsworth, and P. Weightman, *Personal Communication* 2009: Liverpool University
111. Young, L. and J. Billen. *THE PARTICLE TRACKING CODE PARMELA*. in *PAC* 2003. Portland IEEE.
112. Palmer, R., R.C. Fernow, and J. Gallardo, *Cavel Tracking in Open Cavities*, 2008, MICE
113. Fagan, J., *Finite Element Analysis: Theory and Practice*1992: Longman Scientific & Technical.
114. Pryor, R.W., *Multiphysics Modeling Using COMSOL?: A First Principles Approach*2009: Jones & Bartlett Learning.
115. Comsol, *Comsol 4.0a User Guide* C. Multi-Physics, Editor 2010.
116. Comsol, *Comsol 4.0a RF User Guide* C. Multi-Physics, Editor 2010.
117. Guru, B.S. and H.R. Hiziroglu, *Electromagnetic Field Theory fundamentals* Vol. 1. 2004, New York Cambridge University Press 699.
118. Rosenzweig, J.B., *Fundamentals of Beam Physics* 2003, New York: Oxford University Press.

119. Caspers, F., B. Salvant, and G. Kotzian, *Juas RF Course 2010*, 2010, CERN. p. 178.
120. Adam, S., P. Arbenz, and R. Geus, *Eigenvalue solvers for electromagnetic fields in cavities*1997: Citeseer.
121. Alsharoa, M., *Design of Gridded-Tube Structures for the 805 MHz RF Cavity*, Illinois Institute of Technology. p. 17.
122. Reiser, M., *Theory and Design of Charged Particle Beams*. Vol. 2. 2008: Wiley-VCH. 677.
123. Serway, R.A. and J.W. Jewett, *Physics for Scientists and Engineers with Modern Physics,*. Vol. 8. 2010: Brooks/Cole. 1558.
124. Comsol, *Introduction to LiveLink for MATLAB*, C. Multi-Physics, Editor 2012.
125. Press, W.H., et al., *NUMERICAL RECIPES - The Art of Scientific Computing*. Vol. 3rd. 2007, New York CAMBRIDGE UNIVERSITY PRESS. 1262.
126. Press, W.H., *Numerical Recipes 3rd Edition: The Art of Scientific Computing*2007: Cambridge University Press.
127. Schmuser, P., *Basic principles of RF superconductivity and superconducting cavities*, in *CAS - CERN Accelerator School: Intermediate Course on Accelerator Physics*2003, CERN: Zeuthen, Germany. p. 183-202.
128. Kim, S.H. and M. Doleans. *Principles of Superconducting Linear Accelerators* 2013; Available from: https://uspas.fnal.gov/materials/13Duke/Duke_SuperLinearAccel.shtml.
129. Palmer, R., *Muon Accelerators: An Integrated Path to Intensity and Energy Frontier Physics Capabilities*, in *Proton Accelerators for Science and Innovation: second annual meeting*, STFC, Editor 2013, RAL. p. 37.

Appendix A – Publications

WE5PFP001 - The Effects of Field Emitted Electrons on RF Surface

THE EFFECTS OF FIELD EMITTED ELECTRONS ON RF SURFACE

A. Zarrebini-Esfahani#, Mechanical Engineering, Imperial College London, U.K.
R. Seviour, M. Stables, Cockcroft Institute, Lancaster University, Lancaster, U.K.
M. Ristic, A. Kurup, K. Long, J. Pozimski, Imperial College London, U.K.

Abstract

The ever-growing demand for higher RF gradients has considerably increased the risk of breakdown in accelerating structures. Field emission is the most common form of RF breakdown that generates free electrons capable of inflicting irreversible damages on the RF surface. This paper presents a systematic experimental and simulation programme to understand possible sources and their influence on RF cavity operation.

INTRODUCTION

Breakdown which occurs both in RF and DC systems, has been the centre of attention for many year without any general agreement on what triggers this phenomenon [1]. Field emission is the most common problem encountered in superconducting and normal cavities. Grain edges, surface distortions and debris from past breakdown events have been identified as possible emission sites [2, 3]. The presence of defects enhances the local electric field that accelerates emitted electrons. These secondary electrons can cause discontinuities in RF, generate noise, gas burst and damage metallic and insulator surfaces [4]. The heat and stresses exerted by these electrons bombarding the RF surface can lead to surface deformations, creating additional emitting sites [3]. Although breakdown initiates locally, its effects are global.

Currently, the majority of the models focus on surface defects as the only source of emission. In order to develop a better understanding of breakdown, it is vital to study what factors contribute to the formation of such sites, hence lowering the performance of the structure.

PROPOSED RESEARCH PROGRAM

This study is in close partnership with the MUCOOL collaboration at Fermilab. Their ultimate goal is to develop muon-cooling systems for Muon Colliders and Neutrino Factory [5]. A series of high power RF tests are performed on button shaped samples using an 805 MHz closed cell pillbox cavity. Further details regarding the MUCOOL Testing Area (MTA) are given in [5-7].

Experimental Study

As demonstrated in figure 3 of [5], tests at the MTA show a striking drop in the supported RF gradient in the 805 MHz cavity when the solenoidal field is applied. This is of high concern for the Neutrino Factory. The quality and condition of the RF surface plays an important role in determining the performance of the accelerating structure. The MTA has been focusing extensively on testing different materials and surface coatings to evaluate their performance when operated within the solenoid field. However, surfaces can be damaged during production and assembly [3]. In order to understand cavity performance and thereby develop better means of production, one needs to look into how fabrication procedure defined the RF surface. This work is a systematic study proposed by the UKRF consortium (Imperial College London, Lancaster University, Cockcroft Institute) aiming to test copper samples fabricated using various techniques.

Experimental Setup

The design of the new button consists of a support mandrel and removable cap, allowing the use of a number of forming techniques. The cap sitting on top of the mandrel is the subject for high power testing. Currently, the cap is pressed from a flat oxygen free high thermal conductivity copper (OFHC) sheet.

It is vital to characterise the surface after each step right from material selection up to the end of production. The surface topology and chemical composition of the surface are studied by White light Interferometry and X-ray photo spectrometry (XPS). Scratches introduced during fabrication are removed in steps starting by hand polishing the surface with different grades of sand paper to eliminate larger scratches. A chemical etch followed by an ultrasonic bath would remove grease and larger particles. The surface becomes shiny through electro polishing (EP), using a standard 85% phosphoric acid and 15% butanol mix. Finally, the surface is cleared from any residuals through a high-pressure de-ionised water rinse.

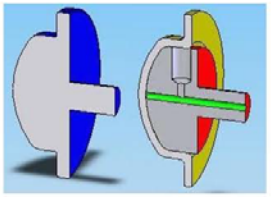

Figure 1: MTA buttons design (left) UKRF button design.

The removal of the damage layer would uncover the virgin copper, ensuring the exposure of the desirable surface to high electric field during testing. A final stage of surface characterisation is conducted once the sample has been tested. By studying the results from each stage of characterisation, it is possible to build a clear picture on how the surface has been changing throughout production. By comparing figures from various

#a.zarrebini06@ic.ac.uk

production methods, it would be possible to see which technique causes less damage, hence increasing the performance of the cavity.

Preliminary Results

In order to assess how the surface topology is being altered, a series of measurements have been conducted on buttons and flat copper samples taken from the same batch used to form the buttons. These are shown below in table 1 where A, B, C and D refer to modal average of received, mechanical polished, chemical etched and electro polished sample respectively.

Table 1: Surface roughness using Interferometer, modal average taken over 5 samples each case.

	Flat Sample		**Button**	
	Ra (nm)	Rq (nm)	Ra (nm)	Rq (nm)
A	106	143	356	459
B	140	194	180	240
C	252	362	220	292
D	93	121	98	120

Ra and Rq are the average surface roughness and the RMS roughness. The further Ra is from Rq, the more pronounced the defects. The pressed cap has a much rougher surface when received compared to flat samples, even when no machining has been performed. This demonstrates the fact that working the metallic surface to create the desired shape alters the surface topology. Figure 2 shows interferometer images of the altering metallic surface in the first and last stages of the surface preparation procedure.

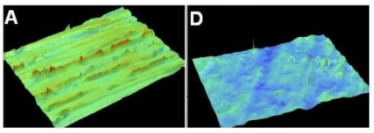

Figure 2: Interferometer images of OFHC copper [8].

The surface is levelled by the phosphoric acid present in the EP mix, while butanol is responsible for providing a greater control over the solution's conductivity. It is known that electro polishing with an 85% phosphoric acid gives rise to oxygen formation. This leads to creation of sever etched pits on the surface [9]. Oxygen formation can be minimised by careful control over the EP current/voltage, maintaining the anode near the critical cusp point as illustrated in figure 3 [10]. It is essential to maintain this profile as steady as possible to minimise alterations in the final polish.

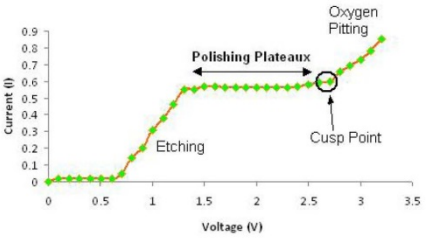

Figure 3: Characteristic plot for electro polishing.

The XPS investigations of figure 4 show fascinating changes in the chemical composition of Cu surface layers. We see a 96% reduction in carbon and oxygen contaminations after mechanical polishing followed by an additional drop of 50% through chemical etching. However, this process was reversed after EP with a 25 and 100 fold increases in carbon and oxygen respectively, due to the chemistry used. More interestingly is the addition of P impurities from EP, bonding in the surface layer to the Cu via 3S and 2P3/2.

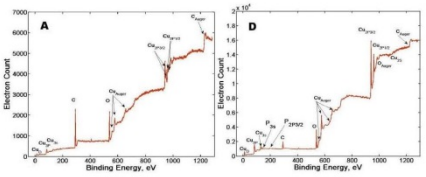

Figure 4: Binding energies of electrons released through XPS of OFHC copper sample [8].

Surfaces, depending on band structure, density of states (DoS) and environmental conditions, are capable of emitting electrons. Secondary Electron yield (SEY) describes the number of electrons emitted from a surface due to the impact of an incident electron. To gain an insight into this behaviour we used the numerical package DMol to calculate variational self consistent solutions to the density functional theory (DFT) equations [11], expressed in a numerical atomic orbital basis, so that we could represent the bonding seen experimental of the P. The solutions to these equations gave the wave functions and electron densities that we used to study the effects of P bonding on the band structure and Dos. The results are shown in figure 5, where we represented the system as an infinite slab of Cu with P introduced into the surface layer. These simulations indicate that the P impurities increase the Dos and band structure, causing overlapping. This indicates a higher ability to stream electrons from the material surface, leading to unpredictable behaviour.

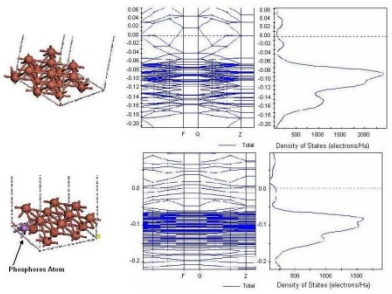

Figure 5: DFT simulations of copper with and without P impurity. Dos (left), band structure (right), dotted lines show the Fermi energy, units are in Hartees [8].

Simulation Study

In additional to the above work, it is important to simulate how free electrons can initiate breakdown depending on the way surface defects alter the electric (E) and magnetic (B) field profile of a cavity.

We use Comsol Multiphysics to create a 3D profile of E and B fields of a cavity. A major advantage of working in 3D is the possibility to place various asperities with different shapes and orientations anywhere in the model. Figure 6 demonstrates a cross sectional view of the E filed profile in an 805 MHz cavity. As expected, local field enhancements are observed around the defect.

The electrons behaviour is being studied using a homegrown particle tracking code that uses Matlab to extract the E and B fields from Comsol at any point in space. Being able to communicate directly with Comsol eliminates the need for pre-defined grid points. This allows precise extraction of parameters in order to track electrons from the emission site up to the point of impact.

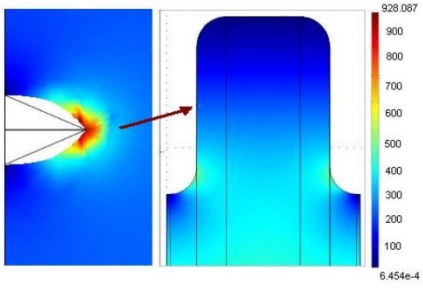

Figure 6: E field enhancement due to presence of defect on a flat surface in an 805 MHz cavity.

FUTURE PLAN

Although we are just beginning, we have some initial results showing how the manufacturing procedure affects the RF surface. This highlights the importance of the proposed study, which should provide vital information regarding manufacturing and assembly. This can lead to the development of more suitable and efficient techniques at later stages. We intend to expand this effort by looking at additional manufacturing techniques. Eventually, we aim to determine whether these electrons leave the systems or simply are trapped into the RF surface, causing secondary emissions. By examining various parameters at the point of impact, it would be possible to determine the level of heat and stresses generated.

REFERENCES

[1] Norem, J., Z. Insepov, and I. Konkashbaev, *Triggers for RF breakdown.* Nuclear Instruments and Methods in Physics Research Section A: Accelerators, Spectrometers, Detectors and Associated Equipment, 2005. **537**(3): p. 510-520.

[2] Norem, J., A. Hassanein, and I. Konkashbaev. *Mechanisms limiting high gradient rf cavities.* in *Particle Accelerator Conference, 2003. PAC 2003.* . 2003.

[3] Norem, J. and M. Pellin. *Gradient Limits And SCRF Performance.* [cited; Available from: http://web5.pku.edu.cn/srf2007/download/proceedings/TUP08.pdf.

[4] Seviour, R., *The Role of Elastic and Inelasting Electron Reflection in Multipactor Discharges.* IEEE Transactions on Electron Devices, 2005. **52**(8): p. 1927 - 1930.

[5] Norem, J., et al. *Recent RF Results From The MUCOOL Test Area.* in *Particle Accelerator Conference*. 2007. Albuquerque - New Mexico: IEEE.

[6] Johnstone, C. *MUCOOL Test Area At FermiLab.* in *Particle Accelerator Conference*. 2005. Knoxville, Tennessee: IEEE.

[7] Norem, J., et al. *The RF Experimental Program In The FermiLab MUCOOL Test Area.* in *Particle Accelerator Conference* 2005. Knoxville, Tennessee: IEEE.

[8] Seviour, R., et al. *UKNF note-44*.

[9] Shih-Chieh, C., et al., *Superpolishing for Planarizing Copper Damascene Interconnects.* Electrochemical and Solid-State Letters, 2003. **6**(5): p. G72-G74.

[10] Jacquet, P.A., in *Metal Finishing* 1949. p. 62 - 69.

[11] Kieron, B., W. Jan, and E.K.U. Gross, *Time-dependent density functional theory: Past, present, and future.* The Journal of Chemical Physics, 2005. **123**(6): p. 062206.

WEPEC051 Proceedings of IPAC'10, Kyoto, Japan

3D SIMULATION OF THE EFFECTS OF SURFACE DEFECTS ON FIELD EMITTED ELECTRONS

A. Zarrebini-Esfahani#*, M. Ristic*, K. Long, Imperial College London, U.K.
R. Seviour, Cockcroft Institute, Lancaster University, Lancaster, U.K.

Abstract

The ever-growing demand for higher RF gradients has considerably increased the risk of breakdown in accelerating structures. Field emission is the most common form of RF breakdown that generates free electrons capable of inflicting irreversible damages on the RF surface. This paper presents a simulation study to understand the effects of defects on local fields and behaviour of field emitted electrons in an RF cavity.

INTRODUCTION

Breakdown which occurs both in RF and DC systems has been the centre of attention for many years without any general agreement on what triggers this phenomenon [1]. Field emission is the most common problem encountered in super and normal conducting cavities. Grain edges, surface distortions and debris from past breakdown events have been identified as possible emission sites [2-3]. The presence of defects enhances the local electric field that accelerates emitted electrons. The heat and stresses exerted by these electrons bombarding the RF surface can lead to surface deformations, creating additional emitting sites and release electrons [3]. These secondary electrons can cause discontinuities in RF, generate noise, gas burst and damage metallic and insulator surfaces [4].

PROPOSED RESEARCH PROGRAM

Although breakdown has been studied for many years, the problem is complex and has many causes. A complete study of such factors is needed to understand the surface science and engineering issues that affect the performance of RF structures. As part of the UKRF collaboration R&D program, the goal is to provide a systematic approach based on experimental work and simulation studies.

Experimental Study

This work is carried out in close partnership with the US MuCool collaboration. The ultimate goal of MuCool is to develop muon-cooling systems for the Muon Collider and the Neutrino Factory. Further details regarding MuCool Test Area (MTA) are given in [5-7].

As demonstrated in figure 3 of [6], tests at the MTA show a striking drop in the RF gradient that can be achieved in a 805 MHz cavity when a solenoidal field is applied. This is of great concern for the Neutrino Factory and Muon Collider communities. The quality and condition of the RF surface plays an important role in determining the performance of the accelerating structure. In order to understand cavity performance and thereby develop better means of production, one needs to look into how fabrication procedures affect the RF surface. A series of high power RF tests have been performed by the MuCool collaboration on button-shaped samples using an 805 MHz closed cell pillbox cavity. This work was presented at PAC09 [8].

Simulation Study

Although RF breakdown may be initiated locally, its effects are felt globally in many forms such as high local Ohmic heating and field/fracture evaporation. Surface defects and impurities play a major role in altering the E and B fields, inducing local enhancements. Such points can then act as field emission sites, leading to eventual RF breakdown. In order to develop a better understanding of RF breakdown, it is vital to investigate how free electrons can initiate breakdown depending on the way surface defects alter the local E and B field of an RF cavity.

This study aims to model the field profile in an RF cavity and use the relevant data to track emitted electrons from the surface. Hence, the model will replicate the behaviour of the electrons and allow the physics of RF breakdown to be investigated.

Model Setup

To maintain compatibility with other collaborators, the model chosen is MuCool 805 MHz pillbox normal-conducting copper cavity shown below in figure 1.

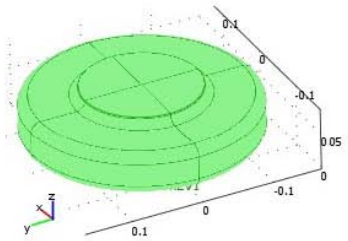

Figure 1: MTA 805 MHz copper pillbox cavity.

Comsol Multiphysics is used to generate a 3D E and B field profile using two different models. The first is a plain cavity. In the second model, a micron size defect is introduced. As predicted, the defect alters the field by inducing a local enhancement shown in figure 2.

#a.zarrebini06@ic.ac.uk *Mechanical Engineering

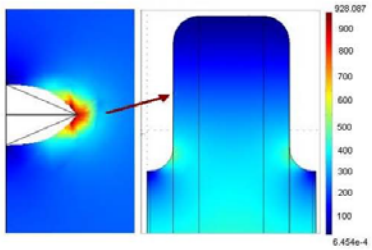

Figure 2: E field enhancement due to a surface defect

Once the field is generated, a home grown particle tracking code based on Matlab, models the behaviour of a free electron released from an emission site. This code is designed to extract field parameters at given points directly from Comsol, enabling the new position and velocity of the travelling electron to be calculated in Cartesian coordinates, using the Lorentz force.

Preliminary Results

In order to validate the code, we have used point A (0, 0, 0) as a benchmark. The physics suggest that the only E field is in the z direction (Ez) should exist. However, our initial results show that a level of error exists in the 3D field profile that is generated. This is more evident in x and y components. This can be reduced by increasing the number of elements, while reducing their average size. An example of mesh refinement is shown below in figure 3, where the iris of the cavity has a higher mesh density.

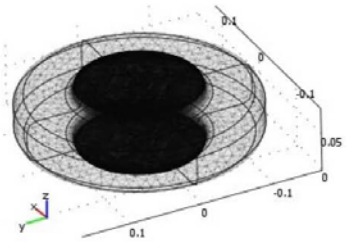

Figure 3: An example of an adaptive mesh refinement.

Although the noise level is reduced through mesh refinement, it is not possible to eliminate them fully due to software limitations. The solution lies within the geometry being modelled. As the cavity is axis-symmetric, it is possible to use a 2D model to meet the standard required for the elements quality. An early examination reveals the dramatic drop in the noise seen in the generated field profile. This demonstrates the ability of Comsol to generate better quality 2D meshes compared to conventional 3D models, while using less computing power. Table 1 demonstrates this in detail.

Table 1: Reduction in maximum E_x value (error) through mesh improvement at point A (0, 0, 0) as a benchmark

	No. of Elements	No. of Mesh Points	Error (V/M)
3D	20,830	51,430	2
	321,169	74,658	0.5
	984,870	234,446	0.4
2D	147,892	80,596	0

Once the correct field map is obtained, it is necessary to evaluate the tracker. The first step would be to compare the fields generated by the tracker to the one obtained with Comsol. As expected, Ez is at its maximum at the centre of the cavity. If Ez is plotted along the central line from one end of the cavity to the other, the maximum field would also be at the cavity's mid-point as demonstrated in figure 4. It is possible to see how the field obtained from Matlab correlates with the one generated through Comsol. Furthermore, a big improvement is observed when comparing the 2D axis-symmetric with initial 3D models as noted in table 1.

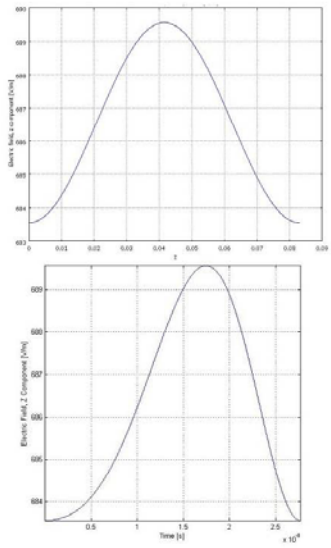

Figure 4: E_z vs. Z produced by Comsol (top), E_z vs. Time produced by Matlab particle tracker (bottom).

Although we only obtain 2D field parameter in cylindrical coordinates (r, z), it is possible to convert this into a 3D plot through several simple mathematical functions. This would provide parameters in a 3D

Cartesian coordinate system. Detailed mathematical functions used can be found in [9]. The second stage of validation consists of releasing an electron from point A, while computing its new velocity and position through a series of integrations using the field parameters.

At point A, only E_z is present with zero B field. As shown in figure 5, it is expected that electron travels in a straight line, demonstrates the ability of the tracker code to produce results in agreement with the theoretical assumptions. In order to test the particle tracker at positions where all six component of the E and B field are present, an electron is released from point B (0.02, 0.02, 0). The plot shown below clearly displays the ability of the tracker to predict the electron's path of motion while under influence of other field components.

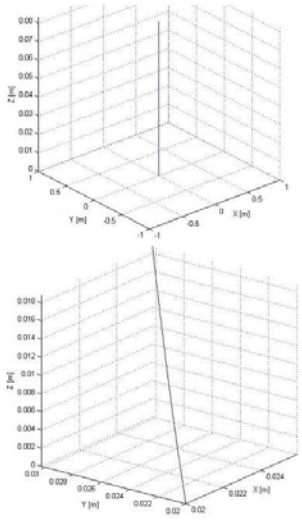

Figure 5: Electron motion at Point A [5eV-v_z] (top), Point B with [5eV, v_x-v_y-v_z] (bottom)

Approach Advantages

The main advantage of the tracker being developed in this study is the great flexibility it provides to the user in comparison to other counterparts out in the community. The results are fed directly from Comsol into Matlab, eliminating the need to follow a pre-defined grid. This in turn would allow different models to be used separately as an input source for the tracker. As a result, 2D symmetrical models can be used, reducing the computational demands and execution time dramatically. By doing so, the user would have the ability to place defects with various shapes at random location on the RF surface. As result, simple and robust 2D field maps are used, while electrons are tracked in 3D.

FUTURE PLAN

Although we are at early stages, we have some initial results demonstrating the ability of the home-grown particle tracker. Currently the introduction of a defect is only possible in a 3D model as it breaks the symmetry of the 2D model. To resolve this issue, two separate models need to be developed. First being the original model used above, this will provide the global field profile of the cavity. The second model would treat the defect as an isolated object, allowing it to be modelled in a 2D axis-symmetric fashion. The electrons will initially be tracked in the first model and the output can serve as initial conditions for the second global model. This would ensure maintaining axis-symmetry at all time and producing 3D plots. Further FEA analysis would be performed by extracting velocity at the point of impact. This in turn can be used to assess the possibility of secondary electron emissions. Moreover, the addition of a time varying E and B field can yield more realistic results.

REFERENCES

[1] Norem, J., Z. Insepov, and I. Konkashbaev, *Triggers for RF breakdown.* Nuclear Instruments and Methods in Physics Research Section A: Accelerators, Spectrometers, Detectors and Associated Equipment, 2005. **537**(3): p. 510-520.

[2] Norem, J., A. Hassanein, and I. Konkashbaev. *Mechanisms limiting high gradient rf cavities.* in *Particle Accelerator Conference, 2003. PAC 2003.* . 2003.

[3] Norem, J. and M. Pellin. *Gradient Limits And SCRF Performance*. Available from: http://web5.pku.edu.cn/srf2007/download/proceedings/TUP08.pdf.

[4] Seviour, R., *The Role of Elastic and Inelasting Electron Reflection in Multipactor Discharges.* IEEE Transactions on Electron Devices, 2005. **52**(8): p. 1927 - 1930.

[5] Johnstone, C. *MUCOOL Test Area At FermiLab.* in *Particle Accelerator Conference*. 2005. Knoxville, Tennessee: IEEE.

[6] Norem, J., et al. *Recent RF Results From The MUCOOL Test Area.* in *Particle Accelerator Conference*. 2007. Albuquerque - New Mexico: IEEE.

[7] Norem, J., et al. *The RF Experimental Program In The FermiLab MUCOOL Test Area.* in *Particle Accelerator Conference* 2005. Knoxville, Tennessee: IEEE.

[8] Zarrebini, A., et al. *The Effects Of Field Emitted Electrons On RF Surface.* in *PAC09*. 2009. Vancouver.

[9] Weisstein, E.W. *Cylindrical Coordinates.* Mathworld - A Wolfram Web Resource 2010; Available from: http://mathworld.wolfram.com/CylindricalCoordinates.html

Appendix B – Source Codes

Initiation Command

```
clc
format long

evx=0;
evy=0;
evz=0;

vx=sqrt((2*evx*1.60217e-19)/9.10938188e-31);
vy=sqrt((2*evy*1.60217e-19)/9.10938188e-31);
vz=sqrt((2*evz*1.60217e-19)/9.10938188e-31);
vx=0;
vy=0;
vz=0;
y0 = [0 0.05 0 vx vy vz];
[t,y]=A11(y0);
```

3D – Tracking Algorithm

```
function [t,y]=B11(y0)

tend=10;
tfield=0;

yfin=[];
tfin=[];
EBy0=[];

temp1=1;
temp2=0;

for i=1:10000
    number=i
    xx(1:3,1)=y0(1,1:3);

    [E B] = field(xx);

     tfield=tfield+10/(1e13);
    w=2*pi*850e6;

    E=E*temp1;
    B=B*temp2;

     [t,y]=ode45(@predpray,[-1e-12+tfield,tfield],y0,[],E,B);

    temp1=cos(w*t(end));
    temp2=cos(w*t(end)+pi/2);

    tfin=[tfin;t];
    yfin=[yfin;y];
    z=[tfin,yfin];
    y0(1:6)=y(end,1:6);
    ebyzero=[E,B,y0];
    EBy0=[EBy0;ebyzero];

    fid=fopen('file.txt','wt');
    fprintf(fid,'t               ,  x          ,     y          ,
z       ,   vx       ,      vy     ,     vz \n\n  ');
    fprintf(fid,'%3.10f %3.10f %3.10f %3.10f %3.10f %3.10f %3.10f
\n',z');
    fclose(fid);
    save('file.mat','z','tfin','yfin');
```

```
    fid=fopen('fieldfile-11-05-14.txt','wt');
    fprintf(fid,'Ex           ,Ey            ,Ez           ,Bx
,By   ,        Bz          ,  x          ,     y          ,     z
,      vx      ,      vy     ,      vz \n\n   ');
    fprintf(fid,'%3.10f %3.10f %3.10f %3.10f %3.10f %3.10f %3.10f
%3.10f %3.10f %3.10f %3.10f %3.10f \n',EBy0');
    fclose(fid);
    save('fieldfile-11-05-14.mat','EBy0');

end

end

function yp=predpray(t,y,E,B)

q=-1.6e-19; % Electron Charge
m=9.1e-31; % Electron Mass

v2=y(4)^2+y(5)^2+y(6)^2;
c2=(3e8)^2;
beta2=v2/c2;
gamma=1/sqrt(1-beta2);
qm=q/m;

yp=zeros(6,1);
yp(1)=y(4);
yp(2)=y(5);
yp(3)=y(6);

yp(4)=qm*sqrt(1-(y(4)^2+y(5)^2+y(6)^2)/c2)*(E(1)+B(3)*y(5)-
B(2)*y(6))-(qm*sqrt(1-(y(4)^2+y(5)^2+y(6)^2)/c2)/c2)*(
y(4)*E(1)+y(5)*E(2)+y(6)*E(3))*y(4);
yp(5)=qm*sqrt(1-(y(4)^2+y(5)^2+y(6)^2)/c2)*(E(2)-
B(3)*y(4)+B(1)*y(6))-(qm*sqrt(1-(y(4)^2+y(5)^2+y(6)^2)/c2)/c2)*(
y(4)*E(1)+y(5)*E(2)+y(6)*E(3))*y(5);
yp(6)=qm*sqrt(1-(y(4)^2+y(5)^2+y(6)^2)/c2)*(E(3)+B(2)*y(4)-
B(1)*y(5))-(qm*sqrt(1-(y(4)^2+y(5)^2+y(6)^2)/c2)/c2)*(
y(4)*E(1)+y(5)*E(2)+y(6)*E(3))*y(6);

end

function [E B]=field(xx)

Arash3D=mphload('805-D1-a5-b5-c6.mph');
Arash3D.hist.disable

[Ex,Ey,Ez]=mphinterp(Arash3D,{'Ex','Ey','Ez'},'coord',xx);
[Bx,By,Bz]=mphinterp(Arash3D,{'emw.Bx*exp(i*pi*90/180)','emw.By*ex
p(i*pi*90/180)','emw.Bz*exp(i*pi*90/180)'},'coord',xx);

a=21e3;
ex=Ex*a;
ey=Ey*a;
ez=Ez*a;
bx=Bx*a;
```

```
by=By*a;
bz=Bz*a;

B = [real(bx) real(by) real(bz)];
E = [real(ex) real(ey) real(ez)];

end
```

2D Tracking Algorithm

```
function [t,y]=A11(y0)

tend=10;
tfield=0;

yfin=[];
tfin=[];
EBy0=[];

temp1=1;
temp2=0;

for i=1:10000
    number=i
    xx(1:3,1)=y0(1,1:3);

    [E B] = field(xx);

  tfield=tfield+10/(1e13);

    w=2*pi*850e6;

    E=E*temp1;
    B=B*temp2;

     [t,y]=ode45(@predpray,[-1e-12+tfield,tfield],y0,[],E,B);

    temp1=cos(w*t(end));
    temp2=cos(w*t(end)+pi/2);

    tfin=[tfin;t];
    yfin=[yfin;y];
    z=[tfin,yfin];
    y0(1:6)=y(end,1:6);
    ebyzero=[E,B,y0];
    EBy0=[EBy0;ebyzero];

    fid=fopen('2D-plain.txt','wt');
    fprintf(fid,'t               ,  x          ,     y          ,
z       ,   vx       ,       vy     ,     vz \n\n  ');
    fprintf(fid,'%3.10f %3.10f %3.10f %3.10f %3.10f %3.10f %3.10f
\n',z');
    fclose(fid);
    save('2D-plain.mat','z','tfin','yfin');

    fid=fopen('field2D-plain.txt','wt');
    fprintf(fid,'Ex           ,Ey             ,Ez           ,Bx
,By   ,        Bz          ,  x          ,     y          ,     z
,      vx       ,       vy     ,      vz \n\n  ');
    fprintf(fid,'%3.10f %3.10f %3.10f %3.10f %3.10f %3.10f %3.10f
%3.10f %3.10f %3.10f %3.10f %3.10f \n',EBy0');
```

```
    fclose(fid);
    save('field2D-plain.mat','EBy0');
end
end

function yp=predpray(t,y,E,B)

q=-1.6e-19; % Electron Charge
m=9.1e-31; % Electron Mass

v2=y(4)^2+y(5)^2+y(6)^2;
c2=(3e8)^2;
beta2=v2/c2;
gamma=1/sqrt(1-beta2);
qm=q/m;

yp=zeros(6,1);
yp(1)=y(4);
yp(2)=y(5);
yp(3)=y(6);

yp(4)=qm*sqrt(1-(y(4)^2+y(5)^2+y(6)^2)/c2)*(E(1)+B(3)*y(5)-
B(2)*y(6))-(qm*sqrt(1-(y(4)^2+y(5)^2+y(6)^2)/c2)/c2)*(
y(4)*E(1)+y(5)*E(2)+y(6)*E(3))*y(4);
yp(5)=qm*sqrt(1-(y(4)^2+y(5)^2+y(6)^2)/c2)*(E(2)-
B(3)*y(4)+B(1)*y(6))-(qm*sqrt(1-(y(4)^2+y(5)^2+y(6)^2)/c2)/c2)*(
y(4)*E(1)+y(5)*E(2)+y(6)*E(3))*y(5);
yp(6)=qm*sqrt(1-(y(4)^2+y(5)^2+y(6)^2)/c2)*(E(3)+B(2)*y(4)-
B(1)*y(5))-(qm*sqrt(1-(y(4)^2+y(5)^2+y(6)^2)/c2)/c2)*(
y(4)*E(1)+y(5)*E(2)+y(6)*E(3))*y(6);

end


function [E B]=field(xx)

Arash2D=mphload('2D-plain1.mph');
disp('Reading 2D model!')

r=sqrt(xx(1)^2+xx(2)^2);
ps=[r;xx(3)];
phi=atan2(xx(2),xx(1)); % angle between r and x. using
arctan2(y/x)

if (r == 0)

    c=5300;

    Ez=mphinterp(Arash2D,{'Ez'},'coord',ps);
    ez=Ez*c;
    Ex=0;
    Ey=0;
    Bx=0;
    By=0;
    Bz=0;
```

```
else

    [Er,Ez]=mphinterp(Arash2D,{'Er','Ez'},'coord',ps);

Bphi=mphinterp(Arash2D,{'emw.Bphi*exp(i*pi*90/180)'},'coord',ps);
    Br=mphinterp(Arash2D,{'emw.Br*exp(i*pi*90/180)'},'coord',ps);

    c=5300;

    ex=Er*cos(phi)*c;
    ey=Er*sin(phi)*c;
    ez=Ez*c;

    bx1=-Bphi*sin(phi)*c;
    by1=Bphi*cos(phi)*c;
    bx2=Br*cos(phi)*c;
    by2=Br*sin(phi)*c;
    bz=0;

    bx=bx1+bx2;
    by=by1+by2;

end

B = [real(bx) real(by) real(bz)];
E = [real(ex) real(ey) real(ez)];

end
```

2D – 3D Tracking Algorithm

```
function [t,y]=C8(y0)

tend=10;
tfield=0;

yfin=[];
tfin=[];
EBy0=[];

temp1=1;
temp2=0;

for i=1:10000
    number=i
    xx(1:3,1)=y0(1,1:3);

    [E B] = field(xx);

     tfield=tfield+10/(1e13);
    w=2*pi*850e6;

    E=E*temp1;
    B=B*temp2;

     [t,y]=ode45(@predpray,[-1e-12+tfield,tfield],y0,[],E,B);

    temp1=cos(w*t(end));
    temp2=cos(w*t(end)+pi/2);

    tfin=[tfin;t];
    yfin=[yfin;y];
    z=[tfin,yfin];
    y0(1:6)=y(end,1:6);
    ebyzero=[E,B,y0];
    EBy0=[EBy0;ebyzero];

    fid=fopen('file.txt','wt');
    fprintf(fid,'t               ,  x          ,     y          ,
z       ,   vx       ,      vy     ,     vz \n\n  ');
    fprintf(fid,'%3.10f %3.10f %3.10f %3.10f %3.10f %3.10f %3.10f
\n',z');
    fclose(fid);
    save('file.mat','z','tfin','yfin');

    fid=fopen('fieldfile-11-05-14.txt','wt');
    fprintf(fid,'Ex           ,Ey             ,Ez           ,Bx
,By   ,        Bz          ,  x          ,     y          ,    z
,     vx      ,      vy    ,      vz \n\n  ');
```

```
    fprintf(fid,'%3.10f %3.10f %3.10f %3.10f %3.10f %3.10f %3.10f
%3.10f %3.10f %3.10f %3.10f %3.10f \n',EBy0');
    fclose(fid);
    save('fieldfile-11-05-14.mat','EBy0');

    end

end

function yp=predpray(t,y,E,B)

q=-1.6e-19; % Electron Charge
m=9.1e-31; % Electron Mass

v2=y(4)^2+y(5)^2+y(6)^2;
c2=(3e8)^2;
beta2=v2/c2;
gamma=1/sqrt(1-beta2);
qm=q/m;

yp=zeros(6,1);
yp(1)=y(4);
yp(2)=y(5);
yp(3)=y(6);

yp(4)=qm*sqrt(1-(y(4)^2+y(5)^2+y(6)^2)/c2)*(E(1)+B(3)*y(5)-
B(2)*y(6))-(qm*sqrt(1-(y(4)^2+y(5)^2+y(6)^2)/c2)/c2)*(
y(4)*E(1)+y(5)*E(2)+y(6)*E(3))*y(4);
yp(5)=qm*sqrt(1-(y(4)^2+y(5)^2+y(6)^2)/c2)*(E(2)-
B(3)*y(4)+B(1)*y(6))-(qm*sqrt(1-(y(4)^2+y(5)^2+y(6)^2)/c2)/c2)*(
y(4)*E(1)+y(5)*E(2)+y(6)*E(3))*y(5);
yp(6)=qm*sqrt(1-(y(4)^2+y(5)^2+y(6)^2)/c2)*(E(3)+B(2)*y(4)-
B(1)*y(5))-(qm*sqrt(1-(y(4)^2+y(5)^2+y(6)^2)/c2)/c2)*(
y(4)*E(1)+y(5)*E(2)+y(6)*E(3))*y(6);

end

function [E B]=field(xx)

if ( (xx(1)> 0.048 && xx(1)<0.052) && (xx(2)> 0.048 && xx(2)<
0.052)  &&  xx(3)< 0.004)

    Arash3D=mphload('805-D1-a5-b5-c6.mph');
    Arash3D.hist.disable

[Ex,Ey,Ez]=mphinterp(Arash3D,{'Ex','Ey','Ez'},'coord',xx);
[Bx,By,Bz]=mphinterp(Arash3D,{'emw.Bx*exp(i*pi*90/180)','emw.By*ex
p(i*pi*90/180)','emw.Bz*exp(i*pi*90/180)'},'coord',xx);

a=21e3;
ex=Ex*a;
ey=Ey*a;
ez=Ez*a;
bx=Bx*a;
by=By*a;
```

```
bz=Bz*a;

else

    Arash2D=mphload('2D-plain1.mph');
disp('Reading 2D model!')

r=sqrt(xx(1)^2+xx(2)^2);
ps=[r;xx(3)];
phi=atan2(xx(2),xx(1)); % angle between r and x. using
arctan2(y/x)

if (r == 0)

    c=5300;

    Ez=mphinterp(Arash2D,{'Ez'},'coord',ps);
    ez=Ez*c;
    Ex=0;
    Ey=0;
    Bx=0;
    By=0;
    Bz=0;

else

    [Er,Ez]=mphinterp(Arash2D,{'Er','Ez'},'coord',ps);

Bphi=mphinterp(Arash2D,{'emw.Bphi*exp(i*pi*90/180)'},'coord',ps);
    Br=mphinterp(Arash2D,{'emw.Br*exp(i*pi*90/180)'},'coord',ps);

    c=5300;

    ex=Er*cos(phi)*c;
    ey=Er*sin(phi)*c;
    ez=Ez*c;

    bx1=-Bphi*sin(phi)*c;
    by1=Bphi*cos(phi)*c;
    bx2=Br*cos(phi)*c;
    by2=Br*sin(phi)*c;
    bz=0;

    bx=bx1+bx2;
    by=by1+by2;

end

B = [real(bx) real(by) real(bz)];
E = [real(ex) real(ey) real(ez)];

end
```

Appendix C – Engineering Drawing

The following pictures shows the engineering drawings drafted prior to design and manufacture various parts needed for the Button assembly and transport Jig used in this study.

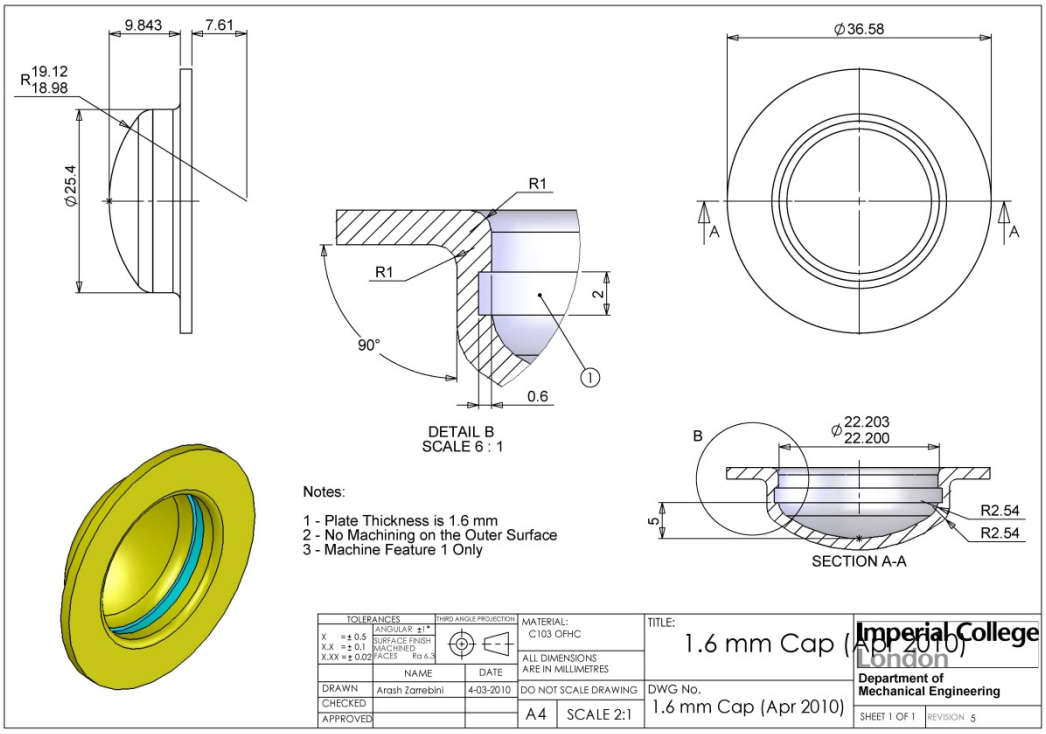

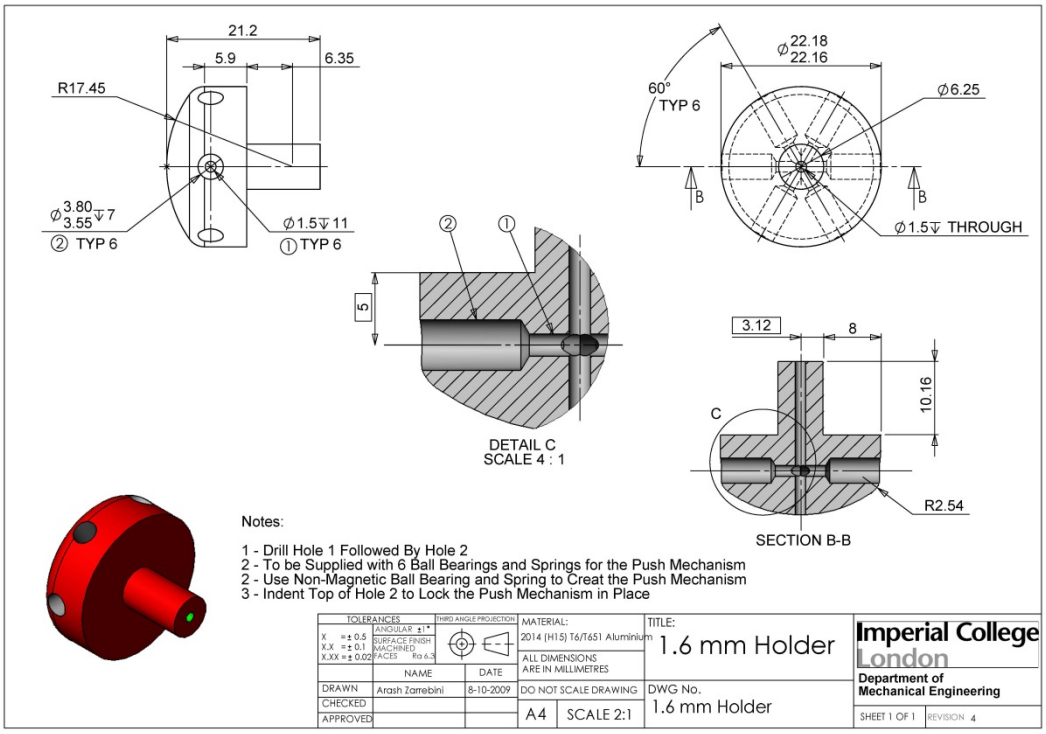

Notes:

1 - Drill Hole 1 Followed By Hole 2
2 - To be Supplied with 6 Ball Bearings and Springs for the Push Mechanism
2 - Use Non-Magnetic Ball Bearing and Spring to Creat the Push Mechanism
3 - Indent Top of Hole 2 to Lock the Push Mechanism in Place

TOLERANCES: X = ± 0.5, X.X = ± 0.1, X.XX = ± 0.02; ANGULAR ±1°; SURFACE FINISH MACHINED FACES Ra 6.3; THIRD ANGLE PROJECTION			MATERIAL: 2014 (H15) T6/T651 Aluminium	TITLE: 1.6 mm Holder	Imperial College London, Department of Mechanical Engineering
	NAME	DATE	ALL DIMENSIONS ARE IN MILLIMETRES		
DRAWN	Arash Zarrebini	8-10-2009	DO NOT SCALE DRAWING	DWG No. 1.6 mm Holder	
CHECKED			A4 SCALE 2:1		SHEET 1 OF 1 REVISION 4
APPROVED					

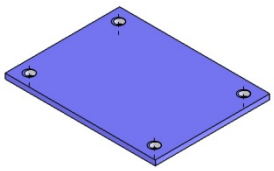

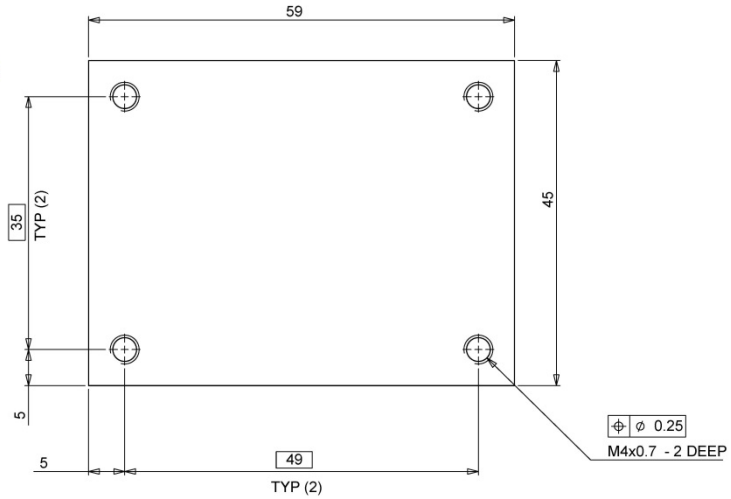

Notes:

1 - PLATE THICKNESS IS 3 mm

2 - REMOVE ALL SHARP EDGES

TOLERANCES: X = ± 0.5, X.X = ± 0.1, X.XX = ± 0.02; ANGULAR ±1°; SURFACE FINISH MACHINED FACES Ra 6.3; THIRD ANGLE PROJECTION			MATERIAL: 2014 (H15) T6/T651 Aluminium	TITLE: Base Plate	Imperial College London, Department of Mechanical Engineering
	NAME	DATE	ALL DIMENSIONS ARE IN MILLIMETRES		
DRAWN	Arash Zarrebini	09-01-2008	DO NOT SCALE DRAWING	DWG No. Base Plate	
CHECKED			A4 SCALE 2:1		SHEET 1 OF 1 REVISION 1
APPROVED					

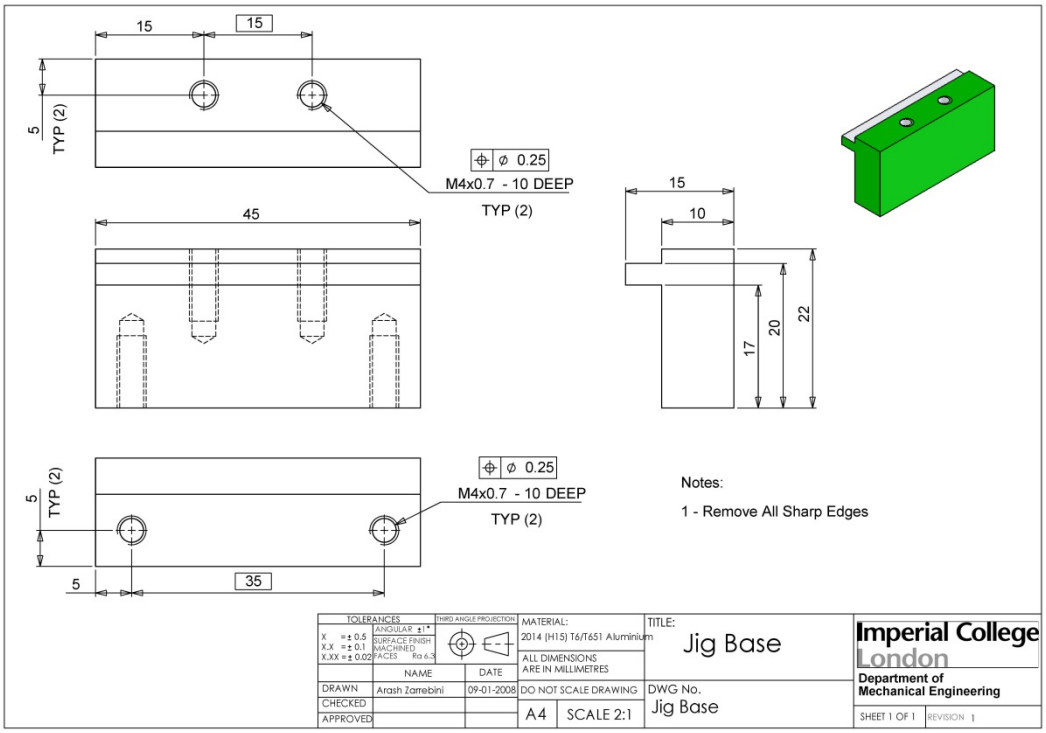
15
15
5
TYP (2)
⌖ Ø 0.25
M4x0.7 - 10 DEEP
TYP (2)
45
15
10
22
20
17
5
TYP (2)
⌖ Ø 0.25
M4x0.7 - 10 DEEP
TYP (2)
5
35
Notes:
1 - Remove All Sharp Edges
TOLERANCES
THIRD ANGLE PROJECTION
X = ± 0.5
X.X = ± 0.1
X.XX = ± 0.02
ANGULAR ±1°
SURFACE FINISH
MACHINED FACES Ra 6.3
MATERIAL:
2014 (H15) T6/T651 Aluminium
ALL DIMENSIONS ARE IN MILLIMETRES
TITLE:
Jig Base
NAME
DATE
DRAWN
Arash Zarrebini
09-01-2008
CHECKED
APPROVED
DO NOT SCALE DRAWING
DWG No.
Jig Base
A4
SCALE 2:1
Imperial College London
Department of Mechanical Engineering
SHEET 1 OF 1
REVISION 1

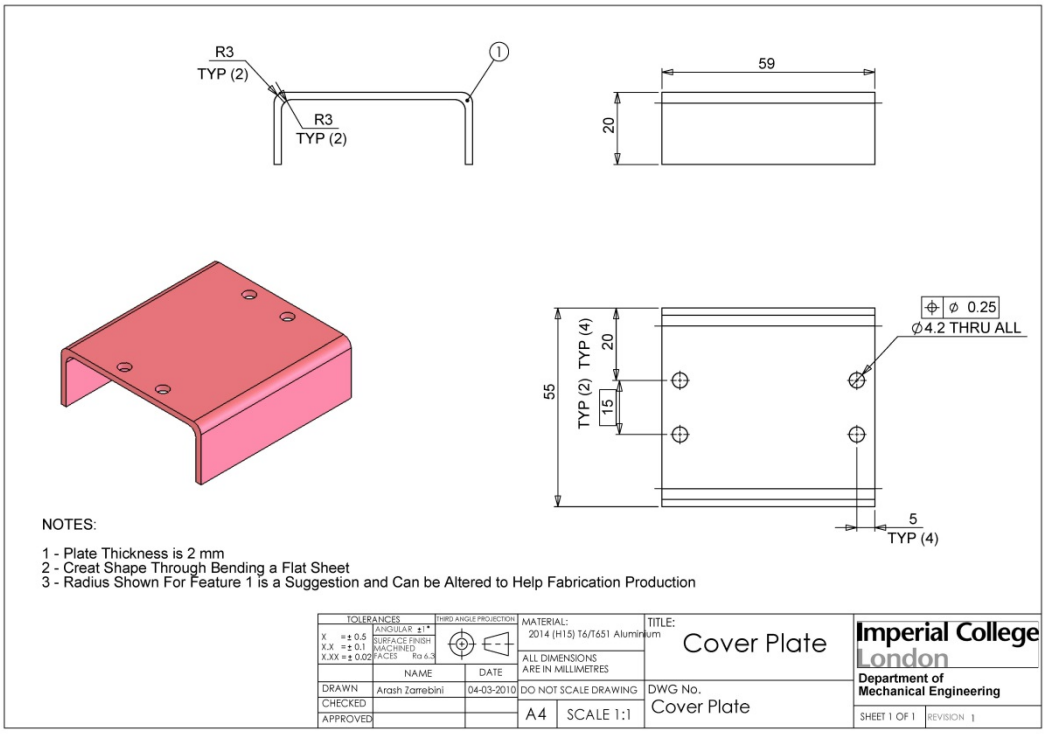
R3
TYP (2)
R3
TYP (2)
1
59
20
55
TYP (2)
TYP (4)
20
15
⌖ Ø 0.25
Ø4.2 THRU ALL
5
TYP (4)
NOTES:
1 - Plate Thickness is 2 mm
2 - Creat Shape Through Bending a Flat Sheet
3 - Radius Shown For Feature 1 is a Suggestion and Can be Altered to Help Fabrication Production
TOLERANCES
THIRD ANGLE PROJECTION
X = ± 0.5
X.X = ± 0.1
X.XX = ± 0.02
ANGULAR ±1°
SURFACE FINISH
MACHINED FACES Ra 6.3
MATERIAL:
2014 (H15) T6/T651 Aluminium
ALL DIMENSIONS ARE IN MILLIMETRES
TITLE:
Cover Plate
NAME
DATE
DRAWN
Arash Zarrebini
04-03-2010
CHECKED
APPROVED
DO NOT SCALE DRAWING
DWG No.
Cover Plate
A4
SCALE 1:1
Imperial College London
Department of Mechanical Engineering
SHEET 1 OF 1
REVISION 1

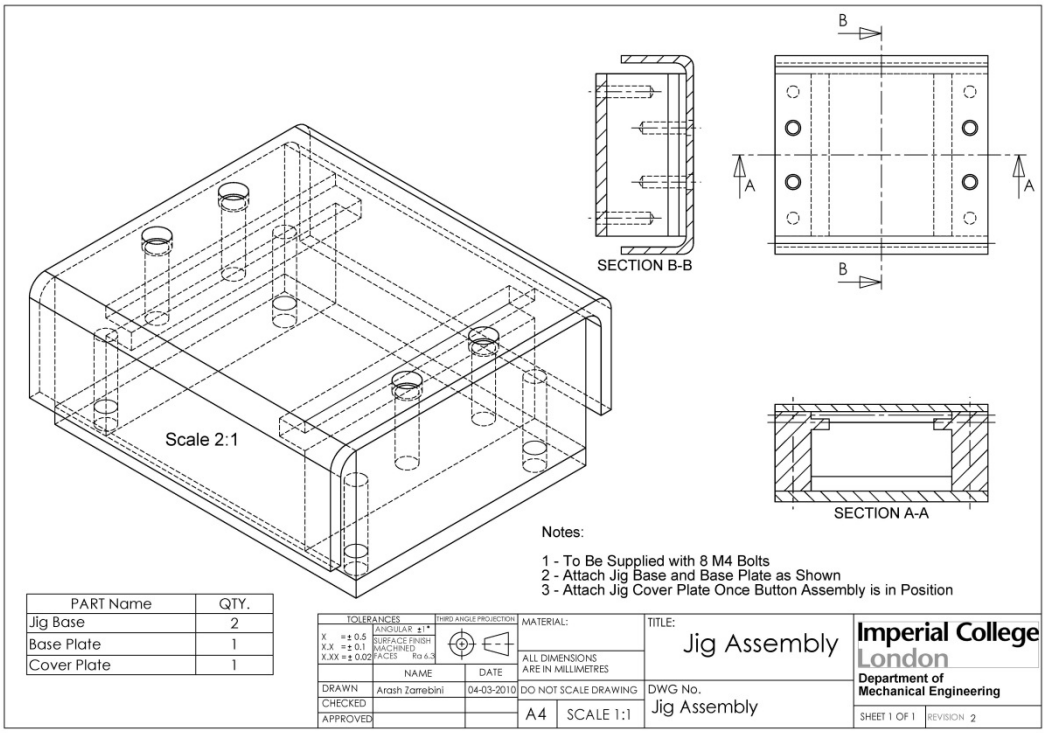

Notes:

1 - To Be Supplied with 8 M4 Bolts
2 - Attach Jig Base and Base Plate as Shown
3 - Attach Jig Cover Plate Once Button Assembly is in Position

PART Name	QTY.
Jig Base	2
Base Plate	1
Cover Plate	1

TOLERANCES: ANGULAR ±1° / X = ±0.5, X.X = ±0.1, X.XX = ±0.02 / SURFACE FINISH MACHINED FACES Ra 6.3	THIRD ANGLE PROJECTION	MATERIAL: / ALL DIMENSIONS ARE IN MILLIMETRES
TITLE: Jig Assembly	Imperial College London, Department of Mechanical Engineering	
NAME	DATE	
DRAWN: Arash Zarrebini	04-03-2010	DO NOT SCALE DRAWING
CHECKED		A4 SCALE 1:1
APPROVED		DWG No. Jig Assembly
SHEET 1 OF 1	REVISION 2	